THE UNIVERSITY *of* EDINBURGH

CELLULAR AND MOLECULAR ANATOMY OF THE MAMMALIAN NEUROMUSCULAR JUNCTION IN HEALTH AND DISEASE

Ines Boehm

A thesis submitted for the degree of

Doctor of Philosophy

The University of Edinburgh

2021

Declaration

(a) that the thesis has been composed by the student, and

(b) either that the work is the student's own, or, if the student has been a member of a research group, that the student has made a substantial contribution to the work, such contribution being clearly indicated, and

(c) that the work has not been submitted for any other degree or professional qualification except as specified, and

(d) that any included publications are the student's own work, except where indicated throughout the thesis and summarized and clearly identified on the declarations page of the thesis.

Signature ……

Date ……..……

Abstract

The vast diversity across the animal kingdom and in particular within the class of mammals is not only of evolutionary interest, but also plays an important role in framing the context of research in which mammalian animal models are utilised. Research addressing neurodegenerative diseases has struggled to translate from the widely used mouse model to humans. We now know the neuromuscular junction (NMJ) - the key player responsible for generation of movement and often a target in disease - is strikingly different between mouse and human, thus questioning the validity of rodent models.

Building upon recent studies assessing the healthy human NMJ, this project directly sought to examine the human NMJ in disease and whether predictions made from mouse models also applied in humans. Furthermore, this project aimed to identify mammalian models more similar to human NMJ morphology, which could be used as alternatives to the mouse. Following morphological NMJ analysis of the human and mammalian NMJ, molecular pathways contributing to the stability of the human NMJ during healthy ageing of muscle were analysed, as this knowledge could prove beneficial in the generation of more translatable animal models and therapies.

To evaluate whether changes at the NMJ as predicted from mouse models also occurred in humans with muscle wasting, NMJ morphology was compared between patients with cancer cachexia, weight stable cancer patients, and control patients. Surgical muscle biopsies were sampled, NMJs were immunofluorescently visualised, imaged and analysed using ‘aNMJ-morph’, a semi-automated macro version built upon the well-established workflow ‘NMJ-morph’. Whilst cancer cachectic patients showed clear signs of muscle atrophy, NMJ morphology was found to be stable with no signs of denervation. This suggests that current mouse models of cancer cachexia, modelling denervation, should be translated with caution.

Given the stark differences between mouse and human NMJs in health and disease, the development of more suitable animal models is fundamental. Therefore, exploration of NMJ morphology across other mammalian species (cat, dog, sheep, pig, and pony) in comparison to the human was required. Overall, sheep and pig proved to be the most similar to human NMJ morphology across pelvic/lower limb muscles, making them attractive models to explore further.

Whilst it is advantageous to explore other mammalian models, it is ultimately critical to better understand the human NMJ in health and disease in order to mimic disease appropriately, regardless of model. The ageing related loss of muscle mass and function, sarcopenia, is a major public health problem and it is thus important to evaluate molecular pathways that occur during healthy ageing at the level of both muscle and the NMJ. Whilst much is known about the ageing of human muscle, the molecular pathways governing healthy ageing at the NMJ itself remain unexplored. This project shows that in comparison to “Middle aged” subjects (40 yo –50 yo), the muscle (devoid of the NMJ) of “Senior” (60 yo) and “Old” (70 yo –80 yo) subjects is in an insulin resistant state, with dysregulation of pathways associated with oxidative phosphorylation and energy production. NMJ-enriched samples of Senior and Old subjects are more similar to Middle aged subjects in protein abundance, and pathways associated with insulin sensitivity are upregulated.

Overall, this project emphasizes the stark morphological difference between NMJs of the mouse and the human, or other mammals. In particular the stability of the human NMJ during muscle wasting diseases such as cancer cachexia, or on a molecular level, during ageing, is striking. Therefore, there is an unmet need to find animal models that are more suitable to model human diseases. This project found that the sheep and pig are suitable to be explored as models of human neuromuscular diseases, opening up avenues of research towards more translatable larger mammalian models.

Lay Summary

Movement of the body is facilitated at the neuromuscular junction (NMJ), where signals from our brain are transmitted to our muscles, causing them to contract. The NMJ has shown to be a major key player in diseases of the neuromuscular system, as changes in its structure can cause well-known motor neurone diseases such as Amyotrophic Lateral Sclerosis (ALS). There are different types of neuromuscular diseases that cause the loss of our muscles which is termed muscle atrophy: physiological atrophy happens when we do not use our muscles enough (lose it our use it principle) or in space within a microgravity environment; pathological atrophy is due to disease in muscle such as genetic conditions, malnutrition or even anorexia; lastly neurogenic muscle atrophy is triggered by insult to the nerve that innervates the muscle. The NMJ can become damaged, or lose its connection to the brain, called the motor nerve, before people show muscle atrophy or start suffering from the disease. Therefore, the NMJ is an important target to develop treatments for diseases that affect our neuromuscular system. However, most information we have about the shape and function of the NMJ comes from animal studies, mostly studies using mice since most experiments in humans are difficult on a number of levels, including ethical considerations and sample size. Recent research has shown that the mouse and human NMJ look very different to each other. The human NMJ is very small and ‘coin’-shaped, called ‘nummular’, whilst the mouse NMJ is much bigger and ‘pretzel’-shaped. How can we now make sure that results from research on mice applies to humans?

First, we need to address the question of what a human NMJ looks like in a disease where mouse models have been predicted to alter their NMJ shape and lose their nerve axon (denervate): cancer cachexia. Cancer cachexia is a disease triggered by cancer where patients lose muscle and/or fat, which causes them to respond more poorly to cancer treatments than cancer

patients without cachexia. Mouse models have predicted that the NMJ is damaged and the muscle loses its connection to the brain and cannot receive signals that tell the muscle to contract. Since mouse models suggest that denervation of the muscle is the main cause of muscle loss in cancer cachexia, therapies that prevent this have been of interest. To study whether human NMJs lose their connection to the brain (denervate) the NMJ structure was compared between patients with cancer cachexia, cancer patients who do not lose weight, and control patients without cancer or weight loss. Cancer cachectic patients were shown to lose weight and muscle mass as expected, but NMJ structure itself showed no changes with no signs of denervation. If the connection between muscle and brain is intact, and the muscle still receives signals telling it to contract, we can start developing therapies such as use of electrical signals that pass through the nerve and the NMJ which stimulate muscle growth.

Since the human NMJ does not behave like the mouse NMJ during cancer cachexia and also looks very different in health, the question arose whether other animal species might look more similar in shape to the human NMJ, to replace mouse models. To investigate this further, the NMJ shape of other mammalian species was studied and the shape of mouse, cat, dog, sheep, pig and pony NMJs was compared to the human. Sheep and pig, already popular models to study neurodegenerative diseases like ALS, are more similar to the human NMJ making them attractive animal species to explore further for research.

Whilst animal models are necessary to study human diseases, we need to know what happens in humans to properly ‘manipulate’ animal models we use and to draw the right conclusions from them. For example, the NMJ is thought to play a role during ageing, and changes in its shape (breaking down of the NMJ into smaller coin-like pieces, denervation) have shown to occur in mouse models of ageing. These changes have not been observed at the human NMJ, which makes us wonder whether there are mechanisms in place that ‘protect’ the NMJ, but not the muscle during ageing. To figure out what these mechanisms could be, a technique called proteomics was

applied, which allows to measure the amount of molecules present in a sample, and identifies which molecules are present. Comparison between Middle-aged (40 yo – 50 yo), Senior (60 yo) and Old (70 yo – 80 yo) patients showed that there are less changes in those molecules at the human NMJ, in comparison to muscle tissue that does not contain the NMJ. Muscle for example loses the ability to efficiently generate energy within mitochondria (the powerhouse of the cell) and becomes more insulin resistant, meaning less able to use glucose for energy production. This is important as muscle requires a lot of glucose to produce energy, which is necessary so that our muscles can contract, and we can move. Tissue that includes the healthy ageing NMJ however, has less problems to use glucose for energy production, which could protect the NMJ in humans and be responsible for its stability during healthy ageing.

Overall, this project highlights how different mouse and human NMJs are, in health and disease and also emphasizes the difference in NMJ shape between other species and the human. The most striking differences between the mouse and human NMJ is how fragile the mouse NMJ is and how quickly it loses its connection to the brain and changes shape. To find out whether the molecules that differ between ageing muscle and the NMJ really protect human NMJs from changing shape, their function will need to be explored in more neuromuscular diseases where the human NMJ stays the same, for example during cancer cachexia. Additionally, the sheep and pig NMJ, which are more similar to the human NMJ in shape than the mouse, will need to be tested to make sure that similar amounts of molecules are present during health and for example ageing. This project opens up the opportunity to find better animal models for many research projects that are interested in exploring human movement disorders.

Acknowledgements

First and foremost, I would like to express my sincere gratitude to Tom Gillingwater and Ross Jones, who believed in my success and assisted me at every stage of the research project. Their valuable guidance taught me that there are no limits to what one can achieve. Second, I am deeply grateful to all the patients who consented to participate in these studies, as without their contribution none of this research would have been possible. Third, I would like to extend my sincere thanks to Janice Miller for all of her support and advice in clinic, as well as Richard Skipworth for his trust, support and insightful comments and suggestions during postdoctoral applications. Additionally, I am deeply grateful to the entire surgical team of the vascular and cancer department who was involved in the sampling of biopsies and the amputation of limbs. Without their continuous efforts to bridge the gap between clinicians and researchers, this project would not have been possible. A particular thank you to Rachel Forsyth, Olivia McBride, Mr Graeme Couper, Ms Anna Paisley, Mr Chris Deans, and Mr Peter Lamb. Fourth, I want to express my gratitude to all the staff at the Roslin Institute and Dryden Farm who were invaluable during sample collection: Chandra Logie, Christopher Proudfoot, Scott Pirie, Greg Markby, Samantha Eaton, Tom Wishart and Rachel Kline, the latter three who were instrumental in completion of the proteomics work. I'm also grateful to Dougie Lamont and Cara Rogers who conducted our mass spectrometry at the FingerPrints proteomic facility in Dundee. Likewise, I would like to express my gratitude to a dear friend Alex Loftus, who provided me with invaluable advice in regard to proteomic analysis and availability of free software.

I would also like to offer my special thanks to every member of the Gillingwater lab who has been part of my academic journey. Thank you to Rachel James, Kiterie Faller, Helena Chaytow and Nikky Huang for all their postdoctoral advice, and to Leire Ledahawsky, Dinja van der Hoorn, Anna Motyl and Ghazi Alanazi for their continuous support during our joint PhD

journey, and in particular Abrar Alhindi who is continuing these projects with the highest enthusiasm.

Furthermore, I am grateful to all the project students who I had the pleasure of co-supervising and who contributed to the completion of this wonderful project: Ana S. Leite, Alyssa Gibbs, Olivia Murray, Mhairi Paterson, Rachel Fu, Lorcan Bailie, Boris Wagner, Ellie Potter, Lara Gibbs, Rizwan Farrukh, Michael Wong, Scott Findlater, Zhenyu Chen, Mohammed Algarni, Thea Mawhinney, Isabel Summers and Qays Foster-Hall. I have learned a lot from all of them and I hope I was able to teach them how to do good science.

My appreciation goes out to my family and friends who encouraged me and kept pushing me to work hard. I'm grateful to every committee member and member of the Edinburgh University Water of Life Society, who has become a close friend, as our joint passion for whisky, castles and Scottish distilleries ensured all our mental health. In particular I want to thank Mr Pickles, without whose tremendous understanding and encouragement in the past two years I would have had less joy in times that were not dedicated to research.

Lastly, I would like to thank the Anatomical Society for the studentship that allowed me to conduct this research.

"Everything is going to be fine in the end.
If it's not fine it's not the end."

— **Oscar Wilde**

Dedication

This work is dedicated to my niece Julia, whose birth encouraged me to pursue the field of neuroscience and dedicate my life to research that allows us to learn more about the human neuromuscular system in health and disease.

Table of Contents

List of Figures

List of Tables

1. Background

1.1. The Neuromuscular System

Synapses play a vital function in signal transduction across all living organisms of a higher order, and synaptic connectivity has been of great interest throughout history due to the major role synapses play in brain function, injury and disease (Katz, 1966; Orlovsky, Deliagina and Grill, 1999). The nervous system consists of nerve cells that connect and communicate with each other, ultimately allowing us to absolve complex tasks such as use memory, temperature or pain sensation, and movement.

Cell bodies of lower motor neurons originate in the ventral horn of the spinal cord and their axons extend from the spinal cord to the periphery of our bodies where they innervate muscle fibres. These axons branch multiple times within muscle prior to innervating target skeletal muscle fibres, where they form the neuromuscular junction (NMJ) at the interface between nerve and target skeletal muscle fibre (Tintignac, H.-R. Brenner and Rüegg, 2015). Because of its reasonable size and easily accessible location in the body, the neuromuscular junction has been utilised as a model synapse from early research, with the hope that findings would translate to other synapses in the central nervous system (Lin and McArdle, 2021). Consequently, this thesis will focus on the peripheral nervous system and the neuromuscular junction.

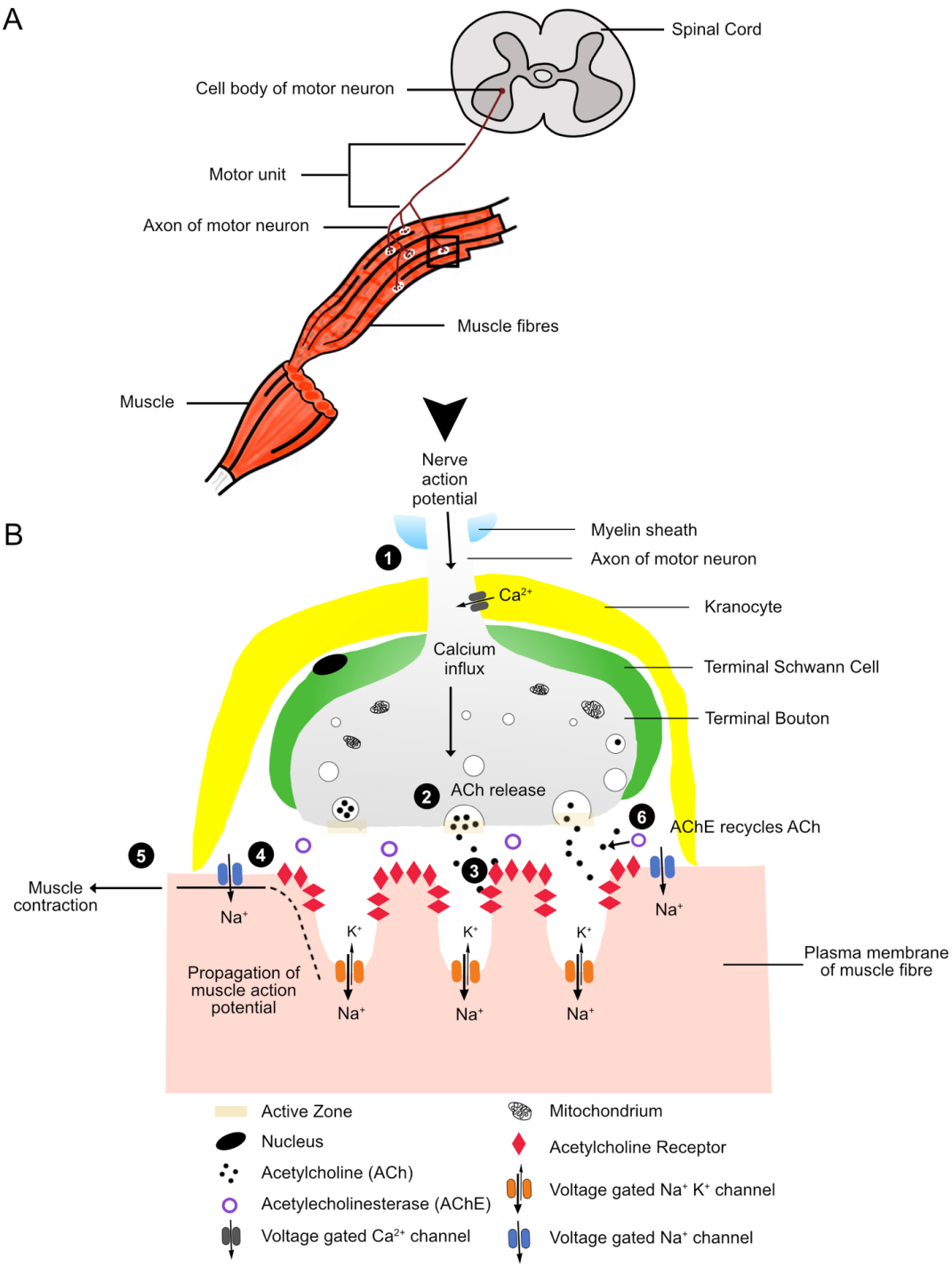

Figure 1-1: Schematic of neuromuscular innervation

(A) Diagram of a motor unit: A motor neuron originates in the grey matter of the spinal cord ventral horn, extending its axon into the periphery of the body. The axon branches shortly before each branch terminates in a neuromuscular junction (small black box) which innervates the muscle.

(B) represents a close-up of the NMJ within the black box in (A).
Legend continues on next page.

Figure 1-1 legend continued from previous page:

Four basic cell types constitute an NMJ: the terminal of a motor neuron (grey, presynapse), the muscle fibre (light red, postsynapse), terminal Schwann cell (green) and kranocyte (yellow). Active zones opposing the post-synaptic invaginations are highlighted with light orange.

(1) If a signal arriving from the spinal cord reaches the end of the motor neuron, voltage gated Ca^{2+} channels open, causing an influx of Ca^{2+} due to greater extracellular concentration.

(2) Influx of Ca^{2+} causes exocytosis of acetylcholine (black dots, ACh) into the synaptic cleft via fusion of synaptic vesicles to the pre-synaptic membrane. This is facilitated by so-called SNARE proteins.

(3) ACh binds to Acetylcholine Receptors (red, AChRs), opening voltage gated sodium potassium channels, resulting in an end plate potential.

(4) Depolarisation of the muscle membrane causes opening of more Na^{+} channels, and propagation of the potential along the muscle fibre membrane, **(5)** generating action potentials on either side of the end plate causing muscle contraction.

(6) Acetylcholinesterase (purple circle, AChE), present within the synaptic cleft, binds to acetylcholine and recycles it, so it can be reused within the pre-synaptic terminal.

1.2. Basic physiology of the neuromuscular system

The smallest elementary unit of the neuromuscular system is defined as a motor unit and is comprised of a single motor neuron and the muscle fibres it innervates as depicted in **Figure 1-1.A** (Sherrington, 1929). The motor unit size is determined by the number of muscle fibres that one motor neuron innervates, and the force of muscle contraction is determined by the number of fibres that are recruited by the motor neuron, i.e. the size of the motor unit.

The more muscle fibres are innervated/ recruited by a motor unit, the stronger the force of contraction that can be elicited by the muscle (Fitts, McDonald and Schluter, 1991). Likewise, the size of the motor neuron (determined by axon diameter) predicts functional properties of the motor unit. For example, smaller motor neurons have a lower activation threshold, due to their smaller surface area, and fatigue less quickly in comparison to larger motor neurons – thus, small motor units (small motor neurons

innervating a small number of fibres) are recruited first according to ‘Henneman’s size principal’ (Henneman and Olson, 1965; Henneman, Somjen and Carpenter, 1965).

Furthermore, different motor unit types have different biochemical properties which are dependent on their physiological function. Small, slow fatigue resistant (SFR) motor units, termed type I motor units, use predominantly oxidative metabolism to generate energy (oxygen and carbohydrates are metabolised). Large, fast fatigue sensitive (FF) motor units, termed type IIb motor units, use predominantly glycolytic metabolisms to generate energy (glucose is metabolised in the absence of oxygen; Schiaffino and Reggiani, 2011). Fast fatigue resistant (FFR) motor units, termed type IIa, have a mixed oxidative and glycolytic metabolism lie in-between type I and type II motor units functionally speaking. The location of these metabolic processes within the cell subsequently determines general morphological differences between slow and fast motor units. Glycolysis mostly takes places within the cytosol and involves only part of the inner mitochondrial membrane – thus, fast glycolytic muscle fibres are larger in diameter, providing more physical space for glycolysis. Oxidative metabolism takes place within mitochondria, thus slow oxidative motor units can afford to be smaller since they have many more mitochondria to meet their functional demand and do not require larger cytosol for glycolysis (Bottinelli and Reggiani, 2000).

The basic make up of motor units differs between species since the main component of skeletal muscle fibres is made up of myosin heavy chain (MyHC) protein and its various isoforms which contribute to different contraction speeds in muscle: Type 2A, type 2X and type 2B. These isoforms are expressed at different ratios in different muscles of the body depending on their functional demand. Whilst fast type 2B muscle fibres can be found in species such as the mouse and pig, the cat, dog and the human do not express type 2B muscle fibres (excellent review on fibre types in mammalian skeletal muscle by Schiaffino and Reggiani, 2011).

Additionally, to muscle fibre type variety there is functional variety of motor neurons that needs to be considered: alpha motor neurons innervate muscle fibres and can therefore be subdivided into three types (SFR, FF, FFR), their respective nerve axons terminate in the here described neuromuscular junctions. Beta motor neurons are much smaller than alpha motor neurons and they innervate muscle spindles which constitute the stretch-sensors of muscle (Kröger and Watkins, 2021). Lastly gamma motor neurons, which are sensory nerves innervating muscle spindles creating a feedback of muscle stretch that allows to adapt to muscle contraction (Stifani, 2014).

Motor unit size is not constant during our life and the variety of muscle fibre types and motor neurons, as well as supporting cell types (i.e. fibro-adipogenic progenitors, schwann cells…), play a role in its plasticity. Overall, it is influenced by factors such as ageing (Wilkinson, Piasecki and Atherton, 2018), exercise (Cartee *et al.*, 2016) and disease such as motor neuron disease (Carleton and Brown, 1979). A decline with age or motor neuron loss during disease progression, such as during Amyotrophic Lateral Sclerosis (ALS), has been proposed to lead to axonal sprouting of surviving neurons and reinnervation of denervated muscle fibres in order to maintain sufficient synaptic transmission. This is meant to preserve overall functional properties, such as strength of skeletal muscle (Tintignac, H.-R. Brenner and Rüegg, 2015; Cartee *et al.*, 2016; Wilkinson, Piasecki and Atherton, 2018). Since impairment of the neuromuscular system implies loss of function, which impacts our overall health and quality of life, fundamental research trying to uncover mechanisms that contribute to health and disease plays an essential role. Due to the important role of the NMJ at the interface between motor neuron and target skeletal muscle fibre, study of their morphology has been a key element providing insight into diseases involving the neuromuscular system.

1.3. Why are we interested in NMJ morphology?

Neuromuscular junctions themselves are dynamic structures, undergoing constant adaptation during their lifetime – exercise, injury/disease, or ageing

in some species have been thought of as the major drivers of NMJ remodelling and functional changes to date (Sieck and Prakash, 1997; Deschenes, Tenny and Wilson, 2006; Valdez *et al.*, 2010; Deschenes, Roby and Glass, 2011). Whilst the basic concept of motor units and their physiological difference has been outlined, the basic make-up of NMJs has yet to be explained, putting their morphology within the context of disease associated changes (**Figure 1-1.B**).

The neuromuscular junction consists of four cell types: the motor nerve that terminates in the pre-synaptic terminal, the post-synaptic membrane at the target skeletal muscle fibre, the terminal Schwann cells that cap the nerve terminal, and kranocytes capping the entire NMJ (Court *et al.*, 2008). Synaptic vesicles within the pre-synaptic terminal are filled with the chemical transmitter acetylcholine (ACh) and are concentrated around specialised 'active zones' (**Figure 1-1.B – 3**). Electric signals that reach the motor nerve terminal open voltage gated Ca^{2+} channels causing influx of Ca^{2+} along a gradient due to greater extracellular calcium concentration. SNARE proteins and calcium ions facilitate fusion and exocytosis of synaptic vesicles to the pre-synaptic membrane, releasing acetylcholine (Han, Pluhackova and Böckmann, 2017).

The pre-synaptic terminal and post-synaptic fibre are separated by a narrow gap, 50–80 nm wide, allowing for the diffusion of ACh. A basal lamina wraps around the muscle fibres, though the composition of the basal lamina within and outside the synaptic cleft differs. The lamina within the synaptic cleft secretes both nerve and muscle stimulated molecules, whilst the lamina outside of the synaptic cleft secrets molecules more specific to the muscle itself (Patton *et al.*, 1997). This is important as structural changes (e.g. damage to the basal lamina) could cause secretion of molecules responsible for ensuring synaptic stability, or lack thereof could cause changes in synaptic morphology at both the pre- or postsynapse.

The post-synaptic membrane is deeply folded, with acetylcholine receptors (AChR) located at the crests of the folds opposite to neighbouring active

zones (which are zones of active transmitter release). The folds increase AChR density via an increase in surface area (larger surface area = more acetylcholine receptors) facilitating a larger capacity to bind ACh and more stable signal transduction (Slater, 2017). Additionally, there is the term 'safety factor' which describes the phenomenon in neuromuscular transmission where more transmitter is released than necessary to elicit an endplate potential. Differences in safety factor have been noted between species and muscles (Wood and Slater, 2001). Furthermore, differences in AChR densities could imply disease associated dismantling of the NMJ via motor neuron or muscle fibre induced signalling, which could also affect the density of active zones. Therefore, the accurate measurement of post- and pre-synaptic morphometric variables and their overlap, is of great interest to be able to distinguish NMJs in health and disease.

Interest in the morphology of the NMJ has began as early as in the 1700s (Tello, 1922; Coers and Woolf, 1959; Slater, 2008) and most current data available on development, maintenance and impairment of the neuromuscular system stems from experiments on rodents (Sanes and Lichtman, 2001; Fox *et al.*, 2007; Murray *et al.*, 2008; Nishimune *et al.*, 2008; Hallock *et al.*, 2010; Murray, Talbot and Gillingwater, 2010; Ling *et al.*, 2012). Unsurprisingly, differences across species were observed on a molecular and cellular level, stressing the importance of stepping back from the "one size fits all" approach regarding NMJ morphology.

Currently, mice are being used in ~50% of all animal research and have developed to be the animal model of choice, mostly due to technological advancements in gene editing, their short lifespan and relatively low efforts associated with housing (Ellenbroek and Youn, 2016). Whilst the NMJ has been well studied across a variety of invertebrates and vertebrates, including electrophysiological study of the human NMJ (Coers and Woolf, 1959; Wood and Slater, 2001; Slater, 2015) a detailed morphological study of the human NMJ has been lacking until recently (Jones *et al.*, 2017).

1.4. The rodent NMJ is different to the human NMJ

Whilst on a gross anatomical level, the disconnect between humans and other species might not seem that extensive (all mammals have a similar basic body plan) significant biological and physiological variations occurred during evolution that contribute to inter- and intra-species diversity (Darwin, 1859). Across species that are capable of developing a nervous system, the principle components comprising the nervous system (such as bipolar nerve cells and supporting glial cells) are the same (Purves *et al.*, 2004), but the degree of conservation and their relevance to function remains unexplored. Many aspects of function between human and lower mammalian species are fundamentally different and need to be taken into account for appropriate translation of research to humans.

A recent publication showcasing vast morphological differences between mouse and human NMJs throws up the question of whether what we model in mice compares to humans, and the degree to which it compares (Jones *et al.*, 2017). Combining morphological techniques, super-resolution imaging and proteomic profiling to compare the cellular and molecular anatomy of the healthy adult human NMJ with rodent NMJs revealed striking morphological differences. Human NMJs were significantly smaller, less complex, and of 'nummular' appearance ('coin-shaped' and therefore more fragmented) and additionally were found to be more stable across the entire adult lifespan (Jones *et al.*, 2017) (**Figure 1-2**). Age related changes, such as denervation and fragmentation of the NMJ, have previously been observed in mice and the NMJ has been thought to play a role in age-related muscle wasting (Balice-Gordon, 1997; Valdez *et al.*, 2010; Gouspillou *et al.*, 2013; Ham and Rüegg, 2018). Jones *et al.,* demonstrated that neither denervation nor fragmentation occurred during healthy ageing of the human NMJ, questioning the translatability of available mouse models of ageing. Jones *et al's* efforts in super-resolution imaging (direct stochastic optical reconstruction microscopy = dSTORM) revealed a difference in distribution of the active zone protein SNAP25, which is involved in exocytosis of synaptic vesicles (Rodríguez Cruz, Palace and Beeson, 2018), and proteomic profiling

further highlighted differences between species, by uncovering the differential expression of pathways that involve core synaptic proteins fundamental for form and function of the NMJ.

1.5. Pathology of the NMJ

The much smaller and more 'fragile' looking NMJ of the human has so far been thought to be more susceptible to ageing and neuromuscular disease (Slater, 2017) than the larger more robust looking mouse NMJ. The crucial function of the NMJ within the mammalian neuromuscular system makes it a vulnerable target for: 1) injury – e.g. autoimmune disease such as congenital myasthenia gravis (CMG) and Lambert-Eaton myasthenic syndrome (LEMS) (Sanders and Juel, 2008); 2) genetic diseases targeting the post-synapse – e.g. myasthenia gravis (MG) (Vincent, 2002) and congenital myasthenic syndrome (CMS) (Maselli *et al.*, 2009; Engel *et al.*, 2015); 3) cerebral palsy (CP) (Volpe, 1994) or 4) other genetic disorders – e.g. spinal muscular atrophy (SMA) (Boido and Vercelli, 2016), amyotrophic lateral sclerosis (ALS) (Dupuis and Loeffler, 2009) and Duchenne muscular dystrophy (DMD) (Gramolini and Jasmin, 1997; Hirsch, 2007).

Morphological changes at the NMJ such as denervation and fragmentation of the endplate, neurofilament accumulation and axonal sprouting have been considered key hallmarks of above-mentioned neuromuscular diseases at the rodent NMJ (**Figure 1-3**).

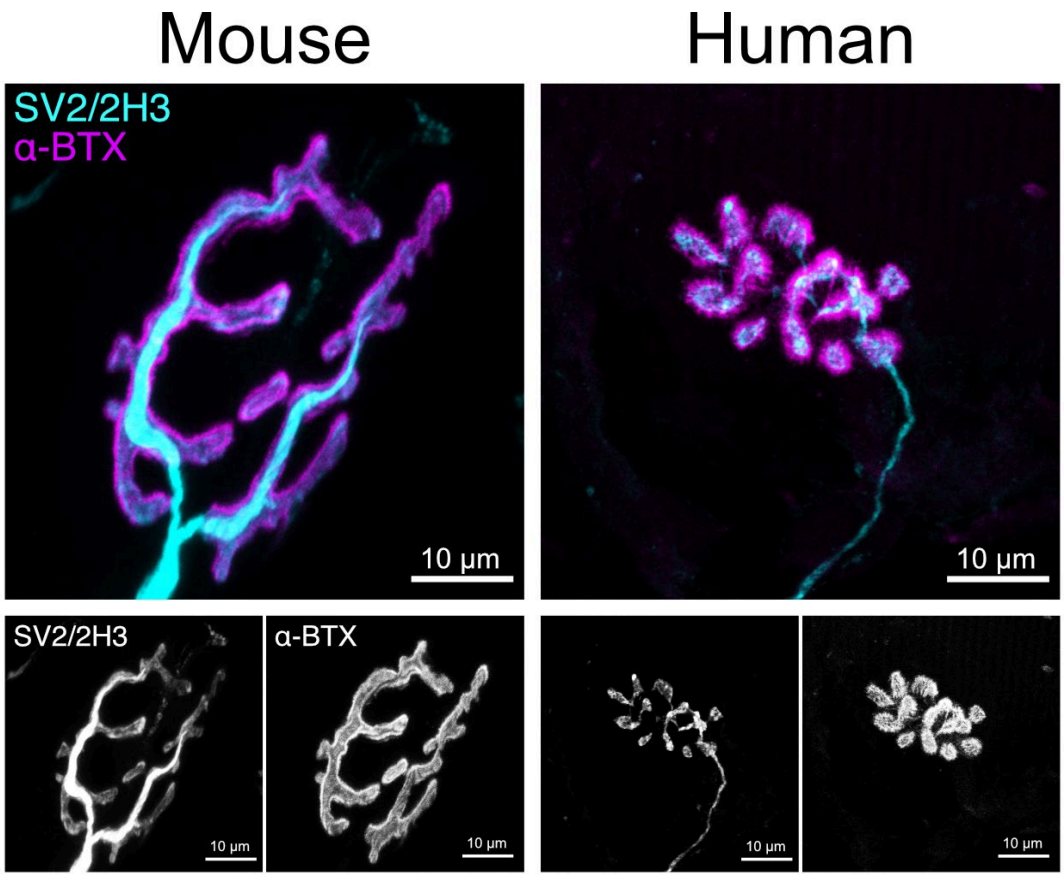

Figure 1-2: Comparison of mouse and human NMJ

Example confocal micrographs of the mouse NMJ (left), which is significantly larger than the human NMJ (right). Composite images show acetylcholine receptors (α-BTX, magenta), axon and nerve terminals (synaptic vesicle protein 2 and neurofilament, SV2/2H3, cyan).

Scale bars = 10 µm

Comparative studies of the NMJ between human and other species in health and disease might therefore help identify mechanisms responsible for the disassembly of the NMJ. Since the contrast in axon diameter (**Figure 1-2**) between human and mouse was particularly noticeable (mice had axon diameters almost four-fold that of the humans), this was considered to further support the fragility of the human NMJ. Considering basic electro-physiological properties of motor units, larger axon diameters would be indicative of larger motor unit activation thresholds; likewise, larger motor unit firing rates are associated with larger motor units of higher activation threshold (Gorassini *et al.*, 2002; Duchateau and Enoka, 2011). With that in mind, mouse and rat motor units (with almost a four-fold larger axon diameter than humans) fire three to four-times faster than the human (Manuel *et al.*, 2019).

All in all, the principle of motor unit recruitment according to 'size' and the correlation with overall anatomy of the neuromuscular system might suggest that human motor units have lower activation-thresholds to overcome compared to mice. To prove this on a single motor unit level in humans has been challenging so far, and there is a lack of comparative studies that reliably assess differences in activation thresholds, including in humans (Manuel *et al.*, 2019). Lower activation thresholds would allow human motor units to be activated more readily and this could have an overall protective influence on the human neuromuscular system, as opposed to the previous hypothesis which suggests fragility and a more ready dismantling of the human NMJ (Slater, 2017). To further evaluate the stability of the human NMJ and to definitively answer the question of whether human NMJs break down more readily than mouse NMJs, this project sought to study the morphology of the human NMJ in health and disease.

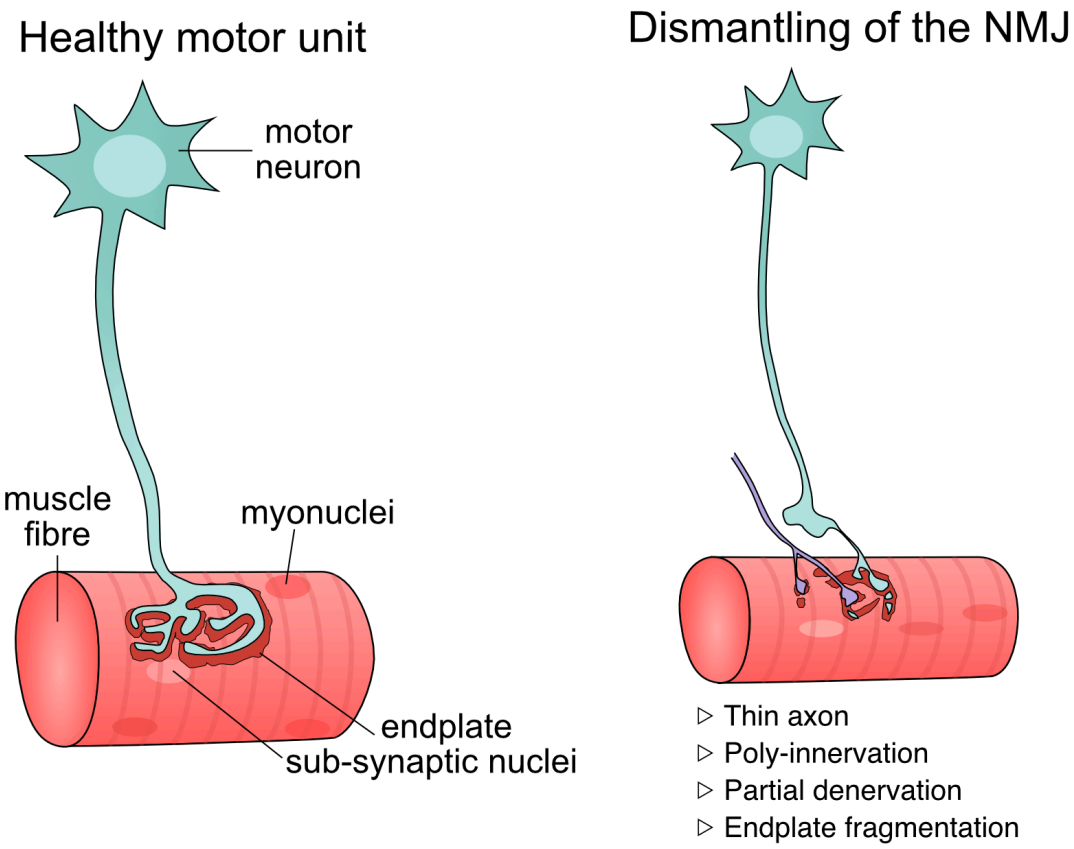

Figure 1-3: Schematic of NMJ pathology

The right panel depicts overall dismantling of the NMJ. The axon diameter is thinner than at the healthy motor unit (left panel), the endplate is fragmented and partially denervated, additionally the endplate is innervated by an axon that stems from a different motor unit (purple axon). This is termed poly-innervation.

1.6. Morphometric analysis of the NMJ

1.6.1. NMJ-morph – a method of quantifying NMJ morphology

One of the major technical challenges in the process of undertaking comparative studies of NMJs between species has been the lack of a robust quantitative platform ('gold standard') for standardised measuring and reporting of NMJ morphometrics. At present, it is challenging to compare data from publications that have used different methodologies to measure and quantify NMJ variables, especially when the definition of 'key' variables differs significantly across studies (e.g. in early studies acetylcholinesterase was used to define the boundaries of endplates; nowadays fluorescently conjugated α-bungarotoxin is used; Wernig and Herrera, 1986; Ogata, 1988; Theroux *et al.*, 2002). Despite the similar 'spread' of AChE within the synaptic cleft and AChRs just underneath (**Figure 1-2**), AChE is seen to occupy a slightly larger area (more diffuse) than the visualised AChRs (**Figure 1-4**).

Additionally, 'size' parameters in early to mid 1900 studies were more loosely defined due to poorer quality immunohistochemical staining compared to today, making it difficult to distinguish boundaries between the endplate, motor nerve and background; nowadays we have better labelling techniques, imaging facilities and elaborate bioinformatic tools to quantify such perimeters, areas and volumes.

For example Carey *et al.* (1946) assessed the secretory mechanism of motor endplates under thermal shock via gold impregnation, though the quantification of motor end plate size variation does not specify what was quantified.

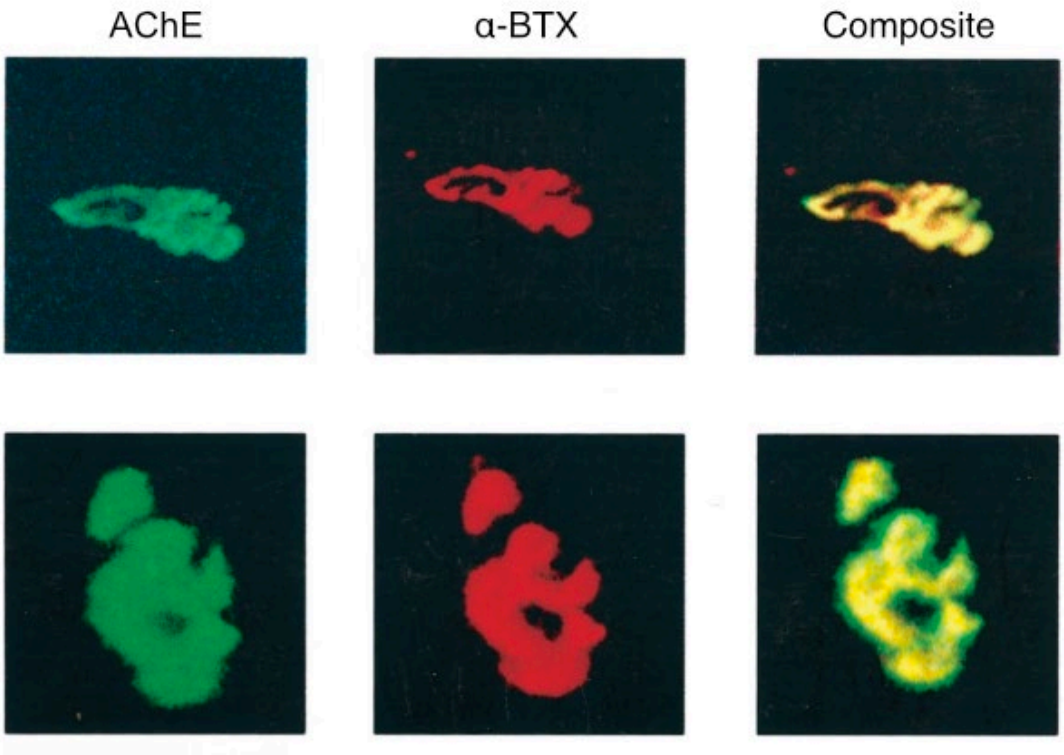

Figure 1-4: Variation between acetylcholinesterase and α-bungarotoxin staining

A difference in endplate area is visible when comparing the use of acetylcholinesterase (AChE, left panels) and α-bungarotoxin (a-BTX, middle panels) to visualize NMJs. The composite channel (right panels) demonstrate that AChE staining is more diffuse and extends beyond acetylcholine receptors. Image adapted from (Theroux *et al.*, 2002).

Thus, the audience can only suppose that ‘size’ in this context refers refer to the endplate diameter as size has been used interchangeably with axonal diameter measurements throughout the particular publication.

Likewise, the seminal volume on “The innervation of muscle; a biopsy study” which is a primary reference containing comparative morphology of the NMJ across species and muscles, Coers and Woolf do not highlight specifically how their sub-neural apparatus (motor endplate) or diameter measurements were made. One can only speculate that either horizontal or the longest diameter through the endplate were measured (Coers and Woolf, 1959).

In 2016 ‘NMJ-morph’, an ImageJ/FIJI based workflow was developed which allows its users to reliably quantify *en face* confocal micrograph images of the NMJ (Jones *et al.*, 2016). This methodology generates 21 morphometric variables, facilitating comparative analysis of the NMJ within and across species. ‘NMJ-morph’ standardises analysis and shows reproducible results with little between user variability, thus aiding in the comparison of NMJs across various species and conditions. A number of research groups have now utilised this approach to gain important insights into NMJ morphology in health and disease.

For example, ‘NMJ-morph’ is a robust tool for comparative studies assessing the cellular and molecular anatomy of the human and mouse NMJ (as highlighted above) (Jones *et al.*, 2017). The sensitivity of ‘NMJ-morph’ allowed for the description of subtle alterations at the NMJ in different muscles in the mouse, and also during their development (Jones *et al.*, 2016; Mech *et al.*, 2020). Furthermore, NMJ-morph has been demonstrated as a robust tool for comparative studies between species (Boehm, Alhindi, *et al.*, 2020), and for comparison of the anatomy of the human and mouse NMJ (Jones *et al.*, 2017). Likewise it helped uncovered subtle changes in fragmentation and compactness that are associated with NMJ degeneration in CHCHD10-encoded mitochondrial myopathy associated with motor neuron

disease (Genin *et al.*, 2019), as well as helped characterise NMJ dysfunction across different mouse models of Charcot-Marie-Tooth disease (Cipriani *et al.*, 2018; Sleigh, Mech and Schiavo, 2020). NMJ-morph proved useful in the analysis of amyotrophic lateral sclerosis mouse models with skeletal muscle specific histone deacetylase 4 (HDAC4) deletion (HDAC4 regulates in particular muscle development), where an increase in denervated NMJs was observed, suggesting that HDAC4 regulates severity of disease onset (Pigna *et al.*, 2019). Furthermore, NMJ-morph has proved beneficial in characterisation of NMJ integrity following therapeutical interventions in rodents, such as treatment with the selective mTORC1 inhibitor rapamycin which concluded that high mTORC1 expression is causative for NMJ deterioration at old age (Ham *et al.*, 2020). These studies highlight the tremendous potential 'NMJ-morph' provides, to make in-depth comparative studies of the NMJ across different models, species and in health and disease.

1.6.2. 'NMJ-morph' in practice – recent biological observations

A plethora of data, 21 variables, result from 'NMJ-morph' analysis and give an extensive overview of NMJ morphology and also allow for analysis of subtle changes within structure as highlighted by its uses so far in the characterisation of the NMJ in murine models. However, one must keep in mind the biological context of these variables to understand what changes any of them mean.

1. Presynaptic variables:

Presynaptic variables describe the overall morphology associated with the size ["Nerve terminal area (μm^2)" and "nerve terminal perimeter (μm)"] and branching network of the presynapse. Changes in variables such as "number of terminal branches", "number of branch points" and "total length of branches (μm)" can all point towards remodelling of the pre-synaptic terminal. "Complexity" is a variable that is derived from all three primary

branching measurements and has been designed to provide a more comprehensive view of nerve terminal branching.

2. Post-synaptic variables:

"AChR area (μm^2)" and "endplate area (μm^2)" are two different descriptors of post-synaptic variables, with AChR area referring to purely bungarotoxin-positive areas, and the endplate area referring to the overall area of the motor endplate including AChR devoid areas. The difference between endplate area or AChR area can easily identify species differences (Jones *et al.*, 2017). "AChR perimeter (μm)" and "endplate perimeter (μm)" refer to the respective perimeters of the afore mentioned areas. The number of discrete AChR clusters at the endplate is given by "Number of AChR clusters", and changes in cluster numbers have been associated with ageing at the rodent NMJ, best described in combination with derived variables such as "fragmentation" (Valdez *et al.*, 2010; Taetzsch and Valdez, 2018). Interestingly, a recent study and review suggested that there is no direct evidence for age-related 'fragmentation' itself as a cause for impaired neuromuscular transmission at the rodent NMJ (Willadt, Nash and Slater, 2016; Slater, 2019).

3. Associated nerve and muscle variables:

"Number of axonal inputs", "Axon diameter (μm)" and "Muscle fibre diameter (μm)" are variables that are indicative of development, denervation/re-innervation and muscle health. The "Number of axonal inputs" in disease models or at the developing NMJ quantifies poly-/multi-innervation patterns and thus the developmental stage of the NMJ (Colman, Nabekura and Lichtman, 1997; Keller-Peck *et al.*, 2001) or whether damage has occurred and the NMJ is undergoing re-innervation by different motor units (see **Figure 1-3**) as previously observed in mice (Kang *et al.*, 2014). However, it is important to distinguish bifurcation of the same motor axon into NMJs (which frequently occurs in human NMJs), or 'actual' poly-innervation where the NMJ is innervated by different axons of a different motor unit. In whole mounts this can usually be determined by tracing the axons from the nerve

terminal backwards to find their point of bifurcation, these tend to merge into the same parental axon not further than a few muscle fibres away if they stem from the same motor unit.

An increase or decrease in “Muscle fibre diameter (µm)” can provide useful data about the overall health of a muscle in comparison to a control group. Increases after exercise intervention can point towards muscle hypertrophy, and a decrease in muscle fibre diameter points towards muscle atrophy, and is thus an indicator for conditions such as cachexia or sarcopenia (Wilkinson, Piasecki and Atherton, 2018).

4. Derived variables:

These variables play an important role in describing biologically relevant changes in branching at the NMJ as highlighted by “complexity”. Changes in “fragmentation” and “compactness (%)” can give insight into age, species, or developmental stage of the NMJ (e.g. rodent NMJs fragment with age, human NMJs are more fragmented or “nummular” than the “pretzel” shaped rodent counterpart, and developing NMJs are more compact and plaque shaped than adult NMJs; Shi, Fu and Ip, 2012; Jones *et al.*, 2017; Taetzsch and Valdez, 2018). “Overlap (%)” on the other hand is a good indicator of denervation, describing the extent to which nerve terminal area overlaps AChR area. A decrease in % overlap between a disease model and control would point towards denervation. With most parameters giving purely structural read outs, the “area of synaptic contact (μm^2)” provides information of functional significance. Alterations that affect the area of synaptic contact of the NMJ will likely have an impact on transmission, signalling efficiency and thus function.

1.6.3. NMJ-morph – summary

Despite over a century of research into mechanisms that govern development and maintenance of the NMJ, it remains unclear as to what causes the differences and commonalities in morphology amongst species and individuals. ‘NMJ-morph’ is an ideal tool to lay the foundation of

quantitative NMJ analysis across areas such as the study of the human NMJ in disease (Chapter 4) or comparison of the mammalian NMJ (Chapter 5). A general approach, utilising immunofluorescence staining and confocal imaging microscopy to directly visualise pre- and post-synaptic parts at the NMJ was adopted throughout.

1.7. Aim of the project

Our current level of knowledge regarding the structure of the healthy human NMJ, and the stark difference between mouse and human NMJ on a morphological and molecular level, have prompted several questions in the research community. How does the human NMJ behave during disease? Are there other species with more similar morphology to the human NMJ? Likewise, given the lack of structural changes at the ageing human NMJ compared to rodents, molecular pathways driving this 'stability' remain to be elucidated.

Here, 'NMJ-morph' was initially used to assess inter-user variability for training purposes, followed by the development of a semi-automated macro "aNMJ-morph" (Chapter 3). aNMJ-morph provided a significant methodological advancement and was therefore applied going forwards.

Due to the marked difference between mouse and human NMJ, the primary aim of this project was to establish whether the morphological changes occurring at the human NMJ during disease mirror those at the mouse NMJ (Chapter 3), or whether the human NMJ is as morphologically stable during disease as it appears to be during healthy human ageing (Jones *et al.*, 2017). Following analysis of the human NMJ in health and disease, the project next sought to explore whether there are mammalian models that more closely resemble the human NMJ than the rodent NMJ (Chapter 5). This information would provide a starting point for the generation of animal models with a more translatable capacity than the currently preferred mouse models. Given the physiological differences outlined between mouse and human NMJ, the next chapter aimed to identify intrinsic age-related

molecular changes that occur during healthy human ageing, which might contribute to the overall stability of the human NMJ.

In order to generate more appropriate animal models, it is also essential to understand molecular pathways at the human NMJ which contribute to health and disease. Thus, the primary aims of this project were to improve the current methods of NMJ analysis and gain biological insights into the human NMJ in health and disease and its translatability to animal models:

Methodological Advancements

1. Development of a semi-automated macro plugin of NMJ-morph to increase reproducibility and speed of NMJ analysis (Chapter 3)

Biological Insights

1. Does the human neuromuscular junction dismantle in cancer cachexia, a condition that includes muscle wasting? (Chapter 4)
2. Which larger mammalian models have similar NMJ morphology to the human, and are there similar/conserved trends in NMJ morphology across species? (Chapter 5)
3. Are there different (or compensatory) molecular mechanisms at ‘the NMJ’ in comparison to ‘the muscle’ which are responsible for its stability during ageing? (Chapter 6)

2. General Methods

2.1. Chapter Summary

The objective of this chapter is to introduce the general research methodologies used throughout this thesis to assess the anatomy of the neuromuscular junction in health and disease. The morphometric analysis platform 'NMJ-morph' is discussed in depth, as well as the training in its workflow and the familiarisation with the image analysis platform Fiji that this workflow is based on. Correlation analysis utilising RStudio was used to assess variability between datasets acquired by trainee and expert user and would confirm quality of morphometric data. To guarantee reliable results, high quality data obtained with both accuracy and precision is essential. Training and quality control provide the foundation for the development of the automated NMJ-morph macro in Chapter 3 (aNMJ-morph: a simple macro for rapid analysis of NMJ morphology) and all subsequent NMJ analysis undertaken in Chapter 4 (Neuromuscular junctions are stable in patients with cancer cachexia) and Chapter 5 (Comparative anatomy of the mammalian neuromuscular junction).

Also elaborated in detail in this chapter are the ethical considerations and the consistent approach to tissue sampling, processing and confocal microscopy that have been used throughout the thesis.

2.2. Research Questions

This project sought to develop methodological advancements:

1. *Create a semi-automated macro plugin of NMJ-morph that increase reproducibility and speed of NMJ analysis? (Chapter 3):*
   Via the creation of a semi-automated macro, aNMJ-morph. This macro is based on NMJ-morph and designed for Fiji/ImageJ. It aims to facilitate rapid analysis of NMJs and requires less overall human input in the process of morphometric analysis. The semi-automated process reduces human error during data transfer and transposition and reduces bias during the overall process of analysis, allowing to dedicate ones focus solely to the crucial steps of thresholding within the workflow.

Following successful development of aNMJ-morph, immunofluorescent labelling and confocal microscopy were utilised to visualise pre- and post-synaptic compartments of the NMJ in human and large mammalian species, followed by analysis with NMJ-morph and aNMJ-morph to gain the following biological insights:

2. *Does the human neuromuscular junction dismantle in cancer cachexia, a condition that includes muscle wasting? (Chapter 4)*
3. *Which large mammalian models have similar NMJ morphology to the human, and are there similar/conserved trends in NMJ morphology across species? (Chapter 5):* Establish a comparative morphological baseline of the mammalian NMJ (mouse, cat, dog, sheep, pig, human and pony) from lower/pelvic limb muscles.
4. *Are different (or compensatory) molecular mechanisms at the NMJ (compared to muscle) responsible for its stability during ageing? (Chapter 6):* Utilise the existing workflow of rapid, fresh tissue sampling within clinic (as described in this chapter) and adapt it for proteomic analysis to study mechanisms that occur during ageing of human NMJs and muscle.

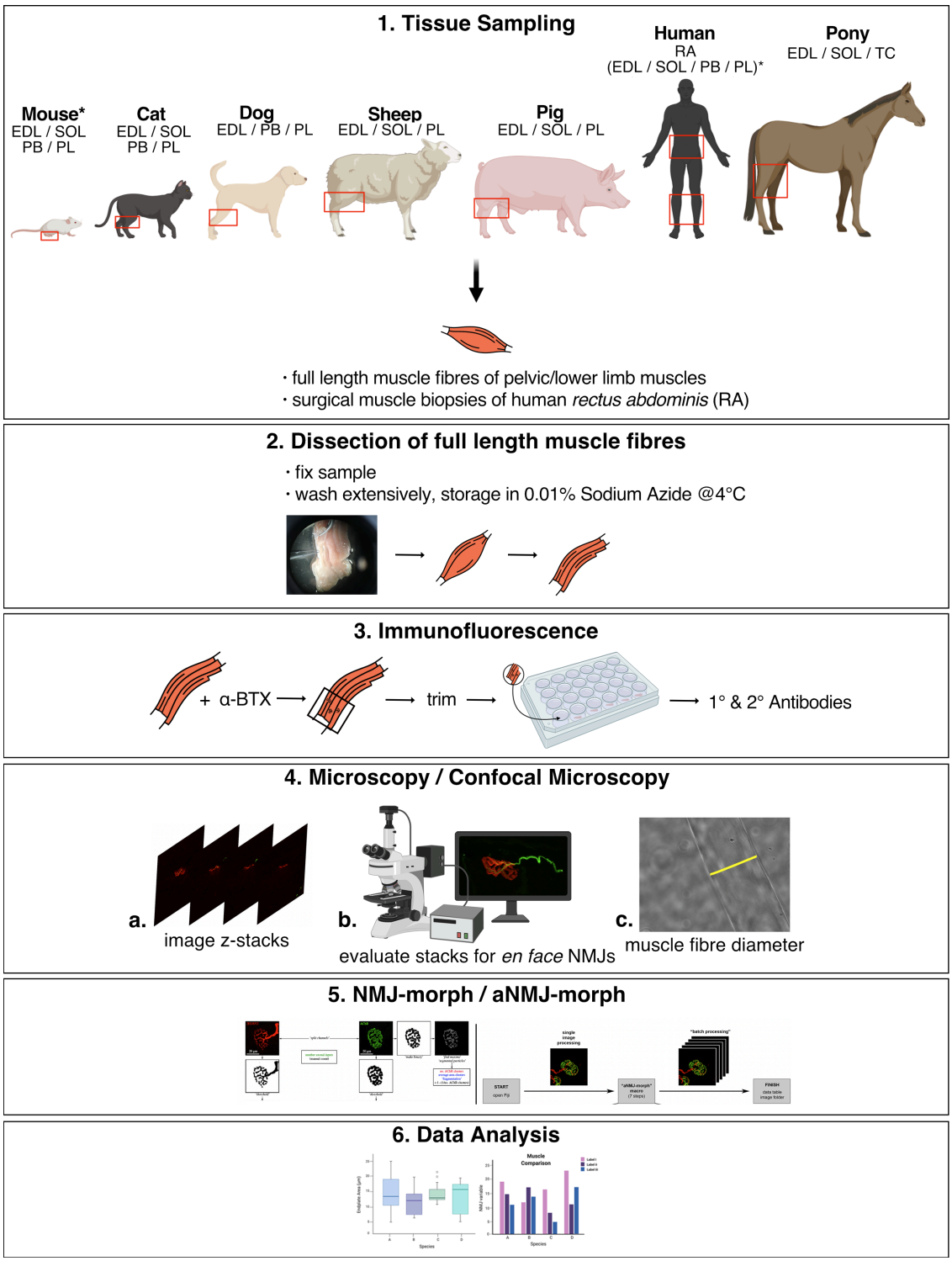

Figure 2-1: Overall workflow of tissue sampling and processing, morphometric analysis, and data interpretation

1.1. Tissue sampling of full length pelvic (mouse*, cat, dog, sheep, pig and pony) or lower limb muscles (human*), and sampling of surgical muscle biopsies of human *rectus abdominis* (RA). *Legend continues on next page.*

Figure 2-1 legend continued from previous page:

EDL = *extensor digitorum longus*; PL = *peroneus longus*; PB = *peroneus brevis*; SOL = *soleus*; TC = *tibialis cranialis*; asterisk (*) refers to human and mouse data from (Jones *et al.*, 2017)

1.2. Full length muscle, or surgical biopsies were immediately fixed after sampling, washed and stored in 0.01% sodium azide until further use. For further processing, samples were dissected into smaller fibre bundles.

1.3. Immunofluorescence: Endplates were visualized with Tetramethylrhodamine α-bungarotoxin (TRITC α-BTX) and endplate bands were fine dissected to allow for quicker location of endplates during confocal microscopy. The pre-synaptic compartment was visualized with primary antibodies against synaptic vesicle and neurofilament protein.

1.4. Microscopy/Confocal Microscopy: **(a)** Confocal images were acquired in z-stacks, **(b)** NMJs that were *en face* were selected for imaging and NMJs which were oblique were excluded at this stage from the imaging process. **(c)** The muscle fibre diameters were imaged on a brightfield microscope, and subsequently analysed in ImageJ/Fiji.

1.5. NMJ-morph or aNMJ-morph were used for analyses of NMJs across species and the human.

1.6. Morphometric data were analysed and interpreted to answer above outlined research questions.

2.3. Methods

2.3.1. Ethics – Human Patient Material and Animals

Ethical approval for use of anonymous human tissue was granted by the Lothian NRS BioResource (SR719, 15/ES/0094) for sampling of lower limb muscle, applicable to patients in Jones *et al.*, 2017 (Chapter 5). Tissue collection was approved by the National Health Service Lothian Ethics Committee (REC 2002/1/22, 2002/R/OST/02 for sampling of lower limb muscle, applicable to patients in Jones *et al.*, 2017 (Chapter 5 and Chapter 6) and IRAS 190214 for sampling of *rectus abdominis* (Chapter 4) following internal (University of Edinburgh) and independent/external ethical review in accordance with the Helsinki Declaration. Only patients aged 18 years or above were approached for recruitment and written informed consent was obtained for all human cases sampled for this thesis. Patients undergoing surgery for cancer resection or lower limb amputations are seldom below the

age of 30; thus, the youngest patient within this thesis is a 42-year-old black male who underwent a below knee amputation.

In compliance with the 3Rs, no animals were sacrificed specifically for this project – all tissue samples used were harvested once experimental endpoints had been reached or from animals that had been submitted for euthanasia to Dryden Farm or The Roslin Institute. All animal work was carried out under the regulations of the Animals (Scientific Procedures) Act 1986. All rodent experiments were conducted in accordance with the guidelines set by the UK Home Office under a registered project license. Previously published mouse and human limb data were utilised as a reference where indicated (Jones *et al.*, 2017; Chapter 5).

2.3.2. Tissue Sampling

The current project aimed to evaluate the cellular and molecular composition of the NMJ across health and disease in human subjects and aimed to establish a baseline of overall NMJ morphology across larger mammalian models (cat, dog, sheep, pig, pony). To achieve this goal, this study set out to build on previously established tissue sampling networks across The University of Edinburgh and the Royal Infirmary of Edinburgh. The capacity to rapidly sample material on site was increased to include sampling from larger mammalian models for a comparative anatomical study (Chapter 5). Tissue sampling and fixation commenced from larger mammalian models on site within 30 minutes after animals had been euthanised (put to sleep, PTS). Additionally, a pony image bank was acquired by a collaborator (Stephen Cahalan) at the Royal Veterinary College. Pelvic limb muscles (*extensor digitorum longus*, *peroneus longus*, *peroneus brevis, tibialis cranialis* and *soleus*) were sampled from cat, dog, sheep, pig and pony, and compared to human and mouse reference lower/pelvic limb muscles (Jones *et al.*, 2017). **Figure 2-1** depicts a schematic of the general experimental design describing tissue collection, processing, and morphometric analysis.

Surgical biopsies from human RA were obtained at the start of the surgical procedure and were immediately fixed within < 3 min after removal from the operating theatre. Human lower limb samples for proteomic analysis were sampled in the preparation room within operating theatre, immediately after disconnection of the lower limb. Samples collected from The Royal Infirmary, when sampled for proteomic processing (Chapter 6), were transported back with urgency in ice cold PBS on ice.

Existing ethical approvals were also utilized: “Biochemical and functional biomarkers of cachexia in cancer patients” in collaboration with Mr. Richard Skipworth and Janice Miller at the Royal Infirmary of Edinburgh (Chapter 4), where the sampling process of freshly fixed *rectus abdominis* biopsies from subjects was followed by morphometric NMJ analysis; “Investigating the way that human tissues produce a biological response (such as fracture healing) from a mechanical stimulus” (Chapter 6) in collaboration with Dr. Thomas Wishart, Samantha Eaton and Rachel Kline at the Roslin Institute Edinburgh, where the workflow in **Figure 2-1.1–1.2** was slightly adapted from that previously described in Jones *et al.*, 2017, such that sampling process of *peroneus longus* from lower limb amputations (for proteomic analyses and tissue processing) was fully undertaken on ice.

2.3.3. Dissection of full-length muscle fibres

Muscle samples were fixed immediately after dissection in 4% paraformaldehyde/formaldehyde solution (PFA, Electron Microscopy Sciences, 15710) for 1–4 hours. Fixation of samples is necessary to retain the shape of morphological structures as depicted in **Figure 2-2.1**. Despite paraformaldehydes tendency to penetrate tissue quickly due to its composition of small molecules, the reaction to crosslink protein molecules through the formation of methylene bridges (-CH2-) is slow. The chemical process of formaldehyde addition to a molecule also requires a protein to be in the vicinity of the ‘formaldehyde+protein’ complex for the subsequent methylene crosslink to occur, and this process therefore takes time (Kiernan,

2000). Given the slow fixation time of PFA it has been almost impossible to over fix samples in the due course of the project – thus, small samples which were normally fixed for 1 hour to achieve seemingly minimal fixation do not appeared noticeably stiffer or with more background in the 488 nm-channel (green visible spectrum) when imaging. The main focus was to prevent under fixation of samples and the time window of 1–4 hours for fixation has proven to be logistically practical for our sample sizes (lower limb/pelvic muscles, RA).

Following fixation, samples were rinsed vigorously with 1x phosphate-buffered-saline (PBS) to remove excess aldehydes in the fixative which might form crystalline compounds (termed Schiff's bases), with amines that are released upon cell death. These have been known to fluoresce under high intensity illumination causing background, but also autofluorescence in the fixed sample (Willingham, 1983; Schnell *et al.*, 2012). Formaldehyde-induced autofluorescence in the spectrum of 420-470 nm in combination with sample inherent autofluorescence which extends up to 650 nm and originates from e.g. flavins, NAD(P)H, collagens and lipofuscins all cause particular issues due to their strong representation in muscle (Viegas *et al.*, 2007; Kajimura *et al.*, 2016). In particular, lipofuscin accumulations in muscle (a sign of inefficient lysosomal degradation) are highly autofluorescent and can present themselves as autofluorescent inclusions (Feeney *et al.*, 2014). Tissue samples were stored in 0.01% Sodium Azide (Fisher Scientific, 12695107) to prevent bacterial growth (Minassian and Huang, 1979). Sodium azide (NaN_3) is a respiratory poison and prevents bacterial growth by inhibition of the metabolic activity of mitochondria. The instantaneous inhibition of mitochondrial metabolic activity has been suggested to have positive effects on preservation of the cellular structure of mitochondria during fixation and leads to sharper cristae and more pronounced mitochondrial structure (Minassian and Huang, 1979). The highly toxic nature and lack of mitochondrial analysis during this project however have prevented us from also adding it to the fixative, and storage in low concentration sodium azide proved sufficient for long-term preservation of tissue.

2.3.3.1. Logistical considerations

The duration of fixation is strongly dependent on the size of the muscle sample and the logistics of sample collection, e.g. the time to travel from Dryden Farm, the Royal (Dick) School of Veterinary Studies (RDSVS) or The Royal Infirmary after sample collection. For example, small samples that would have been fixed for one hour to achieve minimal fixation might have been fixed for 2–3 hours in some cases where total journey time was limited by unforeseen waiting times for buses (every ~1 h) at Dryden Farm and the Roslin Institute, as well as the time accounted travelling by bus (45 min journey), as well as walking to and from the bus (~15 min walk to Dryden Farm, ~15 min walk to Gillingwater Lab).

2.3.4. Immunofluorescence

An adapted protocol for visualisation of the neuromuscular junction (NMJ) was used on all muscle samples, albeit with slight alterations to incubation times of primary and secondary antibodies (Jones *et al.*, 2016, 2017). Muscle fibres were fine dissected into bundles of 10–15 individual fibres and connective tissue with fat and blood vessels removed to reduce background staining. Tissue samples were moved to 24 or 48 well-plates (**Figure 2-1.3**) depending on sample size and incubated in 0.1 M Glycine (Sigma-Aldrich, 410225-50G) in dH_2O for 15 min to further quench autofluorescence. As glycine amino groups bind to free aldehyde groups (e.g. of the fixative) these free aldehydes are masked which prevents binding of antibodies and enhances the overall reduction of non-specific background and autofluorescence (Rosas-Arellano *et al.*, 2016).

To visualise the post-synaptic endplate, samples were first washed 3 x for 10 min with 1xPBS, before incubation with Tetramethylrhodamine α-bungarotoxin (TRITC α-BTX, BTIU00012, VWR International Ltd., in 1xPBS) 2 µg/mL for 15 min to label Acetylcholine receptors (**Figure 2-2.2a**). Samples were subsequently protected from photobleaching at all stages, either by wrapping the plate in aluminium foil, or by placing it underneath a black box.

Given the length of certain muscle fibre samples, it proved beneficial to trim them to their respective AChR endplate bands after visualisation of the endplate bands with α-BTX. To do so, they were placed on microscope slides, straightened with forceps and trimmed with fine dissection spring-scissors underneath an upright Nikon Eclipse 50i fluorescent microscope. Samples were kept moist at all times to prevent drying out and tearing of muscle fibres.

Following labelling of the pre-synaptic endplate, samples were permeabilised in 4% Triton X-100 in (1xPBS) for 1 ½ h. Triton X-100 is a detergent and dissolves lipid structures such as parts of cellular and intracellular membranes to allow for antibodies to access intracellular structures (Jamur and Oliver, 2010). In the present work, these are the antibodies SV2 and 2H3, which recognise the antigens on synaptic vesicles and neurofilament, respectively (**Figure 2-2**). Unspecific binding of primary antibody was reduced via blocking with blocking buffer (4% bovine serum albumin [BSA] and 2% Triton X-100 in 1xPBS) for 30 min.

Following permeabilisation and blocking, tissue was incubated with the following primary antibodies: Mouse monoclonal anti-SV2 MIgG1 to label synaptic vesicles, and anti-2H3 MIgG1 to label neurofilament (both at 1:50, DSHB, University of Iowa) in blocking buffer over night at room temperature, to indirectly label the pre-synaptic terminal (3 nights in secondary antibodies at 4°C for early animal samples).

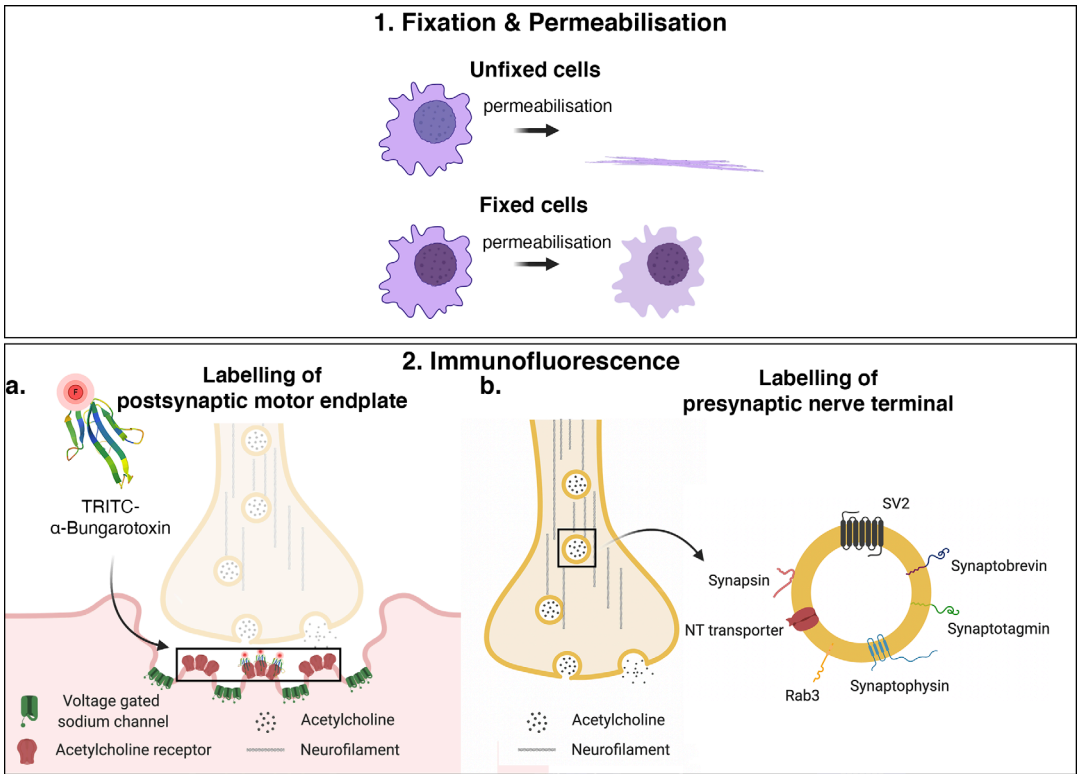

Figure 2-2: Principles underlying sample processing and immunofluorescent labelling

1. Fixation and Permeabilisation: This schematic illustrates the importance of chemical tissue fixation and associated crosslinking of protein structures. Permeabilisation of unfixed tissue with detergent, such as Triton X, will dissolve lipids and the sample will lose all structure. This will render the sample unusable for morphological analysis. Fixation of sample will crosslink proteins within the sample, allowing for preservation of morphological shape. Lipids contained in cellular, nuclear or organelle membranes can be dissolved with detergent to facilitate penetration of antibodies to target locations.

2. Immunofluorescence: Visualisation of post-synaptic motor endplates **(a)** is achieved through binding of fluorescently conjugated TRITC α-bungarotoxin (Tetramethylrhodamine α-bungarotoxin) to acetylcholine receptors with high affinity. Antibodies directed against neurofilament (2H3) and synaptic vesicle 2 protein (SV2) which is located within the membrane of synaptic vesicles **(b)**, followed by fluorescent secondary antibodies allow labelling of the pre-synaptic nerve terminal. Structure of α-bungarotoxin which is a neurotoxin derived from the Taiwanese banded krait snake (Bungarus multicinctus), PDB accession number: 1KFH (Moise *et al.*, 2002);

Subsequently, tissue samples were washed for 4 x 20min with 1xPBS to remove excess antibodies, followed by incubation for 2 ½h in secondary antibodies: Alexa 488-donkey anti-mouse IgG in 1xPBS (1:400, A21202, Life Technologies); at room temperature for human tissue (1 night in secondary antibodies at 4°C for early animal samples), followed by 4 x 20min washes with 1xPBS to remove access antibodies. After successful immunofluorescent labelling, samples were then mounted in Mowiol® (an anti-fading media) on microscope slides and stored at -20°C prior immediate imaging and following imaging.

2.3.5. Confocal Microscopy

NMJ images were acquired in several different ways, depending on the experiment and/or species:

(1) Human images (first two cachexia cases – Chapter 4) and sheep images (Chapter 5): Zeiss LSM710 confocal system via a Zeiss Inverted Axiovert microscope with a Zeiss Plan Apochromat 63× / NA 1.4 oil immersion objective (Carl Zeiss Microimaging). 8-bit pixel, 512x512 frame size, 1-3x optical zoom, 1 µm Z-stack intervals.

(2) Cat and dog images (Chapter 5) were partially processed, and fully acquired and analysed by PhD student Abrar Alhindi (Gillingwater Lab) were included in the overall species analysis: Zeiss LSM510 confocal system via a Zeiss Inverted Axiovert microscope with a Zeiss Plan Apochromat 63× / NA 1.4 oil immersion objective (Carl Zeiss Microimaging). 8-bit pixel, 512x512 frame size, 1-4x optical zoom, 0.5-1 µm Z-stack intervals.

(3) All other images (larger mammals – Chapter 5, human – Chapter 4): Image banks of larger mammalian species (sheep: EDL, SOL, PL; pig: EDL, PL;) were partially analysed by Honours, MSc and visiting students, co-supervised by me. Final data stemmed from: visiting student Ana S. Leite (School of Medicine, UNESP-São Paulo State University, Botucatu, Sao Paulo, Brazil Faculty) and MSc students

Alyssa Gibbs, Olivia Murray and Rizwan Farrukh who analysed the muscle fibre diameter of pig *soleus*.

A Nikon A1R FLIM confocal system via a Nikon Eclipse Ti inverted microscope with a Nikon Apochromat 60× / 1.4 NA oil immersion objective (Nikon Instruments Europe BV, Netherlands), with a pinhole at 1.2 Airy units. 16-bit pixel, 512x512 frame size, 1-4x optical zoom, 0.5-1 µm Z-stack intervals.

(4) Pony images (Chapter 5) were sampled, processed and acquired by our collaborator Stephen Cahalan (PhD student Piercy Group, Comparative Neuromuscular Diseases Laboratory, Pathobiology and Population Sciences, Royal Veterinary College). Image banks were shared for analyses, in addition to muscle fibre diameter and NMJ data of two ponies which were included in the overall species analysis: Leica TCS SP8 Confocal Laser Scanning Microscope (Leica Microsystems Europe)

Red channel – 543 nm excitation, green channel – 488 nm excitation, was used on all microscopes, with brightfield used to capture the muscle fibre in the last human cases imaged on the Nikon A1R FLIM. This allowed better identification, before producing maximum intensity projections, if the very fragmented human endplates were located on one muscle fibre, between two muscle fibres, or were in fact were two separate endplates. Overall, more than **3,080 NMJs** were imaged, with a total of **7,169 NMJs** (including existing images) were used for final analysis. The latter includes the addition of pony, human and mouse NMJs (Jones *et al.*, 2017).

2.3.5.1. Muscle Fibre Diameter Measurements

To prevent bleaching of fluorescent probes before imaging of morphological structures, muscle fibres were imaged following confocal microscopy. Muscle fibres were imaged on an Olympus IX71 microscope and captured on a Hamamatsu C4742-95 camera with Openlab Improvision software at x10–x20 magnification. An average of 40–60 muscle fibres were imaged per muscle, as per **Figure 2-1.4c** or at the cut ends of the muscle fibre. Sufficient

numbers were imaged to allow for analyses of 40 muscle fibres per sample/muscle, to match the number of NMJs that were analysed (**7,155 muscle fibres** in total). Muscle fibre diameter measurements were performed with the line tool in Fiji, taking 3 measurements of individual muscle fibres perpendicular to their long axis and using the mean as a representative.

2.3.6. Image Analysis (NMJ-morph)

Image processing was carried out using Fiji (Schindelin *et al.*, 2012) and the NMJ-morph workflow (Jones *et al.*, 2016) in order to asses 19 morphometric variables of the NMJ, innervation and muscle fibre diameter (**Figure 2-4**), a total of 21 variables. If possible, 40 *en face* NMJs were analysed per muscle (**a total of 7,169 NMJs**) with a cut-off for inclusion of oblique endplate area representing < 10% of the overall endplate area. Oblique endplates are positioned 'sideways' within the field of view therefore, accurate morphometric representation of NMJ morphology cannot be fully guaranteed without the above specified cut-off. Jones *et al.,* 2016 demonstrated that the ideal number of NMJs lies around 40 NMJs per muscle, as the variable-mean gradually plateaus with an increase in sample size. Ideally, oblique NMJs were excluded at the stage of imaging, although depth of field is challenging to perceive in some cases (**Figure 2-3**) and the eye can be misled viewing NMJs through the eyepiece. A more complete view is at hand once all stacks have been collated, and one can navigate through the entire depth of field of a single NMJ before collapsing it into a maximum intensity projection for analysis.

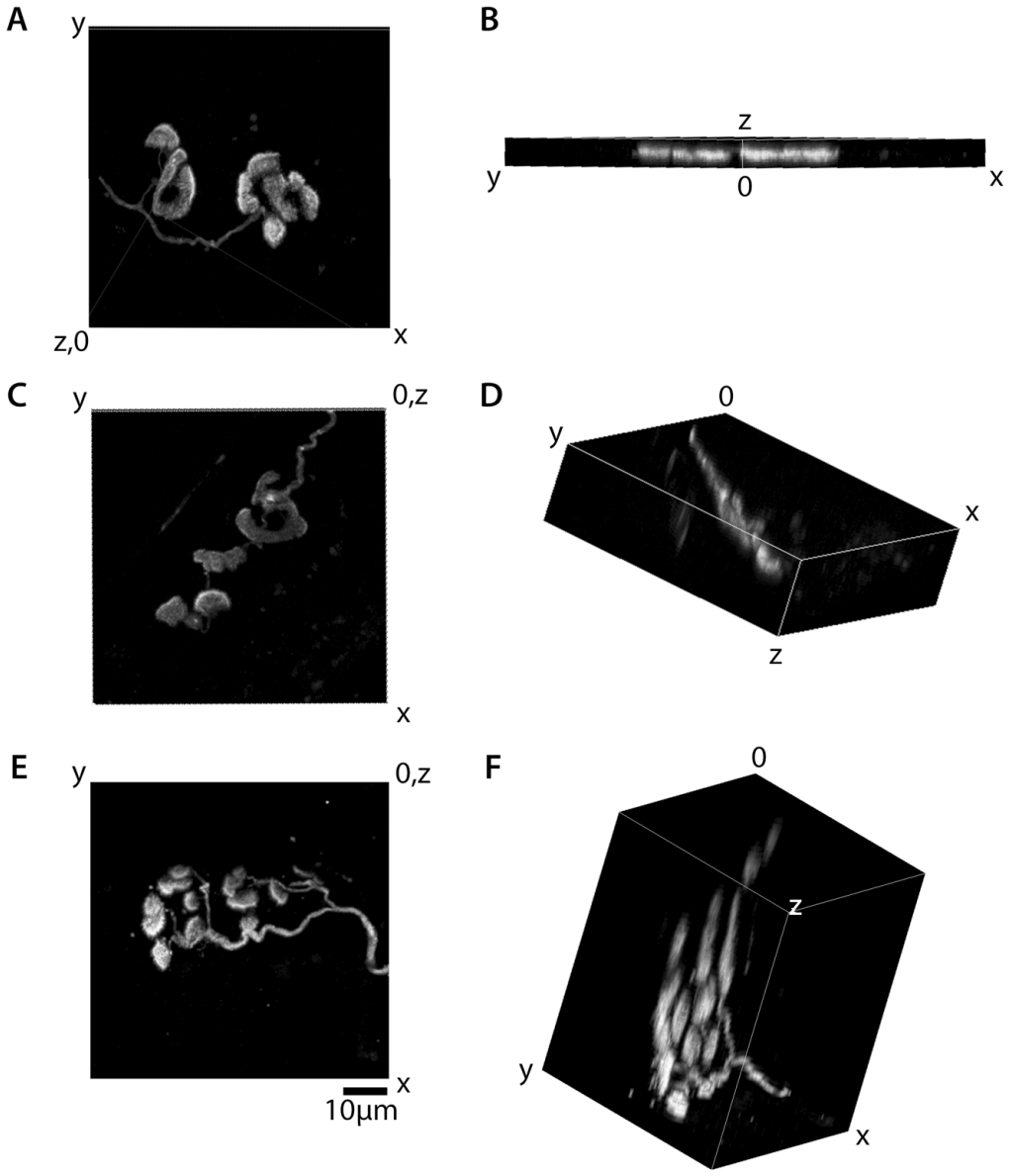

Figure 2-3: Degrees of obliqueness – Volume view of three human NMJs from the same rectus abdominis patient sample

(B), **(D)** & **(F)** depict the difference in positioning of NMJs within the z-stack volume that might not be apparent from the **(A)**, **(C)** & **(E)** Maximum Intensity Projection (MIP) used for analysis. **(B)** shows an NMJ that has clearly been imaged *en face* and lies flat within its z-stack volume, whereas **(D)** is positioned on a slight angle, however, is still < 10% fully oblique. **(F)** Depicts an NMJ that is > 90% oblique, most of the surface is positioned along the z-axis, and was therefore excluded from analysis. Upon generation of a MIP one can appreciate the overall boundaries of both endplate and motor nerve in grey, and how difficult (A, C & E) are to differentiate in terms of orientation within 3D space. Scale bar = 10 µm; grey represents a composite of visualized AChRs and SV2/2H3 (synaptic vesicle protein/neurofilament, both post- and pre-synapse).

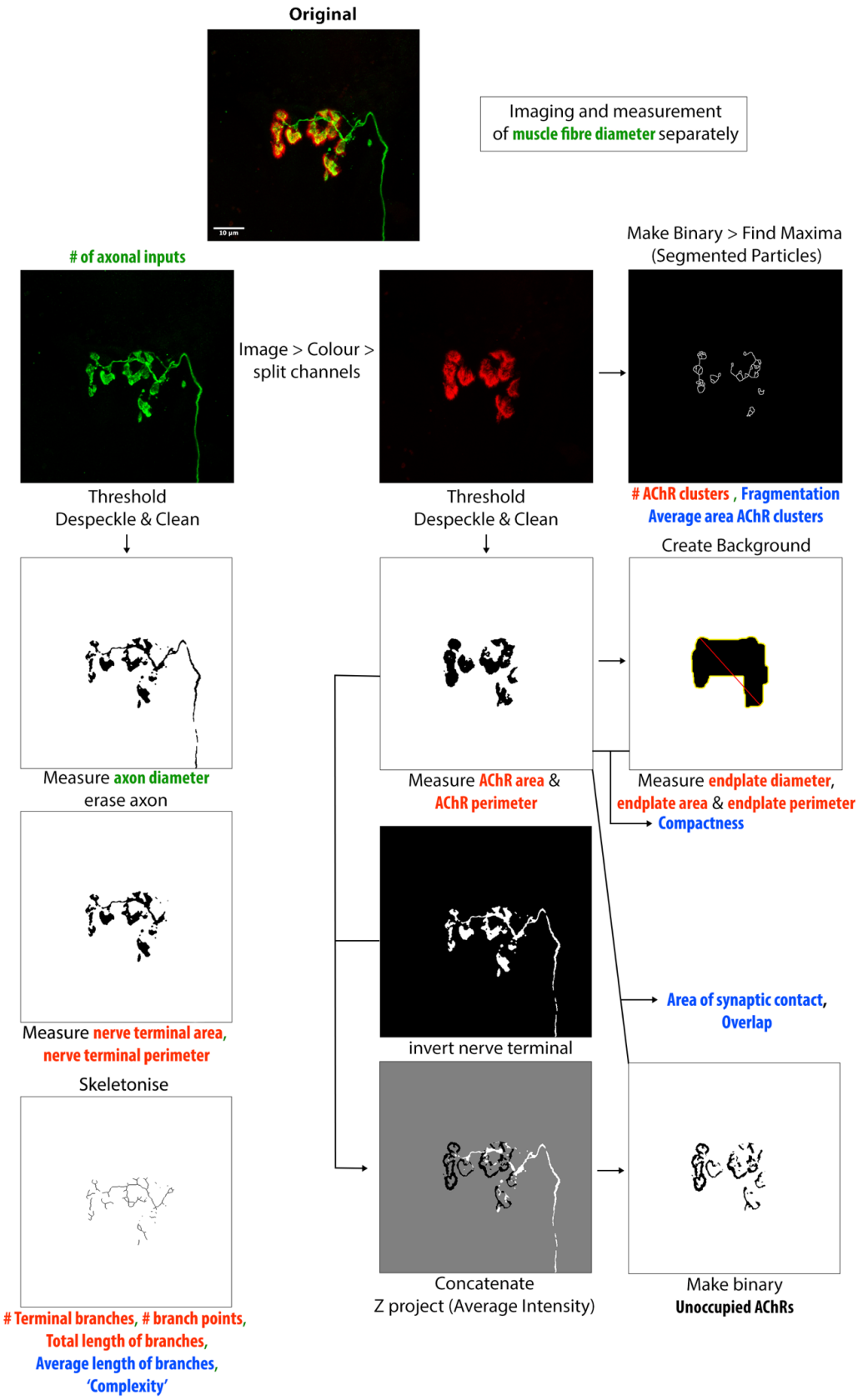

Figure 2-4: NMJ-morph workflow

Legend continues on next page.

Shortened outline of the NMJ-morph workflow on human NMJs (.nd2 picture format). 20 variables are quantified for each NMJ, 21 if the muscle fibre diameter is included which needs to be imaged and measured separately (top right box). Consistent with the original definitions from Jones *et al.,* 2016 the 11 'core variables' are in red, bold font, the 7 derived variables are in blue, bold font, and associated nerve and muscle variables are in green, bold font. Black regular text refers to individual commands between steps within the workflow of ImageJ/Fiji.

In short, the original image (in maximum intensity projection form) is split into its pre- and post-synaptic channels. These are both thresholded with care, 'cleaned' from clear background noise and made binary, leaving a black and white image. Pre- and post-synaptic size variables are measured on each respective channel. The skeletonise function allows for retrieval of branching and complexity indices. Combination of nerve terminal endplate yield derived variables area of synaptic contact and overlap (bottom right). The find maxima function on the binary version of the original post-synaptic channel yields AChR cluster and fragmentation related variables (top right next to original image of postsynapse). Abbreviations: AChR = acetylcholine receptor; # = number; Scale bar = 10 µm.

As **Figure 2-3.E** and **F** show, respective pre- and post-synaptic areas would have been underestimated following analysis of the maximum intensity projection of **Figure 2-3.E** – it was therefore important to screen all NMJs for suitability before analysis. This explains in part why the cut-off of 40 NMJs per muscle was not achieved for all muscles.

2.3.6.1. Training (thresholding, inter-user variability)

In order to familiarise oneself with the workflow of 'NMJ-morph' and the use of the platform Fiji to accurately threshold and measure the 19 pre- and post-synaptic variables of the NMJ, the 20 sample mouse NMJ confocal micrographs which are available on the Edinburgh DataShare (http://dx.doi.org/10.7488/ds/1490) were used in combination with the instruction manual and workflow. A condensed overview of the workflow is depicted in **Figure 2-4**. To evaluate proficiency with 'NMJ-morph' and ensure inter-user variability is not due to easily avoidable mistakes, a 'practice' mouse image bank was consolidated. Easy mistakes are normally due to manual input or user bias, such as differences in appropriate thresholding,

accurate measurement of endplate diameter or manual erasing of axon diameter. The 'practice' image bank entailed 120 CD1 mouse NMJs from male littermates (n = 3, 40 NMJs per muscle; *extensor digitorum longus*, *soleus* and *peroneus longus*) which were measured and correlated to previously recorded data (Jones *et al.*, 2017).

Upon successful training in NMJ-morph, a macro plugin was developed in order to speed up analysis and avoid mistakes associated with data transfer. This is described in more detail in the subsequent Chapter.

2.4. Summary

This overview of the general methods used throughout the future experiments serves as both a brief introduction into Chapters 3–6, and also aims to be a reference that can be revisited at any point throughout the thesis. General principles of sample preparation and immunofluorescence have been described in detail and the underlying workflow of NMJ-morph has been reviewed to provide a basis for Chapter 3 (aNMJ-morph: a simple macro for rapid analysis of NMJ morphology). The logistics behind tissue sampling has been described briefly and more detail on patient and muscle selection will be given in the respective chapters:

Chapter 4: Neuromuscular junctions are stable in patients with cancer cachexia

Chapter 5: Comparative anatomy of the mammalian neuromuscular junction

Chapter 6: The human NMJ-enriched ageing proteome is more stable than that of muscle

3. aNMJ-morph: a simple macro for rapid analysis of NMJ morphology

3.1. Chapter Summary

This chapter showcases the development and proof-of-concept of a semi-automated macro – 'aNMJ-morph' (automated NMJ-morph) – that aimed to speed up and improve the existing NMJ-morph workflow. Preceding this, the training and quality control in NMJ-morph are provided by analysis of 120 NMJs which were required for accurate analysis of subsequent NMJs. 'aNMJ-morph' was designed for rapid analysis of morphometric variables of the NMJ. Forty NMJs were analysed with 'aNMJ-morph' and 'NMJ-morph' and statistical analysis was used to assess whether the macro was a valid substitute for 'NMJ-morph'. Reproducibility of 'aNMJ-morph' was then tested by comparison of manual (NMJ-morph) and semi-automated (aNMJ-morph) analyses of 240 sheep NMJs, conducted by six independent observers. aNMJ-morph showed a significant reduction in analysis time required per NMJ and results demonstrated excellent overall reproducibility. Consequently, the aNMJ-morph approach outlined in this chapter was used across all subsequent chapters (in conjunction with NMJ-morph where detailed). The entire aNMJ-morph workflow was published open access (Minty *et al.*, 2020).

3.2. Background

Assessment of NMJ-morphology plays a crucial role in the examination of disease pathology in humans and animal models, in the comparison of new genetic animal models and the overall evaluation of treatment interventions. Until recently, one of the major technical challenges of comparative study of NMJs between species or disease models was the lack of a robust quantitative platform that provided standard methods of measurement and reporting of NMJ morphology. Generally speaking, it is extremely difficult to reliably and consistently compare data from publications that used different methodologies to measure and quantify NMJ variables. This is especially true when the definition of 'key' variables differs across studies (e.g. in early studies antibodies against acetylcholine esterase were used to define the 'boundaries' of NMJs as per **Figure 1-4**, which is now referred to as endplate area and labelled with fluorescently conjugated α-bungarotoxin) (Theroux *et al.*, 2002).

NMJ-morph, a protocol for ImageJ or Fiji, has recently been developed to reliably quantify *en face* confocal micrographs of NMJs (Jones *et al.*, 2016). The methodology generates 21 variables, 19 morphometric variables of the NMJ, innervation, and muscle fibre diameter, facilitating comparative analysis of the NMJ within and across species. This standardised method has shown reproducible results with little between-user variability and has aided in the comparison of morphometric variables of NMJs across a variety of studies as previously highlighted in the background.

The plethora of studies to date utilising NMJ-morph showcases the tremendous opportunity that this workflow provides to conduct in-depth comparative studies of the NMJ, across species and in health and disease. One particular drawback of NMJ-morph is the time it takes to analyse image sets. The systematic workflow requires two iterations of thresholding (on pre- and postsynapse) and multiple iterations of size and perimeter measurements – thus meticulous care should be taken when transposing

data from Fiji to Excel spreadsheets. Furthermore, attention to detail is required to correctly measure both axon diameter and linear endplate diameter, since both are measured manually.

Since Fiji allows for the recording of workflows in macro form that can then be applied to either folders of images (or individual images) this approach has been used in an attempt to develop a macro version of NMJ-morph. The great benefit of macros is that they rapidly speed up processing time as there is no need to click through the approximately 75 separate drop-down menus within the extensive NMJ-morph (manual) workflow (as these menu options would be embedded into the macro). This chapter therefore describes:

1) Evaluation of proficiency in the use of NMJ-morph
2) Development/scripting of the aNMJ-morph macro
3) Troubleshooting of aNMJ-morph: automation and manual components
4) Proof-of-concept of aNMJ-morph: Within and between user variability, benefits of semi-automation

3.3. Methods

3.3.1. Ethics, tissue sampling, processing and confocal microscopy

Details for underlying ethical approvals and laboratory methodology for visualisation and imaging of NMJs are detailed within Chapter 2 (General Methods). In brief, data from mouse NMJs used as a reference dataset for training in NMJ-morph stem from Jones *et al.,* 2017. The principal development of aNMJ-morph was undertaken on 40 mouse NMJs from Jones *et al.*, 2017, whilst NMJs used for comparison of manual and semi-automated workflows and overall testing of aNMJ-morph reproducibility were obtained from sheep collected at Dryden Farm (RDSVS). Following tissue sampling, muscle fibres were teased and pre- and post-synaptic components of the NMJ were visualised using immunofluorescence. Mounted slides were

imaged via confocal microscopy as described in Chapter 2 (4.1.5 Confocal Microscopy).

3.3.2. Image Analysis

The previously collated image banks and corresponding mouse NMJ data (Jones *et al.,* 2017) were used for training in NMJ-morph and initial quality control of training datasets. Confocal images of various file formats (.lsm and .nd2) were used for the development of aNMJ-morph to ensure the macro plugin worked across images which were acquired by different microscopes. This should ensure reproducibility of results across laboratories.

3.3.2.1. Training (thresholding, between-user variability)

In order to familiarise oneself with the workflow of 'NMJ-morph' and use of the platform Fiji to accurately threshold and measure the 19 pre- and post-synaptic variables of the NMJ, the **20 sample mouse NMJ** confocal micrographs that are available on the Edinburgh DataShare (http://dx.doi.org/10.7488/ds/1490) were used in combination with the instruction manual and workflow (a shortened overview of this workflow is depicted in **Figure 2-4**). To then assess proficiency with 'NMJ-morph' and ensure observed between-user variability was not due to easily avoidable mistakes a 'practice' mouse image bank was consolidated. Simple mistakes are normally due to errors of manual data input or user bias, such as differences in threshold selection, accuracy in endplate diameter measurement or manual erasing of axon diameter. The 'practice' image bank comprised **120 CD1 mouse NMJs** from male littermates (n = 3, 40 NMJs per *extensor digitorum longus*, *soleus* and *peroneus longus*) which were measured and correlated to previously recorded data (Jones *et al.*, 2017).

3.3.3. Scripting of the aNMJ-morph macro

Following establishment of proficiency with the manual NMJ-morph workflow, scripting of the semi-automated aNMJ-morph macro using the ImageJ macro

language (IJM) and was performed in conjunction with and as part of supervised student projects (Alex Hoppen, Aachen University, Germany and Gavin Minty, Edinburgh University). Overall, scripting of aNMJ-morph followed a straight-forward and streamlined approach that involved coding of the correct sequence of drop-down menus and checkboxes, and generation of an appropriately formatted spreadsheet containing the correct formulas for calculation of all variables (the final macro is available under Minty *et al.*, 2020).

The Binary Connectivity plugin which is required for assessment of nerve terminal branching was preloaded and is available at https://blog.bham.ac.uk/intellimic/g-landini-software under the section 'Morphological Operators for ImageJ' (Landini, 2020). Overall, the approximately 75 drop-down menus required to navigate through NMJ-morph were reduced to seven instruction windows (detailed in **Figure 3-1**) that generated a .csv (comma-separated values) file containing data for 19 morphometric variables from either one NMJ or a folder of NMJs if processed in 'batch-processing' mode, data for subsequent NMJs was added to the spreadsheet after each NMJ. The spreadsheet was generated after analysis of the first NMJ and is located in the same directory that the NMJ images are saved in. Should the name of the original spreadsheet be changed during analysis, a new results.csv file will be generated and newly analysed NMJs will be added to the newly created spreadsheet.

To ensure aNMJ-morph was compatible across operating systems (e.g. Windows and Mac OS X) compatibility with Fiji on Mac OS X was continuously assessed within Mac OS X High Sierra (version 10.13.5) using Fiji (ImageJ version 2.0.9-rc-67/1.52i).

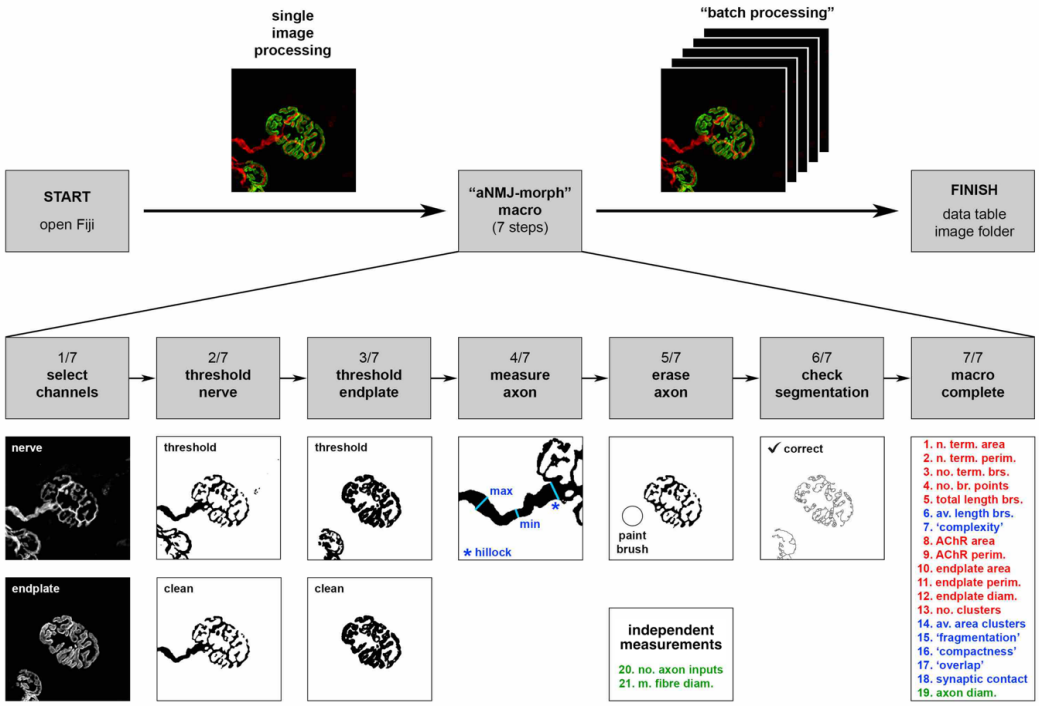

Figure 3-1: aNMJ-morph workflow

The overall workflow of aNMJ-morph is comprised of seven instructional windows. NMJs can be loaded in 1) 'single image processing' mode: the image is opened in Fiji, and the macro is opened by either selection (Plugins > Macro > Run…) within the drop-down menu, or through drag-and-drop of the macro .txt file onto the loaded NMJ; or 2) 'batch processing' mode: the macro is loaded first via the Fiji drop-down menu (Plugins > Macro > Run…), then the folder containing the NMJs for analysis is selected. aNMJ-morph guides the user through 'selection of channels' (step 1/7) which allows assignment of channel 1 and 2 to pre- or postsynapse, and 'thresholding' of the nerve terminal (step 2/7) and endplate (step 3/7).

Measurement of axon at minimum, maximum diameter, and at hillock (blue asterisk in step 4/7) where the motor neuron splits to innervate the endplate, or directly innervates the endplate, requires precision. Following erasure of axon (step 5/7), nerve terminal, endplate size variables, as well as branching pattern and complexity are measured automatically.

The penultimate step (6/7) includes assessment of endplate fragmentation. A pop-up window grants a 'check' to evaluate endplate segmentation, followed by a window informing the user that aNMJ-morph is complete (7/7). In 'batch processing' mode a new NMJ is loaded, or another image has to be loaded manually in 'single image processing' mode. Results following completion of analysis will be saved in a .csv file containing 19 morphometric variables that correspond to the manual NMJ-morph workflow. *Legend continues on next page.*

Figure 3-1 legend continued from previous page:
These 19 variables are listed underneath step 7/7 macro complete. Independent measurements such as number of axonal inputs (20.) and muscle fiber diameter (21.) require manual addition into the spreadsheet. 'Core variables' are shown in red typeface, 'derived variables' in blue and 'associated nerve and muscle variables' in green. Figure from (Minty *et al.*, 2020)

3.3.3.1. Automation within aNMJ-morph

Whilst the original NMJ-morph workflow contained various manual inputs, such as axon diameter, endplate diameter and counting of number of AChR clusters, the goal was to automate these as efficiently as possible (**Figure 3-2**).

Since axon diameter measurement required several decision-making processes, this step remained manual. Measurement of endplate diameter was automated by extracting the 'Feret's diameter' (described by the French physicist Walton; see Walton, 1948) from the endplate measurement (**Figure 3-2.E**). The Feret's diameter is calculated as the longest distance between two tangents that run in parallel along the selected perimeter (**Figure 3-2.E**) and automation of its extraction allows for increase in speed, as well as enhanced accuracy during NMJ analysis (**Figure 3-3**). The last measurement that required automation was 'counting of the number of AChR clusters'. As images to analyse might contain more than one NMJ per field of view, which is easy to distinguish manually, automated count of segmented particles following the 'segmented particles' function is not able to distinguish between particles that belong to the NMJ to be analysed, or a separate NMJ.

To circumvent this issue, the footprint of the endplate area was projected onto these segmented particles via the (Z-project > Average Intensity…) function. Average intensity, as the name suggests, averages out intensities, and areas that cover segmented particles within the endplate will be rendered a darker grey or black as opposed to areas outside of the endplate, which will be rendered a lighter grey (**Figure 3-2.A**). If the image is 'Made binary' thereafter, only the entirely black segmented particles remain. This

process essentially masks segmented particles outside the previously established endplate area. Analysis of particles then automatically reports the count and thus number of AChR clusters.

Whilst automation of AChR cluster counting proved efficient, a few considerations had to be made as on rare occasions, when confocal images yielded aberrant fragmentation/segmentation patterns that prevented counting of AChR clusters (less than 1 in 1000 images) (**Figure 3-2.B–C**). Aberrant segmentation results typically in 'spider web' or 'broken window' like appearance which prevents automated or manual AChR cluster count. In most cases this is due to low image quality with high background – however, in human NMJs in particular (**Figure 3-2.B–C**) this occurs when the contrast between post-synaptically labelled AChR and background is low. This problem also occurred in pony NMJs which were analysed in Chapter 5. A much larger majority (> 20/40) of overall NMJs presented with aberrant segmentation patterns which prevented analysis of AChR clusters. To still continue with analysis whilst retaining the previously measured variables for respective NMJs, an additional check-point window was included in the workflow (**Figure 3-1** step 6/7) asking the user to evaluate segmentation and confirm that it is 'normal'. If the user decides that aberrant segmentation has occurred, then no values will be entered into the spreadsheet for number of AChR clusters and the variables average area of AChR clusters and fragmentation remain empty as well, as these require number of AChR clusters for their calculation.

Low-quality images that are excessively blurry or lacking in contrast should be excluded from any analysis. During the automation of counting of AChR clusters, one should remain vigilant for AChR clusters that lie within the boundaries of other AChR clusters, i.e. separate AChR clusters surrounded by the full perimeter of another AChR cluster (**Figure 3-2.D**).

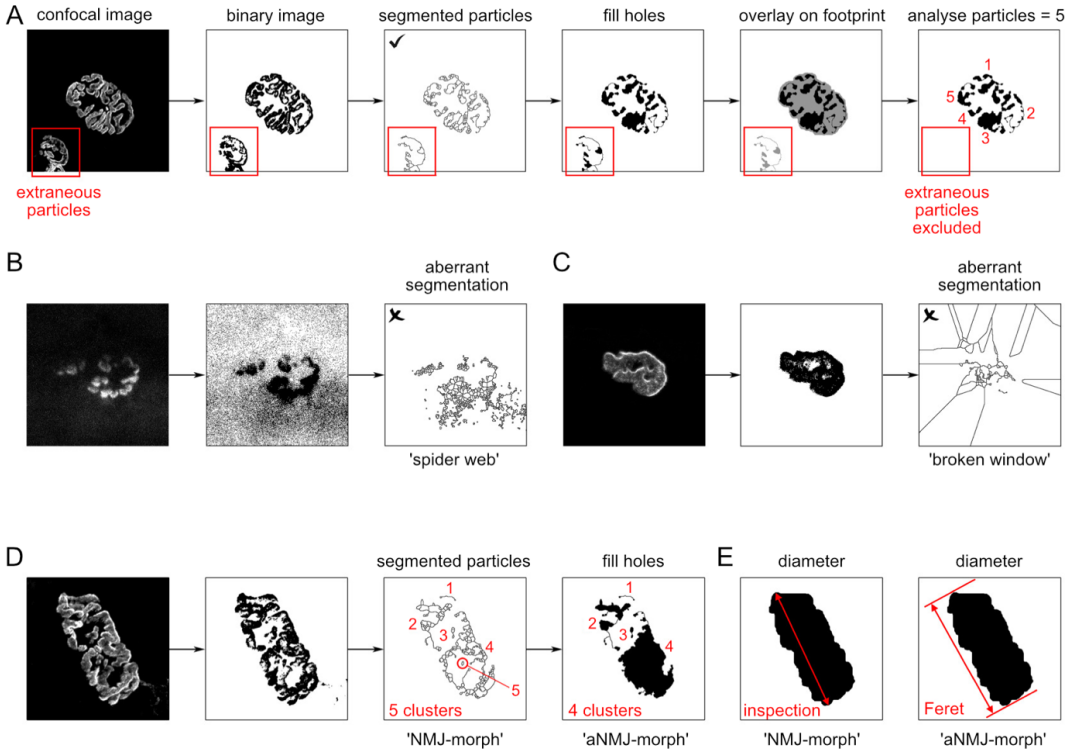

Figure 3-2: Automation within aNMJ-morph

Figure adapted from (Minty *et al.*, 2020) For full automation of the NMJ-morph workflow, the depicted here manual measurements had to be automated.

(A) Counting of number of AChR clusters required adaptation of the script to account for confocal images that might contain more than one NMJ within the field of view. For this, the 'segmented particles' function was run just like in the manual workflow and the resulting image was overlayed on top of the footprint of endplate area. This allowed for exclusion of extraneous particles and one could then proceed with automated count of segmented particles.

(B & C) Example images of aberrant segmentation that occurs in lower quality images, or when contrast between endplate and surrounding area is not sufficiently pronounced. These typically have a 'spider web' (B) or 'broken window' (C) like appearance.

(D) Some NMJs, more so mouse NMJs that consist of a more 'pretzel-like' structure, showed variations in the particle number between aNMJ-morph and NMJ-morph. As particles were counted manually in NMJ-morph, individual particles can be counted 'exactly'. As some NMJs contain AChR clusters within the boundaries of another cluster (D – segmented particles 'NMJ-morph'), these clusters are lost during the 'aNMJ-morph' workflow as the 'fill holes' function fills areas outlined by the 'segmented particles' function. Therefore, this would fill the entire area containing the AChR cluster within another cluster (red circle). The difference, in this example four as opposed to five clusters, does not make a statistical difference between aNMJ-morph and NMJ-morph. *Legend continues on next page.*

Figure 3-2 legend continued from previous page:

(E) Endplate diameter measurement was automated by extracting the Feret's diameter from endplate area measurements.

Figure 3-3 shows a more detailed depiction of the best-case scenario in regard to the difference between manual measurements and those measurements using the Feret's diameter can lead to.

Whilst the fill-holes function fills all outlined perimeters, this function can lose clusters within the outline of larger AChR clusters (as occurred in 3 out of 40 endplates that were 'pretzel' shaped).

3.3.3.2. Manual aspects of aNMJ-morph

As mentioned in the previous section, some manual measurements were retained as they require significant situational judgement and no current ImageJ plugins were available to reliably automate these steps. For example, axon diameter measurement could not be automated. Whilst there are many scripts that allow automated axon diameter measurements, these are mostly designed for cross-sectional images and apply the same principal as the measurement of the Feret's diameter. As axons are in their 'longitudinal' form in confocal images of NMJs, locations such as the hillock (**Figure 3-1** – step 4/7) where the motor nerve branches to innervate the NMJ (or else directly innervates the NMJ) have to be judged appropriately by the investigator, which complicates automation.

Overall, automation of individual steps increases the time to be spent on the first steps of the NMJ-morph/aNMJ-morph workflow: **thresholding**. Since accurate thresholding of pre- and post-synaptic channels is crucial, this step could not be automated, relying as it does on accurate recapitulation of the original 'shape' of the pre- or postsynapse, and the experience of the investigators.

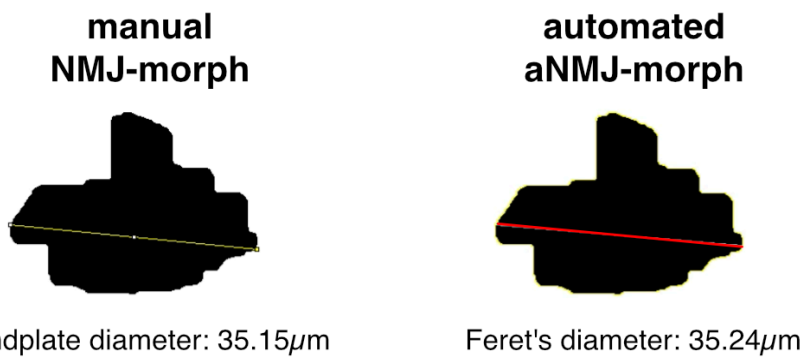

Figure 3-3: Comparison of endplate diameter measurement between NMJ-morph and aNMJ-morph

Despite similarity in diameters drawn between NMJ-morph (thin yellow line) and aNMJ-morph (red line), results differ marginally. As this is a 'simple' endplate shape, it is easy to judge maximal endplate diameter during NMJ-morph analysis. As endplates become rounder, or more abstract in shape, the difficulty in providing accurate manual diameter measurements increases. The Feret's diameter is automatically measured in Fiji when measuring variables of selected areas. This saves time and is undoubtedly more reproducible.

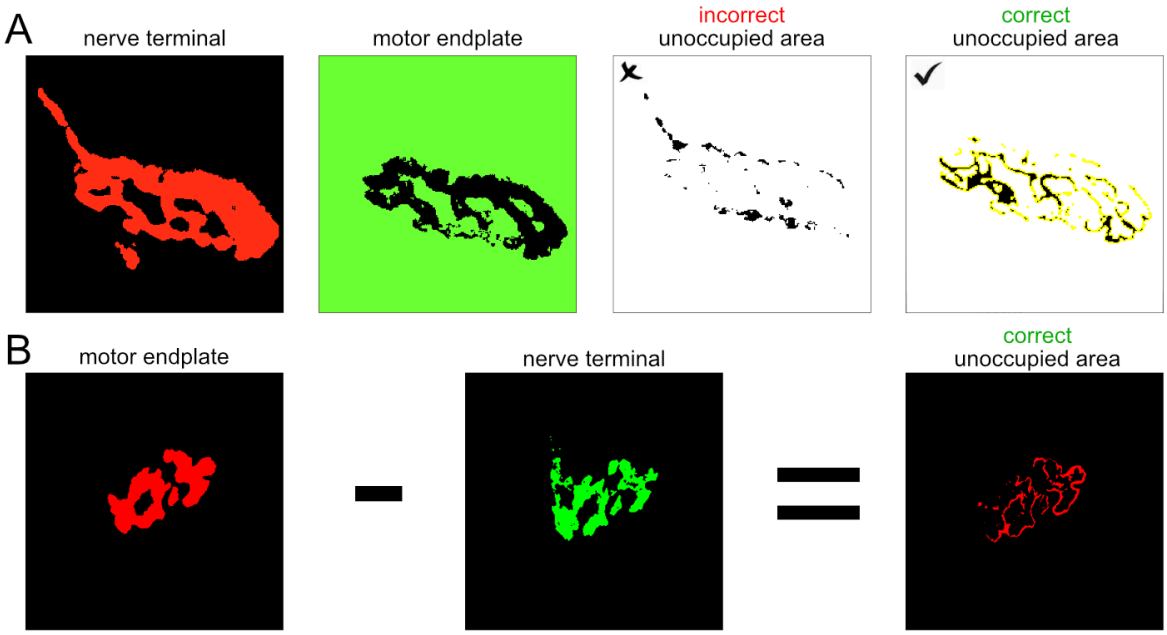

Figure 3-4: Adaptation of unoccupied endplate area calculation

Consistent issues were encountered when calculating unoccupied endplate area with different file formats during aNMJ-morph development.

(A) Inversion of the wrong channel (motor endplate in this case) lead to an incorrect unoccupied area when the macro was trialed on a different file format following a Fiji update. Inversion of the appropriate channel (nerve terminal as depicted here) leads to correct unoccupied area. This means that using NMJ-morph, care has to be given to invert the correct channel. Selection of appropriate unoccupied area is outlined in yellow.

(B) To avoid issues that were encountered with inversion of the wrong channel, a simpler approach was designed for aNMJ-morph to avoid issues with different file formats. Subtraction of the nerve terminal from motor endplate results in the correct unoccupied area.

3.3.3.3. Consideration of different file types and different microscopes

During scripting of aNMJ-morph it became apparent that some microscopes assign different channel orders to different wavelengths that are imaged and thus channel 1 and channel 2 do not necessarily correspond in every file format.

To account for this, a starting window, upon launch of aNMJ-morph, was incorporated that allows for assignment of appropriate channel numbers to the 'Nerve Terminal' and 'Muscle Endplate' (**Figure 3-1** – step 1/7).

Furthermore, as channel order of motor endplate and nerve terminal varied between file formats, measurement of 'unoccupied area' required standardisation. As inversion of the motor endplate is needed for the test images of mouse and human NMJs in .lsm file format, consideration of location of the motor endplate in different channels (either channel 1 or channel 2) across both species had to be taken into account. Additionally, from initial manual analysis with NMJ-morph, it was evident that the nerve terminal required inversion of images in .nd2 format.

In the original NMJ-morph workflow, during measurement of unoccupied area, (required for calculation of the overlap) the thresholded, cleaned and binary versions of the motor endplate and nerve terminal are first opened. Respective channels then require inversion (**Figure 3-4.A**) and both images/channels are concatenated into one image that contains two channels: one inverted, one original. Next, overlay of both stacks with Average Intensity (Image > Stacks > Z-Project… choose Average Intensity) averages dark on dark background to black (the unoccupied AChR area between motor endplate and nerve terminal), white on white backgrounds to white, and white on black backgrounds (area that overlaps between motor endplate and nerve terminal) to grey. The 'make binary' function then preserves only areas that are fully black (unoccupied AChR area) with everything that does not correspond to a black value being rendered white (this principle can be seen in **Figure 3-4.A** – and is the same in **Figure**

3-2.A). Measurement of the remaining area is equal to the unoccupied endplate area that is not covered by the nerve terminal.

As issues were noted in the correct application of the inversion step (the wrong channel was inverted) and given the different requirements between various image formats, a clearer solution was required. A subtraction function was therefore applied that 'subtracts' nerve terminal area from AChR area leaving only the unoccupied area as apparent in **Figure 3-4.B**. This further increased the processing rate of aNMJ-morph as fewer functions were required for the analysis of unoccupied area.

3.3.4. Statistics

For establishment of user proficiency with NMJ-morph, Pearson correlation analysis was performed in RStudio (version 1.2.1335) using the R (version 3.6.3) core package tidyverse 1.3.0 (Wickham *et al.*, 2019) for data manipulation and data tidying, and ggplot2 3.3.2 (Valero-Mora, 2010) for data visualisation (which is generally attached whilst the tidyverse library is loaded). The Pearson correlation coefficient r is reported, with $p < 0.0001$ = ****; $p < 0.001$ = ***; $p < 0.01$ = **; $p < 0.05$ = *; ns = non-significant.

3.3.4.1. Student contributions

All students who contributed to proof-of-concept of aNMJ-morph first underwent training in NMJ-morph to demonstrate adequate user proficiency with the primary workflow before proceeding with the use of aNMJ-morph. Gavin Minty, Edinburgh University, compared aNMJ-morph against the original NMJ-morph workflow.

Between user variability and usability on different platforms were assessed by six project students who were co-supervised by me. Three students used aNMJ-morph to analyse 80 sheep NMJ confocal images in .lsm file format each: Larissa Gibb, Ellie Potter and Boris C. Wagner) and three Honours students used NMJ-morph to analyse the same 80 NMJs each (Lorcan Bailie, Rachel Fu and Mhairi Paterson).

3.3.4.2. Validation of aNMJ-morph

During aNMJ-morph development, aNMJ-morph was first compared against the original NMJ-morph workflow using the same image threshold settings across both methods. To establish compatibility with different file formats (.lsm or .nd2) example confocal images of varying file-type were analysed in batch processing mode via aNMJ-morph. The .lsm file format stemmed from Zeiss microscopes and the .nd2 file format stemmed from Nikon microscopes. The scripting was adapted to yield consistent results. Primarily the calculation of unoccupied area (**Figure 3-4**) had to be altered to yield correct results between file-types.

To validate aNMJ-morph results and establish reproducibility of aNMJ-morph across various users, comparison of NMJ-morph and aNMJ-morph was performed in GraphPad Prism software (version 9.0.1). Within user variability was assessed by correlation analysis on mouse NMJ confocal images in .lsm file format (Jones *et al.*, 2017) that were analysed with the same threshold settings across both methods (**40 NMJs**). Analysis with both workflows was timed to assess differences in speed of analysis between NMJ-morph and aNMJ-morph.

To evaluate between-user variability and reproducibility of results across different operating systems (Windows and Mac OS X), six project students (see student contributions) analysed 80 sheep NMJ confocal images using aNMJ-morph and NMJ-morph. Both slow-twitch (*soleus*) and predominantly fast-twitch (*extensor digitorum longus*) muscles were included for a total of **240 NMJs** (40 NMJs per muscle, 80 NMJs per investigator). These were compared between NMJ-morph and aNMJ-morph by three pairs of investigators and resulting data were correlated via Pearson or Spearman correlation analyses for parametric and non-parametric variables, respectively.

3.4. Results and Discussion

3.4.1. Validation of NMJ-morph user proficiency

To determine the user proficiency with 'NMJ-morph' and the degree of between-user variability, a sample set of 120 previously published mouse NMJs ("Reference Data") was used for training (Jones *et al.*, 2017). Correlation analysis were performed in RStudio between "Reference Data" and "Training" data for all 19 variables listed in **Table 3-1**. An example is shown in **Figure 3-5**.

3.4.1.1. NMJ-morph between user variability

Particular care had to be taken in the initial stage of image analysis. During thresholding the raw maximum intensity projection confocal image of the NMJ is considered the 'blueprint' and during thresholding the aim was to replicate the overall shape as accurately as possible by 'thresholding' it into a binary (black and white) version. Particular care should be taken at this stage and in the assessment of what constitutes an NMJ, as extraneous particles can sometimes be located within the field of view (**Figure 3-2.A**). This becomes apparent when assessing the images and correlation analyses shown in **Figure 3-5.A** and **C** and in **Figure 3-5.B** and **D**. Here A and B include one confocal image of a NMJ in "Training" that was considered to be 'one single' NMJ, whereas in the "Reference Data" the image was considered to contain two separate NMJs. Hence "Reference Data" showed smaller values – roughly half the endplate area and nerve terminal area of "Training" data. Correction of this discrepancy led to an increase in correlation between endplate area from r = 0.946 to 0.981 and nerve terminal area from r = 0.932 to 0.952. This highlights the importance of practice and consistency in analysis and thresholding within the own dataset is. Taking these considerations into account will lead to more reproducible and reliable data.

Following training and correction of endplates as outlined in **Figure 3-5.A** and **B**, overall correlation analysis of "Reference Data" and "Training" data

showed strong concordance, with **** P < 0.0001 for all variables (**Table 3-1**). The strongest correlated variable was endplate area (r = 0.981) which requires the least manual input overall: only thresholding and manual cleaning of the endplate (i.e. removal of background noise if any remains after thresholding). Axon diameter, the variable that required the most manual measurements (i.e. three manual measurements of the axon diameter to calculate the mean axon diameter) had the lowest correlation coefficient as expected (r = 0.694). Furthermore, only 80% (96/120) of axons were measured/had measurable axons. Poor axonal staining, location of the axon outwith the imaging frame or entering the nerve terminal from above or below, make it impossible to accurately measure all axon diameters.

3.4.1.2. Thresholding as a defining factor

As mentioned previously, the degree of thresholding is critical in accurate rendering of the original NMJ. Practice in recognising which structures belong to the NMJ and which are extraneous is crucial throughout the thresholding process. The 'NMJ-morph' guide recommends the thresholding pre-sets '*Huang*' (accurate in ≈80% of images) and '*Yen*' to have highest reproducibility with original confocal micrographs (Jones *et al.*, 2016).

A new thresholding pre-set '*Otsu*' has been made available recently and seemed to reproduce a more accurate representation of the nerve terminal in more cases than the recommended setting 'Huang'. '*Otsu*' was used on ~49% of the endplates and ~63% of the nerve terminals of the overall 120 training images. As recommended '*Huang*' was still appropriate for ~43% of the here analysed endplates (but only ~32% of nerve terminals). As per user manual, manual thresholding should only be used if the user is sure that manual thresholding replicates the original closer than the pre-set: ~7% and ~5% manual thresholding were applied across endplates and nerve terminals, respectively. Only ~2% *'Yen'* were found to suit endplates, and 0% nerve terminals, suggesting that overall, '*Otsu*' provides a much more sensitive rendering of both pre- and post-synaptic components of the NMJ (compared to either '*Huang*' or '*Yen*'). However, use of a different

thresholding pre-set still results in high correlation with “Reference Data” that used only ‘*Huang*’ or ‘*Yen*’. Thus, ‘*Otsu*’ can be reliably used as an additional thresholding pre-set if required as the initial rendering of images is found to be superior to other pre-sets.

3.4.2. Validation of aNMJ-morph

Following familiarisation with NMJ-morph, comparison of results between the manual and semi-automated workflow could proceed. Throughout aNMJ-morph development, the consistency of results between both workflows was continuously confirmed. Overall, within and between user variability was assessed (**Table 3-2**) to validate the use of aNMJ-morph as a robust tool for NMJ analysis.

3.4.2.1. Within user variability – proof-of-concept

First, to compare within user variability during development, 40 NMJs were analysed with both NMJ-morph and aNMJ-morph with identical thresholding settings (**Table 3-2 – Within User**). Identical threshold settings were chosen in order to minimise possible variability due to user bias – as although different thresholding methods (if used appropriately) yield highly comparable results, those results are still not identical (previously discussed in ‘3.4.1.2 Thresholding as a defining factor’). Overall, all results correlated exceptionally well with near identical values across most variables ($r = 0.954–1.000$; all $P < 0.0001$ **Table 3-2 – Within User**).

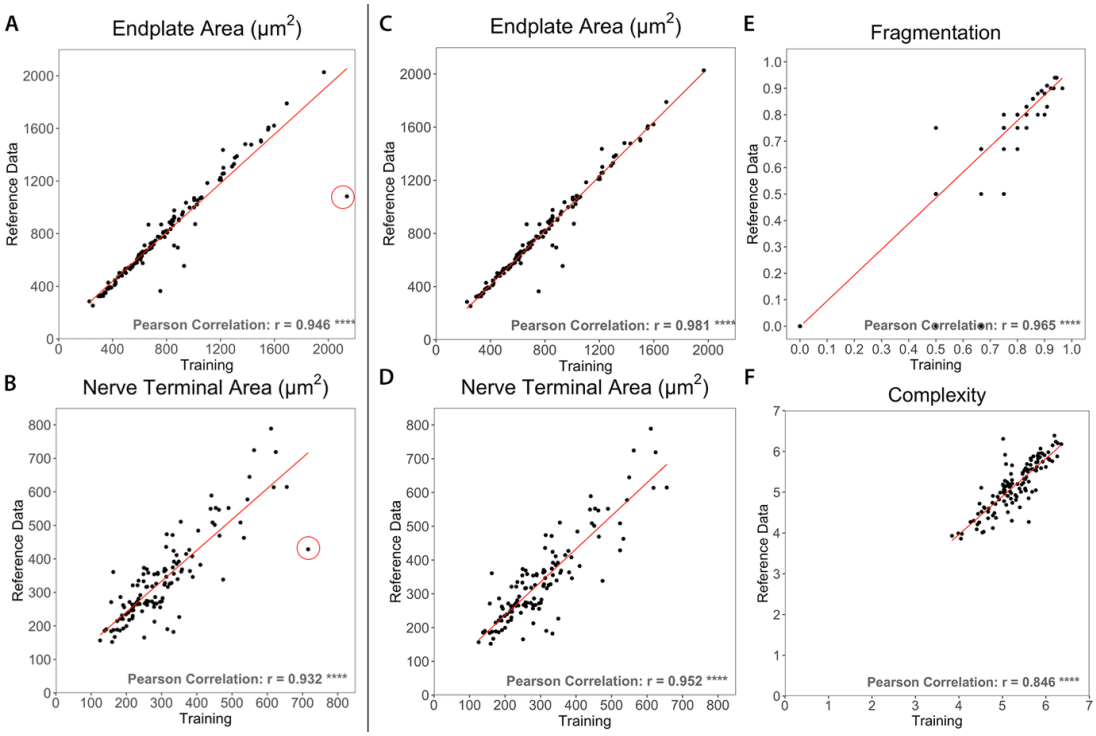

Figure 3-5: Validation of NMJ-morph user proficiency

Each point represents one NMJ, 120 NMJs were correlated overall between "Training" results and "Reference" data taken from (Jones *et al.*, 2017). Strong concordance between "Reference Data" and "Training"-data were found, however the importance of training one's eye to thresholding and the decision as to what constitutes one NMJ or two NMJs becomes apparent when comparing Endplate Area (A) and (C), as well as Nerve Terminal Area (B) and (D). After initial correlation analysis the endplate circled red in (A) and (B) was compared to "Reference Data" and the mistake was corrected leading to much stronger correlations for all variables across (C,D,E,F), all $r \geq 0.694$ with all $P < 0.0001$****.

Variables such as endplate area (**Figure 3-6.A**), endplate perimeter, AChR area and AChR perimeter, which only rely on thresholding of the post-synaptic endplate, correlate perfectly (r = 1.000 ****) suggesting that NMJ-morph and aNMJ-morph yield the same results for manual input and automatic extraction of respective values. Furthermore, variables such as compactness (AChR area divided by endplate area, indicative of how tightly 'packed' with AChR clusters the endplate is) correlated perfectly as well (r = 1.000 ****). This is easily explained as AChR area and endplate area both yielded identical results using NMJ-morph and aNMJ-morph due to use of identical thresholding. Percentage overlap is calculated via subtraction of unoccupied AChR area from AChR area, which results in the total area 'overlapped' or 'area of synaptic contact' between nerve terminal and AChR area, with the subsequent conversion of 'area of synaptic contact' into a percentage. Unoccupied AChR area is derived as explained in

Figure 3-4 for both NMJ-morph and aNMJ-morph. Given the same thresholding values are used for pre- and postsynapse and no manual input is required, unoccupied AChR area is expected to be identical, as is the area of synaptic contact and the overall derived percentage overlap (derived from unoccupied AChR area and AChR area). As **Table 3-2** shows, these variables correlate perfectly, supporting the correct generation of formulae within the .cvs spreadsheet of aNMJ-morph.

Pre-synaptic variables correlated slightly less than the perfect correlation for post-synaptic variables (r = 0.954–0.998) explained by the manual erasing of the axon during step 4/7 in aNMJ-morph (**Figure 3-1**). As it is nearly impossible to replicate identical erasing of the axon between these two workflows, or identical measurement of axon diameter (r = 0.960; **Figure 3-6.B**), a slightly lower correlation across pre-synaptic variables and their derivatives in comparison to post-synaptic variables is to be expected.

Number of AChR clusters is another variable where one might expect perfect correlation. However, as outlined in the automation of aNMJ-morph in

Figure 3-2.D, the fill holes function could occasionally ‘lose’ one AChR cluster that is contained within the boundaries of another, larger AChR clusters. This occurred only in 3/40 endplates during the proof-of-concept trial and still yielded a significantly high correlation coefficient (r = 0.986). The derivatives of ‘number of AChR clusters’ – ‘fragmentation’ and ‘average area of AChR clusters’ – had similarly high correlation. Thus, this difference in methodology between NMJ-morph and aNMJ-morph did not cause a significant difference in overall results. Vigilance is recommended however, as these clusters can always be amended in the final version of the spreadsheet for more accurate results.

Table 3-1: Validation of user proficiency with 'NMJ-morph'

	Mouse Pearson correlation coefficient r n = 3 120 NMJs
core variables	
pre-synaptic	
1) *Nerve Terminal Area (µm²)*	0.952 ****
2) *Nerve Terminal Perimeter (µm)*	0.952 ****
3) *Number of Terminal Branches*	0.759 ****
4) *Number of Branch Points*	0.712 ****
5) *Total Length of Branches (µm)*	0.927 ****
post-synaptic	
6) *AChR Area (µm²)*	0.931 ****
7) *AChR Perimeter (µm)*	0.945 ****
8) *Endplate Area (µm²)*	0.981 ****
9) *Endplate Perimeter (µm)*	0.960 ****
10) *Endplate Diameter (µm)*	0.947 ****
11) *Number of AChR Clusters*	0.880 ****
derived variables	
pre-synaptic	
12) *Average Length of Branches (µm)*	0.542 ****
13) *Complexity*	0.846 ****
post-synaptic	
14) *Average Area of AChR Clusters (µm²)*	0.961 ****
15) *Fragmentation*	0.965 ****
16) *Compactness (%)*	0.854 ****
17) *Overlap (%)*	0.701 ****
18) *Area of Synaptic Contact (µm²)*	0.872 ****
associated nerve & muscle variables	
19) *Axon Diameter (µm)*	0.694 ****

To assess the effect of inter-user variability, a series of 120 mouse NMJs, across n = 3 muscles (*extensor digitorum longus*, *peroneus longus* and *soleus*), were correlated (Pearson correlation). The correlation coefficient was high across all variables, all r ≥ 0.694 with all P < 0.0001****. Table adapted from (Minty *et al.*, 2020)

Table 3-2: Validation of aNMJ-morph within user and between users

	NMJ-morph (manual) compared to aNMJ-morph (macro)	
core variables	**Within User (r) 40 NMJs**	**Between Users (r) 240 NMJs**
pre-synaptic		
1) Nerve Terminal Area (µm²)	0.998 ****	0.892 ****
2) Nerve Terminal Perimeter (µm)	0.994 ****	0.875 ****
3) Number of Terminal Branches†	0.978 ****	0.762 ****
4) Number of Branch Points†	0.987 ****	0.740 ****
5) Total Length of Branches (µm)	0.977 ****	0.791 ****
post-synaptic		
6) AChR Area (µm²)	1.000 ****	0.923 ****
7) AChR Perimeter (µm)	1.000 ****	0.858 ****
8) Endplate Area (µm²)	1.000 ****	0.982 ****
9) Endplate Perimeter (µm)	1.000 ****	0.949 ****
10) Endplate Diameter (µm)	0.992 ****	0.891 ****
11) Number of AChR Clusters†	0.986 ****	0.937 ****
derived variables		
pre-synaptic		
12) Average Length of Branches (µm)	0.954 ****	0.661 ****
13) Complexity†	0.978 ****	0.785 ****
post-synaptic		
14) Average Area of AChR Clusters (µm²)	0.971 ****	0.823 ****
15) Fragmentation†	0.986 ****	0.936 ****
16) Compactness (%)†	1.000 ****	0.827 ****
17) Overlap (%)†	1.000 ****	0.765 ****
18) Area of Synaptic Contact (µm²)	1.000 ****	0.914 ****
associated nerve & muscle variables		
19) Axon Diameter (µm)	0.960 ****	0.758****

Comparison of NMJ-morph and aNMJ-morph to evaluate within user (n = 40 NMJs) and between user (n = 240 NMJs) variability. During aNMJ-morph development a single investigator used both workflows with the same threshold settings to assess accuracy and reproducibility. As expected, correlation coefficients were high due to the same threshold setting. Since correlation coefficients (r) were significant for all variables (**** $P < 0.0001$), aNMJ-morph was tested between users to prove reproducibility. 240 NMJs were analysed between three pairs of individual investigators, who used NMJ-morph and aNMJ-morph. Correlation coefficients (r) were slightly lower, however also significant across all variables (**** $P < 0.0001$). This indicates that aNMJ-morph yields reproducible results, despite different users. Pearson correlation was used for parametric variables, and Spearman correlation for categorical/non-parametric variables which are marked with †. Table adapted from (Minty *et al.*, 2020)

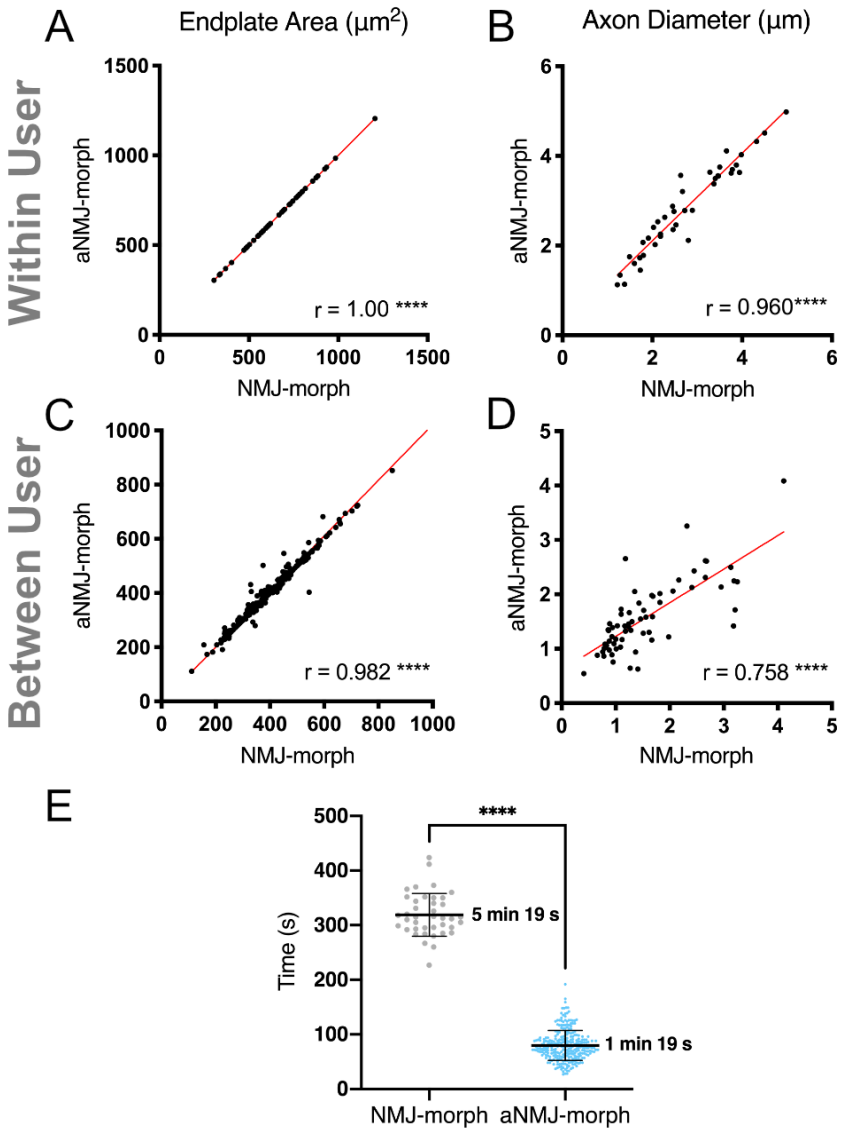

Figure 3-6: Within user and Between user comparison of NMJ-morph (manual) and aNMJ-morph (macro)

(A–B) Within user correlation of variables such as endplate area that requires no manual input (A) or axon diameter which consists of the average of three manual measurements (B) show near perfect correlation. Each dot represents one NMJ, n = 40 NMJs. Pearson correlation; **** P < 0.0001

(C–D) Between User correlation of variables that rely on only thresholding as a user variable (endplate area – C) or axon diameter which relied on thresholding and manual measurements (D) showed very good correlation. Lower correlation was noted between users in the measurement of axon diameter (D) due to the increased manual component as compared with endplate area. Each dot represents one NMJ, n = 240 NMJs. Pearson correlation; **** P < 0.0001. *Legend continues on next page.*

Figure 3-6 legend continued from previous page:

(E) Scatterplot depicting the time it took to analyse NMJs with NMJ-morph (grey dots) and aNMJ-morph (blue dots) between users. Horizontal lines represent the mean duration, given in minutes next to respective column, with error bars representing the standard deviation. For NMJ-morph analysis n = 40 within user NMJs were timed by one proficient investigator, for aNMJ-morph n = 240 between user NMJs were timed by three individual investigators. The macro reduced analysis time by approximately four-fold (~1 min per image) in comparison to the manual workflow (~5 min per image). Unpaired t-test; **** P < 0.0001

3.4.2.2. Between user variability – usability of aNMJ-morph

Having demonstrated that NMJ-morph and aNMJ-morph produce highly comparable results with aNMJ-morph appropriate to use for NMJ analysis, it was important to compare between user variability of data acquisition. This would help to identify the presence of any gross methodological flaws that needed addressing and whether aNMJ-morph remained user friendly across a variety of different users and devices (e.g. Mac OS X and Windows).

Comparison of three pairs of data, consisting of analysis of images obtained from ongoing research projects (sheep *soleus* and *extensor digitorum longus*, 40 NMJs per muscle, 80 NMJs per investigator, n = 240 NMJs in total) showed high correlation between the two workflows across all variables (r = 0.661–0.982; all P < 0.0001; **Table 3-2**). As in previous between-user correlation analysis of NMJ-morph, it is evident that the variables which do not require manual input (such as post-synaptic variables) have higher correlation coefficients across users (r = 0.852–0.982; e.g. endplate area correlated the best across users with r = 0.982; **Figure 3-6.C**).

Pre-synaptic variables that required manual input by erasure of axon correlated much lower (r = 0.740–0.892). All nerve terminal branching variables and axon diameter (r = 0.758; **Figure 3-6.D**) which relied on either manual measurements or erasing of axon had the overall lowest overall correlation coefficients (albeit significant with r = 0.661–0.791) suggesting that despite manual input, high correlation of variables can still be achieved across users.

Given slight methodological differences in the measurement of endplate diameter between NMJ-morph and aNMJ-morph, it was relevant to evaluate the between-user variability in both manual and automated endplate diameter measurements. As automatic measurement of endplate diameter implies a more accurate method of measurement, a significant correlation coefficient (r = 0.891) between NMJ-morph and aNMJ-morph suggests a slight improvement in assessment of endplate diameter – the reason being that subsequent use of an automated method to measure endplate diameter would allow for a more reproducible result overall.

Given the slight discrepancy in number of AChR clusters between both methodologies, it was crucial to assess this difference in a larger sample population across multiple investigators. Strong concordance between both workflows (r = 0.937) provided reassurance that the slight difference in methodology did not influence the overall interpretation of results. Therefore, the use of aNMJ-morph proves to be reliable and reproducible both within and between users.

3.4.2.3. aNMJ-morph is significantly faster than NMJ-morph

Following proof-of-concept that aNMJ-morph delivered reproducible results to NMJ-morph, the next step involved a time analysis of aNMJ-morph (macro) in comparison to NMJ-morph (manual). As the overarching aim of aNMJ-morph development was a reduction in analysis time per NMJ, it was imperative to assess gain in speed from automation of the workflow.

This was assessed by comparison of the time it took to analyse the 40 NMJs that were used for aNMJ-morph development with the manual workflow compared to the 240 NMJs analysed by three independent investigators using the macro (**Figure 3-6.E**). Overall analysis took 5 min 19 s ± 39 s (SD) per NMJ using NMJ-morph (manual) whilst the macro (aNMJ-morph) managed to reduce the time to 1 min 19 s ± 27 s (SD) per NMJ. This was a significant reduction in time ($P < 0.0001$) by fourfold. Whilst analysis of a batch of NMJs consisting of a recommended 30–40 NMJs could previously take up to three hours, depending on proficiency with NMJ-morph, the use of

aNMJ-morph reduces the overall time required to just over half an hour. The significant reduction in time required to analyse NMJs and the nature of the automation allow for more robust analysis of NMJs than was previously possible.

3.5. Conclusion

This chapter has described and demonstrated the following:

1) Proficiency in the use of NMJ-morph
2) "aNMJ-morph" – a semi-automated macro plugin based on NMJ-morph developed to expedite NMJ analysis and make it more accessible
3) aNMJ-morph contains fewer manual steps than NMJ-morph
4) aNMJ-morph is reproducible both within and between users, across different operating systems and supports the most commonly used file formats

Here, 120 mouse NMJs from independent "Training" data have shown high correlation to previously published "Reference data". Despite extensive use of the thresholding pre-set '*Otsu*' across pre- and postsynapse (~50% on both ends) as opposed to '*Huang*' in "Reference data", low between-user variability suggests proficiency in the use of 'NMJ-morph'. Going forward, 'NMJ-morph' can confidently be used for development and use of the macro 'aNMJ-morph', as well as for subsequent analysis of NMJs in health or disease (Chapter 4) and across species (Chapter 5).

The development of aNMJ-morph aimed to speed up and automate the previously manual NMJ-morph workflow. Reduction in time and user input allows users to focus on the first and most important step of the workflow: **thresholding**. Following successful proof-of-concept of aNMJ-morph and perfect correlation of variables with NMJ-morph that had no manual component, it was essential to demonstrate usability across independent investigators, file types and operating systems. Strong correlation coefficients across all variables between aNMJ-morph (macro) and NMJ-morph (manual)

have shown that aNMJ-morph is a robust workflow that allows significantly increased rates of analysis by a four-fold across independent users.

Whilst all NMJ-associated variables are extracted and copied into the spreadsheet automatically, it is still necessary to fill in the missing number of axonal inputs, potentially correct number of AChR clusters and separately measure muscle fibre diameter.

aNMJ-morph has an outstanding advantage in that there is a near complete reduction in errors associated with transfer and transposition of data entered into the results spreadsheet. Given the significant advantages afforded by aNMJ-morph in relation to both the speed and accuracy of data acquisition, the macro was utilised for the remainder of the project (see following chapters where specified).

4. NMJs are stable in patients with cancer cachexia

4.1. Chapter summary

Cancer cachexia is a neglected cause of major patient morbidity and mortality and to date there is no efficacious treatment available. The main symptoms are wasting of skeletal muscle and adipose tissue which progressively lead to loss of function, but underlying mechanisms are poorly understood. As cancer cachexia shares many pathophysiological mechanisms with other neurodegenerative diseases that the Gillingwater laboratory has specialised in, cancer cachexia sparked our interest. Given the major involvement of the neuromuscular system and morphological abnormalities at the rodent NMJ in degenerative diseases such as sarcopenia, Spinal Muscular Atrophy, Amyotrophic Lateral Sclerosis and Duchenne muscular dystrophy, the assumption has been made that similar pathological changes are to be expected in cancer cachexia. With the use of the recently developed aNMJ-morph workflow (Chapter 3) this chapter sought to establish whether NMJs from cancer cachectic patients are morphologically different from cancer weight stable or control patients, additionally to marked weight loss and loss of muscle mass determined through computerized tomography scans. Parts of this chapter on the role of the human NMJ in cancer cachexia have been published (Boehm, Miller, Thomas M. Wishart, *et al.*, 2020).

4.2. Background

Cachexia is a complex multifactorial wasting syndrome associated with chronic disease related weight loss (e.g. due to cancer) and leads to progressive functional impairment (Fearon, Strasser, Stefan D. Anker, *et al.*, 2011). With cancer being the second highest leading cause of death globally, the disease burden of cancer cachexia presents an unmet need for target intervention strategies (Lin *et al.*, 2019). Depending on tumour type, cancer cachexia affects 50–80% of cancer patients and is linked to a poor prognosis and reduced quality of life (Vagnildhaug *et al.*, 2018). Up to 20% of cancer deaths are due to cancer cachexia (Argilés *et al.*, 2014). Despite our recent efforts in modelling human cancer-induced cachexia, and linking disease contributing mechanisms between mice and humans, we are still far from understanding how muscle protein breakdown is facilitated and how function is impaired in the human condition of cancer cachexia (Talbert *et al.*, 2019).

Cancer cachexia shares commonalities in muscle dysfunction with other muscle wasting conditions such as sarcopenia (see review by Argilé S et al., 2015), age-related loss of muscle mass and function, and muscular dystrophies (Berardi, 2017). Mechanisms such as increased protein catabolism (breakdown of muscle) and decrease in protein anabolism (build-up of muscle) lead to an overall breakdown of muscle fibres (**Figure 4-1**) with a reduced capacity for muscle growth (hypertrophy). Breakdown of integral structural proteins within the muscle extracellular matrix can lead to a decrease in muscle integrity and therefore reduction in contractile force, loss of function and patient fatigue (Berardi, 2017). Reduced capacity for muscle regeneration through impairment of satellite cell function, or their depletion through continued activation, is particularly of interest as reversal of this phenotype and targeting of related pathways to improve muscle regeneration could prove to alleviate some of the clinical phenotypes observed in cachexia or muscular dystrophies (He *et al.*, 2013; Berardi *et al.*, 2014).

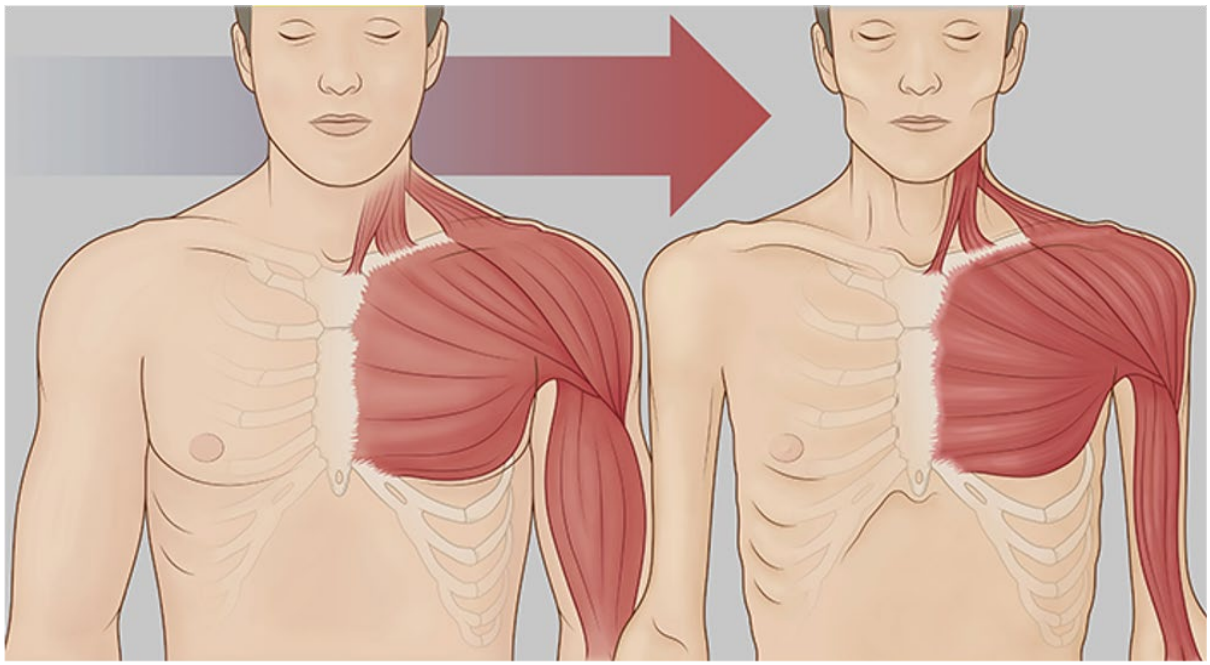

Figure 4-1: Cancer cachexia induced weight loss

Image courtesy of (*Cachexia in Cancer Patients | Cancer Cachexia | OSUCCC – James*, 2021) Cancer cachexia is a multifactorial wasting syndrome. An increase in muscle catabolism and reduction in its regenerative capacity causes loss of muscle mass and adipose tissue (visualised on the right), leading to weight loss and subsequently loss of function.

Despite understanding of key mechanisms that govern muscle homeostasis and mechanisms that lead to anabolic resistance for example (the inability of the muscle to increase protein synthesis in response to anabolic stimuli such as exercise and nutrition; Phillips, Hill and Atherton, 2012) we still do not understand the full spectrum of cellular and molecular mechanisms behind this disease-associated decline in muscle mass and function. As the NMJ is central to the function of the neuromuscular system, denervation and NMJ perturbations are widely associated with muscle atrophy in injury and sarcopenia (Tintignac, H.-R. Brenner and Rüegg, 2015; Taetzsch and Valdez, 2018) and have also been thought to contribute to muscle wasting in cancer cachexia (Daou *et al.*, 2020). Daou *et al* for example showed evidence of displaced myonuclei in mouse and human skeletal muscle fibres during cancer (weight stable and cachectic patients) and therefore concluded that denervation and NMJ dismantling are a key hallmark preceding muscle atrophy, as displaced myonuclei are thought to indicate muscle reinnervation (Daou *et al.*, 2020).

However, these assumptions have been made without actual assessment of NMJ morphology in either species. A more recent study by Yamada *et al.* compared cancer cachectic mice with cancer cachectic mice that underwent sciatic nerve transection. Denervation of muscle fibres and the induced muscle fibre atrophy and weight loss following nerve transection were suggested to be enhanced by cancer cachexia. In this study, denervation was considered to ‘equal’ physical inactivity and cancer cachexia was suggested to disturb compensatory mechanisms that follow denervation/inactivity of muscle that are meant to aid in muscle fibre reinnervation and preservation of muscle mass under normal circumstances (Yamada *et al.*, 2020). However, motor nerve injury and inactivity (e.g. bed rest, microgravity) itself differ significantly in their response within skeletal muscle fibres. During inactivity, type I fibres preferentially atrophy during bed rest since these predominantly account for overall composition of anti-gravity muscles such as *soleus* or *quadriceps* (Parry and Puthucheary, 2015). Thus,

nerve transection, in which type II fibres preferentially atrophy, does not replicate disuse-induced muscle wasting appropriately (Khan *et al.*, 2014). Therefore, it is misleading to draw conclusions from pathways involved in 'denervation + cancer cachexia' mouse models and apply them directly to general mechanisms occurring in 'inactivity + cancer cachexia', and in particular the involvement of NMJ dismantling. Since most of the data stems from research on animal models, with little proof of NMJ instability in cancer cachexia in either rodents or humans to date, the question remains as to whether proposed NMJ dismantling and denervation are actually causative of muscle atrophy in cancer cachexia. Thus, the original work presented in this chapter has contributed significantly to the assessment of human NMJ integrity in cancer cachexia (Boehm, Miller, Thomas M Wishart, *et al.*, 2020).

The pathophysiological complexity and lack of appropriate animal models of this disease have made it challenging to study and develop treatments. General treatment approaches to date focus on nutritional support, exercise or anti-inflammatory treatment (Gingrich *et al.*, 2019). However, nutritional support does not prevent the continuing loss of skeletal muscle mass in cancer cachexia, and protein supplements and drugs counteracting anabolic resistance are required, all of which lack proven effectiveness (Evans *et al.*, 2008; Fearon, Strasser, Stefan D. Anker, *et al.*, 2011; Argilés *et al.*, 2014). Whilst resistance training has shown to be an effective intervention for attenuation of skeletal muscle atrophy in human sarcopenia (Beckwée *et al.*, 2019) there is a lack of randomised controlled clinical trials in cancer cachectic patients, and the role of exercise in its prevention still remains questionable in rodent models (Niels *et al.*, 2020).

A deeper understanding of the involvement of the NMJ in the pathophysiology of cancer cachexia could help develop and direct treatment options and further our understanding of the pathways that direct neuromuscular dysfunction in the human condition. This project therefore aimed to answer the following questions:

1) Can loss of muscle mass in cancer cachectic patients be correlated with a reduction in muscle fibre diameter?
2) Does NMJ morphology of cancer cachectic patients differ in comparison to cancer weight stable and control patients?
3) Is denervation responsible for the loss of muscle mass?
4) Does cancer influence NMJ morphology?

4.3. Methods

4.3.1. Patient recruitment

The project was designed to compare NMJ morphology across cancer cachexia, weight stable cancer and control patients. Therefore, patients with a confirmed diagnosis of gastrointestinal (GI) cancer who were eligible to undergo surgery with curative intent were recruited from the weekly, regional upper gastrointestinal (GI) multi-disciplinary team meetings (N = 20). Cancer weight stable (N = 10) and cancer cachectic (N = 10) patients were differentiated according to consensus definition of cachexia: weight loss > 5% or weight loss > 2% in individuals who already demonstrated a reduction in current bodyweight (body-mass-index [BMI] < 20 kg/m^2) or skeletal muscle mass (e.g. sarcopenia, the ageing related loss of muscle mass) as assessed via computerized tomography (Fearon, Strasser, Stefan D. Anker, *et al.*, 2011). Furthermore, control patients undergoing elective abdominal procedures such as repair of aortic aneurysm (11/12) or donor nephrectomy were suitably age-matched and recruited (N = 12).

Exclusion criteria included previous history of malignancy. Only patients over the age of 18 years were approached and had to provide written and informed consent before the surgery. Ethical approval was granted by the National Health Service Lothian Ethics Committee (IRAS 190214). Patient consent was undertaken by Dr. Janice Miller (Clinical Surgery, Edinburgh Medical School and Royal Infirmary of Edinburgh) and myself.

Clinical details including BMI, weight loss, ECOG and C-reactive protein (a marker of inflammation) were recorded for all patients by the clinical staff. An overview of the patient demographics is depicted in **Table 4-1**. ECOG is a categorical rating system developed by 'The Eastern Cooperative Oncology Group' (ECOG), its eponym, which rates overall performance status in patients from 0–5. Zero represents fully active patients that have no restrictions in mobility or independence, whilst five represents death (Oken, Creech and Davis, 1982). ECOG allows the assessment of disease progression in patients.

The majority of cancer patients (4/10 in weight stable and 7/10 in cachectic patients) underwent surgery due to oesophageal adenocarcinoma, gastric adenocarcinoma (4/10 in weight stable and 1/10 in cachectic patients) or oesophageal squamous cell carcinoma (1/10 in both weight stable and cachectic patients). One cancer cachectic patient underwent surgery due to oesophageal undifferentiated carcinoma, and one weight stable patient due to colonic adenocarcinoma.

4.3.2. Body composition analysis

Routine computerized tomography (CT) scans are commonly performed as a diagnostic tool prior to surgical interventions and to monitor treatment progress. These allow for staging of cancers pre- and post-operatively and reveal crucial information about tumour extent (Verschakelen, Bogaert and De Wever, 2002). Moreover, CT allows for imaging of muscle and adipose content within the body, as it distinguishes tissues based on their density and chemical composition in comparison to water density as the baseline.

Table 4-1: Patient demographics. *Legend continues on next page.*

	Patient Group							
	Ctrl mean ± SD min, max	**Weight Stable** mean ± SD min, max	**Cachexia** mean ± SD min, max	**F (DFn, DFd)** or **Kruskal-Wallis statistic (H)**	**P**	Mean Difference **Ctrl vs Weight Stable**	Mean Difference **Ctrl vs Cachexia**	Mean Difference **Weight Stable vs Cachexia**
Male:Female	11:1	7:3	8:2	/	/	/	/	/
Age (years)	64 ± 8.67 (min 49, max 81)	66 ± 12.3 (min 40, max 83)	68 ± 9.49 (min 49, max 78)	F (2, 29) = 0.28	0.76	-1.03	-3.23	-2.20
BMI	27.68 ± 4.45 (min 20.0, max 36.2)	27.00 ± 5.62 (min 22.4, max 41.1)	25.69 ± 3.56 (min 20.4, max 31.8)	F (2, 29) = 0.52	0.60	0.68	1.99	1.31
% weight loss	0% ± 0% (min 0%, max 0%)	0.89% ± 1.58% (min 0%, max 4.38%)	7.99% ± 5.20% (min 2.70%, max 19.1%)	H = 24.56	< 0.0001 ****	-3.70%	-17.10% ****	-13.40% **
SMI	52.77 ± 4.80 (min 45.4, max 59.6)	56.9 ± 12.6 (min 43.7, max 78.5)	40.3 ± 5.52 (min 30.6, max 52.3)	H = 15.29	< 0.0005 ***	-0.98	13.52 **	14.50 **
CRP	5.00 ± 3.16 (min 2, max 11) n = 6	7.8 ± 11.2 (min 1, max 30) n = 6	12.0 ± 12.9 (min 1, max 30) n = 6	F (2, 15) = 0.75	0.49	-2.50	-7.00	-4.50
VATI	61.5 ± 28.9 (min 15.8, max 111.6)	53.0 ± 52.3 (min 6.73, max 188.4)	73.7 ± 36.2 (min 33.5, max 134.0)	F (2, 29) = 0.69	0.80	8.57	-12.2	-20.73
SATI	63.5 ± 41.1 (min 2.58, max 153.2)	60.3 ± 35.7 (min 18.32, max 132.3)	55.7 ± 14.3 (min 39.1, max 82.1)	H = 0.06	0.97	1.00	0.60	-0.40
ECOG	/	0 (min 0, max 1)	0 (min 0, max 1)	/	/	/	/	/

Table 4-1 legend continued from previous page: Patient data are depicted as the mean ± standard deviation of the mean (SD). Except for gender, which is represented as a ratio between male and female, and ECOG, which is represented as the median and a range. One-way ANOVA with a Tukey's post-hoc test was used to examine the differences in BMI and age. Differences in percentage weight loss, SMI and SATI were assessed via a Kruskal-Wallis test with a Dunn's post-hoc test (Ctrl: N = 12; Weight stable: N = 10; Cachexia: N = 10).

F (DFn, DFd) statistic describes the degrees of freedom (DF = number of groups minus one) from one-way ANOVA and describe the variation between sample means / variation within the samples. Low F-value indicates low variability, a high F-value suggests that the variation among group means is less likely to be due to chance.

The Kruskal-Wallis statistic (H) reflects the difference of mean ranks between groups following a rank-based nonparametric test. Comparison of H to cut-off values indicates whether differences are due to chance, or significant. A high H-value (% weight loss, SMI) suggests that the variation among mean ranks is due to more than chance.

BMI = body mass index; SMI = skeletal muscle index; CRP = C-reactive protein; VATI = visceral adipose tissue index; SATI = subcutaneous adipose tissue index; ECOG = Eastern Cooperative Oncology Group performance status

Given that fat has a lower tissue density than muscle in comparison to water, fat appears darker on CT and muscle appears lighter. Therefore, CT can be utilised to track weight loss and body composition (**Table 4-1**). Adipose compartments and intramuscular adipose tissue can be measured as depicted in **Figure 4-2** (Goodpaster *et al.*, 2000). In cancer patients CT imaging plays an important role in assessment of weight loss during staging and re-staging. The measurement of subcutaneous and visceral fat volume has developed to be a powerful tool in the diagnosis of cancer cachexia and patient response to chemotherapy (Engelke *et al.*, 2018). In this study, a single digital transverse CT image was obtained with a spiral CT scanner at the level of the third lumbar vertebrae (L3) and tissue volumes were estimated using semi-automated software (Slice-o-matic and ABACS software). Skeletal muscle index (SMI) was derived from muscle cross-

sectional area at L3 vertebra level normalised to patient height (squared) = cm^2/m^2 (Portal *et al.*, 2019).

The following SMI (cm^2/m^2) cut-off values are associated with reduced survival and were used to assess low SMI – values below these are defined as sarcopenic (Martin *et al.*, 2013):

- underweight BMI < 20.0 kg/m^2 (men < 43 cm^2/m^2, women < 41 cm^2/m^2)
- normal BMI 20.0–24.9 kg/m^2 (men < 43 cm^2/m^2, women < 41 cm^2/m^2)
- overweight BMI 25.0–29.9 kg/m^2 (men < 53 cm^2/m^2, women < 41 cm^2/m^2)
- obese BMI ≥ 30.0 kg/m^2 (men < 53 cm^2/m^2, women < 41 cm^2/m^2)

4.3.3. Tissue sampling and NMJ immunofluorescence

Sampling of human *rectus abdominis* (RA) was chosen as abdominal wall incisions provide ready access (Flynn and Vickerton, 2020). This provides the logistical opportunity to sample muscle at the start of the surgical procedure. Furthermore, RA is of mixed fibre type and as a non-locomotor muscle it allows to assess neuromuscular morphology influenced by disease (cancer cachexia) irrespective of disuse atrophy (Sakkas *et al.*, 2003).

RA itself is enclosed by the rectus sheath. Since the anterior sheath is closely attached to RA and the posterior sheath is detached from RA (Ellis, 2009), particular care must be taken during dissection to either sample deep within RA or facilitate detachment of the anterior rectus sheath via sharp dissection. Surgeons were asked to sample muscle specimens via sharp dissection, without diathermy (electro-cauterization) to avoid artefactual changes that would ‘burn’ the sample (and therefore also the NMJs) should they lie at the sample’s boundaries. The in-series muscle fibre architecture of RA across its entire length means that discrete endplate bands are lacking (see **Figure 4-3**) and the presence of NMJs could only be confirmed after immunofluorescent visualisation as outlined in Chapter 2 (General Methods) (Woodley, Duxson and Mercer, 2007).

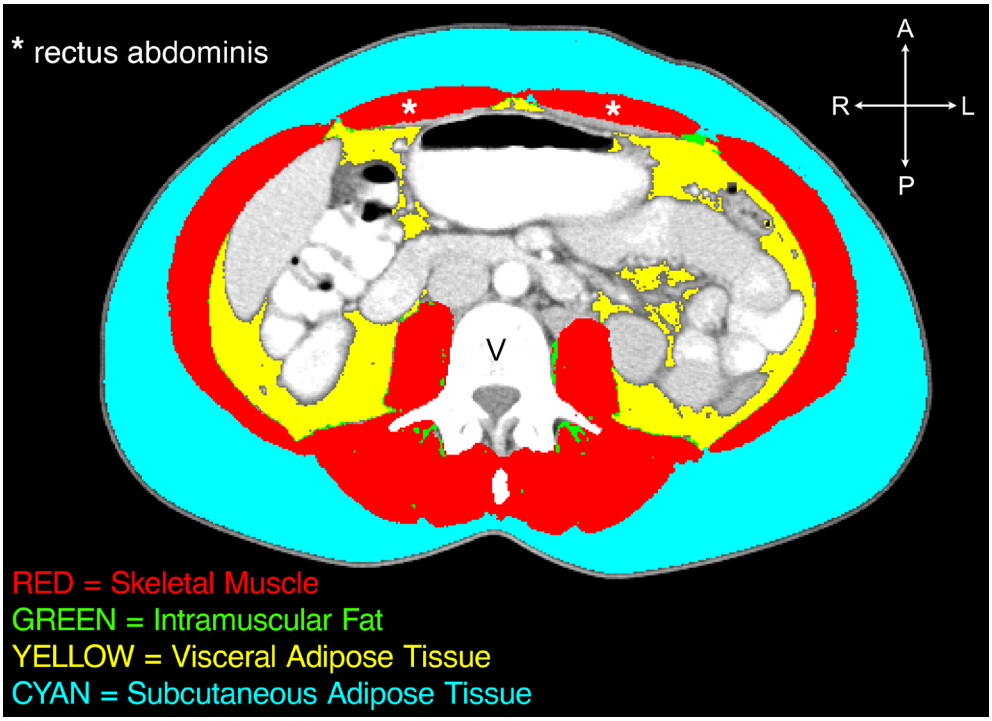

Figure 4-2: Cross sectional CT image at L3 showing division of skeletal muscle and adipose tissue

Boundaries between tissue types were semi-automatedly assigned using the Slice-o-matic and ABACS software. Unassigned regions that clearly belonged to one tissue type (muscle or adipose) were 'painted' in with the respective colour. The white asterisks **(*)** indicate the location of *rectus abdominis*, the muscle from which tissue was sampled. **(V)** indicates the location of the vertebrae/spinal column. The orientation of the scan is indicated by arrows, where A = anterior, P = posterior, R = right hand side of patient and L = left. Original image courtesy of Janice Miller (Clinical Surgery, Edinburgh Medical School and Royal Infirmary of Edinburgh)

Red = Skeletal muscle; Green = Intramuscular Fat; Yellow = Visceral Adipose tissue; Cyan = Subcutaneous adipose tissue; Grey = organs. Image adapted from (Boehm, Miller, Thomas M. Wishart, *et al.*, 2020)

A

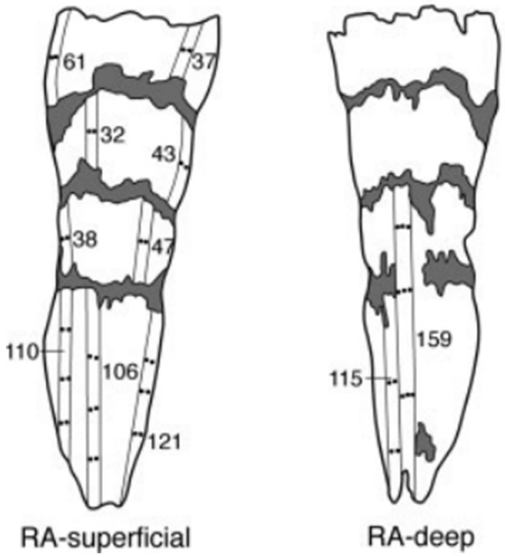

B

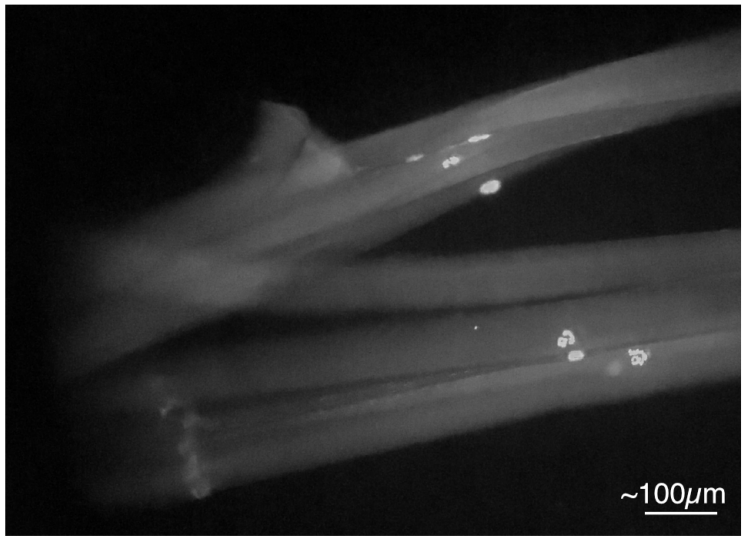

Figure 4-3: Tissue sampling in *rectus abdominis* (RA)

(A) Schematical illustration of in-series innervation on superficial (left) and deep (right) surface of RA. Solid lines indicate fascicles, adjacent numbers represent fascicle length and horizontal 'dots' represent endplate bands. Muscle specimen were sampled in longitudinal fashion, along fascicle length, to increase chances of NMJ inclusion. Grey shaded areas represent the tendinous intersections of RA. Figure adapted from (Woodley, Duxson and Mercer, 2007)

(B) Photograph of visual confirmation of endplate bands in RA muscle fibres captured through the microscope objective. Light grey 'dots' are NMJs fluorescently labelled with TRITC α-BTX. The muscle fibre cut end is visible to the left where the fibres seem to 'fade out'. Scale bar = ~100 μm

In brief, samples were fixed for 1–2 hours in 4% PFA upon receival, washed thoroughly with 1xPBS and fibre bundles of 10–15 individual fibres were fine dissected. Post-synaptic endplates were subsequently visualised with TRITC α-BTX and their presence/absence was confirmed using an upright Nikon Eclipse 50i fluorescent microscope. If NMJs were present, further muscle fibres were dissected and the entire immunofluorescence protocol (as outlined in Chapter 2) was followed through. If no NMJs were found, the sample was discarded appropriately.

4.3.4. Logistical considerations

Despite selection of 32 patients for the final NMJ analysis of this study, a total of 56 patients (22 control and 34 cancer) were recruited and sampled for the study. As highlighted in the above section (**Figure 4-3**), the in-series innervation (Woodley, Duxson and Mercer, 2007) of *rectus abdominis* complicates surgical sampling of muscle biopsies containing endplate bands. Surgeons cannot guarantee sampling of muscle at the exact location of the NMJ, and sampling is thus somewhat arbitrarily.

Incisions are not chosen for the purpose of sampling, but in relation to the operative procedure in concordance with the declaration of Helsinki. At the site of incision, surgeons aimed to sample long and/or wide muscle specimen to increase the chance of NMJ inclusion. Sampling in control patients had a ~63.6% success rate and sampling in cancer patients had a ~58.8% success rate. No clear correlation was found between the success rates of samples based on surgical team, surgeon or type of surgery conducted. Only one surgeon, who continuously sampled very small specimens, delivered zero muscle samples which included the NMJ.

4.3.5. Confocal imaging & aNMJ-morph analysis

To acquire images for subsequent NMJ analysis, mounted slides containing immunofluorescently processed muscle fibres were imaged (as per Chapter

2 – General Methods 2.3.5). In brief, the first two cancer cachexia cases were imaged in Z-stack intervals on a Zeiss LSM710 confocal system. All other subjects were imaged on a Nikon A1R FLIM confocal system. Overall, **~1,515 NMJs** were imaged.

4.3.5.1. Muscle fibre diameter measurements

Muscle fibres were imaged and measured as described in Chapter 2 (General Methods 2.3.5.1). Muscle fibre diameter measurements were performed by Ross Jones (Edinburgh Medical School, Edinburgh University) directly after the slides were imaged using a confocal microscope in parallel to ongoing NMJ analysis. It was important to fully image the slide on the confocal microscope before imaging of muscle fibres – if imaged in reverse order, fluorescent probes would bleach in brightfield mode and confocal imaging of NMJs would result in no or very low signal. Overall, **1,155 muscle fibres** were imaged and analysed. As the muscle fibre diameters measured were not matched to individual NMJs, the MFD of each NMJ represented the mean of the muscle fibre diameter (see also principal components analysis).

4.3.5.2. aNMJ-morph analysis

Analysis of confocal images of RA NMJs was carried out using aNMJ-morph (as per Chapter 3 – aNMJ-morph). Analysis of RA in cancer patients was undertaken blinded as details of CT scans and allocation to cachectic and weight stable group were only shared after imaging and analysis of respective patients. In brief, an entire patient folder of NMJs was opened and screened for suitable NMJs according to the guidelines regarding oblique endplate area (see Chapter 2 – 2.3.6) and image quality (i.e. blurriness). Unsuitable images were removed from the folder (for the duration of the analysis moved one level out of the folder and joined back into the folder after analysis). Subsequently, the aNMJ-morph macro was loaded into Fiji and the ‘filtered’ folder was selected for batch analysis. Channels were selected accordingly and particular care was given whilst thresholding and cleaning both pre- and post-synaptic endplates. The axon was measured on

a ‘zoomed’ nerve terminal for more accuracy, and the macro measured all subsequent variables automatically and saved them in a spreadsheet in .csv format. Once all patients were analysed, the spreadsheets were collated in .csv format and exported to .xlsx format to allow editing, and all patients were pulled into a master spreadsheet. Overall, **1,206 NMJs** were deemed suitable for final analysis: 429 NMJs from 12 control patients, 385 NMJs from 10 cancer weight stable patients and 392 NMJs from 10 cancer cachectic patients.

4.3.6. Statistical analysis

Statistical analyses were conducted in consultation with a biostatistician to ensure appropriate testing (Dr. Martin Simmen, School of Biomedical Sciences, University of Edinburgh). To assess differences in NMJ morphology and patient demographics between control, cancer cachectic and weight stable group, statistical analyses were performed using Graph-Pad Prism 6 software unless otherwise stated. Morphometric variable results were expressed as mean ± standard error of the mean (SEM) and patient data were expressed as mean ± standard deviation (SD). Normality of distributed morphometric data were assessed based on the D’Agostino-Pearson test. If all groups passed the normality test, a one-way ANOVA and Tukey’s multiple comparison test were performed. If one or more groups did not pass the normality test ($P < 0.05$ was considered significant, therefore not a pass), data were analysed by Kruskal-Wallis test and Dunn’s multiple comparison test. $P < 0.05$ was considered significant. Mean patient data were used for this analysis to avoid pseudo replication of NMJ data within patients.

4.3.6.1. Principal Components Analysis

Given the many variables that were being assessed (21 morphometric NMJ variables and 10 clinical variables) a statistical methodology was required that was able to deduce which variables contributed to the most variability within the dataset. Principal components analysis (PCA) is able to do this by

construction of so-called ‘principal components’ that account for the maximal amount of variance within the data. This works through ‘geometrical’ means, with the principal components representing lines that capture ‘perpendicular projections’ of the data that result in the largest scatter and thus the largest variance. The first principal component therefore explains the largest variance within the data, and the second principal component the second largest (as its calculation proceeds in the same way but uncorrelated to the first principal component). That means that the second principal component is geometrically perpendicular to the first principal component, and so forth until the principal components equal the number of input variables. At this point, a PCA will have assigned eigenvectors to the dimensions (the so-called principal components) with eigenvalues which evaluate the amount of variance ‘explained’ by the corresponding eigenvector (i.e., PC).

The eigenvectors allow the ‘reduction’ of dimensions and describe the data within a ‘new’ coordinate system (2D or 3D depending on whether the first two or three principal components are selected).

[A useful analogy is as follows. Peter is going to deliver food to Sue’s house. The directions that Sue has provided on a map are in longitude and latitude which are expressed as the coordinates of the globe. But once Peter leaves his house, he finds himself in his own coordinate system (reduced dimensions) e.g. a 2D world (with 2 principal components) where he represents the point of origin. The eigenvalues of principal component 1 and principal component 2 allow the transformation of latitude and longitude of the original ‘globe’ coordinate system into ‘distances’ (eigenvalues) and directions (eigenvectors) that Peter can work with in order to navigate to Sue. Now Peter knows that he needs to walk north (direction = eigenvector) for 3 blocks (distance = eigenvalue) and then west for 2 blocks until he arrives at Sue’s house.

Ultimately the ‘size’ of the eigenvalue determines to what extent the eigenvector will be transformed/stretched. The larger an eigenvalue of a principal component, the larger the variance explained by that principal

component. Coming back to the Peter/Sue analogy, whilst there are four cardinal points, Peter can now 'reduce' his movement into only two instructions which best describe the ideal directions to take to Sue's, e.g. north and west.]

To conduct the PCA, all analyses were performed using R version 4.0.3 and RStudio version 1.4.1103 (RStudio, 2020). The R packages "tidyverse" (version 1.3.0) were loaded for data manipulation and "cluster" (version 2.1.0) and "factoextra" (version 1.0.7) for their clustering algorithms and visualisation capabilities.

The explored dataset contains p = 31 numerical variables, with n = 1,204 individual measurements for patient NMJs. Missing values (NaN) within number of axonal inputs, axon diameter, number of AChR clusters, average area of AChR cluster, fragmentation, and muscle fibre diameter were input with the patient average for the respective variable during collation of the master spreadsheet. The function "prcomp" was used for analysis of principal components and data were centred and scaled. Choice of principal components to include for further analyses was made by the overall contribution of their variance to the dataset. This was extracted from the 'bend' of the screeplot, selecting for the first few principal components before the 'bend', after which the proportion of variance explained within the data dropped off significantly. The eigenvalues of all principal components were assessed and therefore their overall contribution to the variance. Variables with an eigenvector > 0.25 or < -0.25 were deemed more influential within a principal component and were used as a cut-off. The package "pca3d" (version 0.10.2) was used to generate a 3D-representation of principal components and the "rgl" (version 0.105.13) package was used to export the generated 3D-plot. A biplot of the 5 variables which contribute to the highest overall variance (largest eigenvector) within PC1–PC3 was generated and used to explore the data visually. Individual NMJs were plotted and coloured according to individual patient groups and pathologies/reasons for surgical intervention and 3D graphs were used to assess the contribution of either of these groups to overall NMJ-morphology.

4.4. Results and Discussion

4.4.1. Cancer cachexia causes muscle wasting and atrophy in *rectus abdominis*

Cancer cachexia is characterised by skeletal muscle wasting, with or without loss of adipose mass, and influences overall poor prognosis and reduced quality of life (Fearon, Arends and Baracos, 2013). To differentiate cancer cachectic patients (N = 10) from cancer weight stable patients (N = 10), clinical details were recorded, such as weight loss, and CT scans were analysed to assess attenuation of skeletal muscle and adipose tissue mass. Cancer patients were assigned into their respective groups according to consensus definitions (Fearon, Strasser, Stefan D Anker, *et al.*, 2011). To exclude the influence of cancer on altered NMJ morphology in *rectus abdominis*, patients without a previous history of malignancy (N = 12, undergoing abdominal procedures), were used as controls. Kruskal-Wallis test of patient demographics (**Table 4-1**) showed a significant difference between control and cancer cachectic patients (P < 0.0001****), and cancer weight stable and cachectic patients (P = 0.001**) in % weight loss; and between control and cancer cachectic patients (P = 0.002**), and cancer weight stable and cachectic patients (P = 0.002**) for skeletal muscle index. Low skeletal muscle index, which is a representation of muscularity per height (cm^2/m^2, SMI) and the trend towards lower subcutaneous and higher visceral adiposity (**Table 4-1**) has been previously suggested to correlate with poor outcome and reduced survival in cancer patients (Kazemi-Bajestani, Mazurak and Baracos, 2016; van Dijk *et al.*, 2017).

Having shown that cancer cachectic patients exhibit significant weight loss and loss of skeletal muscle mass in comparison to cancer weight stable and control patients, consistent with the definition of cancer cachexia, the next question was whether muscle fibre diameter was affected. This question is important, as loss of skeletal muscle mass can be due to either loss of muscle fibres or due to muscle atrophy, the reduction in muscle fibre

diameter; the latter has been proposed as the main cause of muscle loss in cachexia (Bloch, 2019; Winje *et al.*, 2019).

As sample availability only allowed for diameter measurements undertaken on teased muscle fibre preparations, muscle loss cannot be absolutely excluded from this patient cohort. Measurements revealed a significant 11.78 ± 1.6% (SD, P < 0.0001****) difference between control (78.8 ± 19.8 μm SD) and cancer cachectic (69.5 ± 19.5 μm SD) muscle fibre diameters. As anticipated, no difference was observed between control and cancer weight stable (79.8 ± 23.6 μm SD) patients (**Figure 4-4**).

A ~25% difference in muscle fibre cross sectional area has previously been observed between non-cachectic and cancer cachectic patients with low muscularity and weight loss (> 2%) (Johns *et al.*, 2014). To compare the ~11% and ~25% difference in muscle fibre diameter and cross-sectional area (CSA) between cancer cachectic and weight stable patients, respectively, 'simple' muscle fibre/cylinder geometry should be considered. Assuming muscle fibres are perfect cylinders, their cross-sectional area would be calculated as the area of a circle:

$$A = r^2\pi = \left(\frac{d}{2}\right)^2 \pi = \frac{\pi \cdot d^2}{4} \qquad \textit{Equation 1}$$

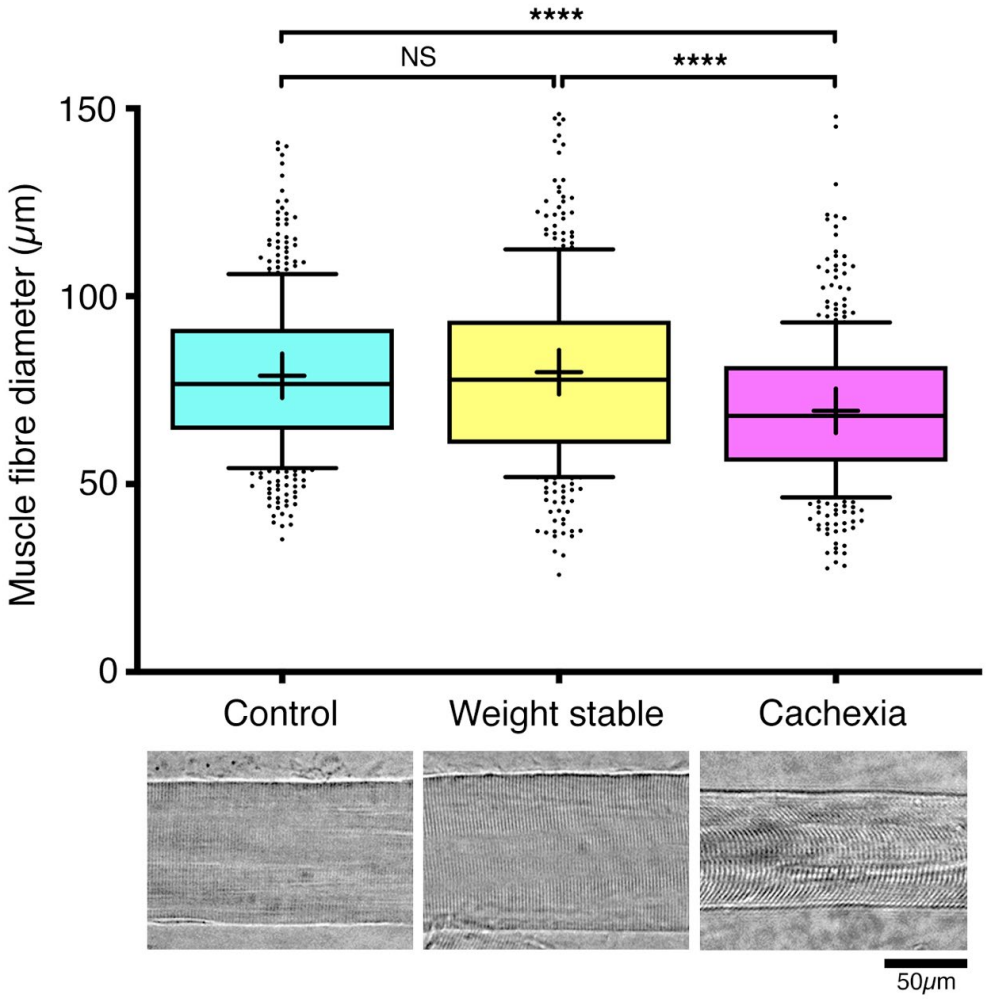

Figure 4-4: Atrophy of skeletal muscle fibres in cancer cachexia

Upper panel: Box and whisker plot of muscle fibre diameters of control (cyan, N = 12, n = 428, 78.8 ± 19.8 μm SD), cancer weight stable (yellow, N = 10, n = 362, 79.8 ± 23.6 μm SD) and cachectic (magenta, N = 10, n = 400, 69.5 ± 19.5 μm SD) patients. Boxes depict the mean (+) and median (line) muscle-fibre diameters and enclose the central 25th–75th percentile of the data, and the whiskers extend from the 10th–90th percentile. Data points outside the 10th–90th percentile are shown beyond the whiskers. ****P < 0.0001; NS = not significant; Kruskal-Wallis test with Dunn's post hoc test.

Lower panel: Representative brightfield micrographs of single teased muscle fibre preparations from control (left), cancer weight stable (middle) and cancer cachectic (right) patient. Intact striations of muscle fibre are clearly visible. All three micrographs are to identical scale. Scale bar = 50 μm; Image adapted from (Boehm, Miller, Thomas M. Wishart, *et al.*, 2020).

To assess whether the reported reduction in CSA by Johns *et al.* coincides with a decrease in CSA seen in this patient cohort (decrease of 11% in MFD), the % diameter decrease into CSA (or circle area) is extrapolated. As the average MFD in cancer cachectic patients is 0.882 times smaller than in control patients (11% smaller), the average CSA of cancer cachectic patients is calculated as such:

$$A = \left(\frac{0.882 \cdot d}{2}\right)^2 \pi = \frac{\pi \cdot 0.7779 \cdot d^2}{4} \qquad \textit{Equation 2}$$

The decrease in area is calculated by subtracting the new cross-sectional area from the original cross-sectional area:

$$A = \frac{\pi \cdot d^2}{4} - \frac{\pi \cdot 0.7779 \cdot d^2}{4} = \frac{0.222 \cdot \pi \cdot d^2}{4} \qquad \textit{Equation 3}$$

The percentage decrease (percentage of area with reduced diameter from the original control area) can subsequently be calculated using the standard percentage transformation (new value x 100 / original value):

$$A = \left(\frac{0.222 \cdot \pi \cdot d^2}{4} \times \frac{4}{\pi \cdot d^2} \times 100\right)\% = 22.2\% \qquad \textit{Equation 4}$$

In brief, since the CSA scales as the square of the diameter, a reduction in diameter by a factor of 0.882 translates to a reduction in CSA of 0.882^2 = 0.778, i.e. 22.2%. This is relatively similar to the 25% decrease in CSA observed between cachectic and non-cachectic patients in Johns *et al.,* 2014. Since the extrapolated reduction in CSA is close to previously reported data, this suggests the methodological difference between measuring cross-sectional areas or diameters of teased muscle fibres as reported here does not grossly impact overall results.

4.4.2. NMJ morphology is heterogeneous across RA and patient groups

Denervation of skeletal muscle fibres is known to cause loss of function and muscle atrophy which is followed by fibre degeneration and infiltration of connective and adipose tissue (Carlson, 2014). To assess whether the significant reduction in muscle fibre diameter and skeletal muscle index in

patients with cancer cachexia is due to denervation, morphometric assessment was performed on confocal images of NMJs from teased and immunofluorescence labelled muscle preparations.

Upon first visual inspection of all NMJs from RA across all three patient groups, the distinct heterogeneity in size and shape within muscles was observed (**Figure 4-5**). NMJs depicted the typical 'nummular' morphology described by Jones *et al.,* 2017 and within all patient groups the presence of small, medium sized and large NMJs was noted.

Not all NMJs were associated with a clearly visible axon. Human NMJs have axons one third the calibre of mouse axons and therefore appear more fragile in comparison to their rodent counterparts (Jones *et al.*, 2017). Despite fixation of tissue, fibre preparation by teasing of muscle fibres has the potential to 'disturb' the innervating nerve bundle. However, given the 3D structure of NMJs and the methodology of imaging (in Z-stacks) there is more reason to believe that in some cases axons weren't captured, as they would innervate the endplate in a perpendicular manner from the 'top' or 'bottom' of the captured Z-stack planes as illustrated in **Figure 4-6**. Therefore, axon diameter could not be measured for all NMJs due to the entry point of innervation beginning above or below the endplate off frame, rather than due to a processing artefact.

In fact, in control patients 103/266 axon diameters were captured (~39%), whereas cancer weight stable patients only had 43/214 axons that could be analysed (~20%). Cancer cachectic patients on the other hand imaged well and had 138/265 axons that could be assessed (~52%), which makes for the highest percentage overall. Given cancer cachectic and weight stable patients were processed, imaged and analysed blinded, bias in analysis can be excluded and this further strengthens the argument that muscle atrophy in *rectus abdominis* of cancer cachexia is not due to denervation of the NMJ.

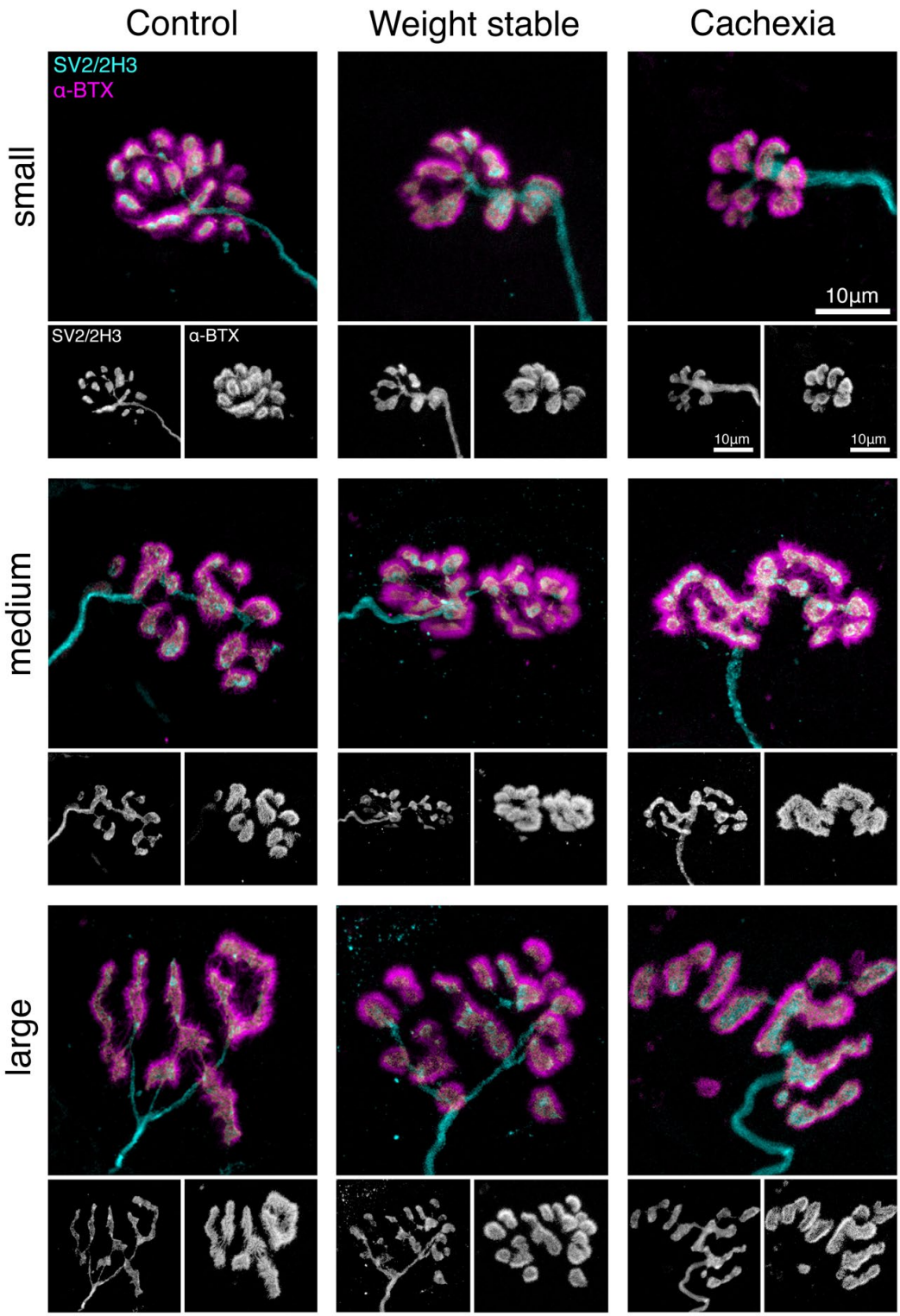

Figure 4-5: Conservation of NMJ morphology in cancer cachexia

Representative confocal micrographs of small (upper panels), medium (middle panels) and large (lower panels) NMJs across all three patient groups. *Legend continues on next page.*

Figure 4-5 legend continued from previous page: Despite overall heterogeneity within individual muscles, NMJ morphology was conserved across all three groups, with no evidence of gross NMJ pathology typical of denervation. Composite images show acetylcholine receptors (α-BTX, magenta), axon and nerve terminals (synaptic vesicle protein 2 and neurofilament, SV2/2H3, cyan). Scale bars = 10 μm; Image adapted from (Boehm, Miller, Thomas M. Wishart, *et al.*, 2020).

So far, no prior studies have demonstrated fibre-type grouping in human cancer cachexia. Only small grouped muscle fibre atrophy, containing both fibre types, was observed in *biceps brachii*, therefore, exploration of fibre type grouping within muscle fibres remains a relevant experimental addition to future studies (Lindboe and Torvik, 1982).

Upon further visual inspection of NMJs from control, cachectic and weight stable group, a small number of 'pathological' NMJs were found in each patient. Here, well-established read-outs of NMJ degeneration were classified as pathological: denervated endplates (Chung *et al.*, 2017), signs of reinnervation by multiple thin axonal processes (Larsson *et al.*, 2019) and neurofilament accumulation or axonal sprouting (Gordon, Hegedus and Tam, 2004). Denervated endplates were categorised as denervated when there was clear lack of nerve terminal and no artifacts of staining or cut off Z-stacks, which are normally clearly visible through visual assessment of the quality of the fluorescent stain. Neurofilament accumulation was classified as distinguishably 'thicker' axons, 'blebs' and swellings. Since axons of human NMJs are particularly thin, swellings across the axon or at the nerve terminal stand out. Given synaptic vesicles and neurofilament are visualised fluorescently, the odds are very high that those 'swellings' within axons are accumulations of neurofilament, as described below.

On average three pathological NMJs were found per patient. Some patients showed more of these NMJs than others (approximately three times more), however given the overall quantity of NMJs imaged per patient (40 NMJs) these 'pathological' NMJs constituted on average only 7.5% of **all** images.

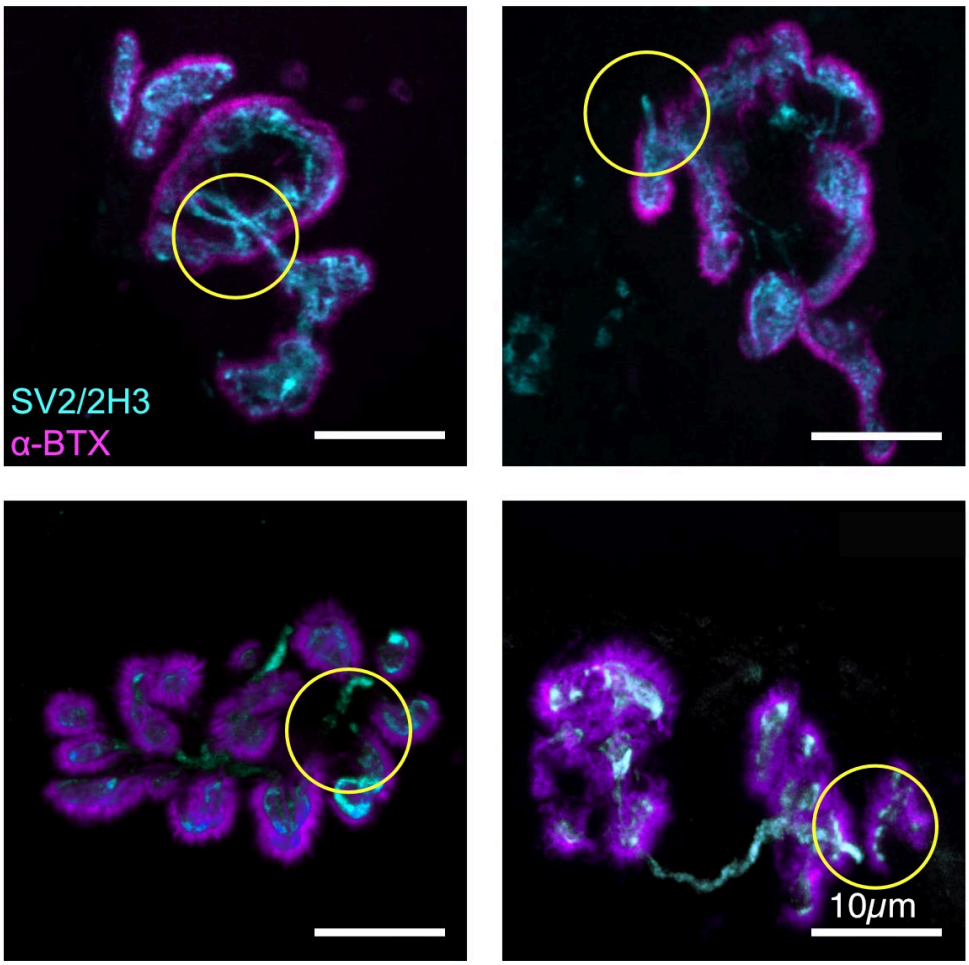

Figure 4-6: Perpendicular innervation pattern of NMJs

Example confocal micrographs of NMJs with axons innervating the endplate from the top or bottom. Point of 'exit/entry' of the axon into the image frame is marked with a yellow circle. Measurement of axon diameter is not accurately possible in these cases as they are not fully captured within the geometry of the Z-stacks that were imaged. In most cases, to capture sufficient of the axon-length to reliably measure diameter, meant additional imaging of a great deal of Z-stacks in up- or down-orientation, adding several minutes of imaging time per NMJ. This was avoided and a significant increase in imaging speed was preferred, with a small trade off in axonal measurements.
Acetylcholine receptors (α-BTX, magenta), axon and nerve terminals (synaptic vesicle protein 2 and neurofilament, SV2/2H3, cyan)

Scale bar = 10 μm.

NMJs from control, cancer cachectic and cancer weight stable RA (**Figure 4-7**) showed the same attributes with respect to pathology, with no particular phenotype being more prevalent in either group.

Whilst individual 'pathological' NMJs (**Figure 4-7**) were found across all three groups (cancer weight stable, cancer cachectic and control) this might indicate that there is some process of de- and reinnervation occurring as a process of NMJ maintenance. Reinnervation processes would correspond with functional read outs of neuromuscular physiology in elderly humans where motor unit number estimates (MUNE) decrease, whilst the motor unit potential (MUP) remains preserved, in comparison to younger adults (Piasecki *et al.*, 2018). This suggests a reduction of motor units, with the remaining motor units rapidly reinnervating the denervated muscle fibres.

4.4.3. The human NMJ is stable in cancer cachexia

Since initial visual assessment highlighted how heterogeneous human NMJs are within and across patient groups, comparison of morphology between groups was required to determine whether the pathological appearance of some NMJs was due to disease or observed heterogeneity. Collation and analysis of morphometric data, which was collected blinded throughout the initial visual assessment stage with aNMJ-morph, confirmed that NMJs from control patients, cancer cachectic patients and cancer weight stable patients, did not differ significantly in any of the 20 morphometric variables (**Table 4-2**). Since denervation causes the nerve terminal to withdraw from the motor endplate, a reduction in nerve terminal area is to be expected.

Furthermore, overlap (the % in overlap between acetylcholine receptors and the nerve terminal) would decrease, as less overall AChR area would be occupied by nerve terminals. In rodents this leads to an increase in AChR fragments and endplate area, as acetylcholine receptors cluster in less close proximity.

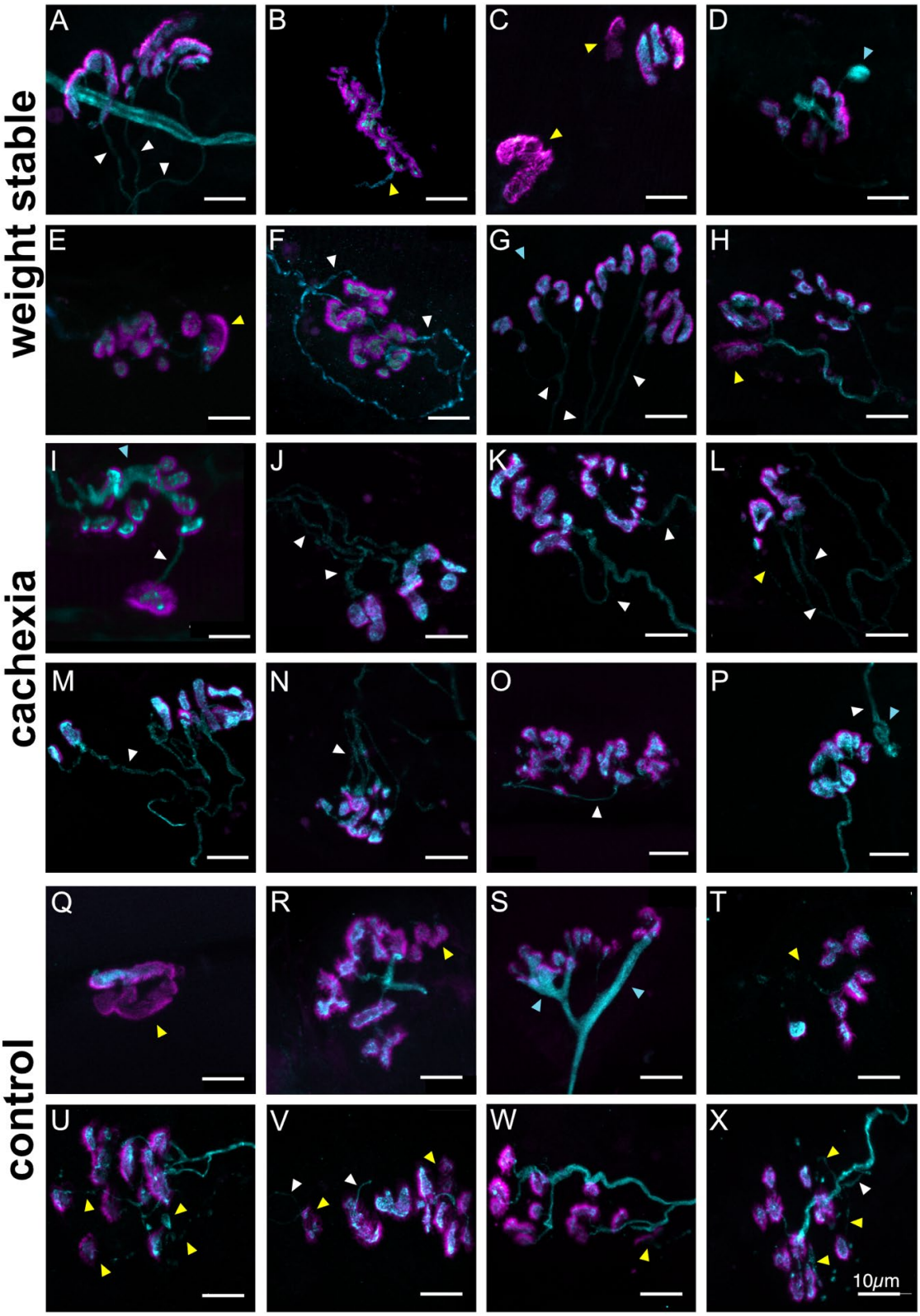

Figure 4-7: Examples of rarely occurring potential pathology of individual NMJs from cancer weight stable, cancer cachectic and control *rectus abdominis*

Legend continues on next page.

Figure 4-7 legend continued from previous page: Example confocal micrographs here show pathological characteristics (as defined in literature) which were noted in rare occasions in cancer weight stable **(A–H)**, cancer cachectic **(I–P)** and control **(Q–X)** patients, and therefore weren't considered the norm. Reinnervation (white arrow) and denervation (yellow arrow) of AChR clusters, neurofilament accumulation or axonal sprouting (light blue arrow) are marked with arrows. White arrows potentially suggest the occurrence of reinnervation of AChR clusters, as multiple thin nerve processes stem from the same motor axon, innervating individual AChR clusters. Denervation of NMJs is visible where yellow arrows point to a break in the motor axon, or clear denervation of endplates without opposing nerve terminals. Overall heterogeneity of NMJs is clearly visible as in previous **Figure 4-5**. All images are to the same scale. Scale bar = 10 μm

This variable is described as 'compactness': the more closely packed the AChRs on a particular endplate area, the more compact the endplate; the further spread out, the less compact. Given that one can infer a lot about the state of an NMJ from these particular variables (nerve terminal area, overlap, compactness and endplate area) this data is summarized in **Figure 4-8**. Individual NMJs per patients are plotted and demonstrate the morphological heterogeneity of NMJs within patients shown in **Figure 4-5** and **Figure 4-7**. Despite marked variability within patients, the means between groups did not differ significantly, and additional variables which would be suggestive of denervation, e.g. increase in fragmentation (~0.63) or increase in AChR area (~122–137 μm^2) were also similar in their means across groups. No changes were observed in any of the 20 morphological variables investigated (**Table 4-2**). Morphology, and heterogeneity, observed at the NMJ was consistent across all three groups, with no significant changes to suggested the involvement of the NMJ in the pathology of cancer cachexia.

Although the significant reduction in muscle fibre diameter in cancer cachectic patients (discussed in 4.4.1 **Table 4-2**) along with predictions based on rodent models might suggest denervation of muscle as a major contributor to the pathogenesis of cachexia (Yamada *et al.*, 2020), this data shows no evidence of signs of denervation or degeneration of the NMJ. Given neither weight stable cancer patients nor cancer cachectic patients

differed in NMJ morphology from the control group, the assumption is that cancer itself does not contribute to altered NMJ morphology. Furthermore, as no morphological alterations in branching patterns, overlap (a marker of denervation), fragmentation (a marker of increased AChR clustering) or compactness (a marker of endplate instability) were observed in cancer cachectic patients, it can be assumed that degeneration of the NMJ is not the early cause of cancer cachexia. Likewise, as the motor nerve was preserved, this suggests that alterations in muscle, rather than the NMJ, are the primary cause of cancer cachexia.

4.4.4. Type of cancer does not affect NMJ morphology

Although no morphological differences were found, it is possible that the type of cancer (or reason for surgery in control patients) might still influence NMJ variables within patient groups. For example, patients suffering from gastric cancer, who have previously been shown to present with the highest incidence of weight loss (Dewys *et al.*, 1980) might still display predominantly denervated NMJs. As 4/5 patients with gastric adenocarcinoma were weight stable, denervation at the NMJ could precede muscle atrophy and cause subsequent weight loss.

In order to assess the influence of clinical variables (e.g. BMI, SMI, weight, ECOG…) on NMJ morphology, a Principal Component Analysis (PCA) was conducted. PCA allows the visualisation of data sets consisting of many variables, using a smaller number of variables than the original data set. Whilst the represented data has 31 variables that can be cross correlated (20 morphological NMJ variables and 11 clinical variables describing musculoskeletal health) this would result in 465 individual pairwise correlation analyses which would have to be interpreted individually ([n x (n – 1) / 2] analysis). A PCA also permits a reduction in the number of dimensions and therefore the number of plots that are required to describe the data, whilst preserving the dimensions, or so called (’principal components’) that contribute most to its overall variance and best describe the data. Thus, the

data can be visualised in 2D or 3D depending on how many principal components are selected for representation of the data.

PCA on all analysed NMJs managed to identify the first three principal components as the ones that contribute to 51.81% of the overall variance within the data (**Figure 4-9.B**). PC1 contributes to 32.38%, PC2 to 11.54% and PC3 to 7.91% of the overall variance. Therefore, principal components thereafter quickly contribute only very little to the proportion of variance explained as visible in the screeplot in **Figure 4-9.A**. The inclusion of the first three principal components was chosen as subsequent principal components showed a significant drop in variance relative to their previous principal component. This observation can be seen as a "bend" that starts to flatten after PC3 in **Figure 4-9.A** and is marked with a red line.

After selection of the first three principal components, this process ultimately reduced the 31 original dimensions (31 variables) to 3 dimensions, which are more manageable in terms of data exploration and visualisation. The resulting eigenvectors and eigenvalues are ultimately applied to individual data points (NMJs) in order to transform the data to the selected dimensions, and the scaled/transformed data were then visualised as a 3D-biplot (**Figure 4-9.C**). Since each individual dot represents one NMJ, the heterogeneity of NMJ morphology is still apparent, and no particular groups or clusters stand out.

One can see that each principal component is driven by a set of distinct descriptive variables: PC1 by overall descriptors of NMJ size, PC2 by descriptors of musculoskeletal health, and PC3 by descriptors of endplate and nerve terminal integrity. Going forth, variables with a loading of > 0.25 or < -0.25 were deemed more influential within a principal component.

Table 4-2: Overview of aNMJ-morph data and comparison across groups

	Ctrl n = 12 429 NMJs	Weight Stable n = 10 385 NMJs	Cachexia n = 10 392 NMJs	F (DFn, DFd) or Kruskal Wallis statistic	P	Mean Difference / P Ctrl vs Weight Stable	Mean Difference / P Ctrl vs Cachexia	Mean Difference / P Weight Stable vs Cachexia
core variables								
presynaptic								
1) *Nerve Terminal Area (µm²)*	79.9 ± 7.7	73.7 ± 11.1	74.9 ± 10.0	F (2, 29) = 0.127	0.881	6.2 / 0.887	5.1 / 0.923	- 1.2 / 0.996
2) *Nerve Terminal Perimeter (µm)*	144.7 ± 9.1	136.2 ± 13.5	134.9 ± 11.7	F (2, 29) = 0.236	0.791	8.6 / 0.851	9.8 / 0.809	1.3 / 0.997
3) *Number of Terminal Branches*	37.0 ± 2.7	37.0 ± 2.6	37.4 ± 2.5	0.098	0.952	- 0.0 / > 0.999	- 0.4 / > 0.999	- 0.4 / > 0.999
4) *Number of Branch Points*	17.0 ± 2.6	17.4 ± 2.0	17.7 ± 1.9	F (2, 29) = 0.023	0.978	- 0.4 / 0.992	- 0.7 / 0.976	- 0.3 / 0.996
5) *Total Length of Branches (µm)*	64.9 ± 5.5	61.3 ± 7.0	60.0 ± 6.0	F (2, 29) = 0.183	0.834	3.7 / 0.903	4.9 / 0.835	1.2 / 0.990
postsynaptic								
6) *AChR Area (µm²)*	137.4 ± 10.7	122.0 ± 14.5	124.8 ± 15.0	F (2, 29) = 0.403	0.672	15.4 / 0.687	12.6 / 0.777	- 2.8 / 0.988
7) *AChR Perimeter (µm)*	153.1 ± 8.9	154.3 ± 15.6	153.9 ± 18.9	F (2, 29) = 0.002	0.998	- 1.2 / 0.998	- 0.8 / 0.999	0.4 / > 0.999
8) *Endplate Area (µm²)*	251.6 ± 20.2	228.2 ± 29.7	221.5 ± 29.8	F (2, 29) = 0.380	0.687	23.4 / 0.801	30.1 / 0.694	6.7 / 0.983
9) *Endplate Perimeter (µm)*	78.8 ± 3.8	77.4 ± 6.4	77.3 ± 6.7	F (2, 29) = 0.024	0.976	1.4 / 0.982	1.5 / 0.980	0.1 / > 0.999
10) *Endplate Diameter (µm)*	27.9 ± 1.3	28.4 ± 2.4	28.0 ± 2.3	F (2, 29) = 0.019	0.981	- 0.5 / 0.980	- 0.1 / 0.999	0.4 / 0.989
11) *Number of AChR Clusters*	4.0 ± 0.3	4.1 ± 0.4	4.3 ± 0.5	F (2, 29) = 0.155	0.857	- 0.1 / 0.962	- 0.3 / 0.844	- 0.2 / 0.958
derived variables								
presynaptic								
12) *Average Length of Branches (µm)*	2.0 ± 0.1	1.82 ± 0.1	1.8 ± 0.1	F (2, 29) = 0.746	0.483	0.2 / 0.562	0.2 / 0.552	< 0.1 / 0.999
13) *Complexity*	4.3 ± 0.1	4.3 ± 0.1	4.4 ± 0.1	F (2, 29) = 0.012	0.988	< 0.1 / 0.999	< - 0.1 / 0.994	< - 0.1 / 0.988
postsynaptic								
14) *Average Area of AChR Clusters (µm²)*	48.2 ± 6.8	37.7 ± 3.6	38.9 ± 2.8	1.663	0.435	10.5 / 0.649	9.3 / > 0.999	- 1.2 / > 0.999
15) *Fragmentation*	0.63 ± 0.03	0.63 ± 0.04	0.62 ± 0.03	F (2, 29) = 0.016	0.984	< - 0.1 / 0.998	< 0.1 / 0.992	< 0.1 / 0.983
16) *Compactness (%)*	56.7 ± 1.2	56.0 ± 1.8	59.0 ± 1.1	F (2, 29) = 1.262	0.298	0.7 / 0.932	- 2.4 / 0.453	- 3.0 / 0.302
17) *Overlap (%)*	45.7 ± 1.4	47.0 ± 2.1	48.2 ± 2.5	F (2, 29) = 0.396	0.676	- 1.3 / 0.893	- 2.5 / 0.651	- 1.2 / 0.909
18) *Area of Synaptic Contact (µm²)*	62.4 ± 6.0	57.0 ± 8.3	58.1 ± 7.4	F (2, 29) = 0.165	0.849	5.3 / 0.855	4.3 / 0.904	- 1.1 / 0.994
associated nerve & muscle variables								
19) *Axon Diameter (µm)*	1.2 ± 0.05	1.0 ± 0.06	1.1 ± 0.05	F (2, 29) = 0.688	0.511	0.1 / 0.486	0.1 / 0.777	< - 0.1 / 0.891
20) *Muscle Fibre Diameter*	78.8 ± 19.9	79.8 ± 23.7	69.5 ± 19.5	54.82 ****	< 0.0001	- 1.0 / > 0.999	9.3 / < 0.0001 ****	10.3 / < 0.0001 ****
21) *Number of Axonal Inputs*	1.04 ± 0.04	1.08 ± 0.04	1.03 ± 0.10	0.362	0.835	- 0.04 / > 0.999	0.01 / > 0.999	- 0.05 / > 0.999

Statistical difference between control (Ctrl, N = 12, n = 12 muscles), cancer weight stable (N = 10, n = 10 muscles) and cancer cachectic patients (N = 10, n = 10 muscles) was calculated using a one-way ANOVA with a Tukey's multiple comparison test on patient means for each variable (to avoid pseudo replication of NMJs). Degrees of freedom (F) are noted. If one group or more didn't pass the D'Agostino & Pearson normality test, the Kruskal-Wallis test with Dunn's test was conducted and the Kruskal-Wallis statistic was noted. Mean values ± SEM are listed for each patient group for 20 distinct morphometric variables. Muscle fibre diameter is given as mean ± SD.

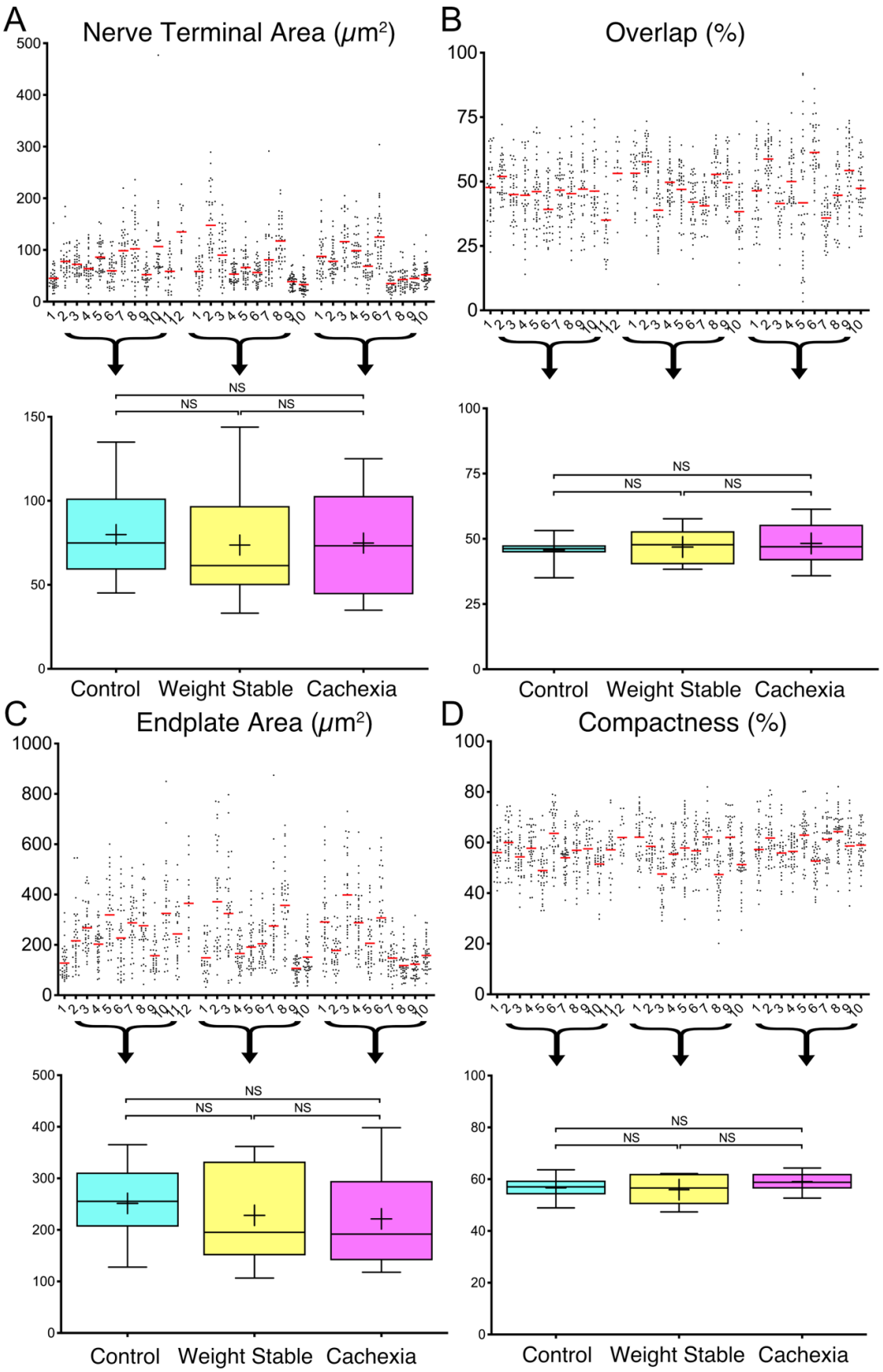

Figure 4-8: Morphology is conserved across the human NMJ in cancer cachexia

Legend continues on next page.

Figure 4-8 legend continued from previous page: Scatterplots on upper panels of (A-D) show individual values of NMJs per patient, which are sorted by increasing age per group, for common markers of denervation: nerve terminal area (A), overlap (B), endplate area (C) and compactness (D). Bottom panel of (A-D) depict box-and-whisker plots of mean patient data of control (N = 12), cancer weight stable (N = 10) and cancer cachectic (N = 10) patients. Whiskers on boxes represent the minimum and maximum values, the boxes enclose the central 25th-75th percentile of data distribution and depict the mean (+) and median (line) for each group. Comparison was conducted on the mean patient data of NMJ variables by one-way ANOVA with a Tukey's multiple comparison test. Neither of the four morphometric variables showed differences across the three groups. NS = not significant

The respective role that variables play within individual principal components was then assessed by evaluation of the contributing eigenvectors to PC1–PC3 and subsequent inspection of the respective loading plots (**Figure 4-10**). These show that size related variables of the NMJ such as perimeters and areas of nerve terminal (nerve terminal perimeter ν = 0.30, nerve terminal area ν = 0.28), endplate (endplate perimeter ν = 0.27, endplate area ν = 0.29) and AChRs (AChR perimeter ν = 0.29, AChR area ν = 0.28), as well as total length of branches (ν = 0.29), complexity (ν > 0.25) and area of synaptic contact (ν = 0.27) contribute to overall variance of PC1 in the same direction. This suggests a scalar relationship between these morphological variables; upon increase or decrease of one, the others will be scaled in the same direction (larger or smaller respectively). As no clinical variables influence the variance of PC1, this again suggests that morphometric variables are independent of clinical variables in *rectus abdominis* across patients.

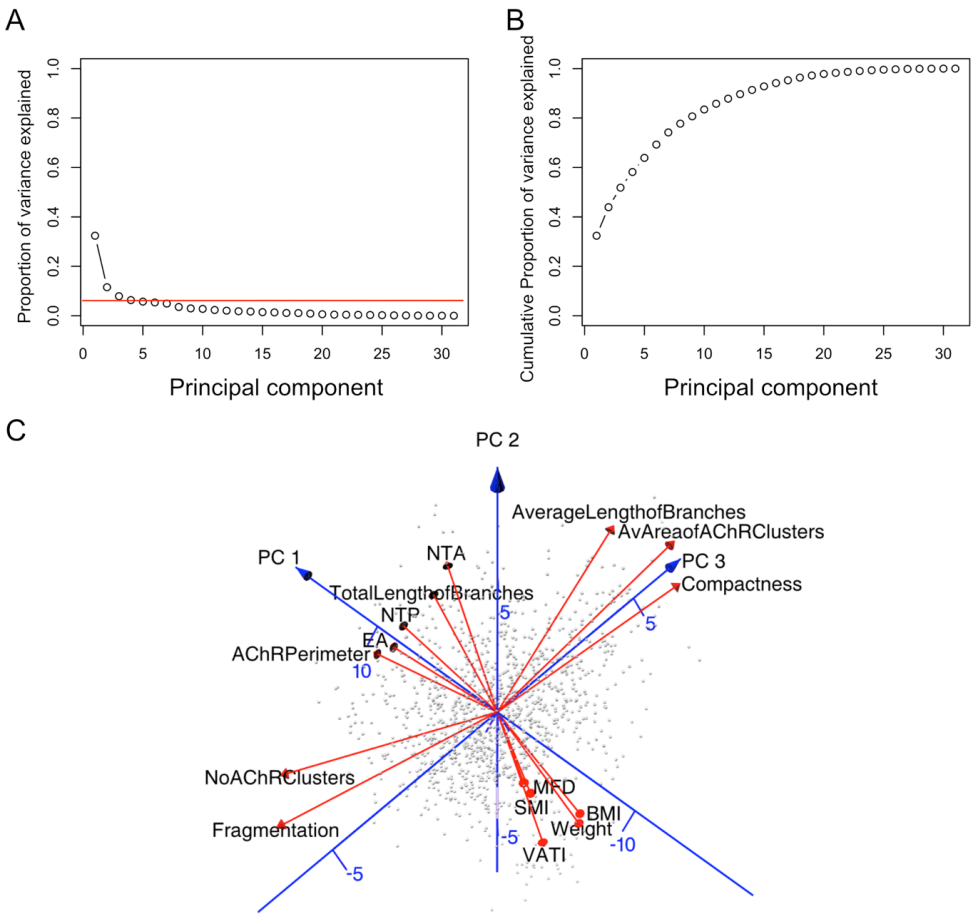

Figure 4-9: Screeplot and biplot explaining contribution of variance and variables

(A) Selection of number of principal components to include (red line) for further analysis was decided by looking at the "bend" of the curve where proportion of variance explained by principal components in relation to previous principal components dropped off. The first three PCs were chosen.

(B) Depiction of the cumulative proportion of variance. The first 3 principal components explain 0.5181 cumulative proportion of the variance, or 51.81%.

(C) For initial data exploration a 3D-biplot was generated depicting all samples and 5 variables (red lines) that have the highest 'loadings' for each of the three PCs (blue lines). For each of the data points that is a NMJ (grey), the data set contains 20 morphometric variables and 11 clinical variables. PC1 runs diagonally from the bottom right to the top left and morphometric size variables are represented across the top left of the axis. PC2 runs vertically from the bottom to the top and clinical variables are clustered at the bottom right. PC3 runs from the bottom left to the top right and variables associated with endplate and nerve terminal integrity influence PC3 along the top right and bottom left of the axis. NTA = nerve terminal area; NTP = nerve terminal perimeter; EA = endplate area;

PC2 on the contrary is driven by the variance of clinical variables which are associated with musculoskeletal health, i.e. BMI (ν = -0.46), weight (ν = -0.39), skeletal muscle index (ν = -0.36), visceral (ν = -0.33) and subcutaneous adipose tissue index (ν < -0.25) and muscle fibre diameter (ν < -0.25), whilst variables associated with NMJ morphology contribute little to PC2. For example, upon increase of patient weight, the values for BMI, skeletal muscle index and visceral adipose index all correlate positively, whilst weight loss correlates negatively (see loading plot in **Figure 4-10**.

Meaning, if patients lose weight, the values for BMI, SMI and VATI should also decrease. In addition, NMJ variables were not driven by clinical appearance, i.e. musculoskeletal health in *rectus abdominis* across patients is independent of NMJ morphology across the different patient groups.

Variables that are associated with overall endplate and nerve terminal integrity describe most of the variance of PC3, i.e. average area of AChR clusters (ν = 0.48), fragmentation (ν = -0.37), average length of branches (ν = 0.34), number of AChR clusters (ν = -0.32) and compactness (ν = 0.32). The loading plot in **Figure 4-10** describes the relationship between these variables have between each other, as an increase in number of AChR clusters correlates with both an increase in fragmentation and a decrease in average area of AChR clusters. As the endplate increasingly fragments, and AChR cluster size decreases, the endplate becomes less compact given that smaller clusters spread out over a larger endplate area.

However, in both PC1 and PC3, none of the clinical variables had large loading variables; NMJ morphology is conserved across patients and is not affected by their clinical status. Although data from aNMJ-morph showed no differences between the three patient groups, the influence of type of carcinoma or reason for surgical intervention (type of aneurysm) on overall NMJ morphology cannot be excluded.

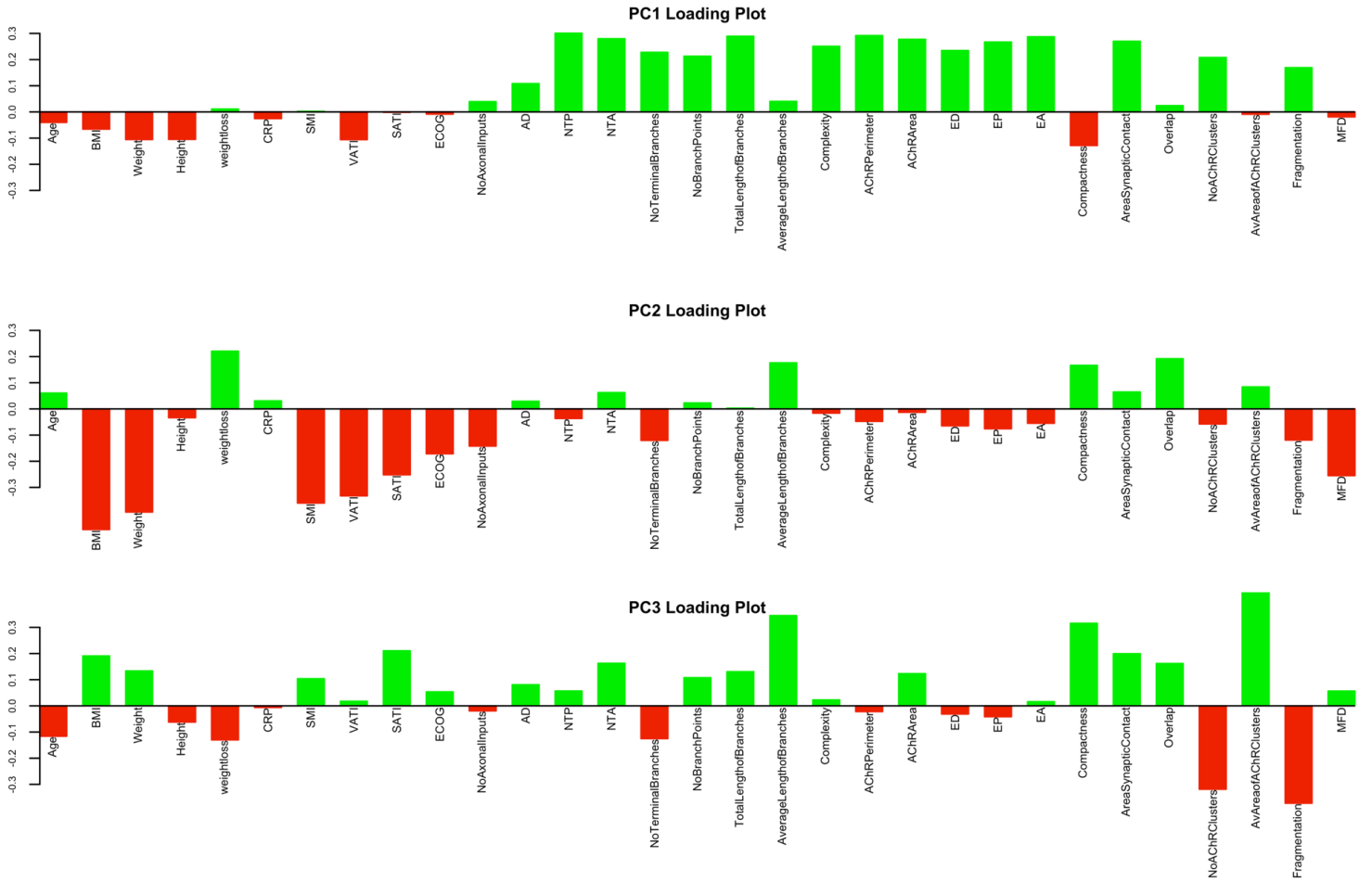

Figure 4-10: Loading plots of the first three principal components

Green (positive) and red (negative) show the directionality the variables contribute to overall variance within the respective principal components in relation to each other. *Legend continues on next page.*

Figure 4-10 legend continued from previous page:
Length of bars indicates how much a variable contributes to overall variance, the longer, the more variance is explained through interaction with this variable within a principal component. PC1 can be described by overall size variables of the NMJ, whereas PC2 describes overall clinical variables associated with musculoskeletal health. PC3 is driven by variables associated with endplate and nerve terminal integrity. BMI = Body mass index; CRP = C-reactive protein; SMI = Skeletal muscle index; VATI = Visceral adipose tissue index; SATI = Subcutaneous adipose tissue index; ECOG = Eastern Cooperative Oncology Group; AD = Axon diameter; NTP = Nerve terminal perimeter; NTA = Nerve terminal area; ED = Endplate diameter; EP = Endplate perimeter; EA = Endplate area; MFD = Muscle fibre diameter.

Visualisation of NMJ data within the space of the first three principal components (colour coded by disease; **Figure 4-11.A**), strengthens the above drawn conclusions that NMJ morphology is conserved across patients. None of the groups 'trended' in either direction across PC1 or PC3 which would have suggested gross differences in NMJ size or integrity.

4.4.4.1. Musculoskeletal health is a predictor of patient health

In concordance with PC2's clinically descriptive variables (**Figure 4-9.C** and **Figure 4-10**) which include BMI, weight, skeletal muscle index, adipose tissue indices and muscle fibre diameter, there is a slight upwards trend towards the positive end of PC2 of NMJs from cancer cachectic patients. This aligns with the previously analysed CT-scans and muscle fibre diameters as per **Figure 4-4**. As PC2 scales clinical variables towards the negative end of PC2 (**Figure 4-9.C**), an increase in the aforementioned variables would move them towards the negative end of PC2; this suggests that muscle fibre atrophy, weight loss, reduced BMI or SMI would cluster patient NMJs towards the opposing end of PC2.

This is visible in **Figure 4-11.A** where cancer cachectic patient NMJs lie towards the top of PC2, with weight stable and control patient NMJs scattered slightly below and towards the negative end of PC2.

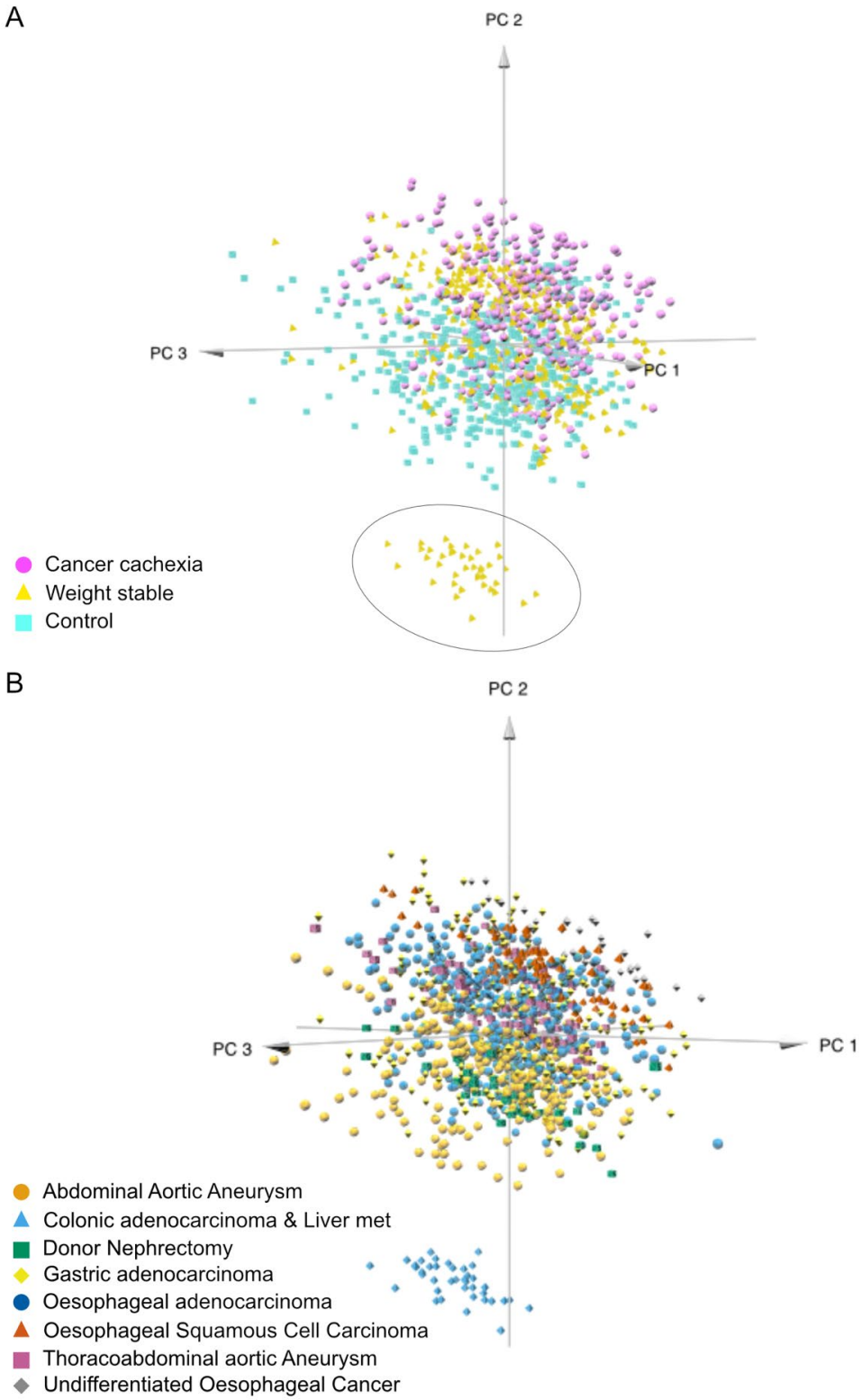

Figure 4-11: 3D-plot of PCA by type of cancer and reason for surgery

Each data point represents an NMJ. The data contains 20 morphometric variables and 11 clinical variables within the first three principal component scores. *Legend continues on next page.*

Figure 4-11 legend continued from previous page:

(A) 3D-plot depicting spread of cancer cachectic (magenta circle), cancer weight stable (yellow triangle) and control (cyan square) NMJs. The bottom, separately clustered NMJs (black circle) belong to the only patient with colonic adenocarcinoma and liver metastasis. This patient was obese (BMI > 40 kg/m^2), the heaviest, with largest values for SMI, VATI and SATI in comparison to all other patients, separating him from all others according to clinical variables.

(B) 3D-plot depicting spread of NMJs sampled from patients with a particular disease status: abdominal aortic aneurysm (orange circle, control N = 7), colonic adenocarcinoma & liver metastasis (light blue triangle, weight stable = 1), donor nephrectomy (green square, control = 1), gastric adenocarcinoma (yellow diamond, weight stable N = 4, cancer cachectic N = 1), oesophageal adenocarcinoma (dark blue circle, weight stable N = 4, cancer cachectic N = 7), oesophageal squamous cell carcinoma (red triangle, weight stable N = 1, cancer cachectic N = 1), thoracoabdominal aortic aneurysm (pink square, control N = 1), undifferentiated oesophageal cancer (grey diamond, cancer cachexia N = 1). The configuration of the plot (slightly different to A) was chosen to best showcase the band like grouping of NMJs of different disease status, due to their differences in musculoskeletal health.

NMJ morphology described through PC1 and PC3 is not influenced by disease, nor by patient pathology.

This suggests that differences in clinical variables between these groups are more able to 'predict' the disease state of patients (control, cancer cachectic or weight stable in this case). This is in concordance with the differences in weight loss and SMI between groups that have previously been explored in **Table 4-1**, where overall patient demographics are compared.

One clear patient outlier is notable. [See **Figure 4-11.A** (circled) and **Figure 4-11.B** (patient with colonic adenocarcinoma and liver metastasis). Note the cluster of yellow triangles at the bottom end of PC2.] This patient presented with a BMI of 41 kg/m^2, 121 kg, and the largest values of SMI, VATI and SATI in comparison to all other patients. In this case, NMJ data across PC1 (descriptive of NMJ size variables) and PC3 (NMJ integrity) is comparable to other patients. However, due to the stark influence of clinical variables on PC2, this patient's NMJs lie towards the negative end of PC2 in comparison

to the other patient's NMJs, which are more comparable to all NMJs in terms of morphological variables.

Further evaluation of the 3D-plot, colour coded by type of carcinoma/reason for intervention (**Figure 4-11.B**) shows no correlation of data with PC1 or PC3. Therefore, cancer type or surgical intervention in controls do not influence the overall morphology of the NMJ. However, slight band like clustering of NMJ data along PC2 is notable, suggesting the influence of pathology on musculoskeletal health and associated variables such as SMI, adipose tissue indices and therefore BMI, as discussed previously. Age itself has not been found to be a driver of NMJ morphology or musculoskeletal health within this patient cohort as evident from **Figure 4-10**. As the overlap in pathology between cachexia and sarcopenia (the age related loss of muscle mass and function) has previously been discussed, this data suggests that cancer cachexia should be differentiated from age-related sarcopenia, since different pathways might be driving muscle wasting (Hepple, 2012; Romanick, Thompson and Brown-Borg, 2013; Zhang *et al.*, 2020).

In summary, despite marked weight loss and muscle atrophy in patients with cancer cachexia, comprehensive assessment of NMJ morphology showed no difference in any of the 20 morphometric variables across control, cancer weight stable and cancer cachectic patients. Furthermore, thorough analysis of NMJ morphology and clinical data utilising principal components analysis showed that neither the type of carcinoma, nor the reason for surgical intervention influences NMJ morphology, but does impact musculoskeletal health. This data therefore supports the previous notion that overall NMJ morphology remains stable in cancer cachexia, whilst metabolic changes within skeletal muscle are likely to represent the primary location of pathology in cancer cachexia (Boehm, Miller, Thomas M Wishart, *et al.*, 2020).

4.5. Conclusion

1) Cancer cachectic patients suffer from significant loss of skeletal muscle mass and muscle atrophy in comparison to both cancer weight stable and control patients.
2) NMJ morphology is stable in patients with cancer cachexia.
3) Denervation of the neuromuscular junction is not a major driver of disease pathogenesis and does not precede muscle atrophy.
4) Musculoskeletal health in *rectus abdominis* across cancer patients is independent of NMJ morphology.

Cachexia is a devastating condition and affects up to 50–80% of cancer patients and depending on tumour type, it is associated with poor responses to chemotherapy and leads to both a reduced quality of life and/or survival (Fearon, Voss and Hustead, 2006; Vagnildhaug *et al.*, 2018). Despite global efforts to find therapeutic interventions, current treatment options such as nutritional support or anti-inflammatory drugs have not been able to reverse the physiological impact of cachexia, despite therapeutical improvements in weight and skeletal muscle mass (Molfino *et al.*, 2016). The causal mechanisms behind onset and progression of cachexia that affect some cancer patients as opposed to others remain less well explored. Therefore, the treatment of weight loss and associated weakness are a topic of high priority and are included in the current (2021) Cancer Grand Challenges (*Cachexia | Cancer Grand Challenges*, 2021) which aim to fund global research projects trying to understand the overall mechanisms behind cancer associated pathologies.

Given the involvement of the peripheral nervous system that is thought to play a causative role in the development of cachexia, assessment of NMJ dismantling in humans remains under investigated area. Fundamental research might help pinpoint whether denervation of the NMJ is responsible for cachexia associated muscle atrophy (Grisold, Grisold and Löscher, 2016). This study shows that the NMJ is stable across healthy control patients,

patients with cancer cachexia and weight stable cancer patients. Therefore, dismantling of the NMJ, preceding muscle atrophy, is unlikely to be initiating the overall loss of skeletal muscle mass observed in cachectic patients. This supports the hypothesis that intrinsic changes within skeletal muscle, rather than changes at the NMJ, represent the primary locus of neuromuscular pathology in cancer cachexia. Since cachexia is a metabolic syndrome, this highlights the importance of healthy muscle homeostasis and indicates that misregulation of anabolic and catabolic processes within both the muscle itself and surrounding supportive cell types (in particular adipose tissue) are key to the onset of cachexia (Porporato, 2016).

The preservation of the NMJ and its associated motor nerve in cancer cachexia opens up new treatment avenues and facilitates a clearer focus on both future research and clinical trials. For example, utilisation of neuromuscular electrical stimulation to induce muscle hypertrophy by evoking an exercise training response in skeletal muscle might prove beneficial in combination with nutritional support and treatments targeting the metabolic syndrome (Toth *et al.*, 2020). Likewise, a ketogenic diet has been suggested to support cancer treatment as tumours have lost their ability to efficiently use fat or ketones and predominantly metabolise glucose as their energy source (Fearon *et al.*, 1988). As the metabolised glucose likely stems from the bloodstream following skeletal muscle autophagy induced by cancer cells (which releases free amino acids for de-novo glucose synthesis into the blood plasma) dietary replacement of glucose with ketone bodies might help prevent tumour growth and alleviate symptoms of excessive skeletal muscle autophagy (Fearon *et al.*, 1988; Porporato, 2016; Weber *et al.*, 2020). Study of combinatorial treatment approaches (e.g. neuromuscular electrical stimulation paired with a ketogenic diet) in randomised controlled clinical trials might allow to targeting of cancer cachexia from multiple therapeutic angles, in an effort to restore ‘normal’ metabolic homeostasis within the neuromuscular system.

5. Comparative Anatomy of the Mammalian NMJ

5.1. Chapter Summary

Mammalian models have long been used in neuroscience to study mechanisms of human diseases. Given the stark differences in cellular and molecular anatomy between the commonly studied rodent NMJ and the human NMJ, and the poor translation of models to human conditions as exemplified by the stability of the human NMJ in cancer cachexia, this chapter aims to examine NMJ morphology across larger mammalian models. The overarching goal was to find a mammalian model that is more similar to the human NMJ than the mouse NMJ. To do so, NMJs were examined from pelvic and hindlimb muscles from the commonly studied dog, sheep, pig and cat, which all lie intermediate in body size between the mouse and the human. Furthermore, the pony was chosen as a representative mammal larger in body size in comparison to the human. No direct relationship was observed between muscle fibre diameter, body size and endplate size. Interestingly, NMJs from smaller mammals differed more from the human NMJ, whilst NMJs from larger mammals were more similar to the human NMJ, suggesting that larger mammalian models such as sheep might be more suitable as models of human neurodegenerative disease, than the mouse. This chapter describes the first comprehensive study of overall NMJ morphology across larger mammalian models. Baseline NMJ data of the here explored species, except pony, have been published in Boehm, Alhindi, *et al.*, 2020.

5.2. Background

The previous chapter emphasised the stability of the human NMJ is in cancer and cancer cachexia (Chapter 4) and how important it is to carefully assess human morphology in health and disease, as opposed to taking a priori statements from rodent models at face value (Boehm, Miller, Thomas M. Wishart, *et al.*, 2020). As discussed in the introduction (Background, Chapter 1) there is a considerable difference between the mouse and human NMJ. Following on from the results in Chapter 4, it is apparent that much research to date has assumed that there 'must' be direct denervation of the neuromuscular junction in human cancer cachexia, as this has been thought to occur in rodent models. Given that the rodent is the most commonly used animal model in research (Ellenbroek and Youn, 2016), the question arises as to what other organism might be more able to model human disease, as preclinical research on humans is ethically challenging. Whilst the rodent proved to be helpful in uncovering many molecular mechanisms associated with the function of the neuromuscular system, it is more limited in its translatability to humans, in particular in preclinical studies of Amyotrophic Lateral Sclerosis (Mitsumoto, Brooks and Silani, 2014; Philips and Rothstein, 2015; Tosolini and Sleigh, 2017).

Whilst the NMJ has been well studied across a variety of both invertebrates and vertebrates, including the human (Coers and Woolf, 1959; Wood and Slater, 2001; Slater, 2015) a detailed morphological study of the mammalian NMJ has been lacking until now (Boehm, Alhindi, *et al.*, 2020). As previously discussed, considerable advances in imaging technology have enabled more accurate measurements of NMJ morphology in comparison to early invertebrate/vertebrate preparations from decades ago, oftentimes captured using camera lucida drawings. Nevertheless, it is remarkable how much detail researchers at that time managed to capture despite technological limitations (Anzenbacher and Zenker, 1963) – see **Figure 5-1.A** (crayfish, tunicate or human).

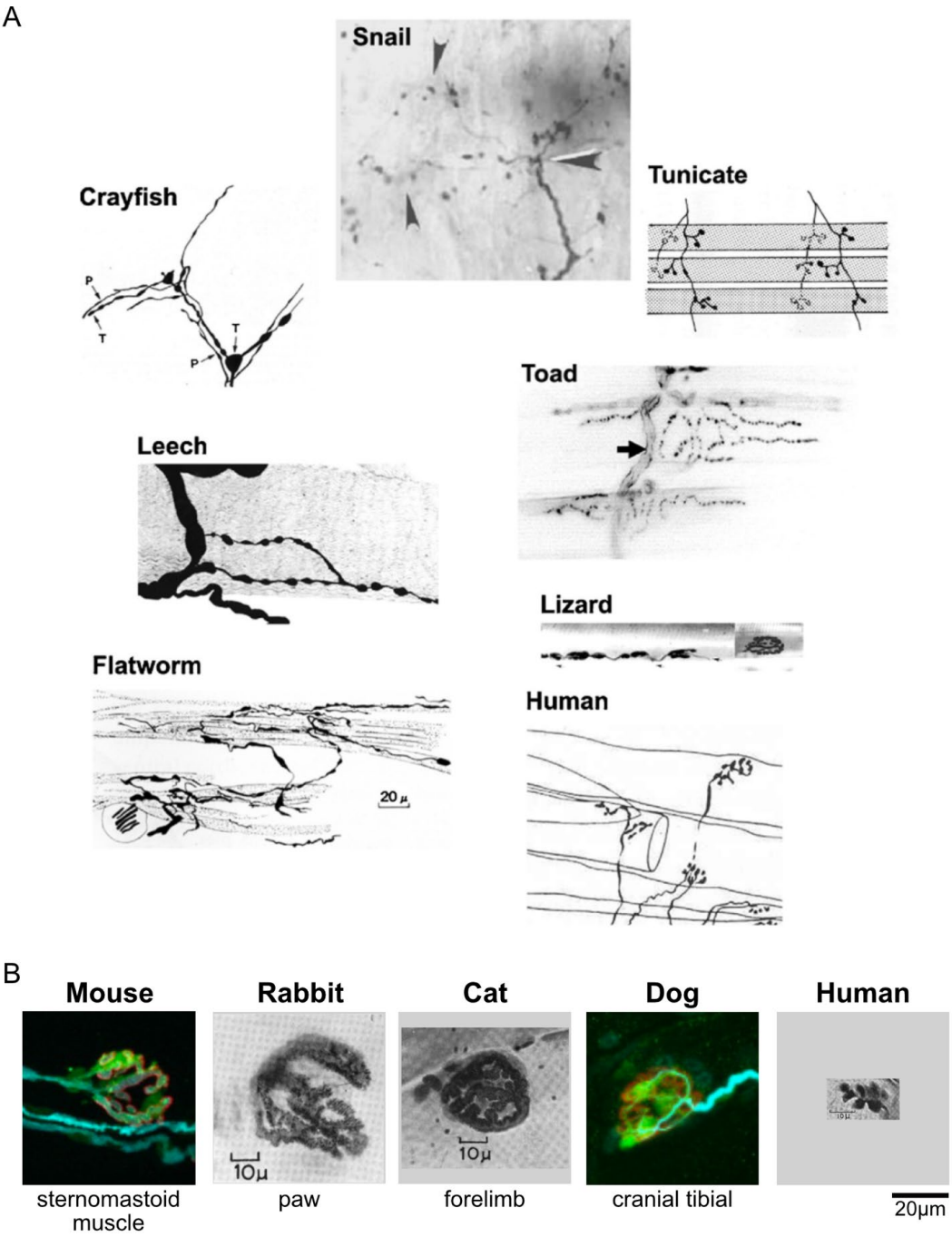

Figure 5-1: Comparative anatomy of the invertebrate and vertebrate NMJ

(A) Comparison of invertebrate motor axon terminals to a schematic (camera lucida drawing) of the human motor axon terminal. 'Nummular' appearance of nerve terminals, or boutons is notable across all depicted species. Approximately all at same magnification as indicated by the scale bar at the flatworm: 20 µm – from (Slater, 2015).

Legend continues on next page.

Figure 5-1 legend continued from previous page:

(B) Comparison of vertebrate NMJs. Mouse and dog NMJs are visualised using immunofluorescent methodologies. AChRs (red), nerve terminal (cyan) and terminal Schwann cells (green) are visible - reproduced from (Haddix *et al.*, 2018). The rabbit and cat endplate (stained by modified Koelle's method), and human motor nerve terminal (stained by methylene blue) are reproduced from (Coers and Woolf, 1959). Images were scaled to be at same magnification, bottom right scale bar of 20μm applies to all depicted confocal micrographs.

Figure 5-1 depicts a broad morphological variety across both invertebrates and vertebrates. In particular the dog (**Figure 5-1.B**), previously utilised as a model for Duchenne Muscular Dystrophy and has shown clear similarities to the mouse NMJ, not only in control animals, but also upon genetic manipulation of animals and onset of muscular dystrophy (Haddix *et al.*, 2018).

Larger mammalian models such as sheep and pig, are gaining more and more traction across the research community. Their capability to more accurately model therapeutic delivery or diseases across longer lifespans such as in Alzheimer's, Huntington's or Parkinson's Diseases (compared to their rodent counterpart) is of great importance for the research community (Holm, Alstrup and Luo, 2016; Eaton and Wishart, 2017; McBride and Morton, 2018).

To evaluate whether the aforementioned mammalian models might be suitable models of human neuromuscular diseases, an in-depth comparison of the mammalian NMJ was conducted across seven mammalian species of different body sizes. In ascending order, these were: mouse, cat, dog, sheep, pig, human and pony. Human and mouse data were reproduced from Jones *et al.,* 2017.

Whilst mouse, dog, sheep and pig are already used as models of human disease, the cat was previously a popular animal to study neuromuscular development and muscle fibre composition (Nystroum, 1968; Burke *et al.*, 1974; Barker and Saito, 1981). Additionally, a larger mammal than the human was also sought. As NMJs of ponies have not been studied in great

detail before, the collaboration with Richard J. Piercy and Stephen Cahalan (PhD student Piercy Group) at the Royal Veterinary College was invaluable.

A common neuromuscular condition affecting predominantly tall horses is recurrent laryngeal neuropathy (RLN) which presents with preferential degeneration of the left recurrent laryngeal nerve and can lead to paralysis affecting airflow (Draper and Piercy, 2018). Whilst degeneration of the widest diameter myelinated axons, muscle fibre type grouping and denervation induced muscle atrophy have been shown to be part of RLN pathology (Rhee *et al.*, 2009), the characterisation of the NMJ and its contribution to denervation has never been performed.

To facilitate this characterisation and to allow for future comparison with disease models of the mammalian series described here, the data presented in this chapter provides a baseline of the healthy mammalian NMJ across seven species. Likewise, commonalities might indicate conserved mechanisms controlling structural development across mammalian species. The primary aim however was comparison of these other species to the human NMJ, to determine which of these species are more similar to the human NMJ and might thus act as a more suitable model than the rodent NMJ. We aimed to address the following questions:

1) Is there a mammalian species (mouse, cat, dog, sheep, pig and pony) that is more similar in NMJ morphology to the human NMJ?
2) Does the phylogenetic distance between species correspond to synaptic differences?
3) Do pre- or post-synaptic cells (motor nerve or muscle) influence mammalian NMJ morphology?
4) Does body size influence muscle fibre diameter and/or NMJ size?

5.3. Methods

5.3.1. Animals and Patients

This animal study was performed in accordance with the Animals (Scientific Procedures) Act 1986, which encompasses regulations regarding the protection of animals used for research purposes and adopts the principles of the 3Rs: Replacement (of animals), Reduction (of animals) and Refinement (of experiments). As previously mentioned in Chapter 2 (2.3.2) the existing research networks across The University of Edinburgh were utilised to sample tissue from larger mammalian models, namely cats (N = 3), dogs (N = 3), sheep (N = 3) and pig (N = 3). Ponies (N = 5) were sampled, processed and imaged by Stephen Cahalan (PhD student Piercy Group) at the Royal Veterinary College. In accordance with the 3Rs, no animals were sacrificed specifically for this project, as tissue was sampled from animals already enrolled in existing experiments (once they have reached their endpoints) or from animals submitted for euthanasia to The Royal (Dick) School of Veterinary Studies. Animals submitted for euthanasia would for example include old or aggressive pets, stray animals or animals from shelters.

Mouse (N = 3) and human (N = 20) lower/hindlimb data were pooled from previously published data by Jones *et al.,* 2017. Human patients ranged from 34–92 years undergoing lower limb amputations for various indications (more detail in Chapter 2 – General Methods) with one male patient undergoing a bilateral amputation of limbs, meaning both limbs were amputated (Jones *et al.*, 2017).

5.3.2. Theoretical and practical considerations – matching animal models to humans

Demographics of animals were chosen to match patient and mouse demographics from Jones *et al.,* 2017 as closely as possible. However,

sampling was restricted by practical availability of age and sex of larger mammalian species. For example, it has been shown that gender affects NMJ size in humans (15 male and 5 female patients) but not in mice, therefore mouse data from only one sex was utilised for comparison in the original 2017 study as well as in this project, in order to adhere to the 3Rs (**Table 5-1**) (Jones *et al.*, 2016). Background data of study animals is summarised in **Table 5-1** and shows that cat and pig were all female, whilst dog and pony samples stemmed from a 2:1 and 2:3 male to female ratio, respectively. In sheep, all samples were from males. Sex differences cannot be excluded at this stage as N numbers were too low for comparison.

Mice at 12 weeks of age have previously been age-matched to middle aged humans (Jones *et al.*, 2017). It is important to recall that 12-week-old mice are considered to be mature adults/young adults (Flurkey, Currer and Harrison, 2007). In comparison to patients from Jones *et al.,* 2017 this would be considered relatively young. Since literature suggests that 12-week-old mice are comparable to ~20–30 year–old humans, this is younger than the present patient series which covered 34–92 years. Nevertheless, 12-week-old mice within the young adult group have been reliably used across the literature as a reference for ageing studies, in comparison to 'old mice' over the age of 6 months, as mice above this age start to exhibit ageing related changes (Flurkey, Currer and Harrison, 2007). Since the aim of Jones *et al.,* 2017 was to compare healthy, non-ageing affected mouse NMJs against healthy human NMJs, the use of these young adult mice was warranted, as it is generally known that fragmentation is a key-hallmark of ageing at the mouse endplate (Valdez *et al.*, 2010) and premature ageing of the rodent neuromuscular system in an otherwise 'comparative' age group could have affected the comparison. Cats themselves have a long lifespan with an upper limit of over 20 years (Cozzi *et al.*, 2017); therefore the age span of 12–16 should be a good representation of older cats and should be comparable to the upper limit of 34–92 year-old patients within the human population.

As discussed in the subsequent results chapter, cat muscle fibre diameters are within the largest and we can therefore exclude ageing related changes

in the cat such as severe muscle fibre atrophy which might have been induced through ageing related changes.

Depending on the breed, dogs have an average lifespan of 10–17 years (Cozzi *et al.*, 2017). With an average age of 6.6 years, dogs are relatively comparable to middle aged human patients. As sheep tend to be considered 'older' at 3 years of age, 1.3 years would likely be young/middle-aged (Okut *et al.*, 1999). Domestic pigs, such as Landrace, are still considered young adults under the age of 6 months (Gutierrez *et al.*, 2015). Given the certainty that pigs of that age will be disease free, the assumption can be made that the sampled muscle and analysed NMJ will be healthy. Similarly, ponies or horses have an average life-expectancy of ~18 years (Cozzi *et al.*, 2017) and therefore 6 years is comparable, and has been age-matched, to human young adults.

Whilst comparison to humans across such a wide age range might initially seem inappropriate, Jones *et al.,* 2017 demonstrated the stability of the human NMJ across the adult lifespan in lower limb muscles. Additionally, age was shown to have no influence on NMJ morphology on *rectus abdominis* in the previous chapter (4.4.4.1 Musculoskeletal health influences clinical variables). Since morphological comparison of other mammalian species to either young-adult, middle-aged or older humans is not likely to demonstrate a statistical difference (as long as other species samples are free of neuromuscular disease and age-related muscle atrophy) this dataset presents to be the same morphologically and can thus be pooled.

Table 5-1: Background data of study animals

Species	Mouse	Cat	Dog	Sheep	Pig	Pony
Sex (M:F)	0:3	0:3	2:1	3:0	0:3	2:3
Age	12 weeks	12.6 ± 3.1 y (min 12, max 16)	6.6 ± 4.6 y (min 4, max 12)	1.3 ± 0.2 y (min 1.3, max 1.5)	0.33 y (same litter)	6.6 ± 1.7 y (min 4.5, max 8.0)
Weight	≃ 19 g	4.3 ± 1.4 kg (min 3.2, max 5.3)	≃ 39 kg	≃ 75 kg	75.6 ± 7.5 kg (min 67, max 80)	312 ± 101 kg (min 180, max 400)
Breed	CD1	Domestic short-haired	Labrador, Staffie X, Lurcher	Texel crosses	Largewhite X landrace	Welsh Mountain Pony (Section A)
Sampled muscles	EDL, PL, PB, SOL	EDL, PL, PB, SOL	EDL, PL, PB	EDL, PL, SOL	EDL, PL, SOL	EDL, SOL, TC
Reason for cull	Experiment	Aggression, hyperthyroidism, chronic kidney disease	Aggression, neoplasia, joint pain	Colony management	Colony management	Colony management

Tissue from larger domestic animals and ruminants was sourced from the Roslin Institute and Dryden Farm, respectively. Ponies stemmed from the Royal Veterinary College. Section component in pony breed refers to their height, section A being the smallest. Mice were sourced from the animal facilities at the University of Edinburgh (Centre for Discovery Brain Sciences). Species are ordered in increasing average weight (the human being sat between pig and pony). Sheep and pig are very similar in weight. Patient demographics for comparison are available in Jones *et al.,* 2017, overall, patients were 34–92 years-old with a 15:5 male to female ratio. However, weights were not available for patients, therefore, an average weight of ~78 kg was presumed for middle aged adults (average age = ~70 y).

Numerical data are mean ± standard deviation (SD). EDL = *extensor digitorum longus*; PL = *peroneus longus*; PB = *peroneus brevis*; SOL = *soleus*; TC = *tibialis cranialis*

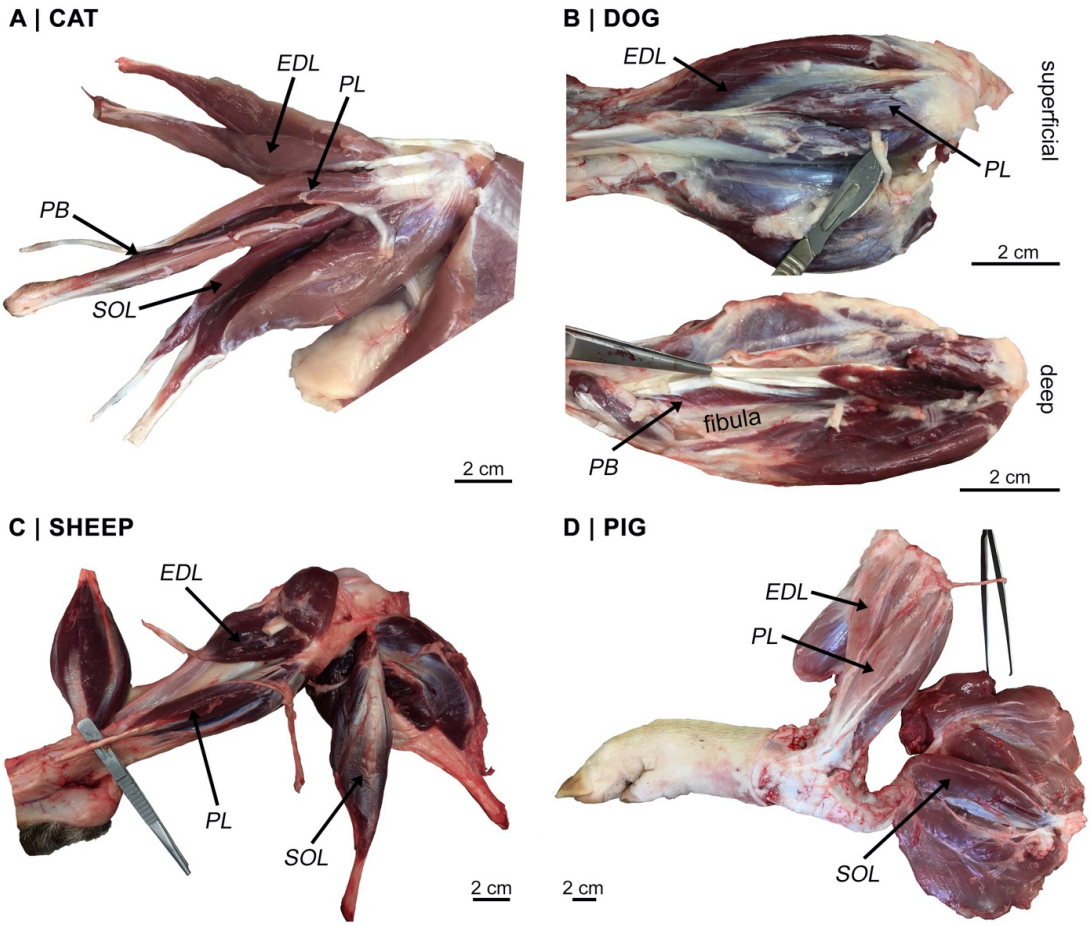

Figure 5-2: Gross anatomy of cat, dog, sheep and pig hindlimb muscles

Illustrative photographs showcasing similarities and differences in gross muscle morphology across species' hindlimbs. For orientation, the proximal side of the limb is on the right-hand side of each limb and the distal side is to the left. As touched upon in 5.3.2.1 (Muscle selection) one can note subtle differences in gross muscle morphology. The dog **(B)** for example lacks *soleus,* and sheep **(C)** and pig **(D)** lack *peroneus brevis*. In dog **(B)** PB lies deep, distally to PL attached to the fibula and it is easiest to first sample all other muscles, then reflect the overlaying muscles, or remove them, to access PB. The cat **(A)** is the only animal that has all four muscles originally sampled in the study from Jones *et al.,* 2017.

Once the skin, fat and fascia were removed and the target muscle was exposed, full-length muscle fibres were sampled and immediately fixed for subsequent tissue processing. Image adapted from (Boehm, Alhindi, *et al.*, 2020) – (A) featured the cover of the Journal of Anatomy.

EDL = *extensor digitorum longus*; PL = *peroneus longus*; PB = *peroneus brevis*; SOL = *soleus*. Scale bar = 2 cm

5.3.2.1. Muscle selection – Gross anatomical differences

As NMJs from larger mammals were subsequently compared to NMJs from previously published human and mouse data (Jones *et al.*, 2017) it was imperative that sampled muscles were comparable to the ones published in Jones *et al.,* 2017. Since NMJs in the previously published study were from *extensor digitorum longus* (EDL), *peroneus brevis* (PB), *peroneus longus* (PL) and *soleus* (SOL) in both mouse and human (in future sections referred to by their abbreviations) the same or comparable hindlimb/pelvic limb muscles were chosen across larger mammalian models.

It is important to note that despite overall similarity in the gross anatomy of lower/hind/pelvic limb across mammals, there are still subtle differences which are worth highlighting (**Figure 5-2**). The cat possesses all four muscles that were analysed in human and mouse, yet the dog lacks SOL (**Figure 5-2.B**) (Worne, 2011; Dyce K.M., Sack W.O., 2015). In ruminants, sheep and pig, EDL, PL and SOL were sampled (**Figure 5-2.C & D**); according to the literature on domestic and farm animals, only carnivores retained PB regardless of its small size and negligible function as evident in the dog (**Figure 5-2.B**) (Bragulla, König and Liebich, 2009). SOL, EDL and *tibialis cranialis* (TC) were sampled from ponies. TC was chosen as a replacement for the peroneal muscles since the only 'peroneal' muscle in ponies, *peroneus tertius*, has developed into a tendon inducing hock flexion. Given that distal flexion represents an analogous function to that of peroneus in other species, TC was thought to be an appropriate alternative (Ashdown and Done, 2011).

5.3.3. Tissue sampling, processing and imaging

Tissue was sampled and processed as previously described in Chapter 2 (General Methods). In brief, full length muscle samples from the aforementioned species were collected at the Roslin Institute or Dryden Farm and immediately transferred into 4% PFA for 2–4 hour fixation and samples were subsequently washed with 1xPBS. Muscles were teased to bundles of

10–15 fibres, the post-synaptic counterpart was visualised with TRITC α-bungarotoxin and the pre-synaptic counterpart was visualised with primary antibodies targeting synaptic vesicle protein and neurofilament, followed by fluorescent secondary antibodies. The first few muscle samples were incubated with primary antibodies for three nights at 4°C and secondary antibodies over night at 4°C; however the protocol was improved throughout the project and all following samples were incubated with primaries over night at room temperature and with secondaries for 2 ½ h at room temperature.

As the pony samples were processed and imaged at a different institution, care was taken to adhere to the same protocol as closely as feasibly possible. The following alterations to the immunofluorescent protocol allowed for better fluorescent staining of pony NMJs: α-BTX Alexa Fluor™ 594 conjugate (1:500, Invitrogen, ThermoFisher Scientific, B13423) for 1 h in 1x Tris buffered saline (TBS) at room temperature. Anti-neurofilament primary antibody: mouse anti-3A10 was used (1:50, DSHB, AB_531874), both primary antibodies for 3 nights at 4°C. Secondary antibody: Goat anti-mouse IgG (H+L) Highly Cross-Adsorbed (1:200, Invitrogen, ThermoFisher Scientific, A-11029) overnight at 4°C. Washes and buffers that normally use PBS were substituted with 1xTBS as this seemed to reduce background.

Slides were imaged on a confocal microscope as detailed in Chapter 2 (2.3.5 Confocal Microscopy). On average a total of 40 *en face* NMJs were imaged per muscle where possible to allow for analysis of at least 30–40 NMJs per sample. Due to Covid-19 induced lockdown, sample processing of the pony was restricted and thus one of the pony EDL muscles only allowed for analysis of 19 NMJs (this had no effect on overall data analysis). Pony image files were acquired as .lif files, where one .lif document/file entailed all NMJs from one muscle and from one animal. To analyse these with aNMJ-morph, images were first screened for suitability and subsequently saved as .tiff files in an individual folder, and afterwards loaded in aNMJ-morph's batch-processing mode.

5.3.3.1. Muscle fibre diameter measurements

A total of 40 muscle fibres were measured per muscle sample to correspond with the average number of NMJs analysed per muscle sample. Muscle fibres were not correlated to individual NMJs and therefore correlation data corresponds to average NMJ data correlated to average muscle fibre diameter per muscle sample. Overall, a total of **6,000 muscle fibres** were analysed.

5.3.4. Student and collaborative contributions

This chapter represented an enormous collaborative effort in regard to data analysis, tissue sampling and overall imaging. Respective tasks undertaken by project students and collaborators have been acknowledged here:

Abrar Alhindi (AA, Edinburgh Medical School, University of Edinburgh and Faculty of Medicine, Department of Anatomy and King Abdulaziz University, Jeddah, Saudi Arabia), a fellow PhD student in the Gillingwater lab, sampled, processed and imaged all cat muscles (EDL, PL, PB and SOL) and PL from one dog (dog 4) under supervision, along with imaging of EDL and PB NMJs from dog 4. Following co-supervised training in NMJ- and aNMJ-morph, AA analysed all cat and dog images (from EDL, PL and PB), the latter of which had previously been processed and imaged by myself. AA imaged and measured all muscle fibre diameters from cat and dog.

All sheep muscles (EDL, PL and SOL) that have previously been sampled, processed and imaged by myself were analysed with aNMJ-morph by Ana S. Leite (School of Medicine, UNESP-São Paulo, State University, Botucatu, Sao Paulo, Brazil).

Pig muscles, sampled, processed and imaged by myself were analysed with NMJ-morph by Anatomy project students that were co-supervised and previously trained in the use of NMJ-morph. Alyssa Gibbs analysed pig PL and recorded and measured pig and sheep PL muscle fibre diameters; Olivia Murray analysed pig EDL and recorded and measured pig and sheep EDL

muscle fibre diameters; Rizwan Farrukh recorded and measured pig and sheep SOL muscle fibre diameters. Pig SOL was analysed with aNMJ-morph by myself.

Pony confocal images were provided by Stephen Cahalan (PhD student Piercy Group, Comparative Neuromuscular Diseases Laboratory, Pathobiology and Population Sciences, Royal Veterinary College). Three ponies were analysed by myself using aNMJ-morph, the other two ponies were analysed by Stephen Cahalan following training in NMJ-morph/aNMJ-morph and data consolidation of data with me. Muscle fibre diameters were recorded and measured by Stephen Cahalan using the same methodology as described in Chapter 2 (2.3.5.1 Muscle Fibre Diameter Measurements). Data were kindly shared for final analysis.

5.3.5. Image Analysis

Analysis of images took place as described above. Prior to analysis, all students were trained in NMJ-morph and/or aNMJ-morph and supervised correlation analysis was conducted as per Chapter 3 (3.4.1 Validation of NMJ-morph user proficiency). Building on Chapter 3, reliability in the use of NMJ- -morph/aNMJ-morph has already been shown, and analysis of larger mammalian NMJs could commence without further additional training.

5.3.6. Statistical Analysis

Previously published data from **2,860 human NMJs** (N = 20 patients; n = 72 muscles) and **960 mouse NMJs** (N = 3 animals; n = 24 muscles;) was used for data analysis in addition to the newly generate data from **465 cat NMJs** (N = 3; n = 12), **341 dog NMJs** (N = 3; n = 9), **313 sheep NMJs** (N = 3; n = 9), **446 pig NMJs** (N = 3; n = 9) and **578 pony NMJs** (N = 5; n = 15). In **total, 5,963 NMJs** were analysed across 7 species, sampled from 150 muscles of 40 individual animals/patients (with mouse and human data pooled from Jones et al., 2017).

To conduct the comparison of morphometric variables, statistical analyses were performed on the mean of each muscle variable per species using Graph-Pad Prism 9 for macOS (Version 9.0.2). Before comparison of groups and multiple comparison testing, the differences in variance and normality of the distributions were assessed. To assess whether sample distribution is heteroscedastic (i.e. unequal variance across groups) a Brown-Forsythe test was conducted. If the Brown-Forsythe test was non-significant (i.e. the variance across groups is equal – a homoscedastic distribution – groups have comparably equal standard deviations/standard error of means) a one-way ANOVA with Dunnett's correction for multiple comparisons was used. Following a significant difference in variance upon conduction of the Brown-Forsythe test (i.e. standard deviations/standard error of means differed between groups) a Brown-Forsythe and Welch ANOVA with Dunnett T3 correction for multiple comparisons was used. A D'Agostino-Pearson omnibus normality test was used prior to evaluate overall normality of the distribution. If the distribution passed the normality test, analysis proceeded with the ANOVA statistical analysis; if the distribution failed the normality test, the non-parametric Kruskal-Wallis test with Dunn's multiple comparison test was conducted.

5.3.6.1. Pearson correlation to assess influence of muscle and motor nerve on NMJ morphology

To assess whether pre- or post-synaptic cells influence morphometric variables across species, correlation analyses were performed using muscle fibre diameter (post-synaptic cell = muscle) or axon diameter (pre-synaptic cell = motor nerve) against variable means (18 core and derived variables) for each individual muscle across all species (n = 150 muscles). The correlation coefficients (r) between morphometric variables and associated nerve and muscle variables and associated P-values were evaluated, with correlations above r = ± 0.7 considered strongly correlated, correlations between r = ± 0.5–0.7 considered moderately correlated and correlations between r = ± 0.5–0 considered as weak or no correlation. Depending on the associated P-value for each species and the global population correlation

(i.e. population referring to across all mammals), the presence of a significant linear relationship between the morphometric variable and associated nerve or muscle variable can be determined. As sample numbers play a role in evaluation of the P-value, correlation coefficients (r) could still be below 0.5 and yet the P-values could be highly significant (****P < 0.0001) – this would suggest that there is only a 0.01% chance that there is **no** linear relationship between the morphometric variable and the associated nerve or muscle variable.

5.3.6.2. Phylogenetic tree & Tanglegram construction

A phylogenetic tree was constructed on http://itol.embl.de using the NCBI species IDs for all seven species, which were subsequently exported: human (*Homo sapiens*, ID 9606); mouse (*Mus musculus* 10090); cat (*Felis catus* 9685); dog (*Canis lupus* 9612); sheep (*Ovis aries* 9940); pig (*Sus scrofa domestica* 9825) and the Welsh Mountain Pony/Horse (*Equus caballus* 9796).

The tanglegram (a so-called comparison between two dendrograms) was constructed in RStudio version 1.4.1103 (RStudio, 2020) using R version 4.0.3. The R packages “tidyverse” (version 1.3.0) for data manipulation and the package “vegan” (version 2.5–7) which allows for creation of a distance matrix and dendrograms by groups (species) (Oksanen *et al.*, 2020) were loaded. To create the tanglegram, the package “dendextend” (version 1.14.0) was loaded. First a .csv file containing mean averages for each analysed muscle across all species was loaded. The original data contained a 20x150 matrix, where 20 represented 20 morphometric variables (innervation was omitted as most muscles had an innervation value of 1 ± 0), and 150 represented the muscles sampled across 40 individual animals/patients. A Euclidean distance matrix was created first, listing pairwise differences between each individual muscle. As we were more interested in species, the “vegan” package was used to extract a distance matrix by group identity (i.e. the species identity). To be able to compare differences between species in pre- and post-synaptic structures, the code was scripted to create distance

matrices for core and derived variables of the presynapse and postsynapse separately (excluding the associated nerve and muscle variables axon diameter and muscle fibre diameter). Following the generation of both distance matrices, dendrograms (trees) of both were created and subsequently compared via use of a tanglegram, utilising the “dendextend” package. A tanglegram allows visualisation of the ‘entanglement’ of two dendrograms and therefore highlights both their similarity and differences in the length of branching and clustering differs. This was further accentuated through visual representation within the graph (e.g. colours and thickness of branches).

5.4. Results & Discussion

Since most research involving the neuromuscular system is undertaken on rodent models (Ellenbroek and Youn, 2016), it is important to find models representative of the human in health and disease. As explored in-depth within the introductory Chapter 1 (Background) there is a striking morphological difference between the mouse and human NMJ; furthermore, the molecular composition of the NMJ differs between both species (Jones *et al.*, 2017). This implies that caution is needed when translating the results of mouse studies to human clinical trials. Therefore, larger mammalian models which might have be more similar in neuromuscular architecture to the human, are of great interest to pre-clinical research. Additionally, it is of particular interest to uncover common morphological trends across mammalian NMJs and identify whether there are evolutionary links between morphological similarities or differences.

In order to determine whether there are larger mammalian models which more closely mirror human NMJ architecture, the previously analysed human NMJs from Jones *et al.,* 2017 were compared to NMJs from six different mammalian species: the mouse, cat, dog, sheep, pig and pony. The choice of muscles was determined from the previously published human and mouse data from Jones *et al.,* 2017: *extensor digitorum longus* (EDL), *peroneus brevis* (PB), *peroneus longus* (PL) and *soleus* (SOL) elaborated in detail in

previous section 5.3.2.1 (Muscle selection). NMJs from each hindlimb or pelvic-limb muscle were immunofluorescently visualised, imaged and analysed via NMJ-morph or aNMJ-morph.

5.4.1. Marked inter-species heterogeneity of NMJ morphology

Overall analysis of **5,963 NMJs** from **150 muscles** of **40 individual animals/patients** generated a baseline of morphometric data across **7 mammalian species**. At first glance the marked inter-species heterogeneity of NMJ morphology was apparent (**Figure 5-3**). Whilst the mouse and human NMJ display their typical 'pretzel' and 'nummular' morphology (Jones *et al.*, 2017) respectively, there are distinct size differences between NMJs of animals of the smallest body size, e.g. the particularly small cat NMJ and the strikingly larger mouse and dog NMJ. Both ruminants, the human and pony, the largest analysed mammal, have on average smaller NMJs than mammals of smaller body-size (apart from the cat).

To assess quantitative differences in NMJ morphology across species, aNMJ-morph or NMJ-morph analysis was performed, yielding an 'average' for each analysed muscle from each species, for each of the 21 morphometric variables. Subsequently, these average variables were compared between all six species and the reference human data set (Jones *et al.*, 2017), which allowed for an in-depth morphometric comparison (**Table 5-2**).

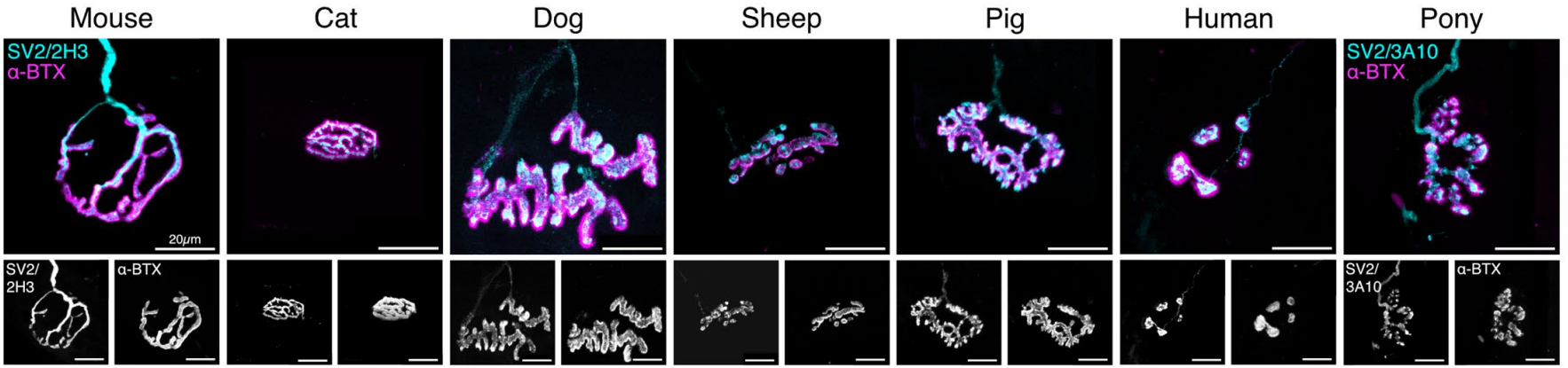

Figure 5-3: Heterogeneity of mammalian NMJs

Confocal micrographs representing average NMJ morphology in endplate size and shape across all seven species in *extensor digitorum longus*, arranged in ascending body-size from smallest (mouse) to largest (pony). Whilst mouse nerve terminals resemble the typical 'pretzel'-shape, cat NMJs are the smallest amongst all the species and the most complex. The dog has the largest overall endplate area, whilst sheep, pig and the 'nummular' human NMJ seem quite similar in overall NMJ size. The pony has a comparatively larger axon than the human NMJ, however also seems fairly fragmented such as the sheep and human. Confocal micrographs in the upper panel have been pseudo-coloured in Fiji. The bottom panels consist of a montage of nerve terminal (left) and motor endplate (right) of the respective pseudo-coloured upper panels. SV2 = synaptic vesicle protein 2 + 2H3 and 3A10 = neurofilament (cyan); α-BTX (α-bungarotoxin) = acetylcholine receptors (magenta);

Scale bar = 20 μm across all images.

Table 5-2: Baseline morphological data of the mammalian NMJ

	Mouse N = 3, n = 24 960 NMJs	Cat N = 3, n = 12 465 NMJs	Dog N = 3, n = 9 341 NMJs	Sheep N = 3, n = 9 313 NMJs	Pig N = 3, n = 9 446 NMJs	Human N = 21, n = 9 2,860 NMJs	Pony N = 5, n = 15 578 NMJs
Core variables							
pre-synaptic							
1) *Nerve Terminal Area (μm^2)*	304.0 ± 11.7 ****	98.5 ± 5.4 *	264.5 ± 28.3 **	145.6 ± 16.9	197.6 ± 24.7	124.7 ± 6.2	182.1 ± 11.4 **
2) *Nerve Terminal Perimeter (µm)*	327.4 ± 9.4 ****	272.1 ± 13.9 ****	441.0 ± 31.7 ****	231.7 ± 12.3 ****	234.7 ± 18.6 **	132.4 ± 5.6	210.4 ± 14.5 ***
3) *Number of Terminal Branches ‡*	30.2 ± 1.2	101.4 ± 7.4 ****	95.6 ± 8.5 ****	45.5 ± 4.4 *	40.1 ± 6.0	27.6 ± 1.4	28.2 ± 2.3
4) *Number of Branch Points ‡*	25.8 ± 0.9 ****	57.6 ± 6.9 ****	62.1 ± 3.5 ****	26.4 ± 2.6 **	38.5 ± 3.2 ****	13.8 ± 0.9	20.3 ± 2.1
5) *Total Length of Branches (µm) †*	166.7 ± 4.8 ****	128.7 ± 7.7 ****	215.7 ± 13.5 ****	109.5 ± 8.1 ***	134.5 ± 12.0 ****	69.3 ± 3.5	103.5 ± 8.3 ***
post-synaptic							
6) *AChR Area (μm^2) †*	424.2 ± 14.1 ****	159.6 ± 9.3	420.8 ± 35.1 ****	182.2 ± 14.0	239.5 ± 25.2	209.2 ± 8.9	212.2 ± 19.1
7) *AChR Perimeter (µm)*	275.8 ± 8.8 ****	332.7 ± 16.5 ****	536.5 ± 41.7 ****	241.6 ± 15.2 **	221.8 ± 18.6 *	152.3 ± 6.4	182.6 ± 16.4
8) *Endplate Area (μm^2) ‡*	678.2 ± 24.3 ****	333.2 ± 19.9	858.9 ± 85.0 ****	365.4 ± 16.8	384.2 ± 38.5	351.3 ± 15.8	367.1 ± 33.2
9) *Endplate Perimeter (µm)*	118.8 ± 2.9 ****	91.4 ± 3.0	139.1 ± 10.2 *	85.1 ± 3.8	95.5 ± 7.2	98.7 ± 2.9	91.1 ± 4.6
10) *Endplate Diameter (µm)*	42.2 ± 1.2 **	30.9 ± 1.1 *	48.1 ± 3.4 *	30.3 ± 1.4 *	32.2 ± 2.0	36.0 ± 1.0	33.5 ± 1.7
11) *Number of AChR Clusters ‡*	2.6 ± 0.1 ***	3.2 ± 0.4	3.8 ± 0.5	5.0 ± 0.4	3.7 ± 0.5	3.9 ± 0.2	3.1 ± 0.3
Derived variables							
pre-synaptic							
12) *Average Length of Branches (µm) ‡*	6.7 ± 0.2 ****	1.4 ± 0.1 ***	2.6 ± 0.2	3.0 ± 0.4	4.4 ± 0.6	3.0 ± 0.1	4.3 ± 0.3 *
13) *Complexity*	4.9 ± 0.0 ****	5.7 ± 0.1 ****	5.9 ± 0.1 ****	4.9 ± 0.1 ****	5.1 ± 0.1 ****	4.1 ± 0.1	4.6 ± 0.1 **
post-synaptic							
14) *Average Area of AChR Clusters (μm^2)*	238.5 ± 8.5 ****	75.8 ± 8.6	175.4 ± 12.6 ***	54.8 ± 6.8	113.0 ± 12.9	72.1 ± 2.9	112.3 ± 16.2
15) *Fragmentation †*	0.40 ± 0.02 ****	0.51 ± 0.04	0.54 ± 0.05	0.67 ± 0.04	0.49 ± 0.04	0.58 ± 0.02	0.52 ± 0.04
16) *Compactness (%) ‡*	64.4 ± 0.6	49.5 ± 1.1 ****	50.4 ± 1.8 ***	51.0 ± 3.1 **	64.5 ± 2.3	62.0 ± 0.7	59.8 ± 1.7
17) *Overlap (%) ‡*	64.2 ± 0.5 ****	45.9 ± 1.1	53.1 ± 1.1	66.4 ± 3.0 ****	71.1 ± 3.6 ****	49.4 ± 1.1	62.4 ± 2.2 ***
18) *Area of Synaptic Contact (μm^2) †*	267.9 ± 9.5 ****	72.4 ± 4.5 ***	224.4 ± 18.1 ***	122.0 ± 13.4	175.0 ± 24.2	105.2 ± 5.1	129.8 ± 11.1
Associated nerve & muscle variables							
19) *Axon Diameter (µm)*	3.1 ± 0.1 ****	1.0 ± 0.1	1.8 ± 0.2 *	1.1 ± 0.1	1.2 ± 0.1 ***	0.8 ± 0.02	1.8 ± 0.1 ****
20) *Muscle Fibre Diameter ‡*	40.2 ± 0.5 ****	84.3 ± 3.5 ***	77.2 ± 3.3 *	63.0 ± 3.3	76.6 ± 6.7	58.9 ± 2.3	54.9 ± 3.8
21) *Number of Axonal Inputs ‡*	1.0 ± 0.0	1.0 ± 0.0	1.0 ± 0.0	1.0 ± 0.0	1.1 ± 0.0 ***	1.0 ± 0.0	1.0 ± 0.0

Legend continues on next page.

Table 5-2 legend continued from previous page:

Average morphological values across species (ascending body-size) mean of individual EDL, PL, PB, SOL, TC muscles within a species ± SEM. Core variables (1–11), derived variables (12–19) and associated nerve and muscle variables (19–21). In each species N = animals, n = muscles, and total NMJs analysed per species are listed. Statistical difference between human and six other mammalian species was compared on variable averages for each muscle (n) using † - one-way ANOVA with Dunnett's multiple comparison test, ‡ - Kruskal-Wallis test with Dunn's multiple comparison test for non-parametric variables, or no label – Brown-Forsythe and Welch ANOVA with Dunnett T3 multiple comparison test for data with unequal variance.

Mouse and human reference data reproduced from Jones *et al.,* 2017.

*P < 0.05; **P < 0.01; ***P < 0.001; ****P < 0.0001; no asterisk = non-significant result.

It is interesting to note that with an increase in body-size, NMJs reveal a closer similarity to human NMJs, with the majority of variables (14/21 in pony; 13/21 in pig; 12/21 in sheep) showing no statistically significant differences. Sheep and pig were highly similar in average body weight as evident in **Table 5-1**. With decreasing body-size, NMJs show a decrease in similarity to the human (no significant differences to human, in descending body size: 5/21 in dog; 9/21 in cat; 3/21 in mouse; cat being the 'odd one out'). And they show an increase in statistically significant differences to the human (8/21 dog; 7/21 cat; and 16/21 mouse; ****P < 0.0001).

As initial observations suggested, mouse and dog NMJs were significantly larger than the human NMJ. Quantitative assessment confirmed this analysis as the majority of core variables (both 10/11 in the mouse and dog) were significantly larger than in the human. Additionally, the axon was almost four- and two-fold the diameter of the human axon in mouse and dog, respectively (**Figure 5-4.A**). Ponies also showed a larger axon diameter, by at least two-fold, in comparison to the human.

Whilst initial observations suggested that the cat NMJ was smaller than the human NMJ, only a few core variables (2/11) were actually smaller in comparison (namely nerve terminal area, on average ~21% smaller than in human and the endplate diameter, on average ~14% smaller than in human).

As evident in **Figure 5-3 – Cat** and **Table 5-2**, the cat NMJ is highly complex and has an intricate branching pattern. This increases the overall perimeter of both nerve terminal and AChR area and therefore allows for more appropriate overlap between both counterparts. This is reflected in the very small size of the NMJ overall, in comparison to the human, yet with much more complex NMJs and significantly larger pre-synaptic core branching variables and pre- and post-synaptic core variables for nerve terminal and AChR perimeter (as described above; 5/11 larger core variables).

Overall, no particular trend of NMJ morphology with species characteristics such as body-size was observed initially (**Figure 5-3** and **Figure 5-4**) and there was broad heterogeneity of average morphology is evident across species in variables such as nerve terminal area and muscle fibre diameter (**Figure 5-4.B–C**).

5.4.2. Phylogenetic distance does not correspond to differences in post- or pre-synaptic morphology across species

Whilst overall, species showed less differences in comparison to the human NMJ, in variables associated with the postsynapse (on average 2.5/6 species differed significantly to the human - **Table 5-2**, **Figure 5-4.D** and Appendix – **Figure 8-2**), pre-synaptic variables associated with the motor nerve were considerably more distinct. On average, 4.7/6 species differed significantly to the human in pre-synaptic core and derived variables (**Table 5-2**, **Figure 5-4.C** and Appendix – **Figure 8-1**).

To evaluate whether these differences in NMJ morphology are associated with evolutionary divergency between mammals, first a phylogenetic tree was constructed containing all seven species **Figure 5-5.A**.

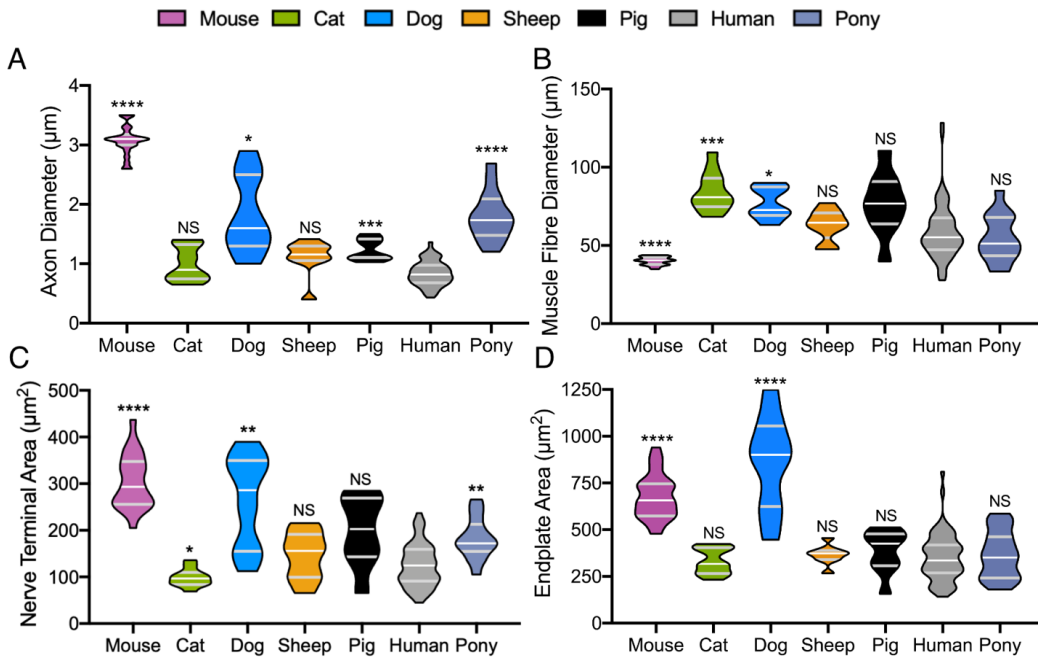

Figure 5-4: Inter-species differences in NMJ morphology

Mouse and dog NMJs are significantly larger than the human (and other species) in nerve terminal **(C)** and endplate area **(D)**. Furthermore, they possess the largest axon diameters **(A)**. The cat has the smallest overall NMJ-morphology in terms of overall size/area, however, cat NMJs seem to innervate the largest overall muscle fibres **(B)**, whilst for example the very large mouse NMJ innervates the smallest overall muscle fibres. The human has the largest spread of muscle fibre diameters and the smallest axon diameters of all species.

'Average' NMJ morphology of individual muscles within a species is plotted in form of a truncated violin plot. The top and bottom of the 'truncated' plot represent the minimum and maximum values, the white 'middle' line represents the median, and the interquartile range (encompassing 50% of the dataset) is bounded by grey, slightly thicker lines, above and below the white line. A violin plot allows to visualize the overall distribution of data and can visually suggest whether data is normally distributed or not. Each violin plot contains the means of all muscles from one species. (Mouse: N = 3 animals, n = 24 muscles; cat: N = 3, n = 12; dog: N = 3, n = 9; sheep: N = 3, n = 9; pig: N = 3, n = 9; human: N = 21, n = 72; pony: N = 5, n = 15) Mouse and human data from Jones *et al.,* 2017.

Brown-Forsythe and Welch ANOVA with Dunnett T3 multiple comparison test for axon diameter and nerve terminal area, and Kruskal-Wallis test with Dunn's multiple comparison test for muscle fibre diameter and endplate area were conducted on variable averages for each muscle (n). NS = non-significant; *P < 0.05; **P < 0.01; ***P < 0.001; ****P < 0.0001

This helps to illustrate the original ‘timeline’ at which species diverged from each other, which can then be used to compare similarity in post- and pre-synaptic morphology in form of a dendrogram. Whilst the primate-rodent clade share a common superorder of mammal (the Euarchontoglires; Kumar, Hallström and Janke, 2013) human and mouse still diverged many million years before the here listed domestic animals studied here. Moreover, it is too simplistic to expect similarity of integral structural components of the neuromuscular system due to a shared superorder, as evident from the stark morphological difference between the mouse and human NMJ (Jones *et al.*, 2017).

Another prime example is the cat and dog. **Figure 5-3** depicts the contrasting morphology between both, whilst **Figure 5-5.A** indicates that the domestic cat and dog only ‘recently’ (many million years ago) diverged from a common ancestor, with NMJ morphology most likely adapted to their individual physiological demands. Mouse and dog (the two outermost branches on **Figure 5-5.A)** on the other hand have very similar NMJ morphology (**Figure 5-3**) in that both pre- and post-synaptic counterparts are large, branched and less fragmented than the human. There is still a debate in the literature as to whether the dog (carnivore) is considered an ‘outgroup’, or whether the rodent should be considered an ‘outgroup’, and therefore whether carnivores should delineate with primates. Neither of these hypotheses entirely explain the similarity in NMJ morphology between rodent and dog NMJ.

Despite advances in molecular studies and improvements in sequencing efforts, we still consider the primate-rodent clade to be the norm (Cannarozzi, Schneider and Gonnet, 2007). With this in mind, it is not entirely improbable that despite evidence for both hypotheses (a primate-rodent and primate-carnivore clade) the dog and rodent might share morphological features from a common superorder, given the triangular relationship between carnivores, rodents and primates.

To further tease apart species overlap, two dendrograms were created to evaluate differences between species in post- and pre-synaptic morphology

based on Euclidean distance using only core and derived variables (19/21 variables). As most species seemed to differ less in post-synaptic variables compared to the human, a ‘tanglegram’ was created (**Figure 5-5.B**) to enable comparison of the two dendrograms (since a tanglegram juxtaposes two dendrograms and visually depicts the difference or similarity in the branching and clustering of the dendrograms).

The tanglegram confirms previous results, indicating that dog and mouse NMJ are inherently different to other species in both post- and pre-synaptic morphology. Furthermore, it suggests that post-synaptic structures amongst the other five species are more similar than their respective pre-synaptic structures, indicated in their smaller distances to the node where species diverge within Euclidean space (~150 comparing post-synaptic variables; ~200 comparing pre-synaptic variables) (**Figure 5-5.B**).

Whilst there is heterogeneity in NMJ morphology **within** a species, apparent in the spread of violin plots in **Figure 5-4**, the heterogeneity of NMJ morphology **between** mammals is much larger. A study looking at NMJs of twenty different species of *Drosophila* showed a similar result. Despite all species belonging to the same genus, the heterogeneity between *Drosophila* species was much larger than within the same species. Further, no relationship was observed between their phylogenetic distance and their phenotypic similarities. The authors suggest that whilst genetic drift is not able to account for the stark differences across *Drosophila* species, selection and adaptation to environmental factors potentially play a much bigger role (Campbell and Ganetzky, 2012). Across the analysed species, a similar selection process might have influenced the observed NMJ morphology of mammalian species rather than pure genetic drift. This might explain the discrepancy between phylogenetic distance between species and the differences in their NMJ morphology. Adaptation and selection, more likely than time and genetic drift, would have shaped the current form and function of mammalian NMJs.

5.4.3. Influence of pre- and post-synaptic cells on NMJ morphology

Since post-synaptic variables were more similar in comparison to the human NMJ, the question arose as to whether motor axon or target skeletal muscle fibre had more influence on NMJ morphology across species (globally) or in a species-specific manner. Given that neurocentric or myocentric influence on NMJ development (i.e. the contribution of either the motor nerve, neurocentric or muscle, myocentric) have been debated in the literature, the following analyses might shed light on these dependencies across species. It has been noted that both components play a key role during development, although pathways for example differ between species: in *Drosophila* muscle cells have been shown to affect post- and pre-synaptic assembly and the motor nerve activates pathways relevant for crucial pre-synaptic differentiation, and in rodents the muscle and terminal Schwann cell primarily affect pre-synaptic differentiation (Wu, Xiong and Mei, 2010). Therefore, it is likely that these pathways also differ between the analysed species, causing species-specific differences in morphology.

In alignment with a myo- and neurocentric view, the assumption in the literature is that NMJ size and overall morphology are strongly influenced by both the innervating motor neuron and the muscle fibre it innervates. This has previously been demonstrated across species such as frog and mouse, where neurotransmitter release affects nerve terminal (Kuno, Turkanis and Weakly, 1971) and motor endplate size (Harris and Ribchester, 1979).

Multiple detailed studies by Coers *et al.,* on a variety of human muscles have suggested that the simpler overall structure and significant heterogeneity of human NMJs is also represented in a marked variation of muscle fibre diameters (this can also be noted in **Figure 5-4.B**).

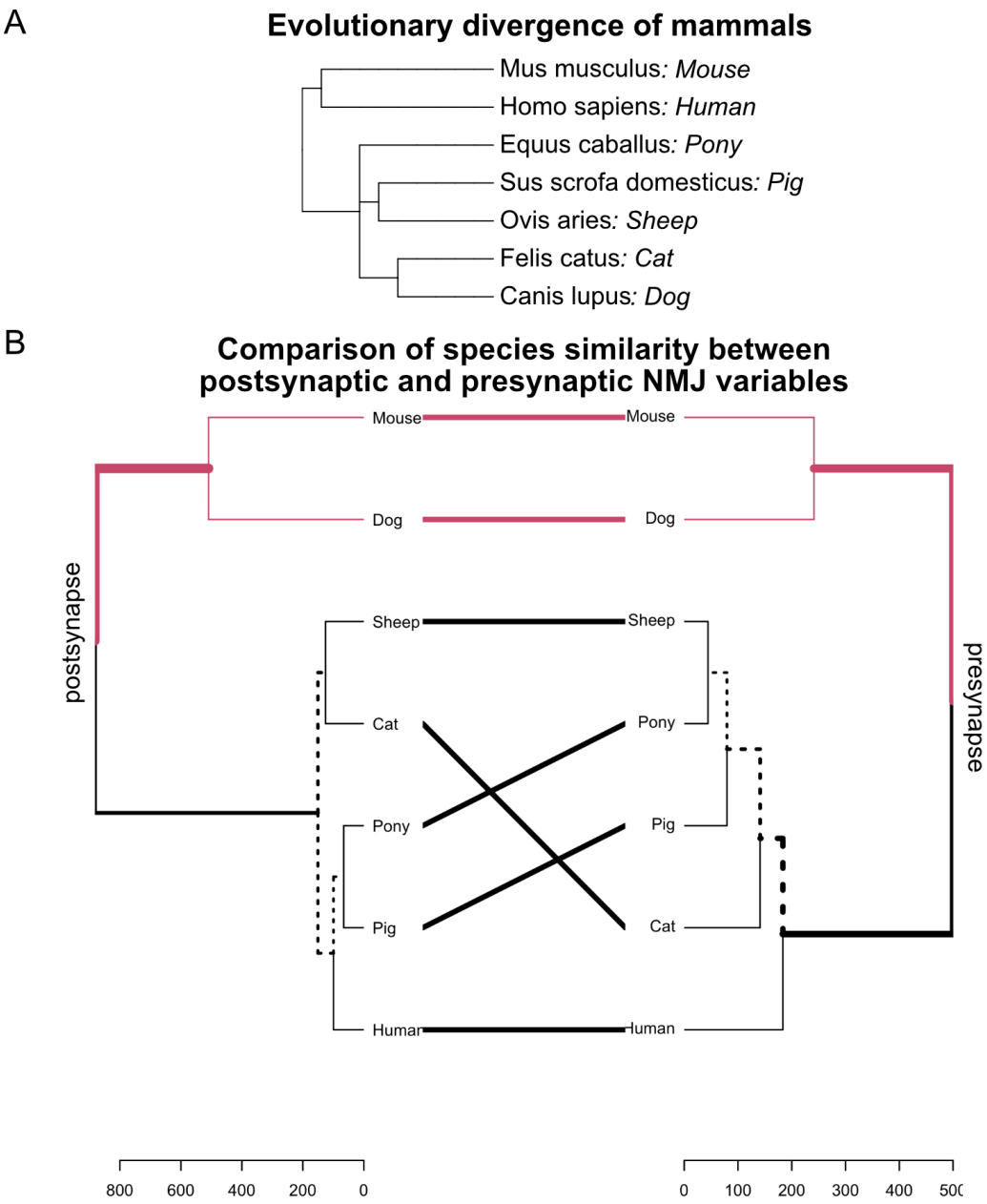

Figure 5-5: Evolutionary divergence of mammals and comparison of species similarity between post- and pre-synaptic counterparts of the NMJ

(A): Phylogenetic tree of the timeline of divergence of the seven here analysed mammalian species. Branch length represents the time until divergence. The primate-rodent clade diverged much sooner from all five listed domestic mammals. Primates however diverged many million years sooner from the rodent (mouse), as domestic animals diverged from each other.

(B): A so called tanglegram, depicting the interaction (entanglement) between two dendrograms. The scale bar on the bottom of the dendrograms indicates the Euclidian distance separating the branches. *Legend continues on next page.*

Figure 5-5 legend continued from previous page:

The left (postsynapse) dendrogram represents clustering of species by similarity using core and derived variables of the post-synapse. The right (pre-synapse) dendrogram represents the clustering of species by similarity using core and derived variables of the pre-synapse. Pink indicates commonalities in subtree branches and suggests that mouse and dog are very similar in post- and pre-synaptic morphology and different from all other five species. Black thick lines (edges of the dendrogram) indicate differences in the distance of branches. This means that domestic animals and the human are further removed from mouse/dog post-synaptic morphology than pre-synaptic morphology (the latter covers a shorter distance), however, all four species are more similar in post-synaptic morphology in Euclidean space. The node at which human and sheep split within the left dendrogram, representing post-synaptic morphology, is roughly at ~150, whilst the node at which the human splits from domestic animals, representing pre-synaptic morphology, is at ~200 in the right-hand side dendrogram.

Dotted lines indicate 'distinct' edges between both dendrograms, which are differences amongst species similarities between post- and pre-synaptic morphology. For example, it is evident that pony and pig are more similar to each other in post-synaptic morphology, however, the sheep and pony are more similar to each other in pre-synaptic morphology.

In regard to humans, Coers and Woolf observed only one muscle, *tibialis anterior*, which correlated in muscle fibre and endplate diameter (Coers and Woolf, 1959). They did however find muscle fibre diameter to correlate with endplate diameter in disease: larger and complex endplates were found in hypertrophic muscle fibres and smaller endplates were found in atrophic muscle fibres (Coers and Woolf, 1959). This has also been demonstrated in more recent rat studies, where muscle atrophy was induced through hindlimb suspension, and muscle hypertrophy via exercise (Deschenes, Tenny and Wilson, 2006).

Furthermore, dependence of NMJ morphology on motor neuron and muscle identity has been shown in rat and mouse. Type II (fast twitch) motor units generally have larger and more complex NMJs, whilst type I (slow twitch) motor units, which are mostly comprised of smaller muscle fibres, are innervated by smaller and simpler NMJs (Ogata, 1988; Prakash *et al.*, 1996). Additionally, not just motor unit type, but also the type of muscle group

(muscle identity) has shown to correlate in diameter with motor endplate size (Oda, 1985).

To evaluate whether pre- or post-synaptic cells could influence NMJ size/morphology, core and derived variables (18/21) were correlated to muscle fibre and axon diameter. Since the described NMJ morphology was measured without matching of muscle fibre diameters, the individual muscle averages were used for each variable and correlated with the respective average muscle fibre diameter.

5.4.3.1. Muscle fibre diameter influences pre-synaptic complexity at the mammalian NMJ

Global Pearson correlation of all 18 morphometric variables with muscle fibre diameter across species showed that overall only 9/18 variables (**Table 5-3**) showed a linear relationship with muscle fibre diameter (MFD). Muscle fibre diameter showed a strong correlation with variables associated with pre-synaptic branching (Appendix – **Figure 8-3**). The larger the muscle fibre diameter, the more terminal branches and branch points one could expect globally at the mammalian NMJ. This also implied that with an increase in muscle fibre diameter the complexity of NMJs increased; however, the average length of branches decreased (Appendix – **Figure 8-4**, **Table 5-3**). Since Coers and Woolf, 1959 and Deschenes *et al.,* 2006 demonstrated that hypertrophic muscle presents with more complex NMJs, this data suggests that this mechanism linking pre-synaptic morphology and muscle prevails generally across mammalian muscles.

Between species correlation coefficients (r) of MFD with post-synaptic variables were much lower. Within species, mouse and cat showed no relationship with muscle fibre diameter in any of the 18 variables, whilst the sheep and pig correlated most strongly in NMJ size related variables.

Table 5-3: Correlation of NMJ variables with muscle fibre diameter

	Mouse (r) N = 3, n = 24 960 NMJs	Cat (r) N = 3, n = 12 465 NMJs	Dog (r) N = 3, n = 9 341 NMJs	Sheep (r) N = 3, n = 9 313 NMJs	Pig (r) N = 3, n = 9 446 NMJs	Human (r) N = 21, n = 9 2,860 NMJs	Pony (r) N = 5, n = 15 578 NMJs	Global Correlation with MFD (r)
Core variables								
pre-synaptic								
1) *Nerve Terminal Area (µm²)*	0.099	0.11	-0.31	0.56	0.81**	0.36**	0.65**	-0.15
2) *Nerve Terminal Perimeter (µm)*	0.27	-0.0048	-0.37	0.43	0.76*	0.41**	0.69**	0.13
3) *Number of Terminal Branches*	0.11	0.22	0.81**	-0.21	0.55	0.40**	0.57*	0.60****
4) *Number of Branch Points*	0.12	0.14	0.75*	0.32	-0.29	0.16	0.85****	0.47****
5) *Total Length of Branches (µm)*	0.0011	0.24	0.94***	0.47	-0.52	0.32*	0.80***	0.10
post-synaptic								
6) *AChR Area (µm²)*	0.076	-0.39	-0.36	0.76*	0.86**	0.39***	0.80***	-0.091
7) *AChR Perimeter (µm)*	0.38	-0.24	-0.24	0.42	0.47	0.30*	0.70**	0.28***
8) *Endplate Area (µm²)*	0.16	-0.15	-0.17	0.37	0.82**	0.37**	0.70**	0.0091
9) *Endplate Perimeter (µm)*	0.060	-0.021	-0.23	-0.24	0.81**	0.37**	0.57*	0.16*
10) *Endplate Diameter (µm)*	0.069	-0.076	-0.21	-0.25	0.81**	0.34**	0.55*	0.067
11) *Number of AChR Clusters*	-0.10	0.41	0.68*	0.097	-0.29	0.051	-0.39	0.14
Derived variables								
pre-synaptic								
12) *Average Length of Branches (µm)*	-0.25	0.057	-0.27	0.35	-0.77*	-0.15	0.34	-0.57****
13) *Complexity*	0.12	0.26	0.85**	0.19	-0.018	0.33*	0.75**	0.39****
post-synaptic								
14) *Average Area of AChR Clusters (µm²)*	-0.10	-0.17	-0.28	0.68*	-0.34	0.31**	0.67**	-0.24**
15) *Fragmentation*	0.037	0.52	0.72*	0.047	-0.23	0.070	-0.55*	0.15
16) *Compactness (%)*	0.11	-0.25	-0.65	0.61	-0.52	-0.027	0.27	-0.32****
17) *Overlap (%)*	-0.13	0.0040	-0.43	0.26	-0.67*	-0.16	-0.096	0.30***
18) *Area of Synaptic Contact (µm²)*	0.15	-0.080	0.68*	0.61	0.81**	0.37**	0.82***	-0.16

5/7 derived variables, and 4/11 core variables correlated significantly with muscle fibre diameter across all species. Pony and human variables showed most significant correlations overall with muscle fibre diameter. Correlation coefficients (r) are listed, and the significance level of the P-value (asterisk) determined through Pearson correlation conducted on variable averages of each muscle (n). *P < 0.05; **P < 0.01; ***P < 0.001; ****P < 0.0001; MFD = muscle fibre diameter

Table 5-4: Correlation of NMJ variables with axon diameter

	Mouse (r) N = 3, n = 24 960 NMJs	Cat (r) N = 3, n = 12 465 NMJs	Dog (r) N = 3, n = 9 341 NMJs	Sheep (r) N = 3, n = 9 313 NMJs	Pig (r) N = 3, n = 9 446 NMJs	Human (r) N = 21, n = 9 2,860 NMJs	Pony (r) N = 5, n = 15 578 NMJs	Global Correlation with AD (r)
Core variables								
pre-synaptic								
1) *Nerve Terminal Area (µm²)*	0.69***	0.24	-0.091	0.72*	0.067	0.55****	-0.21	0.78****
2) *Nerve Terminal Perimeter (µm)*	0.43*	0.14	-0.093	0.56	-0.19	0.44**	-0.35	0.60****
3) *Number of Terminal Branches*	0.22	0.12	-0.38	-0.10	-0.088	0.24	-0.22	-0.0803
4) *Number of Branch Points*	0.18	0.070	-0.36	0.30	0.087	0.45***	-0.35	0.13
5) *Total Length of Branches (µm)*	0.23	0.37	-0.20	0.57	0.13	0.53****	-0.40	0.62****
post-synaptic								
6) *AChR Area (µm²)*	0.57**	-0.13	-0.16	0.49	0.036	0.33*	-0.59*	0.68****
7) *AChR Perimeter (µm)*	0.28	0.29	-0.23	0.19	-0.34	0.18	-0.52*	0.33***
8) *Endplate Area (µm²)*	0.51*	0.051	-0.17	0.81**	-0.13	0.30*	-0.49	0.59****
9) *Endplate Perimeter (µm)*	0.52**	0.31	-0.25	0.49	-0.17	0.36**	-0.42	-0.094
10) *Endplate Diameter (µm)*	0.42*	0.36	-0.25	0.36	-0.13	0.35*	-0.43	0.33****
11) *Number of AChR Clusters*	0.17	0.30	-0.21	0.14	-0.44	0.14	0.58*	-0.26**
Derived variables								
pre-synaptic								
12) *Average Length of Branches (µm)*	-0.10	0.20	0.39	0.53	0.16	0.52****	-0.19	0.75****
13) *Complexity*	0.24	0.30	-0.35	0.18	0.091	0.43**	-0.37	0.34****
post-synaptic								
14) *Average Area of AChR Clusters (µm²)*	0.17	0.079	0.66	0.12	0.58	0.20	-0.67**	0.80****
15) *Fragmentation*	0.077	0.63*	-0.11	0.22	-0.32	0.26	0.58*	-0.31***
16) *Compactness (%)*	0.38	-0.15	0.54	-0.048	0.47	-0.0088	-0.055	0.16
17) *Overlap (%)*	-0.23	-0.079	0.38	0.69*	0.14	0.41**	0.45	0.50***
18) *Area of Synaptic Contact (µm²)*	0.66***	-0.059	0.23	0.60	0.083	0.46***	-0.47	0.78****

6/7 derived variables, and 8/11 core variables correlated significantly with muscle fibre diameter across all species. Human and mouse variables showed most significant correlations with axon diameter. Correlation coefficients (r) are listed, and the significance level of the P-value (asterisk) determined through Pearson correlation conducted on variable averages of each muscle (n). *P < 0.05; **P < 0.01; ***P < 0.001; ****P < 0.0001; AD = axon diameter

The dog positively correlated with nerve terminal branching and endplate variables that were associated with fragmentation and contact between pre- and post-synapse. Human and pony NMJs correlated the most with MFD, in 12/18 and 14/18 variables, respectively. Overall size variables seemed to correlate positively with MFD, more strongly in pony than the human. Furthermore, branching associated parameters correlated strongly with MFD in pony, suggesting that the larger the MFD, the more complex the pony NMJ; again supporting the previous observations on hypertrophy by Coers and Woolf 1959, and Deschenes *et al.,* 2006. Additionally, fragmentation of the pony NMJ decreased with increasing MFD (**Table 5-3**).Whilst muscle fibre diameter seemed to influence NMJ morphology within some species (and in particular some pre-synaptic variables) it did not seem to represent a strong determinant of overall NMJ size across species. However, muscle fibre diameter was seen to have a global influence on nerve terminal branching and complexity. The larger the muscle fibre, the more complex the branching of the nerve terminal (**Figure 5-6.A–B**).

5.4.3.2. Axon diameter influences the size of the mammalian NMJ pre- and post-synaptically

To further evaluate whether the pre-synaptic cell is a predictor of NMJ morphology across species, global Pearson correlation of all 18 morphometric variables with axon diameter was conducted, demonstrating that overall, 14/18 variables (**Table 5-4**) had linear relationship with axon diameter (AD). Since previous correlation with muscle fibre diameter suggested a global correlation across mammals with complexity (increase in MFD prompts increase in complexity) (Appendix – **Figure 8-3.G**) correlation of complexity associated variables with axon diameter was the first relationships of interest. No such linear relationship was observed across mammals in correlation with axon diameter (Appendix – **Figure 8-5.G**). Whilst NMJs did not appear to be more branched with increasing axon diameter across species, NMJ size related variables seemed to have a relationship with size of axon diameter. With a larger axon diameter, NMJs presented with a larger nerve terminal area and nerve terminal perimeter

(Appendix – **Figure 8-5.A–B**). Likewise, an increase in both total length and average length of branches correlated positively with axon diameter. This is intuitive, as an increase in nerve terminal area is coupled with an increase in axon diameter, and NMJs do not appear to increase in complexity (get more branch points) (Appendix Chapter 4 – **Figure 8-5.C–D**, **G**) upon increase in nerve terminal area/axon diameter. In simple terms, the nerve terminal is 'stretched' with an increase of axon diameter; subsequently, both the total length and average length of branches increases (Appendix Chapter 4 – **Figure 8-5.E–F**). In comparison, when muscle fibre diameter increases, overall branch length and complexity increase in order to cater for the increased functional demand of the muscle fibre (Deschenes, Tenny and Wilson, 2006).

Despite considerable global correlation of post-synaptic variables across species (Appendix – **Figure 8-6**), only variables associated with post-synaptic areas correlated positively with axon diameter. Thus, with a larger axon diameter, a larger AChR area, endplate area, average area of AChR clusters and area of synaptic contact is to be expected. It can therefore be assumed that whilst pre-synaptic size variables such as nerve terminal area scale with an increase in axon diameter, post-synaptically associated areas do also. This is in keeping with previous studies suggesting that neurotransmitter release affects nerve terminal (Kuno, Turkanis and Weakly, 1971) and motor endplate size (Harris and Ribchester, 1979) in frog and mouse respectively.

It is interesting to note that axon diameter demonstrated the greatest correlation in humans (12/18, mostly NMJ size and branching related variables) similar to variables correlating with MFD. Mouse on the other hand only correlated in 7/18 variables (all NMJ size/area related variables) with axon diameter, again demonstrating the stark differences compared to the human NMJ. Generally, when assessing **Table 5-4** (Appendix – **Figure 8-5** and **Figure 8-6**) it can be seen that axon diameter seems to influence mammalian NMJ size on a pre- and post-synaptic level (**Figure 5-6.C–D**).

5.4.3.3. Motor unit type as an influencing factor on NMJ-morphology

In addition, to the influence that synaptic transmitter release exerts on nerve terminal and endplate size (Kuno, Turkanis and Weakly, 1971; Harris and Ribchester, 1979), as well as the correlation between muscle hypertrophy, nerve terminal branching, and muscle atrophy induced decline in NMJs size (Coers and Woolf, 1959; Deschenes, Tenny and Wilson, 2006) there is also a proposed dependency of NMJ morphology on motor unit/muscle fibre type (Mantilla and Sieck, 2003). Fast-fatigue motor units are comprised of larger muscle fibres, larger motor nerves, and larger and more complex NMJs; slow motor units are comprised of smaller muscle fibres, smaller motor nerves, and smaller and less complex NMJs.

Whilst direct comparison of NMJs and their corresponding muscle fibres is not possible (excluding judgements of NMJ size/branching in relation to muscle fibre/motor unit type) it is still possible to construct hypotheses from the correlation data. For example, *soleus* is primarily a slow-twitch muscle across mammals, which has previously been shown in several studies [a five mammal comparison (Ariano, Armstrong and Edgerton, 1973), analysis of cat *soleus* (Burke *et al.*, 1974) and in humans (Gollnick *et al.*, 1974)] and approximately a third of all muscles should correlate accordingly. Since correlation with muscle fibre type is purely speculative, none was undertaken. However, future experiments recommendations might include muscle fibre typing and direct measurements of muscle fibre diameter on confocal images of the NMJ.

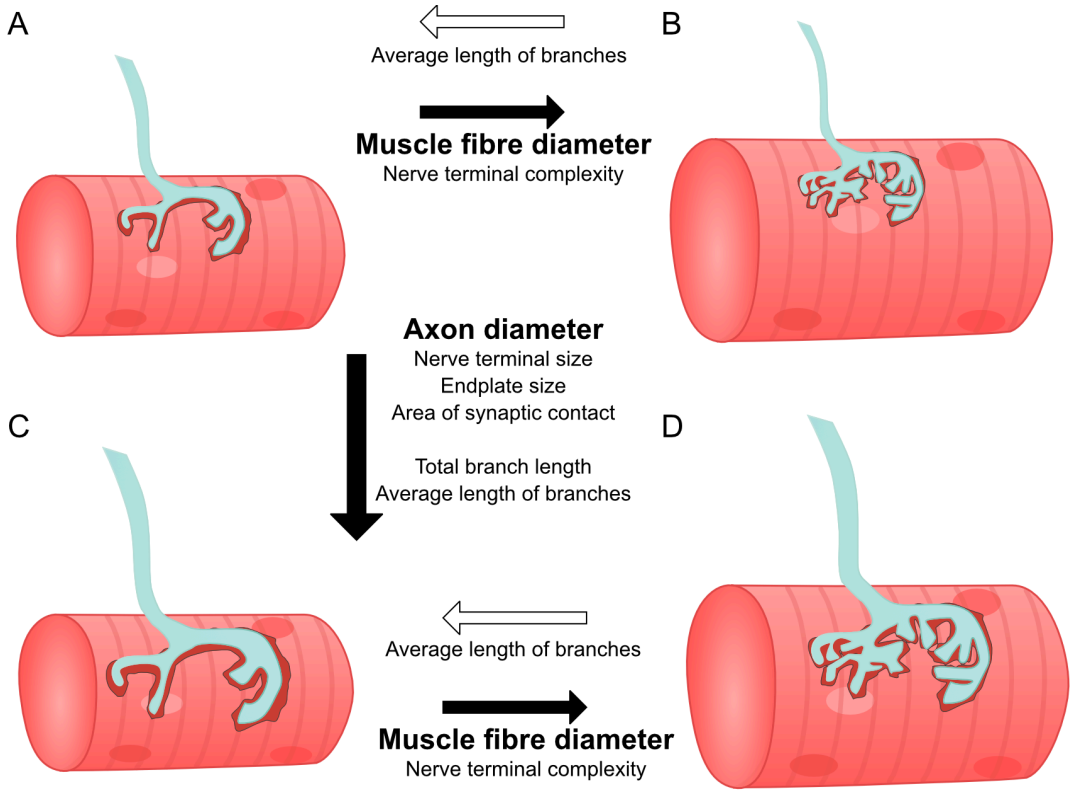

Figure 5-6: Schematic of the correlation between muscle fibre diameter, axon diameter and mammalian NMJ morphology

(A) The muscle fibre (striated red cyclinder) innervated by a simple motor nerve (cyan). In dark red, underneath the motor nerve terminal is the opposing motor endplate. Red oval patches within the muscle fibre represent myonuclei, the lightest 'patch' represents a sub-synaptic nucleus. (A) is a prime example of what would be considered slow motor unit innervation. Small muscle fibres, thin axon diameters, small and simple NMJs.

(B) Upon increase of the muscle fibre diameter, from A to B, (solid black triangle), the complexity of nerve terminal branching increases as well, whilst the average length of branches decreases (white triangle with black border).

(C) Upon increase of the axon diameter, from A to C, (solid horizontal triangle), all NMJ associated areas increase, as well as total branch length and average length of branches.

(D) Larger axon diameter and larger muscle fibre diameter as opposed to A, from A to D, would predict an increase in nerve terminal complexity as in (B), as well as larger overall NMJ areas as per (C). (D) is a prime example of what would be considered fast-fatigue motor unit innervation. Large muscle fibres, large axon diameters, large and complex NMJs.

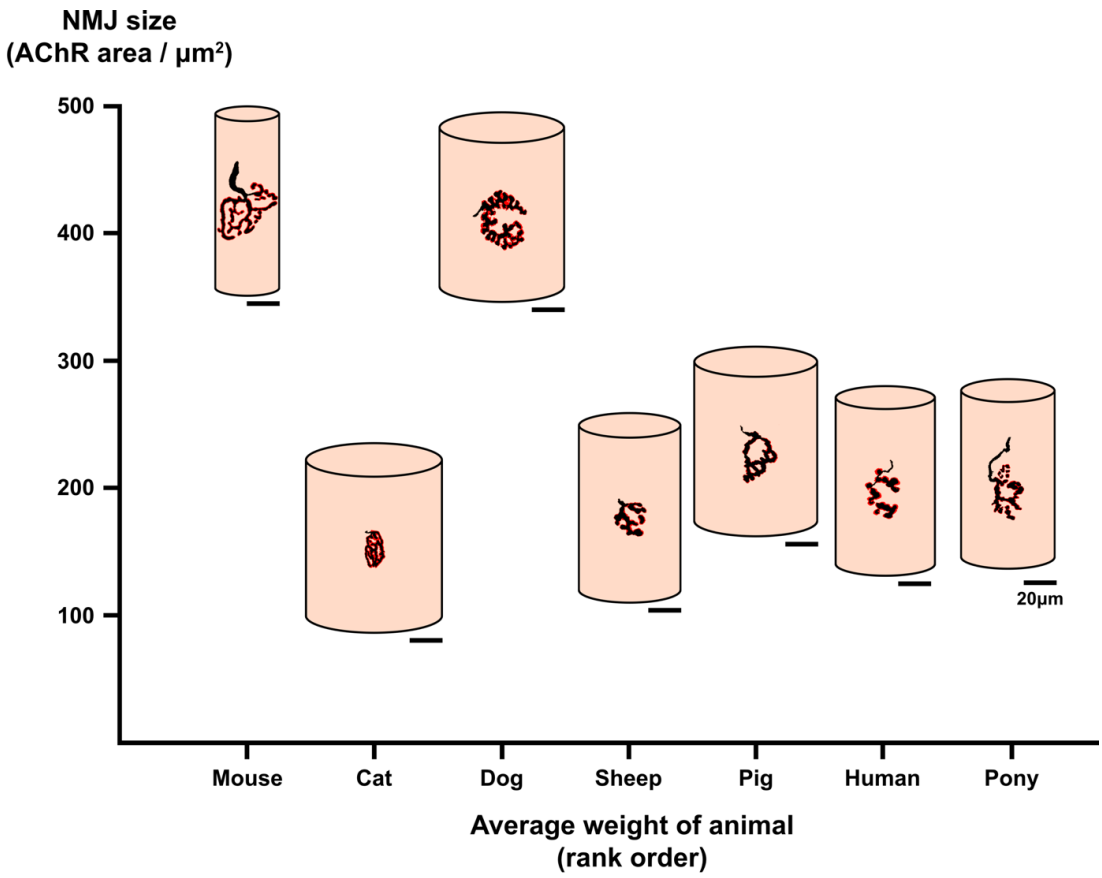

Figure 5-7: Schematic overview of the relationship between average NMJ morphology, muscle fibre diameter and body weight.

The y-axis depicts average AChR area of all species, taken from **Table 5-2**, whilst the x-axis depicts animals in ascending order of body weight, as per **Table 5-1**. Keep in mind that sheep and pig have almost the same average body weights. The cylinder represents the average muscle fibre diameter for each species: scale bar = 20 µm.

No clear correlation can be drawn between body size/weight, NMJ size and muscle fibre diameter. The largest contrast is between the two smallest animals, the mouse with the largest AChR area on the smallest muscle fibres, and the cat with the smallest NMJs on the largest muscle fibres. All larger mammalian species, that were closer in body weight to the human, this includes the pony despite its considerable larger body weight, were more similar to human, than species of smaller body weight. The ratio between NMJ size and muscle fibre diameter might be specific for each species or coupled to muscle composition. Image adapted from (Boehm, Alhindi, *et al.*, 2020).

However, the anatomical relationship between motor unit size, muscle fibre size and NMJ morphology was outlined beautifully in Mantilla *et al.,* 2003 and corresponds with the muscle fibre diameter and axon diameter correlations described here. In the example of a fast-fatigue motor unit consisting of larger muscle fibres, according to mammalian correlation data, larger muscle fibres correspond to more complex nerve terminals, and thus the fast-fatigue motor unit would present with a more complex NMJ. Additionally, fast-fatigue motor units have larger motor neuron cell bodies and larger innervating axons. According to the mammalian correlation data presented here, larger axon diameters correspond to larger NMJs, and thus fast-fatigue motor units would present with larger NMJs (**Figure 5-6.D**). A similar principle should apply for slow motor units (**Figure 5-6.A**).

5.4.4. Body size and muscle fibre diameter are no direct predictor of endplate size across larger mammalian models

Given that muscle fibre diameter does not determine NMJ size, the next question aimed to address whether body size of animals influenced NMJ size or muscle fibre diameter. Whilst an inverse correlation between body weight and NMJ size has been suggested, mouse and rat (which have almost identical NMJ morphology) and the human (no correlation between NMJ and body size was shown, Jones *et al.*, 2017) are at the opposite ends of the spectrum in regard to body size.

To further assess this relationship, mammalian NMJ morphology of intermediate body size (cat and dog), similar body size (sheep and pig) and larger body size (pony) than the human were analysed. To do so, a diagram was constructed depicting the relationship between average body size, AChR area and MFD across the seven mammals analysed. No clear correlations could be drawn between muscle fibre diameter, body size and average NMJ size (here defined as AChR area; **Figure 5-7**). As discussed in 5.4.3.1 (Muscle fibre diameter influences pre-synaptic complexity at the mammalian NMJ) NMJ size and muscle fibre diameter might have a species-

dependent relationship. On the other hand, Anzenbacher *et al*, 1963, compared a variety of muscles across three different species and concluded that the relationship of nerve terminal area with muscle fibre diameter is more dependent on the physiological property of muscle fibres than species. It is therefore possible, that this relationship is dictated by motor unit type as suggested by various other studies (Coers and Woolf, 1959; Anzenbacher and Zenker, 1963; Oda, 1985). This would suggest, that motor neuron identity most likely regulates NMJ size across mammals as per 5.4.3.2 (Axon diameter influences mammalian NMJ size) which has previously been proposed by (Jones *et al.*, 2016, 2017) given the more prominent correlations of motor neuron with NMJ variables than with muscle.

5.5. Conclusion

1) Interspecies heterogeneity is more pronounced than within species heterogeneity

2) Phylogenetic distance (time between evolutionary divergence of species) does not correspond to differences in pre- or post-synaptic morphology across species

3) Larger muscle fibre diameter is associated with more complex and branched nerve terminals. Larger axon diameter is associated with larger NMJs. The motor neuron influences pre- and post-synaptic NMJ size in mammals.

4) Neither body size, nor muscle fibre diameter influence acetylcholine receptor area (or overall NMJ size) across mammals.

The necessity to find more appropriate animal models of human diseases has become increasingly important in for example the field of motor neuron diseases. Here the emergence of newly genetically modified rodent models has proven beneficial in the rapid development of therapeutics that alleviate disease phenotype within models, but which translate poorly to the human (Mitsumoto, Brooks and Silani, 2014; Philips and Rothstein, 2015; Tosolini

and Sleigh, 2017). Whilst rodent models are the most common disease models used (Ellenbroek and Youn, 2016) the translation of such research remains difficult; additionally, experimental design of preclinical studies and appropriate characterisation of new rodent models play an important role (Willmann *et al.*, 2020). In an effort to find mammalian species with NMJ morphology that more closely resembles the human NMJ, a morphological baseline of larger mammalian NMJs was generated.

Broad interspecies heterogeneity was noted when comparing six species of different body size to the human: mouse, cat, dog, sheep, pig, and pony. Mammals of smaller body size were more different to mammals of larger body size (in particular the human) but with no relation to body size (**Figure 5-7**). Whilst dog and mouse NMJs, which have the largest overall NMJs, were the most distinct from the human (and all others) these were also the most similar to each other. Previous studies using canine models of Duchenne muscular dystrophy showed identical response of the large dog NMJ to muscle dystrophy (onset of fragmentation and denervation) as the rodent NMJ (Haddix *et al.*, 2018).

Overall, the cat overall has the smallest and most complex NMJ innervating the largest muscle fibres. This is in contrast to the smallest species, the mouse, which has the largest AChR areas, innervating the smallest muscle fibres. Sheep, pig and pony are remarkably similar to the human NMJ in overall NMJ morphology.

Assessment of the phylogenetic tree of these species shows that time between evolutionary divergence does not correspond to differences in pre- or post-synaptic morphology across species. Evaluation of the influence of pre- and post-synaptic cells on NMJ morphology allows further analysis of species-specific influence of particular cell-types and their influence on overall mammalian NMJ morphology. This demonstrates that the ratio between NMJ size and muscle fibre diameter is species-specific, whilst the motor neuron has a direct relationship with NMJ size in mammals. Muscle fibre diameter itself influences the extent of branching of the mammalian

nerve terminal. Therefore, taken in the context of pre- and post-synaptic cell dependency, global mammalian NMJ morphology can be reduced into two descriptive groups: overall NMJ size, and complexity of nerve terminal branching. In general, larger muscle fibres have more complex nerve terminal branching, and NMJs with larger axon diameters have larger NMJs (**Figure 5-6**). The only exception is the pony where larger axon diameters correlate with smaller NMJs, which might prove disadvantageous when trying to model human diseases. Taken together, this information sheds light on evolutionary conserved and species-specific NMJ morphology across mammals.

Overall, this data suggests that despite the close morphological similarity between humans and ponies, sheep and pigs might be more suitable as animal models of neurodegenerative diseases. Mini pigs are already being used as large animal models for Spinal Muscular Atrophy (Lorson *et al.*, 2011; Duque *et al.*, 2015), models for Alzheimer's, Huntington's and Parkinson's disease, as well as models of Amyotrophic Lateral Sclerosis (Holm, Alstrup and Luo, 2016). Studies using mammals for disruption of the blood-brain barrier for therapeutic delivery show that pig and sheep are the most similar to the human in brain mass and skull thickness, with the sheep being slightly more similar to the human (Pelekanos *et al.*, 2018).

Preliminary analysis of cognitive capacity in sheep led to the assumption that they might be a suitable alternative to non-human primate models of neurodegenerative diseases (McBride and Morton, 2018). Since the sheep sampled in this study have a more similar muscle fibre diameter to the human compared to the pig, this might make the sheep an attractive model for future experiments, such as evaluation of development and ageing of the neuromuscular system. Furthermore, this data supports their current use as models of neurodegenerative conditions such as Batten disease, a lysosomal storage disorder with childhood onset (Amorim *et al.*, 2015; Eaton and Wishart, 2017).

6. The human NMJ-enriched ageing proteome is more stable than that of NMJ-devoid surrounding muscle

6.1. Chapter summary

Whilst previous chapters outlined the need for better models of the human NMJ (Chapter 5) they did not cover mechanisms that occur at the human NMJ. Should we want to create better models of human diseases, we need to first understand what mechanisms underly human diseases such as the ageing related loss of muscle mass – sarcopenia. Sarcopenia is characterised by low muscle strength, loss of muscle mass and frailty. To date there are no effective treatment options available and the increase in lifespan of our ageing population and the associated required palliative care represent a substantial global economic burden. The marked difference between the rodent and human NMJ has previously been highlighted in health and disease (see Background and Chapter 4); however, in order to find appropriate therapies for the human condition it is necessary to understand what intrinsic molecular changes occur at the level of the human neuromuscular proteome during normal ageing. This chapter assesses the human muscle (NMJ-devoid) and NMJ-enriched proteome using gel-free, label-free mass spectrometry across the adult lifespan (40s–80s). Subjects were representatively grouped into Middle-aged (40s–50s), Senior (60s) and

Old (70s–80s), which allows the mapping of the ageing human muscle and NMJ-enriched proteome and the assessment of changes that occur within each of the two tissues.

Human muscle demonstrates defects in oxidative phosphorylation and is proposed to be within a state of insulin resistance, which has been shown in previous proteomic studies of human muscle. The human NMJ-enriched proteome is more stable than muscle, with fewer differentially expressed proteins and fewer changes in oxidative phosphorylation. It is predicted to be in a more insulin sensitive state than muscle, which could potentially be protective and prevent gross morphological changes.

6.2. Background

Sarcopenia is the age-related loss of muscle mass and function and is considered a global key research priority primarily due to the increasing life expectancy of our global population (WHO, 2011, 2017; Cruz-Jentoft *et al.*, 2019). As of 2016, the overall estimate of prevalence for sarcopenia was 10% for both males and females within our ageing population, which has an extensive impact on our global healthcare system due to the ever increasing associated healthcare costs (Shafiee *et al.*, 2017; Bruyère *et al.*, 2019). Sarcopenia progressively affects muscle and leads to an increase in morbidity and risk of injury, which seriously impacts the quality of life and increases mortality (Cruz-Jentoft *et al.*, 2019). To date, many mechanisms have been described that contribute to neuromuscular ageing, such as oxidative stress, inflammation and in particular mitochondrial dysfunction (Short *et al.*, 2005; Dalle, Rossmeislova and Koppo, 2017). Despite understanding some of the mechanisms that govern muscle homeostasis under acute perturbations (i.e. muscle atrophy and hypertrophy) and some of the mechanisms that lead to e.g. anabolic resistance (the inability of the muscle to increase protein synthesis in response to anabolic stimuli such as exercise and nutrition; Phillips, Hill and Atherton, 2012) the full spectrum of cellular and molecular mechanisms behind this age-related decline in muscle mass and function remains unkown. The pathophysiological complexity of sarcopenia in humans has made it challenging to study and develop 'one-size-fits-all' treatments. Additionally, mechanistic studies of muscle wasting and the functional decline that is associated with ageing are difficult to conduct on humans. For this reason, our current state of knowledge is primarily derived from experiments conducted on rodents in vivo and cell culture experiments in vitro (Tintignac, H. R. Brenner and Rüegg, 2015; Dolly, Dumas and Servais, 2020).

The NMJ has been thought to play a pivotal role during this ageing associated loss of function. NMJ dismantling in ageing rodents has therefore

been examined in detail, in particular since denervation and NMJ perturbations have been widely associated with muscle atrophy, injury, and subsequently sarcopenia (Tintignac, H.-R. Brenner and Rüegg, 2015; Taetzsch and Valdez, 2018). Structural alterations at the rodent NMJ, i.e. the increase in fragmentation of the motor endplate has widely been correlated with sarcopenia and ageing (Deschenes *et al.*, 2010; Valdez *et al.*, 2010; Taetzsch and Valdez, 2018). Generally speaking, in mice, both ageing and injury promote morphological hallmarks of NMJ instability, including the aforementioned endplate fragmentation (Li, Lee and Thompson, 2011). In contrast, and despite electrophysiological signs of NMJ transmission instability, such as increase in jiggle (used to describe the shape of motor unit action potentials) of motor unit potentials (Piasecki *et al.*, 2016), human NMJ morphology remains stable during ageing (Jones *et al.*, 2017), traumatic nerve injury (Gupta *et al.*, 2020) and cancer cachexia (Boehm *et al.*, 2020, Chapter 4).

It is currently unclear whether more 'stable/active' compensatory mechanisms govern neuromuscular plasticity, or whether their increased endplate fragmentation masks ageing related changes. For more successful translation of pre-clinical work of rodent models into treatments for human diseases, it is imperative that we deepen our understanding of the mechanisms that occur at the healthy ageing human NMJ. To unravel some of these mechanisms, the aim of this chapter was to:

1) Establish the extent to which NMJ-devoid muscle and NMJ-enriched proteome are similar
2) Assess whether the overall muscle proteome has characteristics of a muscle proteome similar to those previously published in literature
3) Identify changes that occur within the ageing muscle: Are these changes similar to what has been reported in literature?
4) Identify changes that occur at the ageing NMJ-enriched proteome

6.3. Methods

6.3.1. Ethical Approval and patient recruitment

To address whether molecular changes at the muscle or NMJ-enriched specimen occurred during 'healthy' human ageing, muscle biopsies from *peroneus longus* were obtained from subjects following lower limb amputation (**N = 12**). Only subjects over the age of 18 years were approached who had to provide written and informed consent before surgery. Consent was obtained by vascular surgeon Rachael O. Forsythe (University of Edinburgh Centre for Cardiovascular Science). No exclusion criteria were specified. Study approval was obtained from the NHS Lothian Research Ethics Committee (2002/R/OST/02) and was conducted in accordance with the Declaration of Helsinki.

A total of twelve patients were recruited, 6 underwent below-knee amputation (BKA) and 6 underwent above-knee amputation (AKA). Subjects were aged between 42–85 years, the youngest 42-year-old patient was a black male. Two out of the twelve subjects were female. Clinical details and patient demographics are summarised in **Table 6-1**. Patients were categories into three age groups, to examine any changes across the adult lifespan in a stratified manner: **40s–50s (Middle-aged, N = 4)**, **60s (Senior, N = 3)**, **70s–80s (Old, N = 5)** (**Figure 6-1.A**).

6.3.2. Tissue sampling and processing

Full length *peroneus longus* was sampled immediately after disconnection of the limb from the most proximal end of the amputation side as previously outlined in Chapter 2 (General Methods).

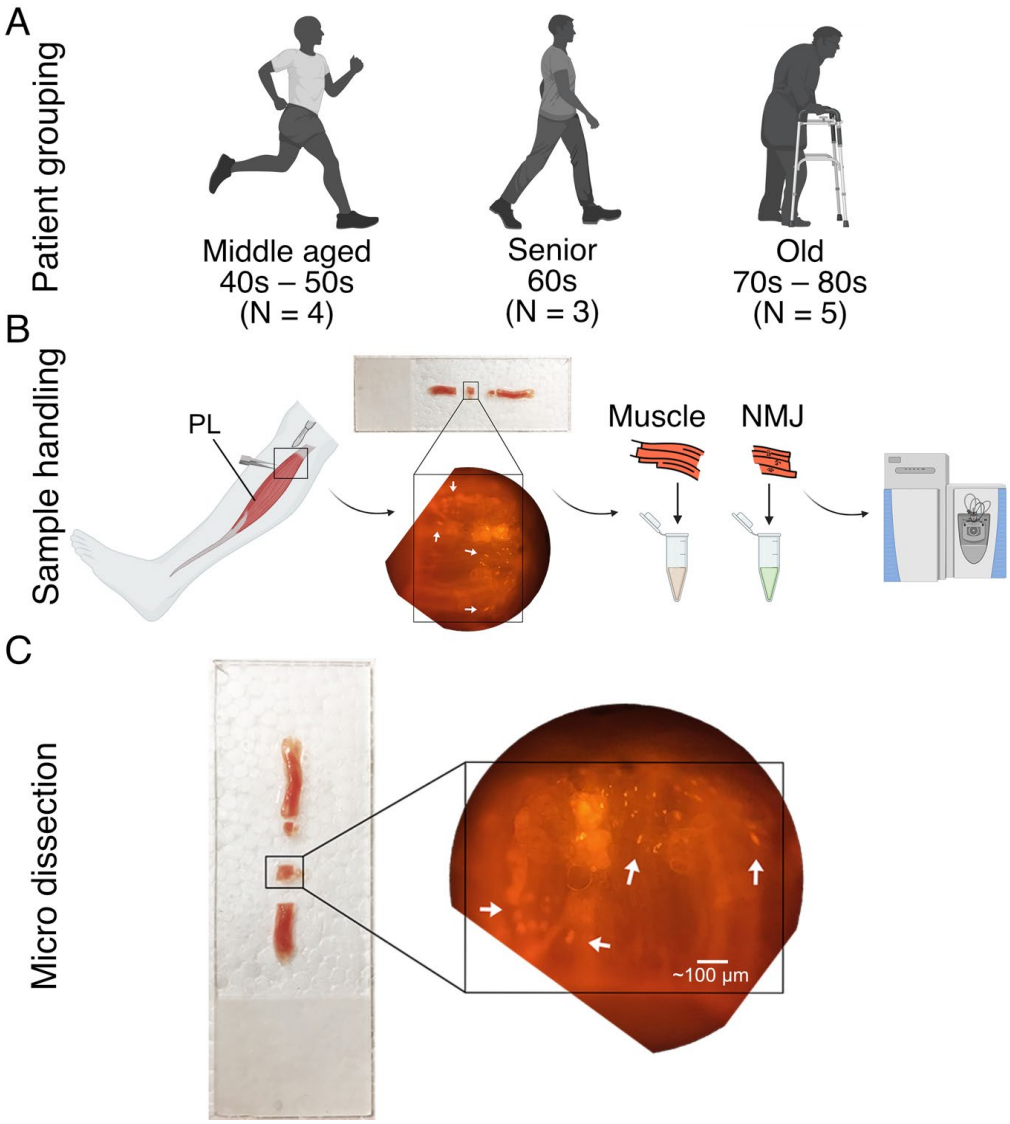

Figure 6-1: Experimental design for the characterization of the human ageing proteome

(A) Illustration of patient grouping into 40s–50s (Middle aged, N = 4), 60s (Senior, N = 3) and 70s–80s (Old, N = 5). Only one patient was each aged in their 40s and 80s.

(B) Schematic depiction of the overall workflow from sample collection (*peroneus longus*) in theatre, to micro dissection of separated muscle fibres under a fluorescent microscope, division of muscle (NMJ-devoid) and NMJ-enriched samples, through to proteomic processing.

(C) Enlarged view of micro dissection. A muscle fibre bundle is visible on a microscope slide which has been laid on top of a Styrofoam box for better contrast. The muscle fibre bundle has been cut into four sections, the second from the bottom (black border) containing the endplate band. Initially the much smaller 'section' (now disconnected above the section enclosed in the black border) was attached to the endplate band within the black border. Upon closer visual inspection of endplate bands and their boundaries, the smaller 'section' was trimmed off, leaving 'enriched' NMJ section. *Legend continues on next page.*

Figure 6-1 legend continued from previous page:
See the enlargement of the black border muscle section as an example - white arrows point to NMJs. This enlarged section depicts the NMJ-enriched section. This process was repeated for every muscle fibre bundle. Scale bar = ~100 µm

This was to ensure that sampling occurred at a point closest to where stump healing would be considered most effective, and where tissue is considered 'healthy' in comparison to diseased distal tissue necessitating the amputation. Indications for amputation are typically limb ischemia (ulcers, diabetic foot, gangrene); to facilitate healing of the stump post-surgery, sufficient healthy tissue must be included in the myocutaneous flaps which form the stump (Sexton and Fleming, 2006). Additionally, the 'health' of the tissue was assessed visually by colour (intense red colour of muscle) and good back-bleeding of the tissue, and does not include muscle with excessive fibrosis or fat infiltration.

Full length muscle fibres were instantly transferred into ice cold 1xPBS and were kept on wet ice during transport from theatre to laboratory in order to slow protein degradation as much as possible. Subsequent tissue processing was fully undertaken on Sylgard dishes (ø ≤ 3 cm) placed on packed wet ice within a small Styrofoam box. Muscle fibres were 'rough' dissected into smaller fibre bundles (unfixed muscle fibres almost tended to 'peel' off in layers) and subsequently a 2 µg/mL TRITC α-BTX solution was poured over the separated muscle fibres and incubated for 5 min to visualise acetylcholine receptors. Labelling of AChRs was undertaken with closed Styrofoam box lid which prevented bleaching of fluorophores and facilitated overall visualisation of endplate bands. Following AChR labelling, TRITC α-BTX was carefully poured off and the Sylgard dish containing the muscle fibres was filled up with 1xPBS.

Table 6-1: Clinical details and patient demographics

Age (y)	Type of op.	Sex	BMI	Mobility pre-op	Comorbidities							Ethnicity	Smoker
42	BKA	M	25	Walking with crutches	Y	Y	N	N	N	N	Y	black	Current
54	AKA	M	31	Previous contralateral BKA, wheelchair bound	Y	Y	Y	Y	Y	N	Y	white	Vapes
56	BKA	M	30	Walking with crutches	Y	Y	Y	Y	N	N	N	white	Current
57	AKA	M	15	Wheelchair	N	N	N	N	N	Y	N	white	Current
63	BKA	M	21	Walking unassisted - no limitation	Y	Y	Y	Y	Y	Y	N	white	Current
64	BKA	M	24	Independent - no limitation	Y	N	N	Y	Y	N	N	white	Ex
68	AKA	F	30	Walking unassisted - no limitation	N	Y	N	N	N	N	N	white	Current
73	BKA	F	25	Limited mobility - uses zimmer frame	Y	Y	Y	N	N	N	Y	white	Non
75	AKA	M	24	Walking unassisted but very limited mobility due to severe angina	N	Y	Y	Y	Y	N	Y	white	Non
75	AKA	M	26	Independent but uses scooter out of house	N	Y	Y	Y	Y	Y	Y	white	Ex
78	BKA	M	21	Previously independent but bedbound for a few weeks prior to admission due to pain/ ulceration	N	Y	N	Y	N	N	Y	white	Ex
85	AKA	M	21	Bedbound	Y	Y	Y	Y	Y	Y	N	white	Ex
					Diabetes	**HTN**	**Hyperchol**	**IHD**	**MI**	**CVA/ TIA**	**CKD**		

Demographics and clinical details of subjects (N = 12) in ascending age are listed in detail including their mobility. Most patients were able to walk unassisted, or still move using mobility assistance prior to surgery. All patients, but two, were smokers or ex-smokers. Patients were subject to at least one comorbidity, most to more.

Abbreviations: op. = operation; AKA = above knee amputation; BKA = below knee amputation; HTN = hypertension; Hyperchol = Hypercholesterol; IHD = ischemic heart disease; MI = myocardial infarction; CVA = cerebrovascular accident; TIA = transient ischemic attack; CKD = chronic kidney disease.

To separate muscle from endplate bands, muscle fibres were micro-dissected under a Nikon Eclipse 50i fluorescence microscope ensuring that the muscle was NMJ-devoid (contained no fluorescent signal of AChRs) and NMJ-enriched samples contained endplate bands as per **Figure 6-1.B–C**. Once muscle fibres were 'trimmed'/enriched, respective parts were moved into small, labelled Eppendorf tubes on dry ice, and stored at -80°C prior to protein extraction.

6.3.3. Protein extraction

Dissected samples were thawed on wet ice and moved to M tubes (GentleMACS™ Miltenyi Biotec) with label free extraction buffer [100 mM Tris-HCl, (pH 7.6) 4% (w/v) SDS] containing 1% protease cocktail inhibitor (Thermo Fisher, UK). Samples were homogenised and lysed using the GentleMACS™ Dissociator (Miltenyi Biotec) using the "M tube protein" cycle. Following homogenisation, samples were centrifuged at 300 x g for 2 minutes and left on ice for 20 minutes, to ensure all of the homogenate is at the bottom of the tube and none is stuck to the top.

As some muscle samples had particularly large 'chunks' which had not lysed/homogenized well after the first "protein" cycle, these were dissociated, centrifuged and left on ice once more. Following the 20 minutes on ice, which allowed the foam to settle, the homogenates were transferred to Lo-Bind 1.5 mL tubes (Sigma Aldrich). These tubes are specifically designed for proteomics and have reduced surface adherence; therefore, they increase recovery of valuable proteomics samples. Muscle samples had to be left on room temperature for a short period of time to allow pipetting of samples, since their high lipid and DNA content contributed to a 'slushy'-like consistency on ice. Samples were centrifuged at 20,000 x g for 20 min at 4°C and the soluble fraction, containing desired proteins (the insoluble fraction contains mostly membrane proteins and larger organelles), was transferred to fresh Lo-Bind tubes. Protein concentration across all 24 samples (12 subjects, muscle and NMJ-enriched sample per subject) was determined

using the Bicinchoninic acid assay (BCA, Pierce, UK). Supernatant was aliquoted for proteomic processing and stored at -80°C.

6.3.4. Sample preparation for mass spectrometry

Sample preparation, desalting and single shot mass spectrometry (MS) were performed by the FingerPrints Proteomics facilities at the University of Dundee in collaboration with Douglas Lamont and Cara Rogers. The design of the protocol and its optimisation were conceptualised by the FingerPrints Proteomics facility, and the following method is included purely for clarity and transparency.

6.3.4.1. Filter aided sample preparation (FASP)

Whilst proteins have been extracted from muscle and NMJ-enriched samples up until here, various sample preparation steps are required before the samples can undergo mass spectrometry. For example: filtering and digestion of proteins into smaller 'chunks' (peptides), which are then analysed by the mass spectrometer by their molecular weight/size. The basic principle of mass spectrometry is to identify chemical compounds within a sample, which occurs through generation of so-called mass spectra. The sample is first ionised (charged), and an ion beam is generated which is subsequently deflected onto the detector by magnetic fields. The smaller the mass of an ion (i.e. the smaller the chemical compound/peptide), the less force the magnetic field needs to exert to deflect the ion. Therefore, lighter ions will be deflected more in comparison to heavier ions within the same magnetic field. Variation of this magnetic field allows to 'separate' which mass/charge (*m/z*) ratio of ions is focussed onto the detector, and the signal arriving at the detector is proportional to the abundance of ions. Peptide sequences can be mapped to these mass spectra computationally, and aid in the identification of sample composition (Han, Aslanian and Yates, 2008).

Protein samples were first thawed at room temperature, then 1/10th of the desired sample volume of 1 M Dithiothreitol (DTT) was added, to make a

final concentration of 100 mM DTT. DTT is a common reducing agent and prevents the formation of disulfide bonds between cysteine residues. As this facilitates unfolding of proteins, this aids in better sequence coverage of proteins during subsequent mass spectrometry (Gundry *et al.*, 2009).

Before separation by mass/charge ratio within the mass spectrometer is possible, the sample is first separated by its molecular weight using liquid chromatography. Since the multi-dimensional liquid chromatography (MDLC) will be performed using different buffers, a buffer exchange is required, as the current proteins contain SDS. To do so, Vivacon 500, 30k MWCO HY filters (Sartorius Stedim Biotech, VN01H22) were rinsed with ddH2O by centrifugation for 5 min at 8 rpm. These filters can take up to 500µL of liquid and have pores with a molecular weight cut-off (MWCO) of 30,000 Dalton, meaning that proteins (impurities and digested peptides) smaller than 30 kDa will pass through the membrane, and high-molecular-weight substances such as proteins or DNA will be retained by the membrane.

Samples were centrifuged briefly on a bench-top centrifuge (Eppendorf MiniSpin) and 1/10th sample and 9/10th FASP1 (8 M urea in 100 mM Tris/HCl pH 8.5) were added to the filter and centrifuged for 25 min at 8 rpm. This step was repeated until all of the sample has been processed. All sample was now bound to the membrane. The buffer at the end was discarded. To buffer exchange, filters were washed with 250 µL FASP1 and centrifuged for 25 min at 8 rpm, this was repeated 5 times. Fresh 50 mM iodoacetamide (IAA) in Tris/HCl pH 8.5 was added to the filters, just enough to cover the filter, and incubated in the dark for 10 min. Iodoacetamide facilitates alkylation of the previously reduced disulfide bonds (*Equation 5*).

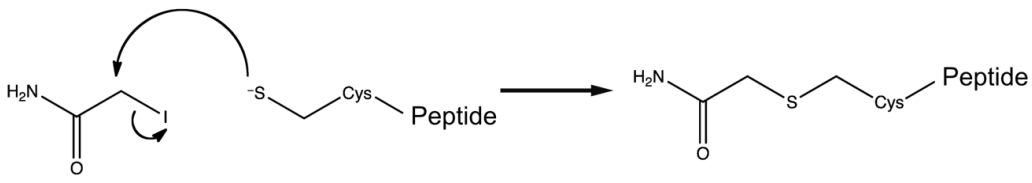

Equation 5: Alkylation of disulfide bonds. Iodoacetamide (to the left) reacts irreversibly with a reduced (S^-) peptide. This prevents generation of 'pseudo-intermolecular disulfide' bonds between peptides. Meaning peptides whose disulfide bonds were previously

broken with DTT, are not able to build disulfide bonds with each other after alkylation with iodoacetamide (Quick *et al.*, 2018).

The alkylated and buffer exchanged samples were centrifuged for 25 min at 8 rpm to remove IAA. Filters were washed with FASP1 and centrifuged as previously described three times. A final wash was conducted with 40 mM ammonium bicarbonate buffer (Ambic). The filters were moved to fresh 2 mL filter vials where the proteins were trypsin digested at 30°C for 4–6 h (fresh trypsin at a 1:200 ratio to protein, in 40 mM Ambic). After the first digestion step, more fresh trypsin was prepared, as before, and added to the filter. The proteins were incubated overnight at 30°C. Following double trypsin digestion, samples were centrifuged again, 25 min at 11 rpm, until all the sample passed through. The trypsin digestion steps 'chop' up the protein into smaller peptides, with smaller molecular weights, allowing them to finally pass through the filter. 100 µL 0.5 M NaCl was added as a final wash step and centrifuged as before and to acidify the peptides, the filtrate was combined with 15 µL 10% Trifluoroacetic acid (TFA).

6.3.4.2. Peptide desalting

Since at this stage, the desired peptides have already been double digested and were in their 'ideal' 'chopped-up' form, ready for mass spectrometry, other factors such as buffers required consideration. Since high salt concentrations are not desired in final buffers, given their potential to build-up in mass spectrometry machines, crystallise and complicate maintenance if not even ruin the HPLC columns through which the sample is being separated, it is necessary to desalt the peptide samples.

To do so, solid phase extraction cartridges (Empore-C18, Agilent Technologies 7 mm/3 mL, 12144002) were utilised and assembled in 15 mL falcon tubes. They were first cleaned using 1 M Methanol (1 mL, MeOh), centrifuged at 300 rcf for 1 min at 4°C, then 0.8 mL 0.1% TFA in 70% Acetonitril (ACN), centrifuged as above, and then 0.8 mL 0.1% TFA, and centrifuged as above. Each sample was loaded through one filter, then

centrifuged as above for 3 min. To ensure all peptides have been transferred, another 0.5 mL 0.1% TFA were added, and the vial was centrifuged as above for 3 mins. This was repeated. Filter vials were transferred to new falcon tubes and 0.6 mL of 70% ACN were added and centrifuged as above. This was repeated. All peptides were collected in the new falcon tubes and transferred to Lo-Bind Eppendorf tubes, and subsequently concentrated in a speed vac (Thermo Savant SPD131DDA) for ~6 h at 30°C.

6.3.5. Mass spectrometry

Following buffer exchange and desalting, peptides were quantified for sample loading normalisation. Samples were normalised for 0.8 µg per injection. Samples were fractionated using a ThermoFisher™ UltiMate® 3000 Proteomics multi-dimensional liquid chromatography (MDLC) system with Buffers A and B consisting of (A) Buffer A: 0.1% Formic acid (FA); and (B) Buffer B: 80% ACN, 0.1% FA. Samples were injected and washed on a C18 trap column (Acclaim PepMap 100, C18, 100 µm x 2 cm) which was equilibrated with 98% Buffer A, at a rate of 0.3 µL/min with 0.1% Trifluoroacetic acid (loading buffer), following washing of the trap column for 3 min, a wash gradient was formed with Buffer A and Buffer B as detailed in **Table 6-2**.

Table 6-2: Gradient settings for sample fractionation

Time (min)	Flow (µl/min)	% Buffer B
0	0.3	2
0	0.3	2
5	0.3	5
130	0.3	35
132	0.3	98
152	0.3	98
153	0.3	2
170	0.3	2

Peptides were first trapped on the C18 PepMap 100 column and then separated on an Easy-Spray PepMap rapid separation liquid chromatography (RSLC) C18 column (75 µm x 50 cm, Thermo Scientific).

6.3.5.1. LC-MS/MS analysis

Following separation of peptides via liquid chromatography, samples were transferred to a mass spectrometer. Analysis of peptides was performed on a Q-Exactive™ Plus Mass Spectrometer (Thermo Scientific), coupled with the previously mentioned UltiMate® 3000 MDLC (Thermo Scientific). Eluents were sprayed onto the Q-Exactive™ Plus via an Easy-Spray source at 50°C and a source voltage of 1.90 kV. This ionised/charged the peptides.

Q-Exactive™ Plus was used in data dependent acquisition mode. The full mass spectrometer methodology/scan cycle consisted of one full MS scan in positive mode (*m/z* range from 350–1600, with a maximum ion injection time of 20 ms, a resolution 70,000 and automatic gain control (AGC) target value of $1x10^6$) followed by 15 sequential-dependent MS scans (with an isolation window set to 1.4 Da, resolution at 17,500, maximum ion injection time at 100 ms and AGC $2x10^5$). The mass spectrometer was calibrated on the first day of the scans, in order to provide mass accuracy.

6.3.5.2. MaxQuant analysis

Label-free raw data were modified by Cara Rogers in MaxQuant (version 1.6.0.16) with final data manipulation in Microsoft Excel 2013. MaxQuant is a platform which is able to generate all peptide sequences present in the sample in silico and perform general normalisation of individual label-free samples, once provided with details of modifications and types of protein digestion that were conducted during sample preparation. These known modifications were listed, e.g. the reaction of reduced cysteine residues with iodoacetamide which is called carbamidomethylation (CAM). Only peptides of a minimum length of seven were included, with a maximum peptide mass of 4,600 Da, min. peptide length for unspecific search was set to 8, and max. peptide length for unspecific search was set to 25. Additionally, parameters

for false discovery rate (FDR) for peptide-spectrum match (PSM), protein match and site match were set at 0.1 for all three.

Adjustment of the false discovery rate is important as the matching process between mass spectra of peptides to their sequences can have errors. It is only logical that the more sequences are being matched, the number of false positives (false discoveries/falsely matched sequences in this case) might increase (Colquhoun, 2014). Imagine making coffee in the morning on a stove top, you put water in the bottom of your cafetiere and coffee in the top. If you make coffee once or twice, the chances of forgetting either water in the bottom or coffee in the top are low. The more often you make coffee, the larger the statistical chance that one day you might forget to put water in the bottom, and that one time the coffee will burn, the cafetiere will heat up and the plastic top and handle will melt off. Whilst during sequence matching no ‘physical’ damage occurs, false discoveries can have negative future impacts, as therapies could have been built upon these false discoveries which subsequently do not translate and would have wasted resources and time. Therefore, controlling the false discovery rate helps to have very stringent cut-offs, allowing for very few false discoveries, which could potentially also lose more real discoveries. Adjustment of the FDR to the right situation is necessary. In this case with the FDR set at 0.1, 10% of matched sequences would be the expected proportion of false discoveries, and 90% of all sequences can be sure to be ‘truly’ matched amongst peptides. This is set ‘reasonably’ high and is one of the reasons why mass spectrometry is a methodology with high accuracy and precision.

The variable peptide spectrum match (PSM) refers to the total number of identified peptide sequences or peptide spectrum matches for a given protein, the PSM can be a high value as certain peptides can be identified repeatedly.

6.3.6. Bioinformatic analysis

Following the above-described methodology and in silico analysis in MaxQuant, raw data were filtered, converted to ratios and normalised in Microscoft Excel. A schematic of the overall workflow of bioinformatic data analysis is depicted in **Figure 6-2**. Identified peptides were filtered to include only peptide candidates which were identified by ≥ 2 unique peptides for both muscle and NMJ-enriched samples. Unique peptides are peptides that are unique, as the name suggests, to only one protein of interest. This filtering approach ensures that the protein is actually present in the sample and not only a degraded peptide sequence has been recognised. Furthermore, to ensure most appropriate ratio expressions and normalisation of samples, the intensity of proteins with intensities of 0, was set to 0.5. The reason for this is, because mathematical manipulation with zero, multiplication and division of zero (exempt division by zero as this is undefined), always results in zero, therefore, calculation of ratios or normalisation of data would not be able to actually normalise or calculate ratios for these particular peptide signals.

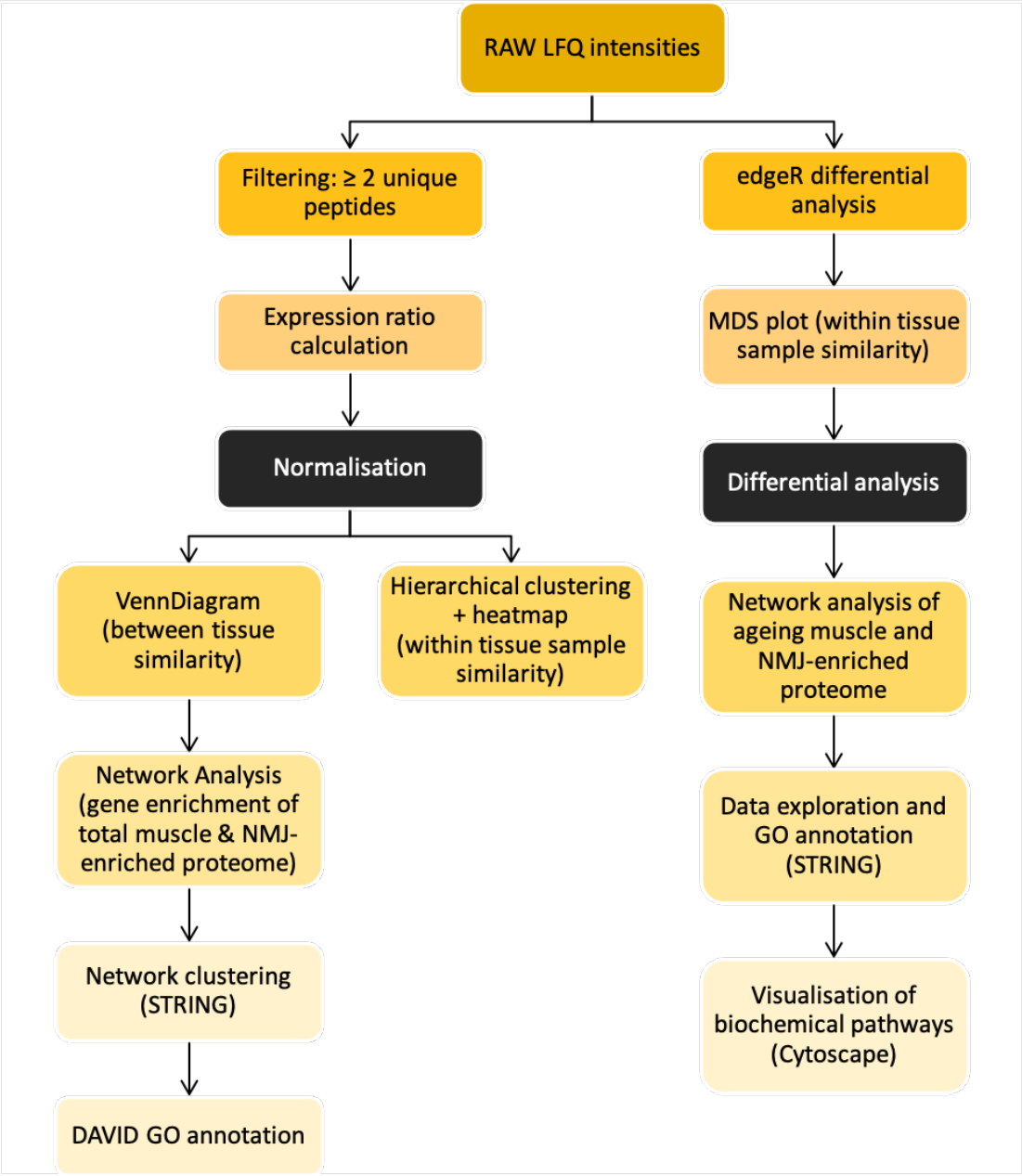

Figure 6-2: Diagram of bioinformatic workflow used in this study

First data were explored as a whole (left arm) to assess similarity between muscle and NMJ-enriched and sample similarity within a tissue. Enriched pathways within the muscle and NMJ-enriched proteome were mapped and visualised as a signalling network.

Second (right arm), differential analysis was conducted to explore changes in protein abundance with age. Sample similarity was visualised in form of a multidimensional scaling plot and differential analysis was conducted on muscle and NMJ-enriched proteome separately for Senior and Old subjects. Pathways that contributed most to age-related changes in protein abundance were listed and biochemical pathways of interest were visualised.

Since calculation of expression ratios and sample normalisation turns LFQ intensities from values in the hundred millions, into expression ratios between 0–8 or 0–10, this would lose the mathematical relationship between proteins that are not expressed at all, and proteins that are expressed at much higher levels. By choosing an intensity value of 0.5, which is many million times smaller than average label free intensities of the samples (LFQ intensities), the relationship between high and low signals remains preserved.

To calculate expression ratios, individual samples were anchored to the Middle-aged patient group. Expression ratios were calculated for all twelve patients for each muscle and NMJ-enriched sample and normalised similar to a total protein stain that is usually conducted in Western Blot practice (Huang *et al.*, 2019). Normalisation meant correction with the median intensity of each of the respective samples. Filtered, normalised data in ratio form (to Middle-aged patients) was used for most part of the subsequent bioinformatic analysis.

6.3.6.1. Analysis in Perseus

Initial statistical analysis of proteomic data were conducted in Perseus (version 1.6.15.0) (Tyanova *et al.*, 2016) on Windows 10 Pro, powered by Parallels Desktop® 15 for Mac OS X (Catalina version 10.5.7). To generate hierarchical clusters (dendrograms) from muscle and the NMJ-enriched proteome, both cleaned (.txt) data files were loaded into Perseus. Categorical annotations, such as age groups and gender, as well as numerical annotations, such as age and BMI, were added to each matrix.

Since endplate bands are physically located within muscle tissue **Figure 6-1.C**, it was important to evaluate the similarity in identified proteins between muscle and NMJ-enriched samples. This was done using the Venn-diagram function based on matching Protein IDs. It shows proteins which are in common between tissues, and gives information about the number, what proteins are unique to each tissue, and how many. The actual Venn-diagram was constructed in RStudio (for versions and initial set up see Chapter - 2

General Methods) using the VennDiagram package (version 1.6.2) (Chen and Boutros, 2011) and the numerical results that stemmed from Perseus.

To compare within tissue similarity of samples, hierarchical clustering using Euclidean distance was performed (same principle as in Chapter 5 during construction of dendrograms) only on columns, which represent ratios of intensities of individual samples, on both muscle and NMJ-enriched samples. The options 'average linkage' with no constraints and k-means pre-processing were selected within Perseus.

6.3.6.2. Differential Expression analysis using edgeR

Differential expression analysis was conducted in RStudio, using edgeR, part of the Bioconductor package (http://bioconductor.org) (Huber *et al.*, 2015). EdgeR itself is a tool which has been developed to conduct differential expression analysis to evaluate relative changes in expression levels between groups, age-groups in this case, and yields results in logarithmic fold change (log-FC) to a 'control'/starting condition, Middle-age in this study. Since edgeR applies its own normalisation to the data, the raw intensity data post filtering was used, before the normalisation and calculation of ratios stage. A straightforward tutorial within the edgeR user guide, which included the respective code, on how to perform differential expression analysis with edgeR was followed step by step (Rueda and Pereira, 2015; Branson and Freitas, 2016; Chen *et al.*, 2020). In brief, the cleaned but raw data file containing the label-free quantitation (LFQ) intensities were loaded, and an appropriate differential gene expression list/matrix was created entailing the LFQ-intensities as the counts, and the column of gene names as the genes. EdgeR here converts values to logarithmic, base 2, counts per million (logCPM).

Whilst care was taken during sample processing to prepare all samples equally, differences in time from theatre to lab could not be avoided. Since these small differences in sample preparation can potentially affect overall expression intensity of samples, normalisation is crucial. As mentioned before during MaxQuant analysis, LFQ-intensities are already minimally

normalised within and between samples. To evaluate whether normalisation in edgeR would make a difference, data were also normalised in parallel. Evaluation of the common dispersion (normally analysed when biological replicates are present), which indicates how 'dispersed' or how much biological variation in this case the data set contains, showed that dispersion factors did not particularly change (~0.02 for both muscle and NMJ) between the original LFQ-data set and the additionally normalised dataset, thus analysis continued with the original data. According to the edgeR tutorial, a common dispersion for human gene/protein expression, which is highly biologically variable, is 0.4. Inter-sample relationship was first explored by visualisation of a 'multidimensional scaling' plot. This function basically conducts a principal component analysis in the background and reduces the dimensions, which allows the plotting of patient samples in two dimensions (x- and y-axis). The sample relationship can be explored here and whether particular samples, if they are far removed from all others, want to be considered as outliers and removed from the dataset. As no biological replicates are present, all samples were included for both tissues, which would ideally best represent biological variability in the human.

As mentioned before, a so-called dispersion factor, common dispersion, is used in edgeR. Since no biological replicates are present, the edgeR online user guide was followed (2.12 What to do if you have no replicates) and the common dispersion was set to 0.4 for both muscle and NMJ, since this has been suggested as a common value for human data. Another benefit of edgeR is its use of quasi-likelihood (QL) methods using negative binomials (NB). As sequencing or proteomics data tend to have little replicates, there is always uncertainty around the actual dispersion for expression of each protein/gene. EdgeR utilises a mathematical approach, which shares this dispersion information between genes, and 'fits' them accordingly to the dispersion trend. The fitted values are used instead of raw values for hypothesis testing within edgeR and overall this has shown to improve the statistical power of testing (Smyth, 2004). Logarithmic fold-change, P-Values, the false discovery rate, degrees of freedom and logarithmic counts per

million were calculated for all genes, for both muscle and NMJ-enriched, between the following age groups: Middle-aged vs. Senior, Middle-aged vs. Old. Plots were created for all four comparisons depicting the log-fold-change and the Average log-counts-per-million of the genes. The results spreadsheets were exported and subsequently used for network analysis.

6.3.6.3. Network Analysis using STRING and Cytoscape

To conduct network analysis and identify enrichment of gene clusters across ageing, gene names identified in the muscle and NMJ proteome were first independently searched within the STRING database (string-db.org) (Szklarczyk *et al.*, 2019). Homo sapiens was chosen as the organism and to keep the network manageable, network settings were set to 'physical network'. To cluster the respective muscle and NMJ proteome into connected networks, the kmeans clustering method was applied, deciding for 10 clusters to be a manageable cluster size. Network images were exported, exclusive of disconnected nodes, proteins that had no known pathways/connections to other proteins within the input proteome. Spreadsheets of the network clustering were exported, and gene ontology analysis was conducted on the resulting clusters. This allows to associate gene names with functional terms describing biological processes (gene ontology biological processes = GOBP), molecular function (gene ontology molecular function = GOMF) or cellular components (gene ontology cellular components = GOCC). To do this the Database for Annotation, Vizualisation and Integrated Discovery (DAVID) was used (https://david.ncifcrf.gov) (Huang, Sherman and Lempicki, 2009). Each cluster was submitted as a gene list for both muscle and NMJ (type: official gene symbol) for Homo sapiens and functional annotation clustering of gene ontology molecular function and cellular components was evaluated through assessment of enrichment scores. The higher the enrichment score, the more contribution the gene group, annotation term, or gene, has to the total gene list. Meaning, if a gene group has a large enrichment score, genes within that gene group

are involved in more enriched, or important functional roles within the submitted gene list.

To tease apart changes in functional networks following differential analysis, first the 'Proteins with Values/Ranks' tab was selected in STRING and genes were input with their logFC change. Gene Ontology of the detected functional enrichment (GOBP, GOMF and GOCC) was exported for visualisation with GraphPad Prism 9. Genes listed within functional terms with the highest enrichment scores were taken into Cytoscape (version 3.8.2) (Shannon *et al.*, 2003) and loaded using the Network STRING protein query, which matches gene names against the previously described STRING database. Fold-changes were loaded and matched to the gene names and a network was visualised, using 'continuous mapping' and logFC to determine the fill colour of the nodes. Blue represented negative fold-change and red represented positive fold-change.

6.4. Results and Discussion

Sarcopenia is a geriatric muscle disease that is characterised by low muscle strength, loss of muscle mass and subsequent decrease in physical function. It affects mobility, increases frailty and thus has a huge impact on quality of life (Cruz-Jentoft *et al.*, 2019; Larsson *et al.*, 2019). Despite our better understanding of the prevalence, key factors of molecular mechanisms contributing to sarcopenia and possibilities to provide palliative care, researchers are still only at the brink of therapy development that could halt/reverse the neuromuscular ageing process (Bruyère *et al.*, 2019). Whilst many studies have previously looked at the human muscle proteome during ageing (Ebhardt *et al.*, 2017; Ubaida-Mohien *et al.*, 2019; Johnson *et al.*, 2020), it is not known whether the human NMJ is equally (or more) susceptible on a molecular level. Studies of ageing rodents point towards susceptibility of the NMJ (Ibebunjo *et al.*, 2013), as well as studies evaluating the transmission instability at the human NMJ during ageing (Piasecki *et al.*, 2016); in contrast human NMJ morphology has shown to remain remarkably stable during ageing (Jones *et al.*, 2017).

In order to evaluate whether pathways within the NMJ proteome matched the stability of NMJ morphology observed in healthy human ageing, *peroneus longus* muscle biopsies (**N = 12**) were divided into **muscle** and **NMJ-enriched** samples using fluorescent visualisation of the endplate band and micro-dissection. Following gel-free, label-free mass spectrometry of muscle and NMJ-enriched samples from each subject, filtering and data clean up, the muscle proteome yielded a total of **728 proteins**, and the NMJ-enriched proteome **692 proteins**. Subjects were divided into three age groups for subsequent analysis: **Middle aged** (40yo–50yo), **Senior** (60yo) and **Old** (70yo–80yo).

6.4.1. Great similarity in proteins identified between the NMJ-devoid muscle and NMJ-enriched proteome, does not mean similarity in protein abundance

As the current methodology (**Figure 6-1.C**) and micro-dissection of fluorescently labelled AChRs only allows for 'enrichment' of NMJs and not for sole isolation of areas in association with only the neuromuscular junction (endplate area, nerve terminal area, synaptic junction), it is to be expected that a great proportion of the overall identified proteins will be similar across both tissues. A much smaller proportion is likely to have been uniquely identified to either muscle or NMJ-enriched samples. Whilst great similarity in the proteins identified between both tissues is expected, the expression of these proteins is likely to vary. To establish the extent to which muscle and NMJ-enriched proteome are similar, a Venn-diagram was generated in Perseus based on matching Protein IDs between both tissues.

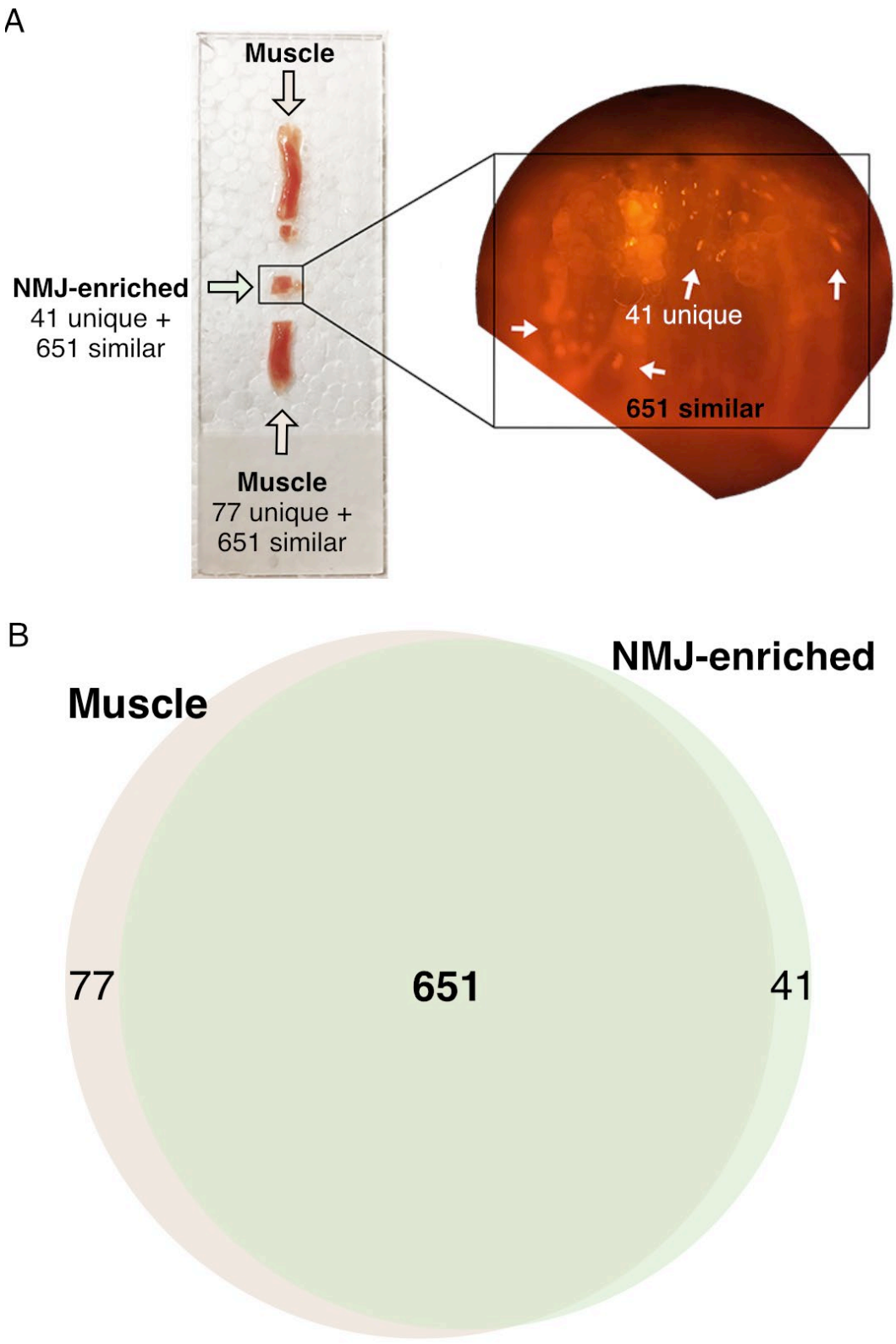

Figure 6-3: Schematic depicting the similarity in proteins identified between muscle and NMJ proteome

A total of 728 proteins were matched to muscle, and 692 proteins to the NMJ. *Legend continues on next page.*

Figure 6-3 legend continued from previous page:

(A) Visual representation of the number of unique and similar proteins that were mapped to muscle and NMJ-enriched. Unique proteins are proteins that were identified in only muscle or NMJ-enriched. Similar proteins are proteins, that were identified across both tissues. 651 of these proteins were similar and are marked in black font within the enlarged NMJ-enriched section. Proteins unique to the NMJ (41) are marked in white and are schematically illustrated to belong to NMJs (white arrows pointing at bright dots).

(B) Venn-diagram visually demonstrating the proportion of uniquely identified proteins within muscle (77) and NMJ-enriched proteome (41), as well as proteins that were mapped to both tissues (651).

This enables visual description of unique proteins for each tissue, as well as the similarity in proteome. As evident from **Figure 6-3** there is a high 89–94% similarity between the proteins (651 proteins) that were matched to the total muscle (728 proteins) and NMJ (692 proteins) proteome, respectively. The NMJ proteome constitutes ~6% unique proteins (41/692) and the muscle proteome constitutes overall ~11% unique proteins (77/728) in proportion to their shared proteome overlap. As expected, NMJ-devoid muscle and NMJ-enriched proteome show high similarity in identified proteins. Overall, one can deduce that great similarity of proteins identified within NMJ-devoid muscle and NMJ-enriched sample, but with differences in ageing-dependant enriched molecular pathways between samples would suggest spatial dependence of protein expression on location within muscle.

To further evaluate whether between tissue similarity implied that the muscle and NMJ-enriched proteome underwent similar or different changes throughout ageing, the overall similarity between patients was evaluated first within a tissue, and then molecular changes were analysed which occur in Senior and Old patients during healthy human ageing.

6.4.2. The muscle proteome is more similar within age groups, whilst the NMJ-enriched proteome is more similar across all ages

Having shown that muscle and the NMJ-enriched proteome share a considerable amount of the same 'base'-proteome as expected, the next point of interest was to assess how similar patient samples were to each other within a tissue. To do this, hierarchical clustering was utilised which follows the same principal as the generation of dendrograms in Chapter 5. This would identify whether some patient samples were more similar to each other than others, and whether this was related to patient age, sex, or BMI for example. Hierarchical clustering builds clusters between samples based on similarity/closeness in their protein expression and results in a dendrogram. To visualise protein expression, a heatmap was used which graphed protein expression according to their colour intensity.

Closeness between samples was calculated in Euclidean space between all twelve NMJ-enriched (**Figure 6-4.A**) and muscle (**Figure 6-4.B**) samples, and the corresponding heatmap shows expression trends. At first glance one can see that expression ratios heavily average around ~1 (green), for both muscle and NMJ-enriched in **Figure 6-4**. Clustering of the NMJ-enriched proteome indicates that samples do not cluster by age group and no clear trend can be seen according to patient age. The only three samples that seem to have a commonality, are the Old and Senior NMJ samples with a BMI of 21, which branches into a fork of three (**Figure 6-4.A**). The 42-year-old patient seems to be the most unique in his NMJ-proteome which might be associated which his ethnicity.

Clustering of the muscle proteome indicates that samples cluster relatively more by age group. All old samples except one cluster together. That respective cluster also includes two Middle-aged, 56-year- (BMI 30) and 57-year-old (BMI 15) patients. Since BMIs of 15 and 30 are classified as severely underweight and obese (Weir and Jan, 2019), respectively, these

patients could both have lower muscle quality, which reflects in their proteome similarity to Old subjects.

An increase in BMI has previously been noted to be associated with a decrease in muscle quality (McGregor, Cameron-Smith and Poppitt, 2014), therefore it also appears logical if this occurs when the BMI decreases to a severely underweight stage, such as in cachexia (Fearon, Strasser, Stefan D Anker, *et al.*, 2011). What is interesting to note is that Middle-aged samples either cluster with one another (56yo and 57yo stem from the same subbranch), one Senior sample (54yo and 64yo), or with both female samples (Senior and Old females cluster with 42yo Middle-aged) (**Figure 6-4.B**). Whilst studies have shown that females have a higher content of slower type-I muscle fibres in comparison to men (Haizlip, Harrison and Leinwand, 2015) and loss of skeletal muscle mass during ageing is attributed to a decline in type-II muscle fibre content in men (Nilwik *et al.*, 2013), younger females could potentially be more similar to older men in their myosin composition.

Even though myosin is the building block of individual fibre types and makes up almost ~50% of the entire muscle proteome (Gonzalez-Freire *et al.*, 2017) we still lack detailed comparison of sexual dimorphism in the human skeletal muscle proteome to be able to accurately quantify at what stage female muscle differs from male muscle.

As is evident from the sample clustering, there are clear differences between the groupings of muscle and NMJ-enriched samples, pointing towards different expression levels of proteins (**Figure 6-4**). Whilst there is great similarity between proteins that were identified to the muscle and NMJ-enriched proteome (**Figure 6-3**), local regulation of transcription and protein translation within muscle is likely responsible for the differences noted between muscle and NMJ-enriched samples.

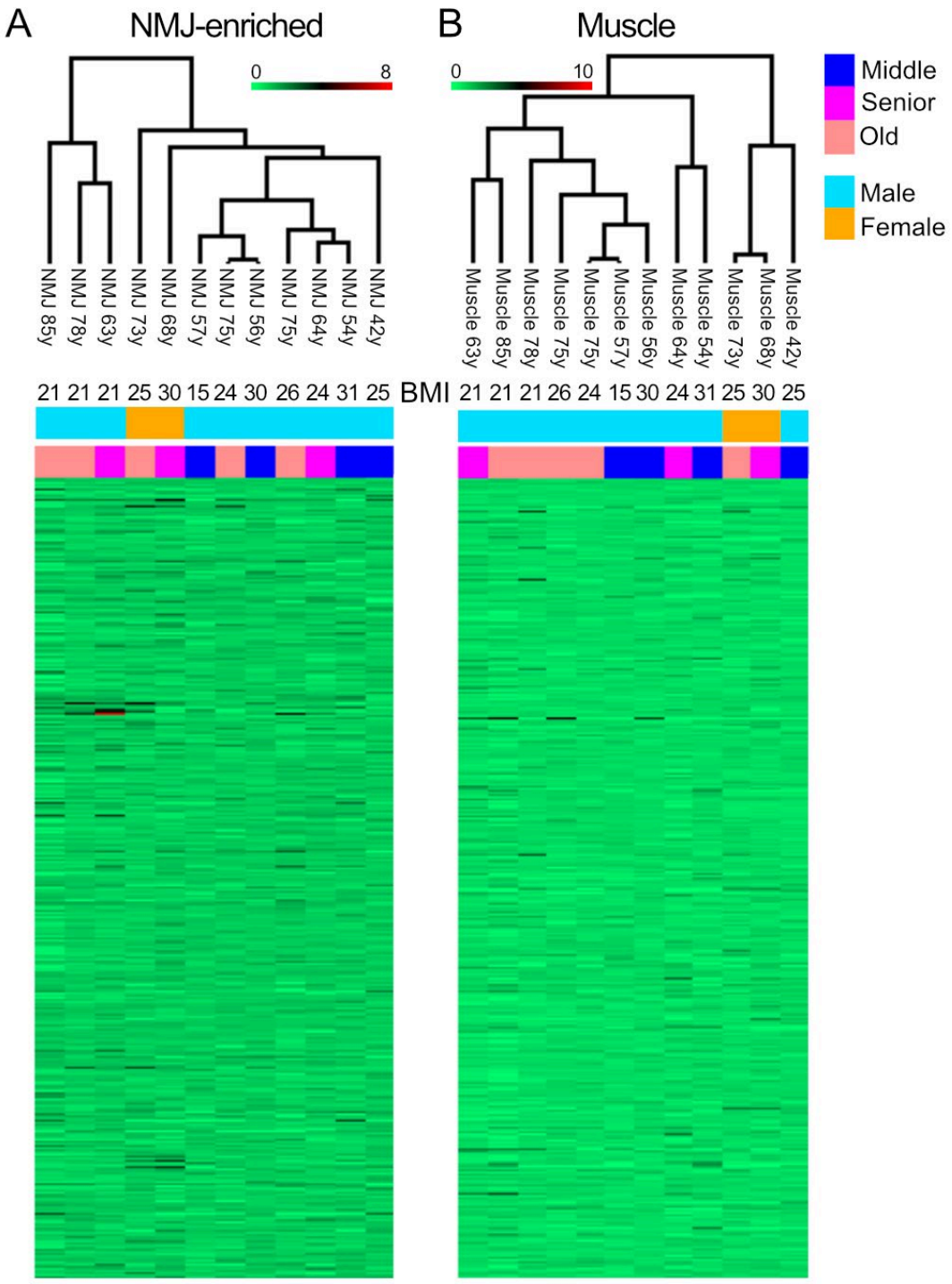

Figure 6-4: Similarity between patient samples within (A) NMJ-enriched and (B) muscle proteome

The dendrogram depicts patient grouping by similarity in proteome. Protein expression is visualised as a heatmap. Groupings are not identical between muscle and NMJ-enriched proteome. The coloured gradient (green – red) depicts the colour legend to which the heatmap refers to. (green = lower protein expression ratios; red = larger ratios) Age, BMI, gender and age group are listed. *Legend continues on next page.*

Figure 6-4 legend continued from previous page:

Male = light blue; Female = orange. Middle aged = blue; Senior = pink; Old = peach.

(A) Hierarchical clustering of the NMJ-enriched proteome based on sample similarity. The dendrogram indicates the branching and distance in Euclidean space that NMJ-enriched samples are distant from each other. For example, all NMJ proteomes of subjects with a BMI of 21 cluster together, despite them being in two different age categories. Old samples are 'interspersed' between Middle aged and Senior samples, with no clear 'trend' or grouping by age group.

(B) Hierarchical clustering of the muscle proteome. The dendrogram shows that samples cluster more by age group than NMJ-enriched samples. In comparison to NMJ-enriched, the muscle proteome of both female samples is very similar, as shown in the very short distance between the connecting branches. Additionally, whilst subjects with BMI of 21 do not fall into the same cluster of three as in the NMJ proteome, they do cluster together in a larger group of Old and Senior patients (leftmost branch).

Gene regulation responsible for plasticity and synaptic stability of the neuromuscular junction is strongly regulated by targeted gene expression which occurs at specialised so-called sub-synaptic nuclei. These are located under the synapse as the name suggests. Whilst muscle fibres are multinucleated and have many nuclei that are responsible for localised gene expression within a muscle fibre, the function of sub-synaptic nuclei is their specialisation in synaptic genes (Belotti and Schaeffer, 2020). Differences in these signalling pathways are therefore to be expected when comparing muscle samples (lacking sub-synaptic nuclei) and NMJ-enriched samples (which contain sub-synaptic nuclei).

Having established that there are differences in expression between muscle and NMJ-enriched samples (despite their similarity in identified proteins) it was next important to address what age-related changes occurred in the muscle and the NMJ-enriched proteome. To do so, differential expression analysis was conducted individually on both tissues, and is first discussed for muscle.

6.4.3. Ageing of the human muscle proteome

6.4.3.1. An overview over the human muscle proteome

Following initial data exploration, it was key to first assess whether the identified muscle proteome matched expected expression patterns of human muscle. Likewise, it was important to evaluate whether differentially expressed pathways of the ageing human muscle proteome resemble those already published in the literature. To do so, network clustering was conducted in STRING using gene IDs from the entire muscle proteome. This allowed clustering of genes by their known function, and individual clusters were then explored in DAVID where Gene Ontology (GO) enrichment analysis was conducted. GO enrichment can point towards a set of pathways, functions, or cellular structures that have a strong representation within a sample, which can therefore help in validation of the muscle proteome for example (**Figure 6-5.A**).

Typical gene ontology annotations associated with muscle proteomes were identified and enriched across all ten clusters, implying that the muscle proteome of this study is similar in its overall functional enrichment to previous studies (Gonzalez-Freire *et al.*, 2017). For example, proteins associated with biological regulation, transport, metabolism and protein synthesis make up a large percentage of the muscle proteome (Gonzalez-Freire *et al.*, 2017). These biological processes can also be identified in each one of the ten clusters in **Figure 6-5.A**. For example, two clusters (light-green and medium-green, both top-left) were enriched for functional terms associated with skeletal muscle, purple was enriched for terms associated with calcium trafficking which is necessary for muscle contraction (Kuo and Ehrlich, 2015), and other clusters were highly enriched for mitochondria and oxidative enzymes. The latter have been shown to be enriched in slow-twitch muscles, and their higher abundance in mitochondria and oxidative proteins correlates with their functional properties and makes these fibres fatigue resistant (Schiaffino and Reggiani, 2011).

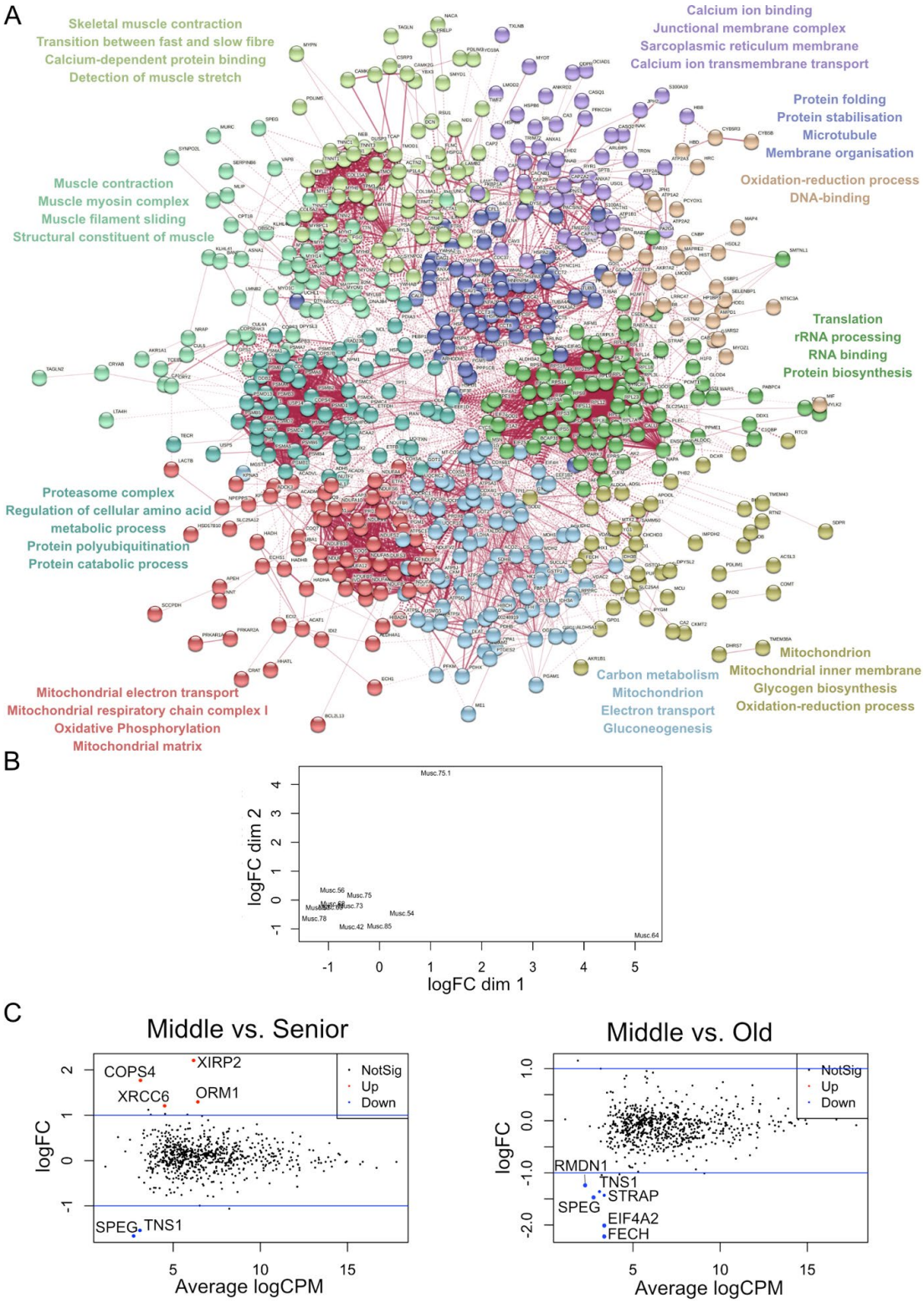

Figure 6-5: Network clustering of the human muscle proteome, and differential analysis across Senior and Old subjects

(A) Network clustering (k = 10 clusters) of the muscle proteome. Each ball represents a gene; lines are drawn between genes with known interactions. *Legend continued on next page.*

Figure 6-5 Legend continued from previous page: Four examples of the most enriched gene ontology annotations are listed for each cluster, in matching colour.

(B) Similarity in expression (in logarithmic fold change = logFC) between patient samples is plotted on a multi-dimensional plot. The first two dimensions are shown, dim 1 and dim 2. This graph helps to illustrate similarities or stark differences between samples.

(C) Differential analysis was conducted using edgeR, between Middle-aged vs. Senior and Middle-aged vs. Old subjects. More proteins are differentially down regulated between Middle-aged vs. Old subjects in comparison to Middle-age vs Senior as can be seen on the y-axis (logFC = log fold-change). The average log CPM depicts the average logarithmic counts per million, which is the intensity/abundance of the measured proteins. Gene names with a logFC = ±1.2 were highlighted and labelled.

logFC = logarithmic fold change; logCPM = logarithmic counts per million;

Whilst human *peroneus longus* is of mixed fibre-type, it contains > 50% type I fibres, explaining the high content of mitochondrial proteins (Niyomchan *et al.*, 2019). Having established that the muscle proteome is comparable to human muscles proteomes across literature, the next question sought to address what happens to the muscle proteome during ageing.

6.4.3.2. Differential analysis of proteins in ageing human muscle

Differential analysis can answer questions relating to how the abundance of a protein changes across ageing. Assessment of the difference between Middle-aged vs Senior and Middle-aged vs Old groups can indicate whether the abundance of a protein decreases or increases with age. This analysis was conducted in R using edgeR, which is 'programmed' to calculate the logarithmic fold-change between assigned groups, in this case Middle-aged vs both, Senior and Old.

Whilst edgeR is fast and reliable for statistical testing, and has great advantages in the case of low replicates (e.g. manual adjustment of dispersion rate as discussed in the methods) (Rueda and Pereira, 2015), it still functions using general statistical and mathematical principals. This means that when comparing a large number of proteins between two age groups (both with high biological variance as can be expected from human

tissue) detection of changes is unlikely, as the false discovery rate and subsequently the P-value will both be adjusted to account for multiple testing.

To first visualise the spread in patient data, a multi-dimension plot was generated (**Figure 6-5.B**) which shows that two muscle samples are more different to the other 10 samples. Under normal circumstances after assessment of this graph, these would be removed from analysis and would be counted as outliers; however, as there are no biological replicates present, these are thought to represent natural biological variation of the human, which is known to be broad (Kushner *et al.*, 2018).

To evaluate differences in expression in relation to Middle-aged patients, differential analysis was conducted. **Figure 6-5.C** depicts the log fold-change of proteins between Middle-age vs Senior (left) and Middle-age vs Old (right). The closer to the centre (zero-line) the proteins, the fewer changes, and the further from the centre the larger the fold-change in protein abundance.

As discussed above, edgeR included statistical testing is unable to find statistical differences between the expression of proteins. This could be due to the fact that there are no significantly differentially expressed proteins, or due to the reason outlined above (high biological variability) which is more likely. The large dispersion within human samples and the sheer volume of statistical tests being conducted would therefore mask any differences. Ideally, a larger sample population within each age group and more subjects who are of matched age would help to better account for biological variability. For these outlined reasons, proteins with a logFC change of ± 1.2 were highlighted within the graph, and their gene names were annotated in **Figure 6-5.C**.

For example, EIF4A2 is decreased in Old subjects. The Eukaryotic initiation factor 4A-II is a complex required for mRNA binding to the ribosome and it has been proposed that during functional muscle homeostasis following muscle atrophy, EIF4A2 should increase, thereby facilitating translation of mRNAs required to respond to stress. In metabolic conditions such as

diabetes or cancer, EIF4A2 has been shown to decrease in skeletal muscle (Lecker *et al.*, 2004).

To get a better overview over changes that occur across ageing, functional enrichment analysis was conducted. This allows to do GO analysis, as previously described, however with the input of associated logFC changes. Thus, the top pathways involved in ageing in Senior or Old patients can be listed, proteins that were identified within these pathways, and the confidence with which these have been mapped (the lower the false discovery rate, the higher the confidence). Once dysregulated pathways were identified through GO analysis, proteins identified to these pathways, and their interactions, can be visualised through a signalling network. The logFC can be superimposed on top of signalling pathways, which allows for intuitive differentiation between proteins that are up- or downregulated.

To do so, gene IDs and their logFC were put through STRING for Middle-aged vs Senior and Middle-aged vs Old subjects, resulting in a list of highly enriched biological processes associated with ageing (**Figure 6-6.A** and **C**). As evident from **Figure 6-6**, mitochondrial processes are highly enriched across both Senior and Old subjects. Upon exploration of these top four enriched biological processes within STRING, it can be seen that the majority of proteins were downregulated across both Senior and Old.

To visualise this, the most highly enriched biological process was selected for both these age groups: mitochondrial respiratory chain complex I assembly (**Figure 6-6.B** and **D**). In Senior subjects (**Figure 6-6.B)** AIFM1 (red) is upregulated (logFC = 0.14), proteins such as NDUFB7 (logFC = -0.03) and NDUFAB1 (logFC = -0.01) are barely changed, whilst in Old subjects (**Figure 6-6.D)** this ‘global’ decrease in protein abundance decreases even further within this signalling network. This is most striking in AIFM1 (logFC = -0.33), NDUFB7 (logFC = -0.24) and NDUFAB1 (logFC = -0.34), which all decrease in old patients. Overall, as visible from the nodes in **Figure 6-6.D** that are of darker blue in comparison to **B**, most proteins have lower abundance.

Apoptosis-inducing factor mitochondrion-associated-1 (AIFM1) is known to play an important role in mitochondrial bioenergetic housekeeping, and lack of it has shown to cause altered oxidative phosphorylation on a widespread transcriptional level. Oxidative phosphorylation is essential for the generation of energy in form adenosine triphosphate (ATP). Impairment of AIFM1 causes mitochondrial and metabolic diseases as well as neurodegenerative disorders and has also been associated with cancer and inflammatory conditions (Bano and Prehn, 2018). A recent study on mouse-models has shown that animals with mutant AIFM1 suffer from mitochondrial dysfunction and myopathy (Wischhof *et al.*, 2018). It is not impossible that AIFM1 could play an important role in the ageing associated loss of muscle function, since lack of AIFM1 would lead to energy deficiency as a function of time. To better visualise which pathways are affected within the mitochondrial inner membrane in Old subjects, the respective biochemical pathway was constructed and superimposed with logFC changes.

The biochemical pathway included respiratory electron transport and ATP synthesis and was constructed in Cytoscape (**Figure 6-6.E**). Differentially expressed proteins within this pathway were primarily associated with Complex I and its assembly, ketone body metabolism (ACAT1, logFC = -0.23) and mitochondrial fatty acid beta-oxidation (ACADS, logFC = -0.48; ACAA2, logFC = -0.27; ACOT13, logFC = -0.25). Whilst at least 15 NDUFV and NDUFS genes encode for complex I (Kirby *et al.*, 2004), AIFM1 likely orchestrates their expression on a transcriptional level as the pathway suggests in **Figure 6-6.B** and **D**. This could also explain why most signalling pathways in **Figure 6-6.E** are downregulated.

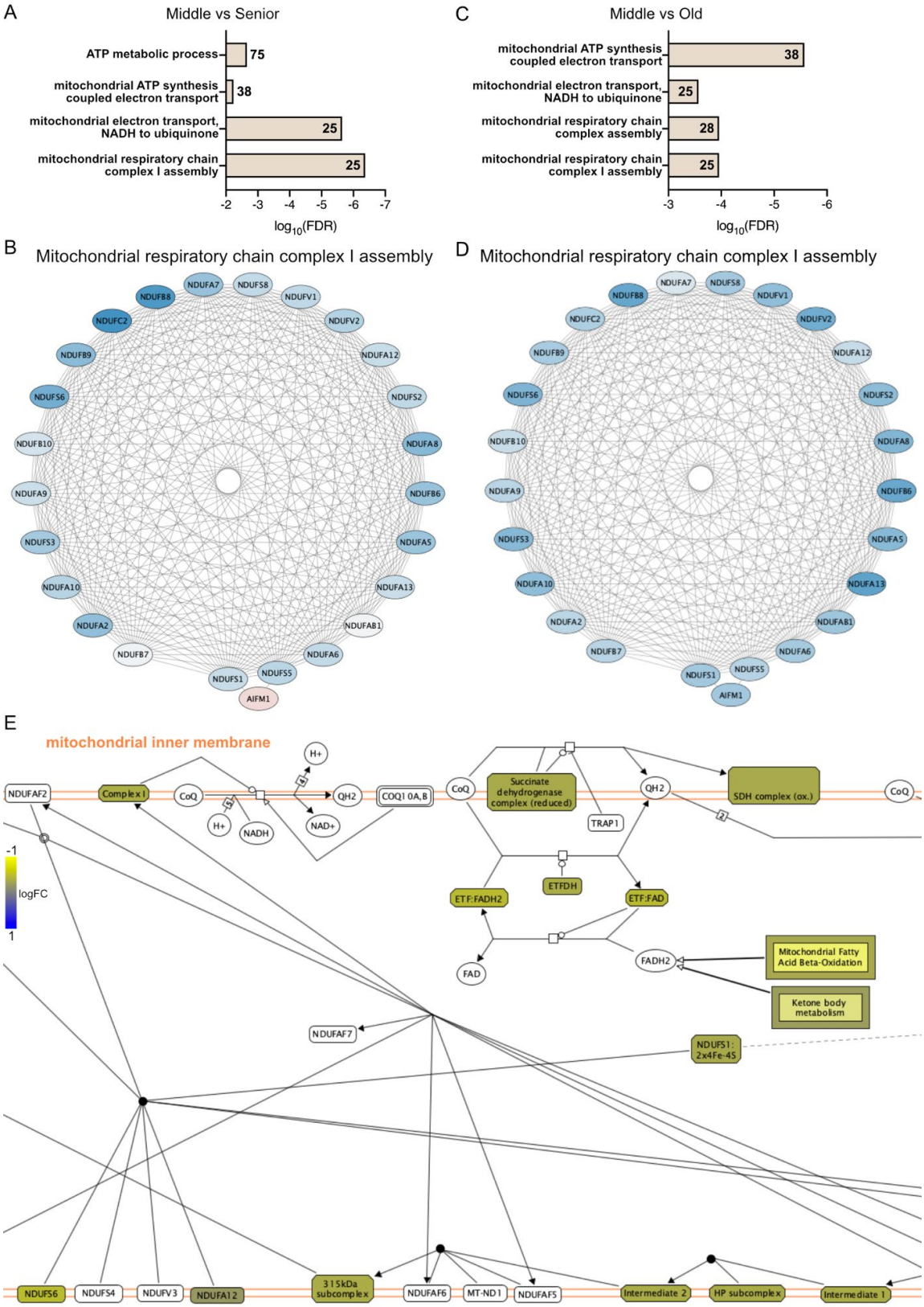

Figure 6-6: Mitochondrial pathways are predominantly affected in ageing muscle

Legend continues on next page.

Figure 6-6 legend continued from previous page:

(A, C) The four most highly enriched gene ontology biological processes in ageing muscle of (A) Senior and (C) Old subjects. The bar-chart shows the FDR (false discovery rate) for each biological process as log 10. The lower the FDR (bigger bar chart), the higher the confidence that proteins have correctly been 'discovered' towards these biological processes. The numbers noted within the bars describe the number of proteins identified within these pathways.

(B, D) Signalling network of the 'mitochondrial respiratory chain complex 1 assembly' process which was enriched in Senior and Old subjects. The colours of the nodes (circles with the gene names) represent the logFC (logarithmic fold change), blue meaning downregulated, red meaning upregulated (positive logFC). Middle-aged vs Old **(D)** has a larger proportion of blue nodes than Middle-aged vs Senior **(C)**.

(E) Partial diagram of the respiratory electron transport within the mitochondrial inner membrane (orange) of Old subjects with dysregulated proteins superimposed. The space outside the orange membrane represents the intermembrane space. Colours represent the logFC between Middle-aged vs Old subjects (yellow = downregulated). All nodes that are white, were not present within the filtered proteome and therefore no value was ascribed. Mitochondrial fatty acid beta-oxidation and ketone body metabolism seem the most affected.

In mitochondria acetyl-CoA acetyltransferase mitochondrion-associated-I (ACAT1) catalyses the reaction from acetoacetyl-CoA to two acetyl-CoA during ketogenesis/ketone body metabolism (Goudarzi, 2019). Acetyl-CoA itself is essential in human metabolism. As coenzyme A is a fundamental carrier substrate within cell metabolism, its derivative acetyl-CoA is metabolised in relevant pathways such as fatty acid synthesis, mitochondrial fatty acid transport regulation, cholesterol and ketone body synthesis, histone and protein acetylation and several more (Czumaj *et al.*, 2020). Decrease of ACAT1 would reduce its capacity to produce acetyl-CoA or catalyse the reverse reaction to acetoacetyl-CoA if required. This would impair all downstream pathways just highlighted. Since increased or decreased levels of CoA in muscle have shown to cause skeletal myopathy, it seems crucial to maintain this fine balance within mitochondria (Czumaj *et al.*, 2020). Ageing

related changes in muscle could therefore cause associated metabolic imbalance.

The gene acyl-CoA Dehydrogenase Short Chain encodes the enzyme SCAD (short-chain acyl-CoA dehydrogenase) which is required for fatty acid beta-oxidation. Once larger CoA fatty acids of different lengths have been transported across the mitochondrial inner membrane via CPT1 (carnitine-palmitoyl transferase 1), these are oxidized by acyl-CoA dehydrogenases, depending on their length. SCAD oxidizes short-chain acyl-CoA fatty acids, MCAD medium-chain length acyl-CoA fatty acids and LCAD long-chain acyl-CoA fatty acids. During this cycle of beta-oxidation NADH is formed, one acetyl-CoA and one acyl-CoA which is two carbon atoms shorter than the original input into this cycle. This continues until the original substrate has been broken down to acetyl-CoA (van Eunen *et al.*, 2013). It is essential that fatty acids are broken down completely, as overload of fatty acid beta-oxidation with excess lipids can cause 'incomplete' fat oxidation and can lead to lipid-induced insulin resistance (Koves *et al.*, 2008). For example, poor diet or lack of exercise (principle of calories in calories out) can cause for an increased demand of fatty acid beta-oxidation. With an increased input of lipids into the oxidative pathway within mitochondria, there is still the same pool of enzymes to draw from to catalyse oxidation. With each oxidative cycle that long fatty-acids undergo, there will be shorter carbon fatty-acids competing for short-chain acyl-CoA dehydrogenases, leading to accumulation of short carbon fatty-acids (until they have eventually been all oxidized) contributing to skeletal muscle insulin resistance (Koves *et al.*, 2008; van Eunen *et al.*, 2013). Insulin resistance means an overall reduced capacity of the body to take up glucose, which is associated with clinical comorbidities such as diabetes type II, hypertension, heart disease, or ageing (Ryan, 2000). Since muscle uses glucose to contract, most glucose in the body is stored as glycogen within skeletal muscle, therefore insulin resistance has largely been contributed to defective fatty acid metabolism (Turcotte and Fisher, 2008). These defects include among others lipid

accumulation in muscle, or in mitochondria as described above (Koves *et al.*, 2008; Turcotte and Fisher, 2008).

Overall, the human ageing muscle shows broad variability in protein expression across individual patients. Despite this variability, changes in mitochondrial pathways associated with insulin resistance and ageing are enriched in Senior and Old subjects. With a mostly negative log fold-change in Old subjects, this points towards a decrease in overall oxidative capacity of muscle mitochondria, and dysfunction of pathways associated with fatty acid oxidation which are essential for muscle homeostasis.

6.4.4. Ageing at the level of the human NMJ-enriched proteome

6.4.4.1. An overview over the human NMJ-enriched proteome

Having first shown that the human muscle proteome was in fact representative of muscle, and second that molecular changes within the ageing human muscle proteome were changes that could be 'expected' following evaluation of literature, the NMJ-enriched proteome could be analysed confidently using the same workflow. Thus, network clustering was performed across the filtered NMJ-enriched proteome (692 proteins). Whilst the NMJ-enriched proteome contained a large cluster (red) highly enriched for muscle, sarcomere and motor activity associated proteins, overall mitochondria associated pathways were less enriched than in muscle (**Figure 6-7.A)**.

Fatty acid and lipid metabolism were highly enriched (enrichment score 3.99, brown cluster), including valine, leucine and isoleucine degradation. These are branched-chain amino acids and essential substrates for protein synthesis. Their decrease, for example through their degradation, would inhibit the ubiquitin-proteasome system, halting effective clearance of accumulated proteins (Holeček, 2018). Proteins associated with the proteasome complex (gold cluster, bottom left) and protein

folding/stabilisation (dark blue) were also enriched, suggesting a ‘connection’ between these three clusters.

6.4.4.2. Differential analysis of the ageing human NMJ-enriched proteome

To evaluate ageing-related changes that occur in Senior and Old subjects, differential analysis was conducted just as before described on muscle. To first visualise the spread in patient data/biological variation, a multi-dimension plot was generated (**Figure 6-7.B**), depicting that samples are more similar to each other than samples within the muscle proteome (**Figure 6-5.B**), by at least two orders of magnitude.

Ageing related changes in protein abundance were plotted for Senior and Old subjects, and as before, proteins with a logFC change of ± 1.2 were highlighted and the gene names annotated (**Figure 6-7.C**). In both Senior and Old subjects, apolipoprotein A 1 (APOA1, logFC = 1.52 and 1.67 respectively), which plays a role in cholesterol transport and regulation of inflammation, is increased. So far, most studies of neurodegenerative diseases such as Parkinson or Alzheimer disease have shown that APOA1 is primarily decreased in plasma or cerebral spinal fluid (Keeney *et al.*, 2013), additionally, APOA1 has been suggested to be a promising prognostic biomarker of inflammation (Sirniö *et al.*, 2017). In particular in cancer studies high APOA1 levels were associated with improved overall survival and reduced systemic inflammation (Sirniö *et al.*, 2017). Therefore, this increase in APOA1 is interesting to note, and inflammatory protection via local gene expression could play a role in the mechanisms that contribute to the stability of the human NMJ.

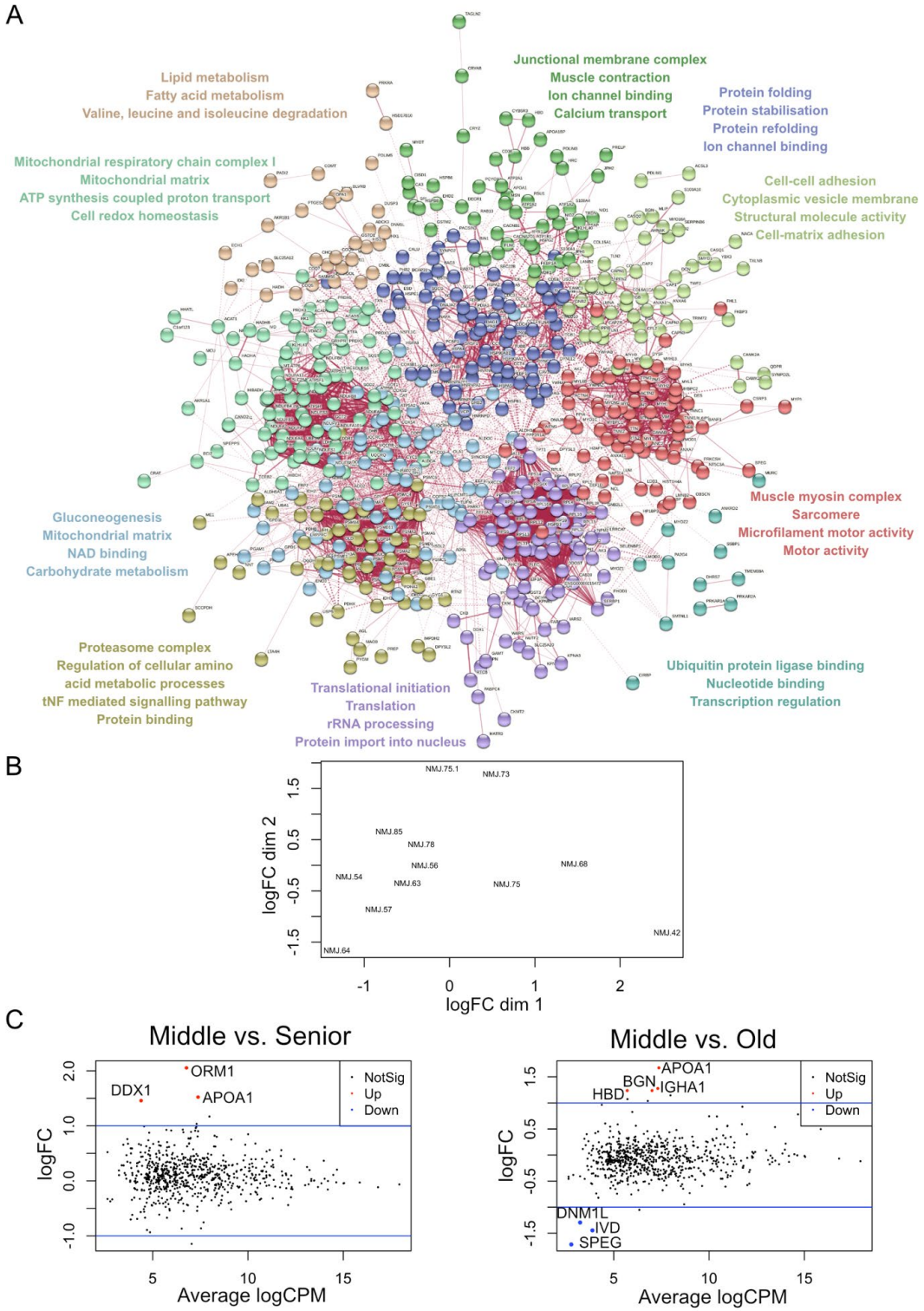

Figure 6-7: Network clustering of the human NMJ-enriched proteome, and differential analysis across Senior and Old subjects

(A) Network clustering (k = 10 clusters) of the NMJ-enriched proteome. *Legend continues on next page.*

Figure 6-7 Legend continued from previous page: Each ball represents a gene; lines are drawn between genes with known interactions. Four examples of the most enriched gene ontology annotations are listed for each cluster, in matching colour.

(B) Similarity of NMJ-enriched samples is plotted on a multi-dimensional plot. The first two dimensions are shown, dim 1 and dim 2.

(C) Ageing related changes in expression in Senior and Old subjects at the NMJ-enriched proteome. More proteins are differentially up and down regulated between Middle-aged vs. Old subjects when comparing the y-axis (logFC = log fold-change) between both age comparisons. The average log CPM depicts the average logarithmic counts per million, which is the intensity of the measured proteins expressed per million on a logarithmic scale. Gene names with a logFC = ±1.2 were highlighted.

logFC = logarithmic fold change; logCPM = logarithmic counts per million;

APOA1 is the main component of high-density lipoproteins (HDL), which play an important role in the absorption and transport of cholesterol. Therefore, APOA1 levels have been inversely associated with insulin resistance as APOA1 'clears' cholesterol so to speak, and high cholesterol plasma levels as well as elevated free fatty acid (FFA) levels are both associated with insulin resistance: low APOA1 levels, more cholesterol, high levels of free fatty acids, high insulin resistance and lower capacity to move glucose into cells (Sirniö *et al.*, 2017).

To get a better overview of biologically enriched pathways, pathway analysis was conducted on gene names and their fold-change in Senior and Old subjects (**Figure 6-8**). Whilst in muscle, most dysregulated pathways were enriched for mitochondrial pathways, including a substantial number of proteins that were mapped to these pathways (> 20), the comparison of NMJ-enriched Senior subjects entailed only a moderate number of proteins highly enriched for the top 4 biological processes (**Figure 6-8.A** and **C**). As one can see, the top four enriched pathways each only identified between 3–5 proteins that would significantly contribute to the difference between Middle-aged vs Senior NMJ-enriched proteome (keratan sulfate catabolic process and keratan sulfate biosynthetic process entailed the same three proteins within their pathways). Exploration of the top four gene ontology

biological processes in Senior and Old subjects showed that these were both a mix of down- and upregulated proteins. Since APOA1 previously stood out as being upregulated, further exploration of 'regulation of interleukin-1 production' seemed relevant, as this process entailed APOA1. Proteins mapped to this pathway were depicted as a signalling network, and fold-changes were superimposed. The signalling pathway was comparable between Senior and Old (**Figure 6-8.B** and **D**); only APOA1 had a higher fold-change. As discussed above, APOA1 plays in important role in cholesterol transport and insulin resistance.

To better visualise what pathways might be affected by APOA1, the biochemical pathway associated with plasma lipoprotein assembly, remodelling and lipoprotein clearance was generated, and fold-changes of protein abundance in Old subjects were superimposed (

Figure 6-9). APOA1 is highly involved in high density lipoprotein metabolism and has been implicated to play a crucial role in global insulin resistance.

High levels of APOA1 have been suggested to be protective, increasing insulin sensitivity as they help with cholesterol clearance (Sirniö *et al.*, 2017; Fritzen *et al.*, 2020). Therefore, a mechanism could be conceived whereby ageing muscle is overall insulin resistant and impaired in overall glucose metabolism, whilst local transcription at the NMJ protects the NMJ from this metabolic condition, allowing for higher glucose uptake, increasing insulin sensitivity in comparison to muscle.

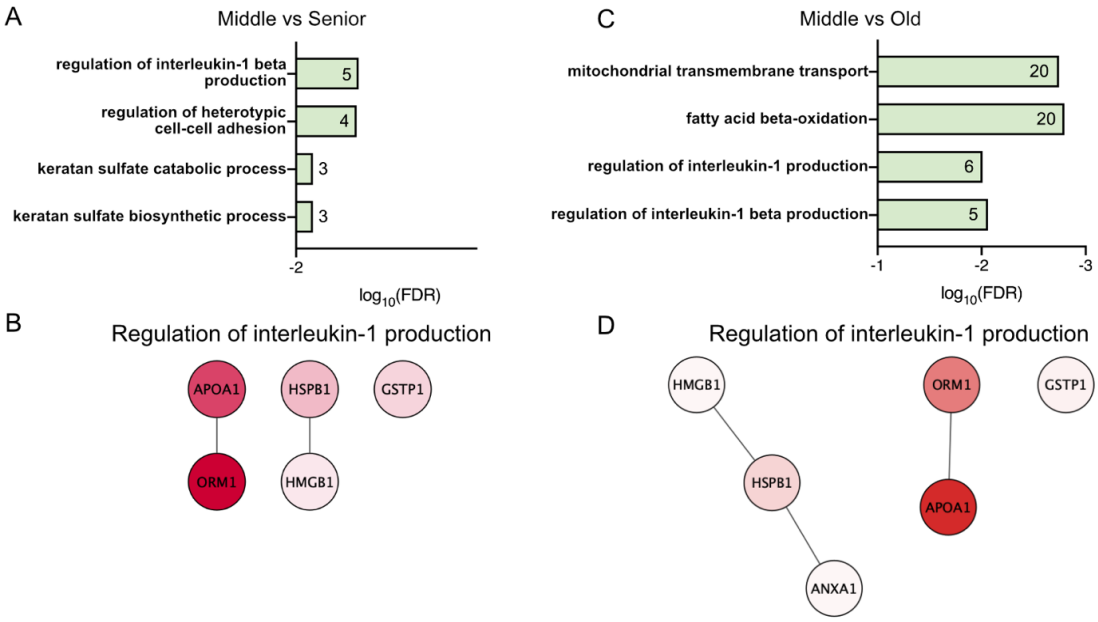

Figure 6-8: Fewer proteins are affected at the ageing NMJ-enriched proteome

(A, C) Diagram of the four most enriched gene ontology biological processes at the ageing NMJ between Middle-aged vs Senior and Middle-aged vs Old subjects. The bar-chart shows the FDR for each biological process as log 10, the lower the FDR (bigger the bar chart), the higher the confidence that proteins have been correctly 'discovered' towards these biological processes. The numbers noted within the bars describe the number of proteins that were ascribed towards these pathways.

log10(FDR) = log 10 false discovery rate;

(B, D) Signaling network of the 'regulation of interleukin-1 production' which was highly enriched in Senior and Old subjects. The colours of the nodes (circles with the gene names) represent the logFC (logarithmic fold change), blue meaning downregulated (none in this case), red meaning upregulated (positive logFC). Middle-aged vs Old **(D)** and Middle-aged vs Senior **(C)** do not differ prominently. In Old subjects most proteins have a slightly lower fold-change, apart from APOA1 which has a larger fold-change. Additionally, the protein annexin A1 (ANXA1) is included in this pathway.

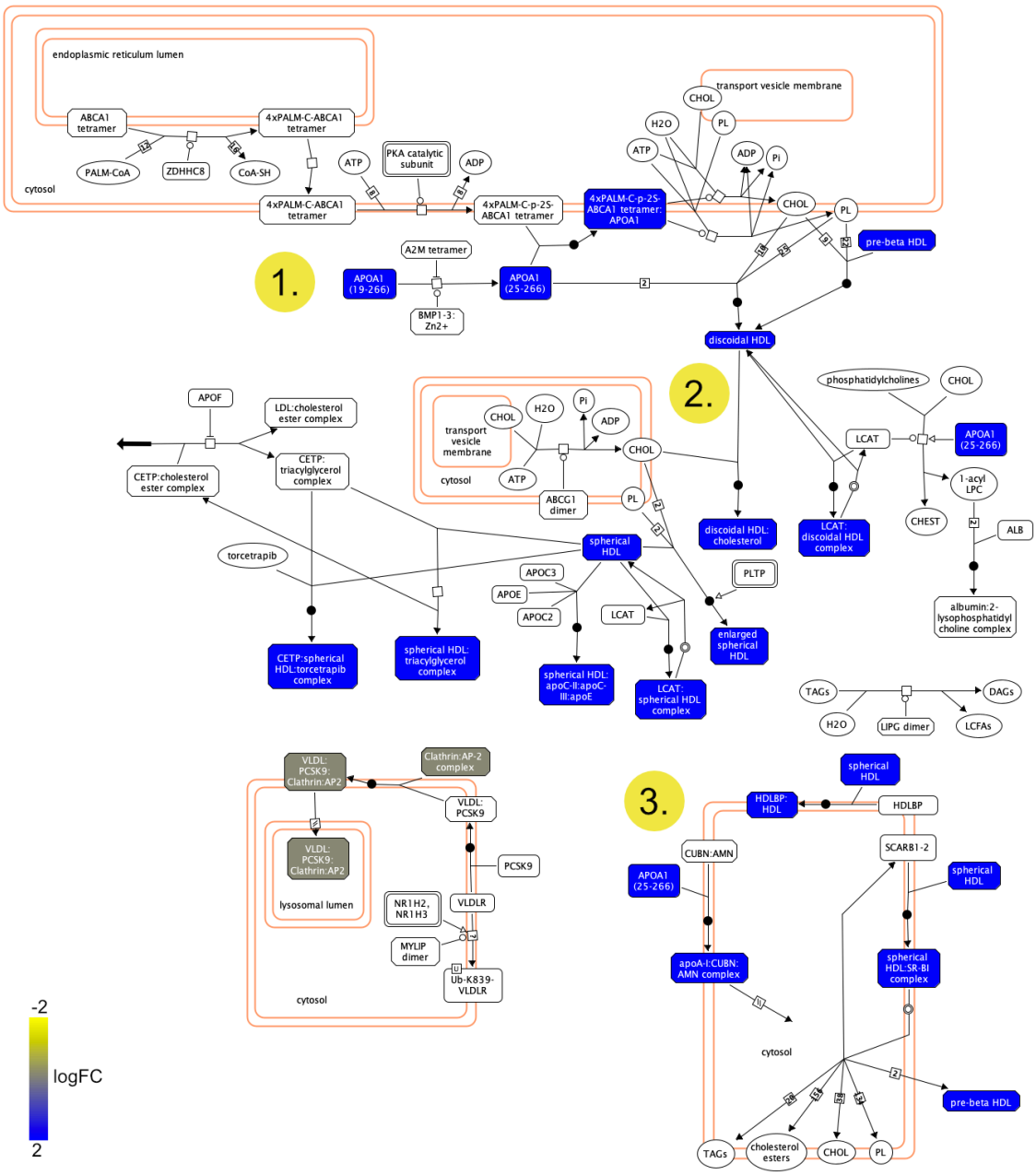

Figure 6-9: Partial diagram of the plasma lipoprotein assembly, remodelling and clearance and APOA1 involvement in Old subjects

APOA1 is highly involved in this pathway (all the nodes in blue, logFC = 1.67). Black thick arrows indicate where pathways still continue, however proteins have not been pulled up as differentially expressed between Middle-aged vs Old and therefore have been excluded for a better overview. The colours represent the logFC between Middle-aged vs Old subjects, a colour legend is given on the left-hand bottom side with yellow representing downregulated pathways and blue upregulated proteins. All nodes that are white, were not present within the filtered proteome and therefore no value was be ascribed. Orange lines represent organelle membranes. *Figure legend continues on next page.*

Figure 6-9 legend continued: Other proteins involved are clathrin (CLTC) and protein disulfide-isomerase (P4HB) which are both barely changed (logFC = -0.1 and -0.01 respectively).
(1) High density lipoprotein (HDL) assembly occurs in the liver and the intestines; HDLs then travel into circulation (plasma/serum). **(2)** High density lipoprotein remodelling: This process is highly dynamic; APOA1 moves between lipid-poor and lipid-rich form. The discoidal (disc-shaped) HDL form is highly reactive and accepts cholesterol, forming spherical (ball/sphere-shaped) HDL complexes (Barter, 2002). Cells incorporate cholesterol, and 'reverse transport' it back to the liver, see clearance. **(3)** HDL clearance: To clear cholesterol from circulation, APOA1-cholesterol complexes are metabolized and degraded in the liver (Bailey and Mohiuddin, 2020).

6.5. Conclusion

1) The NMJ-enriched proteome contains a great proportion of proteins also found in the NMJ-devoid muscle proteome. However, the difference lies within their expression.
2) The analysed muscle proteome and the ageing NMJ-devoid muscle proteome are enriched for similar signalling pathways that have previously been identified across literature.
3) Mitochondrial pathways and oxidative phosphorylation, previously associated with insulin resistance and ageing, are altered in ageing human muscle.
4) The human NMJ-enriched proteome shows fewer changes in mitochondrial pathways and seems more 'stable' across ageing. Pathways associated with insulin sensitivity are enriched.

Understanding the molecular pathways underlying human disease is crucial if better therapies are to be developed. Whilst the previous chapter (Chapter 5) has discussed how successful therapy development in rodent models often translates poorly to humans (Mitsumoto, Brooks and Silani, 2014; Philips and Rothstein, 2015; Tosolini and Sleigh, 2017), this chapter has sought to

explore what molecular mechanisms occur at the human muscle and NMJ-enriched samples during ageing.

Even though NMJ-enriched samples shared similar proteins with pure muscle samples, the ageing proteomes of both tissues were very different to each other. In both tissues there was large biological variability, which is well acknowledged in human tissue (Kushner *et al.*, 2018). However, muscle had a much broader variability than the NMJ-enriched proteome, which suggested 'stability' of the NMJ-enriched proteome across subjects, despite great biological variability.

The muscle proteome was in particular enriched for signalling pathways associated with mitochondrial assembly and ATP synthesis, where the majority of proteins were downregulated in Senior and Old subjects. Many previous studies have shown a correlation between oxidative stress and ageing muscle, and mass spectrometry has frequently linked mitochondrial dysfunction to dysfunctional contractile machinery (Lourenço dos Santos *et al.*, 2015). Here the data points towards mitochondrial dysfunction, as the decrease in proteins associated with mitochondrial assembly and AIFM1, which is required for energy production, could cause an overall energy deficit. Likewise, overload of fatty acids in mitochondria due to faulty beta-oxidation would subsequently increase free fatty acid levels, inducing insulin resistance in muscle (Sirniö *et al.*, 2017). The here utilised workflow demonstrates to be highly robust, as despite the limited patient size, trends within the healthy ageing proteome correspond to global transcriptomic changes identified from a much larger patient cohort (Tumasian *et al.*, 2021).

In contrast, the NMJ-enriched human proteome was remarkably stable in both Senior and Old subjects. Pathways that are particularly enriched in both groups are associated with regulation of interleukin-1 beta production and entail increased levels of apolipoprotein A1 (APOA1). APOA1 plays a crucial role in high density lipoprotein assembly and has been suggested to have anti-inflammatory properties as it clears cholesterol. Further, APOA1 positively correlates with a positive prognosis of various co-morbidities such

as cancer, cardiovascular disease or type 2 diabetes, and is associated with increased insulin sensitivity (Barter, 2002; Keeney *et al.*, 2013; Sirniö *et al.*, 2017).

Studies to date investigating the correlation between denervation and insulin resistance suggest that denervation leads to local insulin resistance and global metabolic changes, which upon reinnervation subside to normal levels (Nunes and De Mello, 2005). So far, there is no evidence which shows that insulin resistance causes denervation per se, thus these observed metabolic changes could likely be a consequence of induced denervation, rather than causative of the denervation.

Since ageing has the qualities of a metabolic disease, it would be interesting to explore the potential of 'metabolic' protection at the NMJ further. The data here points towards insulin resistance at the ageing muscle and hypothesises that increased insulin sensitivity at the NMJ-enriched proteome might be protective (Sergi *et al.*, 2019).

Whilst there were fundamental differences in primarily affected pathways between muscle and the NMJ-enriched proteome, mitochondrial pathways were still dysregulated in both; however, these were much less enriched within the NMJ-enriched proteome. Additionally, these changes were less pronounced than in muscle. It still remains to be determined what molecular pathways are altered directly through transcriptional regulation from sub-synaptic nuclei, as the methodology used here cannot answer this question. Recent advancements in sequencing technologies, in particular single nuclear sequencing, in addition to mass spectrometry, could tease apart changes evoked by sub-synaptic nuclei (Petrany *et al.*, 2020).

A much simpler approach to identify differences in APOA1 between muscle and the NMJ would be its immunofluorescent visualisation across young and old samples, with the hypothesis that APOA1 expression is enriched in the region at the NMJ.

The methodology described here shows a unique approach to obtaining high resolution data from both human muscle and the NMJ-enriched proteome.

Having established a ‘baseline’ of the ageing human NMJ-enriched proteome, this paves the way for future proteomic studies of the human NMJ in sarcopenia, to evaluate the changes occurring on a molecular level in age-related muscle wasting.

7. Future Directions

Recent knowledge highlighting the stark difference between mouse and human NMJ on a morphological and molecular level has opened up a plethora of questions regarding the human NMJ in health and disease. The aim of this thesis was to answer some of these questions via exploration of the mammalian neuromuscular junction in health and disease. The following questions were addressed in respect to methodological advancements and biological insights:

Methodological Advancements

1. Development of a semi-automated macro plugin of NMJ-morph to increase reproducibility and speed of NMJ analysis (Chapter 3)

Biological Insights

1. Does the human neuromuscular junction dismantle in cancer cachexia, a condition that includes muscle wasting? (Chapter 4)
2. Which larger mammalian models have similar NMJ morphology to the human, and are there similar/conserved trends in NMJ morphology across species? (Chapter 5)
3. Are different, or compensatory, molecular mechanisms at the NMJ in comparison to muscle responsible for its stability during ageing? (Chapter 6)

This chapter aims to follow up on previous discussions and elaborate to what extent this project has achieved all four objectives and their research contributions. Future directions of interest to the research community will also be discussed.

7.1. aNMJ-morph

Accurate morphometric analysis of the NMJ is crucial in the field of neuromuscular research as changes in morphology can imply functional impairment and could be used as prognostic markers of disease. As previously discussed in Chapter 3, there has been a lack of standardised methodologies to analyse the NMJ. The development of NMJ-morph was the first step towards a robust, reproducible workflow yielding a plethora of morphometric variables associated with NMJ morphology (Jones *et al.*, 2016); however, analysis was laborious and time consuming. The main contributions of this chapter were:

1. The development of a semi-automated macro plugin for Fiji/ImageJ, called aNMJ-morph.
2. Expedited NMJ analysis with an overall reduction in errors associated with manual data transformation.

Automation of manual processes within the NMJ-morph workflow and replacement of manual measurements (e.g. manual diameter measurement was replaced with automated measurement of the Feret's diameter), increases reproducibility and data acquisition speed by almost four-fold.

Whilst this is an outstanding improvement, there are undoubtedly more adaptations that could make aNMJ-morph the analysis method of choice across the research community. For example, the addition of volumes would be highly informative and more subtle changes in volume overlap could help tell apart disease status, or better differentiate the fundamentally heterogeneous human NMJ. As visualised in Chapter 2 (General Methods), the orientation of the NMJ makes a difference and an NMJ that is partially oblique could end up resulting in smaller area measurements as NMJs that are fully *en face*.

Volumetric measurements however are tricky in particular due to axial distortion during confocal microscopy in z-direction. This is a light phenomenon where the light is 'stretched'/distorted along the z-axis to a much larger proportion than along x- or y-axis. This means that the 'depth' of

a shape to be measured would be longer than the real structure, and when calculating volumes this would result in erroneous measurements (Schwertner, Booth and Wilson, 2007). To date there are a couple of solutions that can aid in best approximation of volumes: imaging with ideal Nyquist ratio to acquire all necessary image information (that means ideal z-stack height and distance between stacks), calibration of axial distortion with fluorescent beads, and mathematical algorithms that account for axial distortion. Whilst many of these algorithms have been developed, one should still not solely rely on volume measurements. Therefore, the addition of volumes TO the already existing 21 morphometric variables could prove to be highly informative in assessment of the NMJ during health and disease.

Whilst semi-automation is a great step forward, the ultimate goal would be to achieve full automation of the aNMJ-morph workflow as explored with the development of NMJ-Analyser by Mejia Maza *et al.*, 2020. Whilst the general principle behind NMJ-Analyser shapes the next stage of method development for NMJ-morph, it would be interesting to see how other approaches tackle the same question.

Deep-learning methods within the field of image analysis could aid in automation of thresholding, and decision-making processes such as the manual channel selection at the start of analysis, and during acknowledgement of aberrant segmentation. Neural networks and associated deep-learning approaches are already being successfully used in cancer diagnostics, as well as across research invested in cellular morphology (Schubert *et al.*, 2019).

7.2. The human NMJ in cancer cachexia

Development of aNMJ-morph (Chapter 3) allowed for expedited NMJ analysis in subsequent chapters. Whilst Chapter 4 gave a detailed description of why denervation of the NMJ was implied to be a pathological hallmark of cancer cachexia (mostly from poorly designed animal models),

the role of the human NMJ still remained to be determined. The main contributions of this chapter were:

1. The demonstration of the stability of the human NMJ in cancer cachexia, as well as cancer.
2. Proof that denervation of the NMJ is not the primary cause of muscle atrophy in cancer cachexia.

Cancer cachexia is a multifactorial disease, with many signalling pathways across many different tissues (muscle, adipose tissue, immune system) contributing to overall pathogenesis. Having shown that dismantling or denervation of the NMJ are not pathological hallmarks of cancer cachexia, it would be of interest to identify what molecular mechanisms 'protect' the NMJ from denervation. To do so one could use the same approach as in Chapter 6 and conduct proteomic analysis on both muscle and NMJ-enriched tissue for control, cancer cachectic and cancer weight stable patients. Resulting data might infer what molecular pathways drive muscle wasting in cancer cachexia, and what pathways regulate the stability of the human NMJ.

Additionally, it would be of interest to study the human NMJ in a variety of other neuromuscular disorders. For example, given the rodent NMJ dismantles during age-related muscle loss, sarcopenia, the question remains whether the human NMJ is also stable during sarcopenia, which warrants further investigation. Study of the human NMJ in motor neuron diseases such as ALS or Spinal Muscular Atrophy (SMA) could also provide important information about the behaviour of NMJ morphology during disease. Since ALS is genetically heterogeneous, which subsequently results in a broad heterogeneity of mouse models, knowledge about the human NMJ during disease onset and progression could prove beneficial in the development of more appropriate mouse models (Li and Wu, 2016). Whilst the human NMJ has previously been subject of investigation in ALS, there are more studies which suggest 'more subtle' changes at the NMJ that are only visible using electron microscopy (EM) (Bruneteau *et al.*, 2015). Changes in NMJ morphology using immunofluorescence requires further studies in ALS, as

most observed changes, such as fragmentation of the endplate and ‘abnormal’ terminal Schwann cells (in comparison to knowledge from rodent terminal Schwann cells), have shown to be normal features of human NMJ morphology (Jones *et al.*, 2017; Alhindi *et al.*, 2021).

Whilst proteomic study of pathways is crucial, it would also be of interest to study human NMJs in disease using electron microscopy and include visualisation of terminal Schwann cells in future studies that use immunofluorescence. This will allow to deduce whether terminal Schwann cells contribute to overall stability of NMJ morphology, or whether changes on EM level correspond with changes observed using confocal microscopy.

7.3. Comparative anatomy of the mammalian NMJ

The need for better animal models which represent the human condition more appropriately has been discussed in depth in Chapter 4 and 5. Given the vast morphological difference between the mouse and human NMJ, it was imperative to conduct an in-depth comparative analysis of the NMJ across a variety of larger mammalian species than the rodent. This chapter’s contributions were:

1. Generation of morphometric baseline data of the mammalian NMJ across 5 newly analysed species: cat, dog, sheep, pig and pony.
2. The sheep and pig have most similar NMJ morphology to the human NMJ and might prove to be suitable alternatives to the mouse NMJ.
3. The identification of conserved morphological relationships across mammals: larger muscle fibres are associated with a larger complexity of preterminal branching, and larger axon diameters are associated with larger NMJs.

The research implications of this chapter are broad, as future prospects include not only the validation of suitability of sheep and pig as more appropriate larger mammalian disease models. Additional fundamental research in health is crucial to evaluate how the NMJ of these models behaves during common diseases such as ageing, which are known to

induce endplate fragmentation in rodents, but not in humans. Molecular analysis of pathways driving development and plasticity within the neuromuscular system (de- and reinnervation) and their comparison between rodent, larger mammal and human, could identify mechanisms that are conserved across species. A recent study evaluating changes in gene transcription across ageing between mouse, rat and human demonstrated that some pathways are conserved only between two species, whilst they differ significantly between the other two (Börsch *et al.*, 2021). A similar approach could prove helpful in the stratification of future animal model development, as the knowledge of what pathways are alike, or differ between what species, can help in the generation of more translatable animal models.

Likewise, the structure function relationship still remains to be explored across species. Since sheep and pig are proposed to be more similar to the human NMJ, it still remains to be determined via electrophysiological means whether their function relates to the function of the human NMJ. As suggested for the analysis of diseased human NMJs, EM studies of both sheep and pig NMJ could prove important to explore similarities between aforementioned species and the human on a cellular level. Differences in for example mitochondria distribution, in particular depth of post-synaptic folding, and distribution of terminal Schwann cells remain to be explored.

7.4. The human NMJ-enriched ageing proteome is more stable than that of muscle

So far, this project had focussed solely on morphometric analysis of the NMJ in health and disease; however, expression is tightly linked with NMJ plasticity. Following the overall theme of Chapter 5, trying to build better models of human disease, Chapter 6 focussed on mechanisms occurring at the healthy ageing human muscle and NMJ. Once we understand what mechanisms govern NMJ stability throughout human ageing, we will be able to more appropriately model animal models of ageing. The main contributions of this chapter were:

1. More ageing related changes occur within the human ageing muscle proteome, in comparison to the NMJ-enriched proteome.
2. Human healthy ageing in muscle is driven by pathways linked to insulin resistance and dysfunctional oxidative phosphorylation, whilst ageing at the NMJ-enriched proteome indicates that compensatory mechanisms more likely cause increased insulin sensitivity.

Studies with a much larger patient size increase confidence in above results (Gonzalez-Freire *et al.*, 2017; Tumasian *et al.*, 2021), and highlight how unique analysis of NMJ-enriched data is. So far, no study has managed to 'isolate' human NMJs for proteomic assessment, and '-omics' approaches, bulk or single cell, have mostly been conducted on needle biopsies, disregarding the NMJ. As we are fully aware of the crucial role that the NMJ plays within the neuromuscular system, it is imperative to separate muscle and NMJ for future proteomic analysis of the ageing NMJ to identify what pathways are causative of sarcopenia. Only then the research community will be able to differentiate between changes occurring in ageing muscle and at the NMJ.

Since currently the study of human NMJs on a morphological and molecular level only includes NMJs from adults, the development of the human NMJ pre- and postnatally poses another significant research milestone. Knowledge derived from morphological and molecular analysis of the human foetal neuromuscular system, postnatal development and paediatric samples will allow to paint a comprehensive picture of the human NMJ across the entire human lifespan.

In principal, genes driving neuromuscular junction stability and plasticity are primarily transcribed in sub-synaptic nuclei and translated in nearby ribosomes (Castets, Ham and Rüegg, 2020), therefore, it is of interest to identify common and species-specific signatures of ageing in sub-synaptic nuclei from mice and humans using single nuclear RNA-seq (snRNA-seq). This approach allows to differentiate gene expression that occurs in sub-synaptic nuclei, from myonuclei and nuclei associated with supporting tissue

types, e.g. fibro-adipogenic progenitor cells or the terminal Schwann cell. A multidisciplinary approach, combining the here described proteomic approach, and snRNA-seq, might be able to establish a more complete view of the central dogma within the human and rodent ageing neuromuscular system. The subsequently identified commonalities and differences between the ageing mouse and human neuromuscular system could help in the generation of more appropriate mouse models, as well as adapted in silico models that predict translation of drugs.

Overall, this thesis has not only provided methodological advancements for analysis of NMJ morphology but has also paved the way to a better understanding of the human NMJ in health and disease. This knowledge, combined with the gained understanding of mammalian NMJ morphology across species, will aid in the exploration and design of more appropriate animal models of human neuromuscular diseases.

7.5. Publications

- The development of aNMJ-morph (Chapter 3) was described and published as an open access Fiji/ImageJ macro plugin (Minty *et al.*, 2020).

  Minty G*, Hoppen A*, **Boehm I***, Alhindi A, Gibb L, et al. aNMJ-morph: A simple macro for rapid analysis of neuromuscular junction morphology. Royal Society Open Science 2020;7. https://doi.org/10.1098/rsos.200128 (* joint first author)
- The results from Chapter 4 and Chapter 5 were published with open access (Boehm, Alhindi, *et al.*, 2020; Boehm, Miller, Thomas M Wishart, *et al.*, 2020).

  Boehm I, Miller J, Wishart TM, Wigmore SJ, Skipworth RJE, Jones RA, et al. Neuromuscular junctions are stable in patients with cancer cachexia. Journal of Clinical Investigation 2020;130:1461–5. https://doi.org/10.1172/JCI128411

Boehm I, Alhindi A, Leite AS, Logie C, Gibbs A, Murray O, et al. Comparative anatomy of the mammalian neuromuscular junction. Journal of Anatomy 2020;237:827–36. https://doi.org/10.1111/joa.13260

- Parts of Chapter 5 are currently being prepared for a review.
- Work detailed in Chapter 6 is currently under preparation for a publication.

7.6. Work presented at conferences

- Chapter 3 and 4 were presented at the virtually organised 'Muscle Science Talks – Trainee & Postdoc series) in 2020. Talk title – "Comparative anatomy of the mammalian neuromuscular junction"
- Chapter 4 was presented in form of a poster at the SMA Europe congress in Evry (France) in 2020, the Anatomical Society Summer Meeting in Oxford (UK) in 2018, as well as during the Edinburgh Neuroscience Day in 2019. Poster title – "Comparative anatomy of the neuromuscular junction: large animal models for SMA and neuromuscular disease research" and "Comparative anatomy of the mammalian neuromuscular junction", respectively
- Chapter 4 was presented at the Edinburgh University Neuroscience Autumn School in 2019, as well as at the SMA UK conference in Keele (UK) in 2019. Talk title – "Comparative anatomy of the mammalian neuromuscular junction" and "Comparative anatomy of the neuromuscular junction: Implications for larger animal models in SMA", respectively
- Chapter 4 was also presented at LMU Munich (Germany) to the laboratory of Prof Stephan Kröger in 2018. Talk title – "Comparative anatomy of the neuromuscular junction"
- Chapter 3 was presented in form of a poster at the International Federation of Associations of Anatomists (IFAA) 2019 in London (UK). Poster title – "The Neuromuscular Junction is stable in human patients with Cancer Cachexia"

- General aims of this thesis following up on research by Jones *et al.,* 2017 and 2016 were presented in form of a poster at the SMA Europe congress 2018 in Krakow (Poland). Poster title – “Cellular and molecular anatomy of the human neuromuscular junction (NMJ) and its relevance to Spinal Muscular Atrophy (SMA) research”
- Overall methodology was presented in form of an invited talk to the ‘Methodologies in musculoskeletal research’ congress 2019 (Hosts: Dr Mathew Piasecki and Dr Beth Phillips) in Nottingham (UK). Talk title – “Imaging of the human neuromuscular junction”
- Chapter 3 was presented in form of an invited talk at the ALS Seminar Series (Host: Dr Andrew Tosolini) of the UCL Institute of Neurology (UK) in 2019. Talk title – “The human neuromuscular junction in health & disease”

References

Alhindi, A., Boehm, I., Forsythe, R. O., Miller, J., Skipworth, R. J. E., Simpson, H., *et al.* (2021) 'Terminal Schwann cells at the human neuromuscular junction', *Brain Communications*, 3(2).

Amorim, I. S., Mitchell, N. L., Palmer, D. N., Sawiak, S. J., Mason, R., Wishart, T. M., *et al.* (2015) 'Molecular neuropathology of the synapse in sheep with CLN5 Batten disease', *Brain and Behavior*, 5(11), pp. 600–601.

Anzenbacher, H. and Zenker, W. (1963) 'Über die Grössenbeziehung der Muskelfasern zu ihren motorischen Endplatten und Nerven', *Zeitschrift für Zellforschung und Mikroskopische Anatomie*, 60(6), pp. 860–871.

Argilé S, J. M., Busquets, S., Stemmler, B. and Ló Pez-Soriano, F. J. (2015) 'Cachexia and sarcopenia: mechanisms and potential targets for intervention Cachexia and sarcopenia: definitions and common trends', *Current Opinion in Pharmacology*, 22, pp. 100–106.

Argilés, J. M., Busquets, S., Stemmler, B. and López-Soriano, F. J. (2014) 'Cancer cachexia: Understanding the molecular basis', *Nature Reviews Cancer*, pp. 754–762.

Ariano, M. A., Armstrong, R. B. and Edgerton, V. R. (1973) 'Hindlimb muscle fiber populations of five mammals.', *The journal of histochemistry and cytochemistry : official journal of the Histochemistry Society*, 21(1), pp. 51–55.

Ashdown, R. R. and Done, S. H. (2011) *Color Atlas of Veterinary Anatomy, Volume 2, The Horse.* Elsevier Health Sciences UK.

Bailey, A. and Mohiuddin, S. S. (2020) *Biochemistry, High Density Lipoprotein (HDL)*, *StatPearls*. StatPearls Publishing. Available at: http://www.ncbi.nlm.nih.gov/pubmed/31747209 (Accessed: 29 March 2021).

Balice-Gordon, R. J. (1997) 'Age-related changes in neuromuscular innervation', *Muscle and Nerve*, 20(SUPPL. 5), pp. S83–S87.

Bano, D. and Prehn, J. H. M. (2018) 'Apoptosis-Inducing Factor (AIF) in

Physiology and Disease: The Tale of a Repented Natural Born Killer', *EBioMedicine*, 30, pp. 29–37.

Barker, D. and Saito, M. (1981) 'Autonomic innervation of receptors and muscle fibres in cat skeletal muscle', *Proceedings of the Royal Society of London - Biological Sciences*, 212(1188), pp. 317–332.

Barter, P. . (2002) 'Hugh Sinclair Lecture: The regulation and remodelling of HDL by plasma factors', *Atherosclerosis Supplements*, 3(4), pp. 39–47.

Beckwée, D., Delaere, A., Aelbrecht, S., Baert, V., Beaudart, C., Bruyere, O., *et al.* (2019) 'Exercise Interventions for the Prevention and Treatment of Sarcopenia. A Systematic Umbrella Review', *Journal of Nutrition, Health and Aging*, 23(6), pp. 494–502.

Belotti, E. and Schaeffer, L. (2020) 'Regulation of Gene expression at the neuromuscular Junction', *Neuroscience Letters*, 735(June), p. 135163.

Berardi, E., Annibali, D., Cassano, M., Crippa, S. and Sampaolesi, M. (2014) 'Molecular and cell-based therapies for muscle degenerations: A road under construction', *Frontiers in Physiology*. Frontiers Media SA, p. 119.

Berardi, E. (2017) 'Muscular Dystrophies and Cancer Cachexia: Similarities in Chronic Skeletal Muscle Degeneration', *Journal of Functional Morphology and Kinesiology*, 2(4), p. 39.

Bloch, W. (2019) 'The countermeasure for cancer cachexia related muscle wasting does not need to be muscle hyperplasia', *Acta Physiologica*, 225(3), pp. 1–2.

Boehm, I., Alhindi, A., Leite, A. S., Logie, C., Gibbs, A., Murray, O., *et al.* (2020) 'Comparative anatomy of the mammalian neuromuscular junction', *Journal of Anatomy*, 237(5), pp. 827–836.

Boehm, I., Miller, J., Wishart, Thomas M., Wigmore, S. J., Skipworth, R. J. E., Jones, R. A., *et al.* (2020) 'Neuromuscular junctions are stable in patients with cancer cachexia', *Journal of Clinical Investigation*, 130(3), pp. 1461–1465.

Boehm, I., Miller, J., Wishart, Thomas M, Wigmore, S. J., Skipworth, R. J. E., Jones, R. A., *et al.* (2020) 'Neuromuscular junctions are stable in patients with cancer cachexia', *Journal of Clinical Investigation*, 130(3), pp. 1461–1465.

Boido, M. and Vercelli, A. (2016) 'Neuromuscular Junctions as Key Contributors and Therapeutic Targets in Spinal Muscular Atrophy', *Frontiers in Neuroanatomy*, 10, p. 6.

Börsch, A., Ham, D. J., Mittal, N., Tintignac, L. A., Migliavacca, E., Feige, J. N., *et al.* (2021) 'Molecular and phenotypic analysis of rodent models reveals conserved and species-specific modulators of human sarcopenia', *Communications Biology*, 4(1), p. 194.

Bottinelli, R. and Reggiani, C. (2000) 'Human skeletal muscle fibres: Molecular and functional diversity', *Progress in Biophysics and Molecular Biology*. Pergamon, pp. 195–262.

Bragulla, H., König, H. E. and Liebich, H.-G. (2009) *Veterinary anatomy of domestic mammals: textbook and colour atlas ; with 53 tables*. Sixth, rev. Edited by H. E. König et al. Stuttgart: Schattauer. Available at: http://books.google.com/books?id=QoXiBjSp368C&pgis=1.

Branson, O. E. and Freitas, M. A. (2016) 'A multi-model statistical approach for proteomic spectral count quantitation', *Journal of Proteomics*, 144(614), pp. 23–32.

Bruneteau, G., Bauché, S., Gonzalez de Aguilar, J. L., Brochier, G., Mandjee, N., Tanguy, M.-L., *et al.* (2015) 'Endplate denervation correlates with Nogo-A muscle expression in amyotrophic lateral sclerosis patients', *Annals of Clinical and Translational Neurology*, 2(4), pp. 362–372.

Bruyère, O., Beaudart, C., Ethgen, O., Reginster, J.-Y. and Locquet, M. (2019) 'The health economics burden of sarcopenia: a systematic review', *Maturitas*, 119, pp. 61–69.

Burke, R. E., Levine, D. N., Salcman, M. and Tsairis, P. (1974) 'Motor units in cat soleus muscle: physiological, histochemical and morphological

characteristics', *The Journal of Physiology*, 238(3), pp. 503–514.

Cachexia | Cancer Grand Challenges (2021). Available at: https://cancergrandchallenges.org/challenges/cachexia (Accessed: 22 February 2021).

Cachexia in Cancer Patients | Cancer Cachexia | OSUCCC – James (2021). Available at: https://cancer.osu.edu/for-cancer-researchers/clinical-research/clinical-research-areas/cancer-cachexia (Accessed: 31 March 2021).

Campbell, M. and Ganetzky, B. (2012) 'Extensive morphological divergence and rapid evolution of the larval neuromuscular junction in Drosophila', *Proceedings of the National Academy of Sciences*, 109(11), pp. E648–E655.

Cannarozzi, G., Schneider, A. and Gonnet, G. (2007) 'A Phylogenomic Study of Human, Dog, and Mouse', *PLoS Computational Biology*. Edited by P. E. Bourne, 3(1), p. e2.

Carey, E. J. and Massopust, L. C. (1946) 'Studies on ameboid motion and secretion of motor endplates; experimental pathology of the secretory mechanism of motor end-plates in thermal shock', *The American journal of pathology*, 22(1), pp. 175–233. Available at: http://www.ncbi.nlm.nih.gov/pubmed/19970861%0Ahttp://www.pubmedcentral.nih.gov/articlerender.fcgi?artid=PMC1934157-- (Accessed: 29 May 2019).

Carleton, S. A. and Brown, W. F. (1979) 'Changes in motor unit populations in motor neurone disease', *Journal of Neurology Neurosurgery and Psychiatry*, 42(1), pp. 42–51.

Carlson, B. M. (2014) 'The biology of long-term denervated skeletal muscle', *European Journal of Translational Myology*, 24(1), pp. 5–11.

Cartee, G. D., Hepple, R. T., Bamman, M. M. and Zierath, J. R. (2016) 'Exercise Promotes Healthy Aging of Skeletal Muscle', *Cell Metabolism*, pp. 1034–1047.

Castets, P., Ham, D. J. and Rüegg, M. A. (2020) 'The TOR Pathway at the Neuromuscular Junction: More Than a Metabolic Player?', *Frontiers in*

Molecular Neuroscience, 13(August), pp. 1–19.

Chen, H. and Boutros, P. C. (2011) 'VennDiagram: A package for the generation of highly-customizable Venn and Euler diagrams in R', *BMC Bioinformatics*, 12(1), p. 35.

Chen, Y., McCarthy, D., Ritchie, M., Robinson, M., Smyth, G. and Hall, E. (2020) 'edgeR: differential analysis of sequence read count data User's Guide', *R package*, (June), pp. 1–121.

Chung, T., Park, J. S., Kim, S., Montes, N., Walston, J. and Höke, A. (2017) 'Evidence for dying-back axonal degeneration in age-associated skeletal muscle decline', *Muscle & Nerve*, 55(6), pp. 894–901.

Cipriani, S., Phan, V., Médard, J. J., Horvath, R., Lochmüller, H., Chrast, R., *et al.* (2018) 'Neuromuscular junction changes in a mouse model of charcot-marie-tooth disease type 4C', *International Journal of Molecular Sciences*, 19(12), p. 4072.

Coers, C. and Woolf, A. L. (1959) *The Innervation of Muscle: A Biopsy Study*, *Charles C Thomas*. Springfield, Ill.,.

Colman, H., Nabekura, J. and Lichtman, J. W. (1997) 'Alterations in synaptic strength preceding axon withdrawal', *Science*, 275(5298), pp. 356–361.

Colquhoun, D. (2014) 'An investigation of the false discovery rate and the misinterpretation of p -values', *Royal Society Open Science*, 1(3), p. 140216.

Court, F. A., Gillingwater, T. H., Melrose, S., Sherman, D. L., Greenshields, K. N., Morton, A. J., *et al.* (2008) 'Identity, developmental restriction and reactivity of extralaminar cells capping mammalian neuromuscular junctions', *Journal of Cell Science*, 121(23), pp. 3901–3911.

Cozzi, B., Ballarin, C., Mantovani, R. and Rota, A. (2017) 'Aging and veterinary care of cats, dogs, and horses through the records of three university veterinary hospitals', *Frontiers in Veterinary Science*, 4(FEB), pp. 1–11.

Cruz-Jentoft, A. J., Bahat, G., Bauer, J., Boirie, Y., Bruyère, O., Cederholm,

T., *et al.* (2019) ‘Sarcopenia: Revised European consensus on definition and diagnosis’, *Age and Ageing*, 48(1), pp. 16–31.

Czumaj, A., Szrok-Jurga, S., Hebanowska, A., Turyn, J., Swierczynski, J., Sledzinski, T., *et al.* (2020) ‘The pathophysiological role of CoA’, *International Journal of Molecular Sciences*, 21(23), pp. 1–30.

Dalle, S., Rossmeislova, L. and Koppo, K. (2017) ‘The role of inflammation in age-related sarcopenia’, *Frontiers in Physiology*, 8(DEC).

Daou, N., Hassani, M., Matos, E., De Castro, G. S., Galvao Figueredo Costa, R., Seelaender, M., *et al.* (2020) ‘Displaced Myonuclei in Cancer Cachexia Suggest Altered Innervation’, *International Journal of Molecular Sciences*, 21(3), p. 1092.

Darwin, C. (1859) ‘On the origins of species by means of natural selection’, *London: Murray*.

Deschenes, M. R., Roby, M. A., Eason, M. K. and Harris, M. B. (2010) ‘Remodeling of the neuromuscular junction precedes sarcopenia related alterations in myofibers’, *Experimental Gerontology*, 45(5), pp. 389–393.

Deschenes, M. R., Roby, M. A. and Glass, E. K. (2011) ‘Aging influences adaptations of the neuromuscular junction to endurance training’, *Neuroscience*, 190(7), pp. 56–66.

Deschenes, M. R., Tenny, K. A. and Wilson, M. H. (2006) ‘Increased and decreased activity elicits specific morphological adaptations of the neuromuscular junction’, *Neuroscience*, 137(4), pp. 1277–1283.

Dewys, W. D., Begg, C., Lavin, P. T., Band, P. R., Bennett, J. M., Bertino, J. R., *et al.* (1980) ‘Prognostic effect of weight loss prior tochemotherapy in cancer patients’, *The American Journal of Medicine*, 69(4), pp. 491–497.

van Dijk, D. P. J., Bakens, M. J. A. M., Coolsen, M. M. E., Rensen, S. S., van Dam, R. M., Bours, M. J. L., *et al.* (2017) ‘Low skeletal muscle radiation attenuation and visceral adiposity are associated with overall survival and surgical site infections in patients with pancreatic cancer’, *Journal of Cachexia, Sarcopenia and Muscle*, 8(2), pp. 317–326.

Dolly, A., Dumas, J. and Servais, S. (2020) ‘Cancer cachexia and skeletal muscle atrophy in clinical studies: what do we really know?’, *Journal of Cachexia, Sarcopenia and Muscle*, 11(6), pp. 1413–1428.

Draper, A. C. E. and Piercy, R. J. (2018) ‘Pathological classification of equine recurrent laryngeal neuropathy’, *Journal of Veterinary Internal Medicine*, 32(4), pp. 1397–1409.

Duchateau, J. and Enoka, R. M. (2011) ‘Human motor unit recordings: Origins and insight into the integrated motor system’, *Brain Research*, 1409, pp. 42–61.

Dupuis, L. and Loeffler, J.-P. (2009) ‘Neuromuscular junction destruction during amyotrophic lateral sclerosis: insights from transgenic models’, *Current Opinion in Pharmacology*, 9(3), pp. 341–346.

Duque, S. I., Arnold, W. D., Odermatt, P., Li, X., Porensky, P. N., Schmelzer, L., *et al.* (2015) ‘A large animal model of spinal muscular atrophy and correction of phenotype’, *Annals of Neurology*, 77(3), pp. 399–414.

Dyce K.M., Sack W.O., W. C. J. G. (2015) *Dyce, Sack, and Wensing’s Textbook of Veterinary Anatomy, 5th edition*. Available at: https://www.elsevier.com/books/dyce-sack-and-wensings-textbook-of-veterinary-anatomy/singh/978-0-323-44264-0 (Accessed: 2 March 2021).

Eaton, S. L. and Wishart, T. M. (2017) ‘Bridging the gap: large animal models in neurodegenerative research’, *Mammalian Genome*, 28(7–8), pp. 324–337.

Ebhardt, H. A., Degen, S., Tadini, V., Schilb, A., Johns, N., Greig, C. A., *et al.* (2017) ‘Comprehensive proteome analysis of human skeletal muscle in cachexia and sarcopenia: a pilot study’, *Journal of Cachexia, Sarcopenia and Muscle*, 8(4), pp. 567–582.

Ellenbroek, B. and Youn, J. (2016) ‘Rodent models in neuroscience research: is it a rat race?’, *Disease Models & Mechanisms*, 9(10), pp. 1079–1087.

Ellis, H. (2009) ‘Anatomy of the anterior abdominal wall and inguinal canal’, *Anaesthesia and Intensive Care Medicine*, 10(7), pp. 315–317.

Engel, A G, Shen, X-M, Engel, Andrew G, Shen, Xin-Ming, Selcen, D. and Sine, S. M. (2015) 'Congenital myasthenic syndromes: pathogenesis, diagnosis, and treatment', *The Lancet Neurology*, 14, pp. 420–434.

Engelke, K., Museyko, O., Wang, L. and Laredo, J.-D. (2018) 'Quantitative analysis of skeletal muscle by computed tomography imaging—State of the art', *Journal of Orthopaedic Translation*, 15, pp. 91–103.

van Eunen, K., Simons, S. M. J., Gerding, A., Bleeker, A., den Besten, G., Touw, C. M. L., *et al.* (2013) 'Biochemical Competition Makes Fatty-Acid β-Oxidation Vulnerable to Substrate Overload', *PLoS Computational Biology*, 9(8), pp. 2–9.

Evans, W. J., Morley, J. E., Argilés, J., Bales, C., Baracos, V., Guttridge, D., *et al.* (2008) 'Cachexia: A new definition', *Clinical Nutrition*, 27(6), pp. 793–799.

Fearon, K., Strasser, F., Anker, Stefan D, Bosaeus, I., Bruera, E., Fainsinger, R. L., *et al.* (2011) 'Definition and classification of cancer cachexia: an international consensus', *The Lancet Oncology*, 12(5), pp. 489–495.

Fearon, K., Strasser, F., Anker, Stefan D., Bosaeus, I., Bruera, E., Fainsinger, R. L., *et al.* (2011) 'Definition and classification of cancer cachexia: An international consensus', *The Lancet Oncology*, 12(5), pp. 489–495.

Fearon, K., Arends, J. and Baracos, V. (2013) 'Understanding the mechanisms and treatment options in cancer cachexia', *Nature Reviews Clinical Oncology*, 10(2), pp. 90–99.

Fearon, K. C. H., Borland, W., Preston, T., Tisdale, M. J., Shenkin, A. and Calman, K. C. (1988) 'Cancer cachexia: Influence of systemic ketosis on substrate levels and nitrogen metabolism', *American Journal of Clinical Nutrition*, 47(1), pp. 42–48.

Fearon, K. C., Voss, A. C. and Hustead, D. S. (2006) 'Definition of cancer cachexia: Effect of weight loss, reduced food intake, and systemic inflammation on functional status and prognosis', *American Journal of*

Clinical Nutrition, 83(6), pp. 1345–1350.

Feeney, E. J., Austin, S., Chien, Y. H., Mandel, H., Schoser, B., Prater, S., *et al.* (2014) 'The value of muscle biopsies in Pompe disease: Identifying lipofuscin inclusions in juvenile- and adult-onset patients', *Acta Neuropathologica Communications*, 2(1), pp. 1–15.

Fitts, R. H., McDonald, K. S. and Schluter, J. M. (1991) 'The determinants of skeletal muscle force and power: Their adaptability with changes in activity pattern', *Journal of Biomechanics*, 24(SUPPL. 1), pp. 111–122.

Flurkey, K., Currer, J. M. and Harrison, D. E. (2007) 'Chapter 20 Mouse Models in Aging Research', *The Mouse in Biomedical Research*, pp. 637–672.

Flynn, W. and Vickerton, P. (2020) *Anatomy, Abdomen and Pelvis, Abdominal Wall*, *StatPearls*. StatPearls Publishing. Available at: http://www.ncbi.nlm.nih.gov/pubmed/31869113 (Accessed: 5 February 2021).

Fox, M. A., Sanes, J. R., Borza, D. B., Eswarakumar, V. P., Fässler, R., Hudson, B. G., *et al.* (2007) 'Distinct Target-Derived Signals Organize Formation, Maturation, and Maintenance of Motor Nerve Terminals', *Cell*, 129(1), pp. 179–193.

Fritzen, A. M., Domingo-Espín, J., Lundsgaard, A.-M., Kleinert, M., Israelsen, I., Carl, C. S., *et al.* (2020) 'ApoA-1 improves glucose tolerance by increasing glucose uptake into heart and skeletal muscle independently of AMPKα2', *Molecular Metabolism*, 35(March), p. 100949.

Genin, E. C., Madji Hounoum, B., Bannwarth, S., Fragaki, K., Lacas-Gervais, S., Mauri-Crouzet, A., *et al.* (2019) 'Mitochondrial defect in muscle precedes neuromuscular junction degeneration and motor neuron death in CHCHD10 S59L/+ mouse', *Acta Neuropathologica*, 138, pp. 123–145.

Gingrich, A., Volkert, D., Kiesswetter, E., Thomanek, M., Bach, S., Sieber, C. C., *et al.* (2019) 'Prevalence and overlap of sarcopenia, frailty, cachexia and malnutrition in older medical inpatients', *BMC Geriatrics*, 19(1), p. 120.

Gollnick, P. D., Sjödin, B., Karlsson, J., Jansson, E. and Saltin, B. (1974) 'Human soleus muscle: A comparison of fiber composition and enzyme activities with other leg muscles', *Pflügers Archiv European Journal of Physiology*, 348(3), pp. 247–255.

Gonzalez-Freire, M., Semba, R. D., Ubaida-Mohien, C., Fabbri, E., Scalzo, P., Højlund, K., *et al.* (2017) 'The Human Skeletal Muscle Proteome Project: a reappraisal of the current literature', *Journal of Cachexia, Sarcopenia and Muscle*, 8(1), pp. 5–18.

Goodpaster, B. H., Kelley, D. E., Thaete, F. L., He, J. and Ross, R. (2000) 'Skeletal muscle attenuation determined by computed tomography is associated with skeletal muscle lipid content', *Journal of Applied Physiology*, 89(1), pp. 104–110.

Gorassini, M., Yang, J. F., Siu, M. and Bennett, D. J. (2002) 'Intrinsic activation of human motoneurons: Possible contribution to motor unit excitation', *Journal of Neurophysiology*, 87(4), pp. 1850–1858.

Gordon, T., Hegedus, J. and Tam, S. L. (2004) 'Adaptive and maladaptive motor axonal sprouting in aging and motoneuron disease', *Neurological Research*, 26(2), pp. 174–185.

Goudarzi, A. (2019) 'The recent insights into the function of ACAT1: A possible anti-cancer therapeutic target', *Life Sciences*, 232(June), p. 116592.

Gouspillou, G., Picard, M., Godin, R., Burelle, Y. and Hepple, R. T. (2013) 'Role of peroxisome proliferator-activated receptor gamma coactivator 1-alpha (PGC-1α) in denervation-induced atrophy in aged muscle: facts and hypotheses', *Longevity & Healthspan*, 2(1), p. 13.

Gramolini, A. O. and Jasmin, B. J. (1997) 'Duchenne muscular dystrophy and the neuromuscular junction: The utrophin link', *BioEssays*, 19(9), pp. 747–750.

Grisold, W., Grisold, A. and Löscher, W. N. (2016) 'Neuromuscular complications in cancer', *Journal of the Neurological Sciences*, 367, pp. 184–202.

Gundry, R. L., White, M. Y., Murray, C. I., Kane, L. A., Fu, Q., Stanley, B. A., *et al.* (2009) 'Preparation of proteins and peptides for mass spectrometry analysis in a bottom-up proteomics workflow', in *Current Protocols in Molecular Biology*. Hoboken, NJ, USA: John Wiley & Sons, Inc., pp. 255–262.

Gupta, R., Chan, J. P., Uong, J., Palispis, W. A., Wright, D. J., Shah, S. B., *et al.* (2020) 'Human motor endplate remodeling after traumatic nerve injury', *Journal of Neurosurgery*, 1(aop), pp. 1–8.

Gutierrez, K., Dicks, N., Glanzner, W. G., Agellon, L. B. and Bordignon, V. (2015) 'Efficacy of the porcine species in biomedical research', *Frontiers in Genetics*, 6.

Haddix, S. G., Lee, Y. Il, Kornegay, J. N. and Thompson, W. J. (2018) 'Cycles of myofiber degeneration and regeneration lead to remodeling of the neuromuscular junction in two mammalian models of Duchenne muscular dystrophy', *PLOS ONE*. Edited by W. D. Phillips, 13(10), p. e0205926.

Haizlip, K. M., Harrison, B. C. and Leinwand, L. A. (2015) 'Sex-based differences in skeletal muscle kinetics and fiber-type composition', *Physiology*, 30(1), pp. 30–39.

Hallock, P. T., Xu, C. F., Park, T. J., Neubert, T. A. and Burden, T. C. S. J. (2010) 'Dok-7 regulates neuromuscular synapse formation by recruiting Crk and Crk-L', *Genes and Development*, 24(21), pp. 2451–2461.

Ham, D. J., Börsch, A., Lin, S., Thürkauf, M., Weihrauch, M., Reinhard, J. R., *et al.* (2020) 'The neuromuscular junction is a focal point of mTORC1 signaling in sarcopenia', *Nature Communications*, 11(1), p. 4510.

Ham, D. J. and Rüegg, M. A. (2018) 'Causes and consequences of age-related changes at the neuromuscular junction', *Current Opinion in Physiology*, 4, pp. 32–39.

Han, J., Pluhackova, K. and Böckmann, R. A. (2017) 'The multifaceted role of SNARE proteins in membrane fusion', *Frontiers in Physiology*, 8(JAN).

Han, X., Aslanian, A. and Yates, J. R. (2008) 'Mass spectrometry for

proteomics', *Current Opinion in Chemical Biology*, 12(5), pp. 483–490.

Harris, J. B. and Ribchester, R. R. (1979) 'The relationship between end-plate size and transmitter release in normal and dystrophic muscles of the mouse.', *The Journal of Physiology*, 296(1), pp. 245–265.

He, W. A., Montanaro, F., Guttridge, D. C., Berardi, E., Cardillo, V. M., Acharyya, S., *et al.* (2013) 'NF-κB-mediated Pax7 dysregulation in the muscle microenvironment promotes cancer cachexia', *The Journal of Clinical Investigation*, 123(11), p. 4821.

Henneman, E. and Olson, C. B. (1965) 'Relations Between Structure and Function in the Design of Skeletal Muscles', *Journal of neurophysiology*, 28(3), pp. 581–598.

Henneman, E., Somjen, G. and Carpenter, D. O. (1965) 'Excitability and inhibitability of motoneurons of different sizes', *Journal of neurophysiology*, 28(3), pp. 599–620.

Hepple, R. T. (2012) 'Muscle atrophy is not always sarcopenia', *Journal of Applied Physiology*, 113(4), pp. 677–679.

Hirsch, N. P. (2007) 'Neuromuscular junction in health and disease', *British Journal of Anaesthesia*, 99(1), pp. 132–138.

Holeček, M. (2018) 'Branched-chain amino acids in health and disease: metabolism, alterations in blood plasma, and as supplements', *Nutrition & Metabolism*, 15(1), p. 33.

Holm, I. E., Alstrup, A. K. O. and Luo, Y. (2016) 'Genetically modified pig models for neurodegenerative disorders', *The Journal of Pathology*, 238(2), pp. 267–287.

Huang, D. W., Sherman, B. T. and Lempicki, R. A. (2009) 'Systematic and integrative analysis of large gene lists using DAVID bioinformatics resources', *Nature Protocols*, 4(1), pp. 44–57.

Huang, Y. T., van der Hoorn, D., Ledahawsky, L. M., Motyl, A. A. L., Jordan, C. Y., Gillingwater, T. H., *et al.* (2019) 'Robust comparison of protein levels

across tissues and throughout development using standardized quantitative western blotting', *Journal of Visualized Experiments*, 2019(146), pp. 1–9.

Huber, W., Carey, V. J., Gentleman, R., Anders, S., Carlson, M., Carvalho, B. S., *et al.* (2015) 'Orchestrating high-throughput genomic analysis with Bioconductor', *Nature Methods*, 12(2), pp. 115–121.

Ibebunjo, C., Chick, J. M., Kendall, T., Eash, J. K., Li, C., Zhang, Y., *et al.* (2013) 'Genomic and Proteomic Profiling Reveals Reduced Mitochondrial Function and Disruption of the Neuromuscular Junction Driving Rat Sarcopenia', *Molecular and Cellular Biology*, 33(2), pp. 194–212.

Jamur, M. C. and Oliver, C. (2010) 'Permeabilization of Cell Membranes', in Oliver, C. and Jamur, M. C. (eds) *Methods in molecular biology (Clifton, N.J.)*. Totowa, NJ: Humana Press, pp. 63–66.

Johns, N., Hatakeyama, S., Stephens, N. A., Degen, M., Degen, S., Frieauff, W., *et al.* (2014) 'Clinical Classification of Cancer Cachexia: Phenotypic Correlates in Human Skeletal Muscle', *PLoS ONE*. Edited by I. E. Gallouzi, 9(1), p. e83618.

Johnson, A. A., Shokhirev, M. N., Wyss-Coray, T. and Lehallier, B. (2020) 'Systematic review and analysis of human proteomics aging studies unveils a novel proteomic aging clock and identifies key processes that change with age', *Ageing Research Reviews*, 60(March), p. 101070.

Jones, R. A., Reich, C. D., Dissanayake, K. N., Kristmundsdottir, F., Findlater, G. S., Ribchester, R. R., *et al.* (2016) 'NMJ-morph reveals principal components of synaptic morphology influencing structure–function relationships at the neuromuscular junction', *Open Biology*, 6(12), p. 160240.

Jones, R. A., Harrison, C., Eaton, S. L., Llavero Hurtado, M., Graham, L. C., Alkhammash, L., *et al.* (2017) 'Cellular and Molecular Anatomy of the Human Neuromuscular Junction', *Cell Reports*, 21(9), pp. 2348–2356.

Kajimura, J., Ito, R., Manley, N. R. and Hale, L. P. (2016) 'Optimization of Single- and Dual-Color Immunofluorescence Protocols for Formalin-Fixed, Paraffin-Embedded Archival Tissues', *Journal of Histochemistry and*

Cytochemistry, 64(2), pp. 112–124.

Kang, H., Tian, L., Mikesh, M., Lichtman, J. W. and Thompson, W. J. (2014) 'Terminal Schwann Cells Participate in Neuromuscular Synapse Remodeling during Reinnervation following Nerve Injury', *Journal of Neuroscience*, 34(18), pp. 6323–6333.

Katz, B. (1966) 'Nerve, muscle, and synapse', *193*.

Kazemi-Bajestani, S. M. R., Mazurak, V. C. and Baracos, V. (2016) 'Computed tomography-defined muscle and fat wasting are associated with cancer clinical outcomes', *Seminars in Cell and Developmental Biology*, 54, pp. 2–10.

Keeney, J. T. R., Swomley, A. M., Förster, S., Harris, J. L., Sultana, R. and Butterfield, D. A. (2013) 'Apolipoprotein A-I: Insights from redox proteomics for its role in neurodegeneration', *PROTEOMICS - Clinical Applications*, 7(1–2), pp. 109–122.

Keller-Peck, C. R., Walsh, M. K., Gan, W. B., Feng, G., Sanes, J. R. and Lichtman, J. W. (2001) 'Asynchronous synapse elimination in neonatal motor units: Studies using GFP transgenic mice', *Neuron*, 31(3), pp. 381–394.

Khan, M. A. S., Sahani, N., Neville, K. A., Nagashima, M., Lee, S., Sasakawa, T., *et al.* (2014) 'Nonsurgically induced disuse muscle atrophy and neuromuscular dysfunction upregulates alpha7 acetylcholine receptors', *Canadian Journal of Physiology and Pharmacology*, 92(1), pp. 1–8.

Kiernan, J. A. (2000) 'Formaldehyde, Formalin, Paraformaldehyde And Glutaraldehyde: What They Are And What They Do', *Microscopy Today*, 8(1), pp. 8–13.

Kirby, D. M., Salemi, R., Sugiana, C., Ohtake, A., Parry, L., Bell, K. M., *et al.* (2004) 'NDUFS6 mutations are a novel cause of lethal neonatal mitochondrial complex I deficiency', *Journal of Clinical Investigation*, 114(6), pp. 837–845.

Koves, T. R., Ussher, J. R., Noland, R. C., Slentz, D., Mosedale, M., Ilkayeva, O., *et al.* (2008) 'Mitochondrial Overload and Incomplete Fatty Acid

Oxidation Contribute to Skeletal Muscle Insulin Resistance', *Cell Metabolism*, 7(1), pp. 45–56.

Kröger, S. and Watkins, B. (2021) 'Muscle spindle function in healthy and diseased muscle', *Skeletal Muscle*, 11(1), pp. 1–13.

Kumar, V., Hallström, B. M. and Janke, A. (2013) 'Coalescent-Based Genome Analyses Resolve the Early Branches of the Euarchontoglires', *PLoS ONE*. Edited by H. Ellegren, 8(4), p. e60019.

Kuno, M., Turkanis, S. A. and Weakly, J. N. (1971) 'Correlation between nerve terminal size and transmitter release at the neuromuscular junction of the frog', *The Journal of Physiology*, 213(3), pp. 545–556.

Kuo, I. Y. and Ehrlich, B. E. (2015) 'Signaling in Muscle Contraction', *Cold Spring Harbor Perspectives in Biology*, 7(2), p. a006023.

Kushner, I. K., Clair, G., Purvine, S. O., Lee, J. Y., Adkins, J. N. and Payne, S. H. (2018) 'Individual Variability of Protein Expression in Human Tissues', *Journal of Proteome Research*, 17(11), pp. 3914–3922.

Landini, G. (2020) 'Novel context-based segmentation algorithms for intelligent microscopy'. Available at: https://blog.bham.ac.uk/intellimic/g-landini-software/ (Accessed: 22 April 2020).

Larsson, L., Degens, H., Li, M., Salviati, L., Lee, Y. Il, Thompson, W., *et al.* (2019) 'Sarcopenia: Aging-related loss of muscle mass and function', *Physiological Reviews*, 99(1), pp. 427–511.

Lecker, S. H., Jagoe, R. T., Gilbert, A., Gomes, M., Baracos, V., Bailey, J., *et al.* (2004) 'Multiple types of skeletal muscle atrophy involve a common program of changes in gene expression', *The FASEB Journal*, 18(1), pp. 39–51.

Li, H. F. and Wu, Z. Y. (2016) 'Genotype-phenotype correlations of amyotrophic lateral sclerosis', *Translational Neurodegeneration*, 5(1), pp. 1–10.

Li, Y., Lee, Y. Il and Thompson, W. J. (2011) 'Changes in aging mouse

neuromuscular junctions are explained by degeneration and regeneration of muscle fiber segments at the synapse', *Journal of Neuroscience*, 31(42), pp. 14910–14919.

Lin, L., Yan, L., Liu, Y., Yuan, F., Li, H. and Ni, J. (2019) 'Incidence and death in 29 cancer groups in 2017 and trend analysis from 1990 to 2017 from the Global Burden of Disease Study', *Journal of Hematology & Oncology*, 12(1), p. 96.

Lin, W. and McArdle, J. J. (2021) 'The NMJ as a model synapse: New perspectives on synapse formation, function, and maintenance', *Neuroscience Letters*, 740, p. 135431.

Lindboe, C. F. and Torvik, A. (1982) 'The effects of ageing, cachexia and neoplasms on striated muscle', *Acta Neuropathologica*, 57(2–3), pp. 85–92.

Ling, K. K. Y., Gibbs, R. M., Feng, Z. and Ko, C. P. (2012) 'Severe neuromuscular denervation of clinically relevant muscles in a mouse model of spinal muscular atrophy', *Human Molecular Genetics*, 21(1), pp. 185–195.

Lorson, M. A., Spate, L. D., Samuel, M. S., Murphy, C. N., Lorson, C. L., Prather, R. S., *et al.* (2011) 'Disruption of the Survival Motor Neuron (SMN) gene in pigs using ssDNA', *Transgenic Research*, 20(6), pp. 1293–1304.

Lourenço dos Santos, S., Baraibar, M. A., Lundberg, S., Eeg-Olofsson, O., Larsson, L. and Friguet, B. (2015) 'Oxidative proteome alterations during skeletal muscle ageing', *Redox Biology*, 5, pp. 267–274.

Mantilla, C. B. and Sieck, G. C. (2003) 'Invited Review: Mechanisms underlying motor unit plasticity in the respiratory system', *Journal of Applied Physiology*, 94(3), pp. 1230–1241.

Manuel, M., Chardon, M., Tysseling, V. and Heckman, C. J. (2019) 'Scaling of motor output, from mouse to humans', *Physiology*, 34(1), pp. 5–13.

Martin, L., Birdsell, L., MacDonald, N., Reiman, T., Clandinin, M. T., McCargar, L. J., *et al.* (2013) 'Cancer cachexia in the age of obesity: Skeletal muscle depletion is a powerful prognostic factor, independent of body mass index', *Journal of Clinical Oncology*, 31(12), pp. 1539–1547.

Maselli, R. A., Ng, J. J., Anderson, J. A., Cagney, O., Arredondo, J., Williams, C., *et al.* (2009) 'Mutations in LAMB2 causing a severe form of synaptic congenital myasthenic syndrome', *Journal of Medical Genetics*, 46(3), pp. 203–208.

McBride, S. D. and Morton, A. J. (2018) 'Indices of comparative cognition: assessing animal models of human brain function', *Experimental Brain Research*, 236(12), pp. 3379–3390.

McGregor, R. A., Cameron-Smith, D. and Poppitt, S. D. (2014) 'It is not just muscle mass: A review of muscle quality, composition and metabolism during ageing as determinants of muscle function and mobility in later life', *Longevity and Healthspan*. BioMed Central Ltd., p. 9.

Mech, A. M., Brown, A., Schiavo, G. and Sleigh, J. N. (2020) 'Morphological variability is greater at developing than mature mouse neuromuscular junctions', *Journal of Anatomy*, 237(4), pp. 603–617.

Mejia Maza, A., Jarvis, S., Lee, W. C., Cunningham, T. J., Schiavo, G., Secrier, M., *et al.* (2021) 'NMJ-Analyser identifies subtle early changes in mouse models of neuromuscular disease', *Scientific Reports*, 11(1), pp. 1–17.

Minassian, H. and Huang, A. N. (1979) 'Effect of sodium azide on the ultrastructural preservation of tissues', *OJournal of Microscopy*, 117(2), pp. 243–253.

Minty, G., Hoppen, A., Boehm, I., Alhindi, A., Gibb, L., Potter, E., *et al.* (2020) 'aNMJ-morph: a simple macro for rapid analysis of neuromuscular junction morphology', *Royal Society Open Science*, 7(4), p. 200128.

Mitsumoto, H., Brooks, B. R. and Silani, V. (2014) 'Clinical trials in amyotrophic lateral sclerosis: Why so many negative trials and how can trials be improved?', *The Lancet Neurology*, 13(11), pp. 1127–1138.

Moise, L., Piserchio, A., Basus, V. J. and Hawrot, E. (2002) 'NMR structural analysis of α-bungarotoxin and its complex with the principal α-neurotoxin-binding sequence on the α7 subunit of a neuronal nicotinic acetylcholine

receptor', *Journal of Biological Chemistry*, 277(14), pp. 12406–12417.

Molfino, A., Amabile, M. I., Rossi Fanelli, F. and Muscaritoli, M. (2016) 'Novel therapeutic options for cachexia and sarcopenia', *Expert Opinion on Biological Therapy*, 16(10), pp. 1239–1244.

Murray, L. M., Comley, L. H., Thomson, D., Parkinson, N., Talbot, K. and Gillingwater, T. H. (2008) 'Selective vulnerability of motor neurons and dissociation of pre- and post-synaptic pathology at the neuromuscular junction in mouse models of spinal muscular atrophy', *Human Molecular Genetics*, 17(7), pp. 949–962.

Murray, L. M., Talbot, K. and Gillingwater, T. H. (2010) 'Review: Neuromuscular synaptic vulnerability in motor neurone disease: Amyotrophic lateral sclerosis and spinal muscular atrophy', *Neuropathology and Applied Neurobiology*, 36(2), pp. 133–156.

Niels, T., Tomanek, A., Freitag, N. and Schumann, M. (2020) 'Can Exercise Counteract Cancer Cachexia? A Systematic Literature Review and Meta-Analysis', *Integrative Cancer Therapies*, 19, p. 153473542094041.

Nilwik, R., Snijders, T., Leenders, M., Groen, B. B. L., van Kranenburg, J., Verdijk, L. B., *et al.* (2013) 'The decline in skeletal muscle mass with aging is mainly attributed to a reduction in type II muscle fiber size', *Experimental Gerontology*, 48(5), pp. 492–498.

Nishimune, H., Valdez, G., Jarad, G., Moulson, C. L., Müller, U., Miner, J. H., *et al.* (2008) 'Laminins promote post-synaptic maturation by an autocrine mechanism at the neuromuscular junction', *Journal of Cell Biology*, 182(6), pp. 1201–1215.

Niyomchan, A., Panichareon, B., Siriphorn, A. and Wongtawatchai, T. (2019) 'Age-related structural-mechanical property changes in human peroneus longus muscle', *Folia Morphologica*, 78(2), pp. 401–407.

Nunes, W. M. S. and De Mello, M. A. R. (2005) 'Glucose metabolism in rats submitted to skeletal muscle denervation', *Brazilian Archives of Biology and Technology*, 48(4), pp. 541–548.

Nystroum, B. (1968) ‘Postnatal Development of Motor Nerve Terminals in “Slow-Red” and “Fast-White” Cat Muscles’, *Acta Neurologica Scandinavica*, 44(3), pp. 363–383.

Oda, K. (1985) ‘The Relationship between Motor Endplate Size and Muscle Fiber Diameter in Different Muscle Groups of the Rat’, *The Japanese Journal of Physiology*, 35(6), pp. 1091–1095.

Ogata, T. (1988) ‘Structure of motor endplates in the different fiber types of vertebrate skeletal muscles.’, *Archives of Histology and Cytology*, 51(5), pp. 385–424.

Oken, M. M., Creech, R. H. and Davis, T. E. (1982) ‘Toxicology and response criteria of the Eastern Cooperative Oncology Group’, *American Journal of Clinical Oncology: Cancer Clinical Trials*, pp. 649–655.

Oksanen, A. J., Blanchet, F. G., Friendly, M., Kindt, R., Legendre, P., Mcglinn, D., *et al.* (2020) *Package ‘ vegan ’*.

Okut, H., Bromley, C. M., Van Vleck, L. D. and Snowder, G. D. (1999) ‘Genotypic expression with different ages of dams: III. Weight traits of sheep’, *Journal of Animal Science*, 77(9), pp. 2372–2378.

Orlovsky, G. N., Deliagina, T. and Grill, S. (1999) *Neuronal Control Of Locomotion: From Mollusc To Man (Oxford Neuroscience)*, *Oxford University Press, Oxford*. Available at: http://isbn.im/download/0198524056.pdf%5Cnpapers3://publication/uuid/CAE3E833-6B0E-4BAD-91E0-F8F973BC6FC8.

Parry, S. M. and Puthucheary, Z. A. (2015) ‘The impact of extended bed rest on the musculoskeletal system in the critical care environment’, *Parry and Puthucheary Extrem Physiol Med*, 4, p. 16.

Patton, B. L., Miner, J. H., Chiu, A. Y. and Sanes, J. R. (1997) ‘Distribution and function of laminins in the neuromuscular system of developing, adult, and mutant mice’, *Journal of Cell Biology*, 139(6), pp. 1507–1521.

Pelekanos, M., Leinenga, G., Odabaee, Mostafa, Odabaee, Maryam, Saifzadeh, S., Steck, R., *et al.* (2018) ‘Establishing sheep as an experimental

species to validate ultrasound-mediated blood-brain barrier opening for potential therapeutic interventions', *Theranostics*, 8(9), pp. 2583–2602.

Petrany, M. J., Swoboda, C. O., Sun, C., Chetal, K., Chen, X., Weirauch, M. T., *et al.* (2020) 'Single-nucleus RNA-seq identifies transcriptional heterogeneity in multinucleated skeletal myofibers', *Nature Communications*, 11(1), p. 6374.

Philips, T. and Rothstein, J. D. (2015) 'Rodent Models of Amyotrophic Lateral Sclerosis', *Current Protocols in Pharmacology*, 69(1), pp. 5.67.1-5.67.21.

Phillips, B. E., Hill, D. S. and Atherton, P. J. (2012) 'Regulation of muscle protein synthesis in humans', *Current Opinion in Clinical Nutrition and Metabolic Care*, 15(1), pp. 58–63.

Piasecki, M., Ireland, A., Stashuk, D., Hamilton-Wright, A., Jones, D. A. and McPhee, J. S. (2016) 'Age-related neuromuscular changes affecting human vastus lateralis', *Journal of Physiology*, 594(16), pp. 4525–4536.

Piasecki, M., Ireland, A., Piasecki, J., Stashuk, D. W., Swiecicka, A., Rutter, M. K., *et al.* (2018) 'Failure to expand the motor unit size to compensate for declining motor unit numbers distinguishes sarcopenic from non-sarcopenic older men', *Journal of Physiology*, 596(9), pp. 1627–1637.

Pigna, E., Simonazzi, E., Sanna, K., Bernadzki, M., Proszynski, T., Heil, C., *et al.* (2019) 'Histone deacetylase 4 protects from denervation and skeletal muscle atrophy in a murine model of amyotrophic lateral sclerosis', *EBioMedicine*, 40, pp. 717–732.

Porporato, P. E. (2016) 'Understanding cachexia as a cancer metabolism syndrome', *Oncogenesis*, 5(2), p. 200.

Portal, D., Hofstetter, L., Eshed, I., Dan-Lantsman, C., Sella, T., Urban, D., *et al.* (2019) 'L3 skeletal muscle index (L3SMI) is a surrogate marker of sarcopenia and frailty in non-small cell lung cancer patients', *Cancer Management and Research*, 11, pp. 2579–2588.

Prakash, Y. S., Miller, S. M., Huang, M. and Sieck, G. C. (1996) 'Morphology of diaphragm neuromuscular junctions on different fibre types', *Journal of*

Neurocytology, 25(1), pp. 88–100.

Purves, D., Augustine, G. J., Fitzpatrick, D., Hall, W. C., Lamantia, A.-S., Mcnamara, J. O., *et al.* (2004) *Neuroscience*, *Sunderland*.

Quick, M. M., Crittenden, C. M., Rosenberg, J. A. and Brodbelt, J. S. (2018) 'Characterization of Disulfide Linkages in Proteins by 193 nm Ultraviolet Photodissociation (UVPD) Mass Spectrometry', *Analytical Chemistry*, 90(14), pp. 8523–8530.

Rhee, H. S., Steel, C. M., Derksen, F. J., Robinson, N. E. and Hoh, J. F. Y. (2009) 'Immunohistochemical analysis of laryngeal muscles in normal horses and horses with subclinical recurrent laryngeal neuropathy', *Journal of Histochemistry and Cytochemistry*, 57(8), pp. 787–800.

Rodríguez Cruz, P., Palace, J. and Beeson, D. (2018) 'The Neuromuscular Junction and Wide Heterogeneity of Congenital Myasthenic Syndromes', *International Journal of Molecular Sciences*, 19(6), p. 1677.

Romanick, M., Thompson, L. D. V. and Brown-Borg, H. M. (2013) 'Murine models of atrophy, cachexia, and sarcopenia in skeletal muscle', *Biochimica et Biophysica Acta - Molecular Basis of Disease*, 1832(9), pp. 1410–1420.

Rosas-Arellano, A., Villalobos-González, J. B., Palma-Tirado, L., Beltrán, F. A., Cárabez-Trejo, A., Missirlis, F., *et al.* (2016) 'A simple solution for antibody signal enhancement in immunofluorescence and triple immunogold assays', *Histochemistry and Cell Biology*, 146(4), pp. 421–430.

RStudio (2020) *RStudio | Open source & professional software for data science teams - RStudio*. Available at: https://rstudio.com/ (Accessed: 22 April 2020).

Rueda, O. and Pereira, B. (2015) *Differential Expression Analysis using edgeR*, *Bioconductor*. Available at: https://bioinformatics-core-shared-training.github.io/cruk-bioinf-sschool/Day3/rnaSeq_DE.pdf.

Ryan, A. S. (2000) 'Insulin Resistance with Aging', *Sports Medicine*, 30(5), pp. 327–346.

Sakkas, G. K., Ball, D., Mercer, T. H., Sargeant, A. J., Tolfrey, K. and Naish, P. F. (2003) 'Atrophy of non-locomotor muscle in patients with end-stage renal failure', *Nephrology Dialysis Transplantation*, 18(10), pp. 2074–2081.

Sanders, D. B. and Juel, V. C. (2008) 'The Lambert-Eaton myasthenic syndrome.', *Handbook of clinical neurology*, 91, pp. 273–83.

Sanes, J. R. and Lichtman, J. W. (2001) 'Induction, assembly, maturation and maintenance of a post-synaptic apparatus', *Nature Reviews Neuroscience*, 2(11), pp. 791–805.

Schiaffino, S. and Reggiani, C. (2011) 'Fiber Types In Mammalian Skeletal Muscles', *Physiol Rev*, 91, pp. 1447–1531.

Schindelin, J., Arganda-Carreras, I., Frise, E., Kaynig, V., Longair, M., Pietzsch, T., *et al.* (2012) 'Fiji: An open-source platform for biological-image analysis', *Nature Methods*, pp. 676–682.

Schnell, U., Dijk, F., Sjollema, K. A. and Giepmans, B. N. G. (2012) 'Immunolabeling artifacts and the need for live-cell imaging', *Nature Methods*, 9(2), pp. 152–158.

Schubert, P. J., Dorkenwald, S., Januszewski, M., Jain, V. and Kornfeld, J. (2019) 'Learning cellular morphology with neural networks', *Nature Communications*, 10(1), pp. 1–12.

Schwertner, M., Booth, M. J. and Wilson, T. (2007) 'Specimen-induced distortions in light microscopy', *Journal of Microscopy*, 228(1), pp. 97–102.

Sergi, D., Naumovski, N., Heilbronn, L. K., Abeywardena, M., O'Callaghan, N., Lionetti, L., *et al.* (2019) 'Mitochondrial (dys)function and insulin resistance: From pathophysiological molecular mechanisms to the impact of diet', *Frontiers in Physiology*, 10(May).

Sexton, A. T. and Fleming, L. L. (2006) 'Lower extremity amputations', in *Medical Management of the Surgical Patient: A Textbook of Perioperative Medicine*. Cambridge University Press, pp. 741–743.

Shafiee, G., Keshtkar, A., Soltani, A., Ahadi, Z., Larijani, B. and Heshmat, R.

(2017) ‘Prevalence of sarcopenia in the world: A systematic review and meta- analysis of general population studies’, *Journal of Diabetes and Metabolic Disorders*, 16(1).

Shannon, P., Markiel, A., Ozier, O., Baliga, N. S., Wang, J. T., Ramage, D., *et al.* (2003) ‘Cytoscape: a software environment for integrated models of biomolecular interaction networks.’, *Genome research*, 13(11), pp. 2498–504.

Sherrington, C. (1929) ‘Ferrier Lecture: Some Functional Problems Attaching to Convergence’, *Proceedings of the Royal Society B: Biological Sciences*, 105(737), pp. 332–362.

Shi, L., Fu, A. K. Y. and Ip, N. Y. (2012) ‘Molecular mechanisms underlying maturation and maintenance of the vertebrate neuromuscular junction’, *Trends in Neurosciences*, 35(7), pp. 441–453.

Short, K. R., Bigelow, M. L., Kahl, J., Singh, R., Coenen-Schimke, J., Raghavakaimal, S., *et al.* (2005) ‘Decline in skeletal muscle mitochondrial function with aging in humans’, *Proceedings of the National Academy of Sciences of the United States of America*, 102(15), pp. 5618–5623.

Sieck, G. C. and Prakash, Y. S. (1997) ‘Morphological Adaptations of Neuromuscular Junctions Depend on Fiber Type’, *Canadian Journal of Applied Physiology*, 22(3), pp. 197–230.

Sirniö, P., Väyrynen, J. P., Klintrup, K., Mäkelä, J., Mäkinen, M. J., Karttunen, T. J., *et al.* (2017) ‘Decreased serum apolipoprotein A1 levels are associated with poor survival and systemic inflammatory response in colorectal cancer’, *Scientific Reports*, 7(1), pp. 1–8.

Slater, C. R. (2008) ‘Structural factors influencing the efficacy of neuromuscular transmission’, *Annals of the New York Academy of Sciences*, 1132, pp. 1–12.

Slater, C. R. (2015) ‘The functional organization of motor nerve terminals’, *Progress in Neurobiology*, pp. 55–103.

Slater, C. R. (2017) ‘The structure of human neuromuscular junctions: Some

unanswered molecular questions', *International Journal of Molecular Sciences*, 18(10), p. 2183.

Slater, C. R. (2019) '"Fragmentation" of NMJs: a sign of degeneration or regeneration? A long journey with many junctions', *Neuroscience*, 439, pp. 28–40.

Sleigh, J. N., Mech, A. M. and Schiavo, G. (2020) 'Developmental demands contribute to early neuromuscular degeneration in CMT2D mice', *Cell Death and Disease*, 11(7).

Smyth, G. K. (2004) 'Linear Models and Empirical Bayes Methods for Assessing Differential Expression in Microarray Experiments', *Statistical Applications in Genetics and Molecular Biology*, 3(1), pp. 1–25.

Stifani, N. (2014) 'Motor neurons and the generation of spinal motor neuron diversity.', *Frontiers in cellular neuroscience*, 8(OCT), p. 293.

Szklarczyk, D., Gable, A. L., Lyon, D., Junge, A., Wyder, S., Huerta-Cepas, J., *et al.* (2019) 'STRING v11: protein–protein association networks with increased coverage, supporting functional discovery in genome-wide experimental datasets', *Nucleic Acids Research*, 47(D1), pp. D607–D613.

Taetzsch, T. and Valdez, G. (2018) 'NMJ maintenance and repair in aging', *Current Opinion in Physiology*, 4, pp. 57–64.

Talbert, E. E., Cuitiño, M. C., Ladner, K. J., Rajasekerea, P. V., Siebert, M., Shakya, R., *et al.* (2019) 'Modeling Human Cancer-induced Cachexia', *Cell Reports*, 28(6), pp. 1612-1622.e4.

Tello, J. F. (1922) 'Die Entstehung der motorischen und sensiblen Nervenendigungen: I. In dem lokomotorischen Systeme der höheren Wirbeltiere. Muskuläre Histogenese', *Zeitschrift für Anatomie und Entwicklungsgeschichte*, 64(4–6), pp. 348–440.

Theroux, M. C., Akins, R., Miller, F. and Dabney, K. (2002) 'Neuromuscular Junction in Cerebral Palsy. Presence of Extrajunctional Acetylcholine Receptors', *Anesthesiology Abstracts of Scientific Papers Annual Meeting*, (2000), p. 1306.

Tintignac, L. A., Brenner, H.-R. and Rüegg, M. A. (2015) ‘Mechanisms Regulating Neuromuscular Junction Development and Function and Causes of Muscle Wasting’, *Physiological Reviews*, 95(3), pp. 809–852.

Tintignac, L. A., Brenner, H. R. and Rüegg, M. A. (2015) ‘Mechanisms regulating neuromuscular junction development and function and causes of muscle wasting’, *Physiological Reviews*, 95(3), pp. 809–852.

Tosolini, A. P. and Sleigh, J. N. (2017) ‘Motor neuron gene therapy: Lessons from spinal muscular atrophy for amyotrophic lateral sclerosis’, *Frontiers in Molecular Neuroscience*, 10(December).

Toth, M. J., Voigt, T. B., Tourville, T. W., Prior, S. M., Guigni, B. A., Schlosberg, A. V., *et al.* (2020) ‘Effect of neuromuscular electrical stimulation on skeletal muscle size and function in patients with breast cancer receiving chemotherapy’, *Journal of Applied Physiology*, 128(6), pp. 1654–1665.

Tumasian, R. A., Harish, A., Kundu, G., Yang, J., Ubaida-Mohien, C., Gonzalez-Freire, M., *et al.* (2021) ‘Skeletal muscle transcriptome in healthy aging’, *Nature Communications*, 12(1), p. 2014.

Turcotte, L. P. and Fisher, J. S. (2008) ‘Skeletal Muscle Insulin Resistance: Roles of Fatty Acid Metabolism and Exercise’, *Physical Therapy*, 88(11), pp. 1279–1296.

Tyanova, S., Temu, T., Sinitcyn, P., Carlson, A., Hein, M. Y., Geiger, T., *et al.* (2016) ‘The Perseus computational platform for comprehensive analysis of (prote)omics data’, *Nature Methods*, 13(9), pp. 731–740.

Ubaida-Mohien, C., Gonzalez-Freire, M., Lyashkov, A., Moaddel, R., Chia, C. W., Simonsick, E. M., *et al.* (2019) ‘Physical Activity Associated Proteomics of Skeletal Muscle: Being Physically Active in Daily Life May Protect Skeletal Muscle From Aging’, *Frontiers in Physiology*, 10(MAR).

Vagnildhaug, O. M., Balstad, T. R., Almberg, S. S., Brunelli, C., Knudsen, A. K., Kaasa, S., *et al.* (2018) ‘A cross-sectional study examining the prevalence of cachexia and areas of unmet need in patients with cancer’, *Supportive Care in Cancer*, 26(6), pp. 1871–1880.

Valdez, G., Tapia, J. C., Kang, H., Clemenson, G. D., Gage, F. H., Lichtman, J. W., *et al.* (2010) 'Attenuation of age-related changes in mouse neuromuscular synapses by caloric restriction and exercise', *Proceedings of the National Academy of Sciences*, 107(33), pp. 14863–14868.

Valero-Mora, P. M. (2010) 'ggplot2: Elegant Graphics for Data Analysis', *Journal of Statistical Software*, 35(Book Review 1), pp. 245–246.

Verschakelen, J. A., Bogaert, J. and De Wever, W. (2002) 'Computed tomography in staging for lung cancer', *European Respiratory Journal*, 19(Supplement 35), pp. 40S-48s.

Viegas, M., Martins, T. C., Seco, F. and Do Carmo, A. (2007) 'An improved and cost-effective methodology for the reduction of autofluorescence in direct immunofluorescence studies on formalin-fixed paraffin-embedded tissues', *European Journal of Histochemistry*, 51(1), pp. 59–66.

Vincent, A. (2002) 'Unravelling the pathogenesis of myasthenia gravis', *Nature Reviews Immunology*, 2(10), pp. 797–804.

Volpe, J. J. (1994) 'Brain Injury in the Premature Infant - Current Concepts', *Preventive Medicine*, 23(5), pp. 638–645.

Walton, W. H. (1948) 'Feret's Statistical Diameter as a Measure of Particle Size', *Nature*, 162(4113), pp. 329–329.

Weber, D. D., Aminzadeh-Gohari, S., Tulipan, J., Catalano, L., Feichtinger, R. G. and Kofler, B. (2020) 'Ketogenic diet in the treatment of cancer – Where do we stand?', *Molecular Metabolism*, 33(July 2019), pp. 102–121.

Weir, C. B. and Jan, A. (2019) *BMI Classification Percentile And Cut Off Points*, *StatPearls*. StatPearls Publishing. Available at: http://www.ncbi.nlm.nih.gov/pubmed/31082114 (Accessed: 26 March 2021).

Wernig, A. and Herrera, A. A. (1986) 'Sprouting and remodelling at the nerve-muscle junction', *Progress in Neurobiology*, pp. 251–291.

WHO (2017) *Summary - Global strategy and action plan on ageing and health (2016 -2020)*, *World Health Organization*. Available at:

https://www.who.int/ageing/global-strategy/en/ (Accessed: 19 October 2020).

WHO, W. H. O.- (2011) *Preface Overview Humanity's Aging Living Longer New Disease Patterns Longer Lives and Disability New Data on Aging and Health Assessing the Cost of Aging and Health Care Changing Role of the Family Suggested Resources*, *National Institutes of Health*. Available at: https://www.who.int/ageing/publications/global_health.pdf (Accessed: 22 June 2020).

Wickham, H., Averick, M., Bryan, J., Chang, W., McGowan, L., François, R., *et al.* (2019) 'Welcome to the Tidyverse', *Journal of Open Source Software*, 4(43), p. 1686.

Wilkinson, D. J., Piasecki, M. and Atherton, P. J. (2018) 'The age-related loss of skeletal muscle mass and function: Measurement and physiology of muscle fibre atrophy and muscle fibre loss in humans', *Ageing Research Reviews*, 47(July), pp. 123–132.

Willadt, S., Nash, M. and Slater, C. R. (2016) 'Age-related fragmentation of the motor endplate is not associated with impaired neuromuscular transmission in the mouse diaphragm', *Scientific Reports*, 6(1), p. 24849.

Willingham, M. C. (1983) 'An alternative fixation-processing method for preembedding ultrastructural immunocytochemistry of cytoplasmic antigens: the GBS (glutaraldehyde-borohydride-saponin) procedure.', *Journal of Histochemistry & Cytochemistry*, 31(6), pp. 791–798.

Willmann, R., Lee, J., Turner, C., Nagaraju, K., Aartsma-Rus, A., Wells, D. J., *et al.* (2020) 'Improving translatability of preclinical studies for neuromuscular disorders: lessons from the TREAT-NMD Advisory Committee for Therapeutics (TACT)', *Disease Models & Mechanisms*, 13(2), p. dmm042903.

Winje, I. M., Sheng, X., Hansson, K. A., Solbrå, A., Tennøe, S., Saatcioglu, F., *et al.* (2019) 'Cachexia does not induce loss of myonuclei or muscle fibres during xenografted prostate cancer in mice', *Acta Physiologica*, 225(3), pp. 1–9.

Wischhof, L., Gioran, A., Sonntag-Bensch, D., Piazzesi, A., Stork, M., Nicotera, P., *et al.* (2018) 'A disease-associated Aifm1 variant induces severe myopathy in knockin mice', *Molecular Metabolism*, 13(May), pp. 10–23.

Wood, S. J. and Slater, C. R. (2001) 'Safety factor at the neuromuscular junction', *Progress in Neurobiology*, 64, pp. 393–429. Available at: www.elsevier.com/locate/pneurobio (Accessed: 23 August 2018).

Woodley, S. J., Duxson, M. J. and Mercer, S. R. (2007) 'Preliminary observations on the microarchitecture of the human abdominal muscles', *Clinical anatomy*, 20(7), pp. 808–813.

Worne, F. (2011) *Color atlas of veterinary anatomy. Volume 3: the dog and cat*, *Australian Veterinary Journal*. Mosby/Elsevier.

Wu, H., Xiong, W. C. and Mei, L. (2010) 'To build a synapse: signaling pathways in neuromuscular junction assembly', *Development*, 137(7), pp. 1017–1033.

Yamada, T., Ashida, Y., Tatebayashi, D., Abe, M. and Himori, K. (2020) 'Cancer Cachexia Induces Preferential Skeletal Muscle Myosin Loss When Combined With Denervation', *Frontiers in Physiology*, 11(April), pp. 1–9.

Zhang, Y., Wang, J., Wang, Xulin, Gao, T., Tian, H., Zhou, D., *et al.* (2020) 'The autophagic-lysosomal and ubiquitin proteasome systems are simultaneously activated in the skeletal muscle of gastric cancer patients with cachexia', *American Journal of Clinical Nutrition*, 111(3), pp. 570–579.

8. Appendices

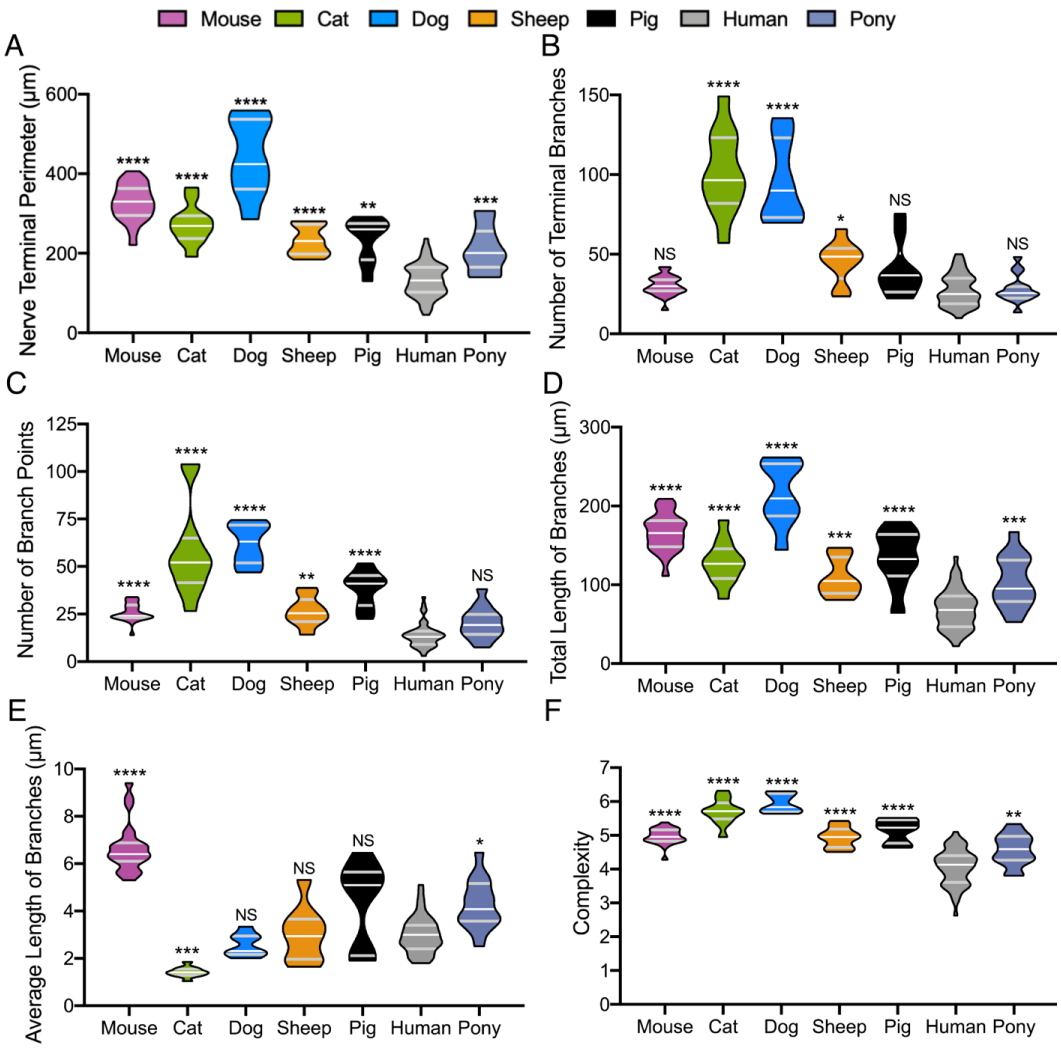

Figure 8-1:Inter-species difference at the mammalian pre-synaptic nerve terminal

A-D core-variables, **E & F** derived variables. Kruskal-Wallis test with Dunn's multiple comparison test for nerve terminal branches, number of branch points and average length of branches, conducted on variable averages of each muscle (n). Brown-Forsythe and Welch ANOVA with Dunnett T3 multiple comparison test for nerve terminal perimeter and complexity. One-way ANOVA with Dunnett's multiple comparison test for total length of branches.

‘Average’ NMJ morphology of individual muscles within a species is plotted in form of a truncated violin plot. The top and bottom of the ‘truncated’ plot represent the min and max values, the white ‘middle’ line represents the median, and the interquartile range (encompassing 50% of the dataset) is bounded by grey, slightly thicker lines, above and below the white line.

(Mouse: N = 3 animals, n = 24 muscles; cat: N = 3, n = 12; dog: N = 3, n = 9; sheep: N= 3, n = 9; pig: N = 3, n = 9; human: N = 21, n = 72; pony: N = 5, n = 15) Mouse and human data from Jones et al., 2017.

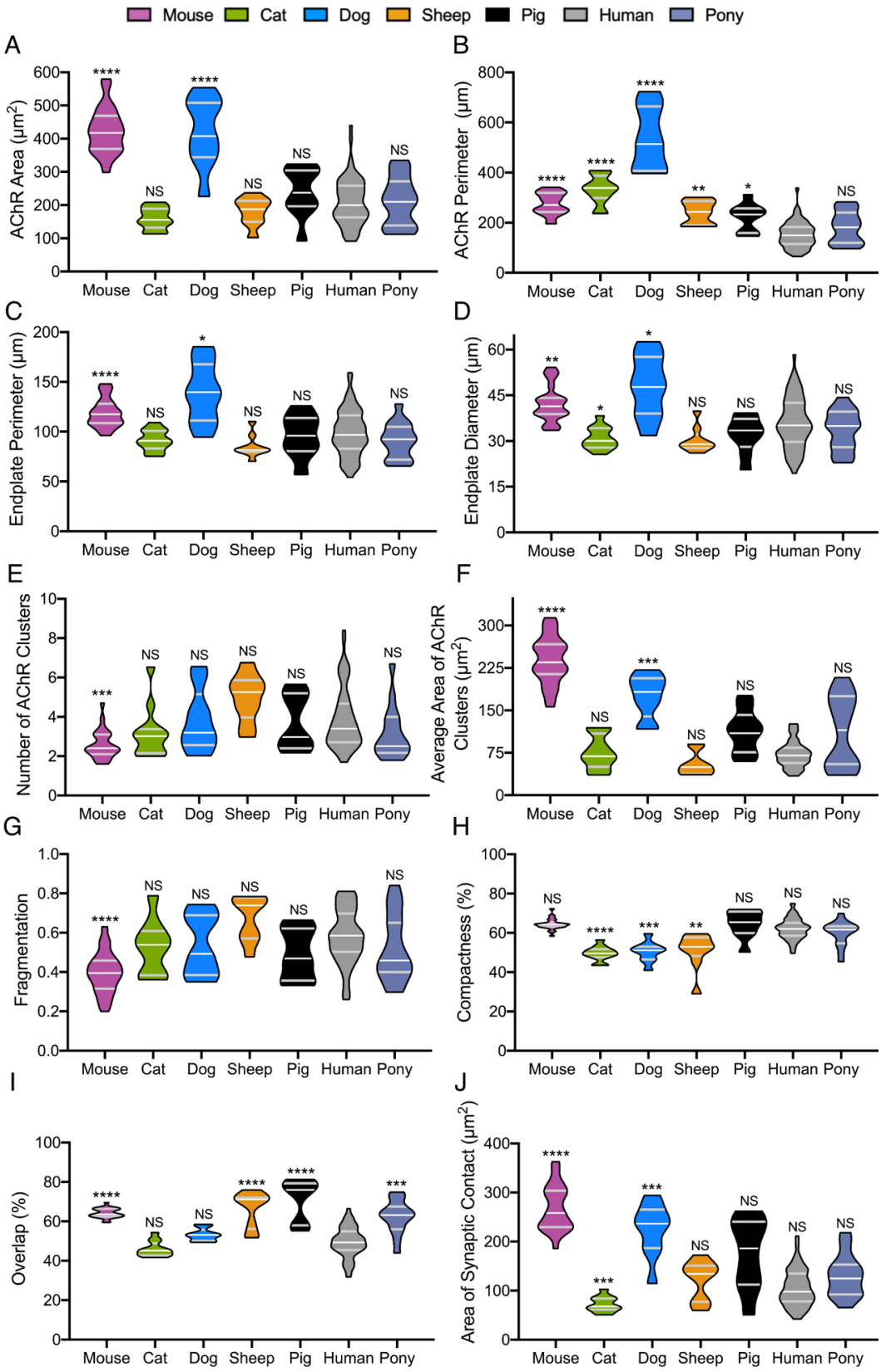

Figure 8-2: Inter-species difference at the mammalian post-synaptic motor endplate

(A–E) core variables, **(F–J)** derived variables. Kruskal-Wallis test with Dunn's multiple comparison test endplate area, number of AChR clusters and compactness. Brown-Forsythe and Welch ANOVA with Dunnett T3 multiple comparison test for AChR perimeter, endplate perimeter, endplate diameter and average area of AChR clusters. One-way ANOVA with Dunnett's multiple comparison test for AChR area, fragmentation and area of synaptic contact. Conducted on variable averages of each muscle (n)

'Average' NMJ morphology of individual muscles within a species is plotted in form of a truncated violin plot. The top and bottom of the 'truncated' plot represent the min and max values, the white 'middle' line represents the median, and the interquartile range (encompassing 50% of the dataset) is bounded by grey, slightly thicker lines, above and below the white line.

(Mouse: N = 3 animals, n = 24 muscles; cat: N = 3, n = 12; dog: N = 3, n = 9; sheep: N= 3, n = 9; pig: N = 3, n = 9; human: N = 21, n = 72; pony: N = 5, n = 15) Mouse and human data from Jones et al., 2017.

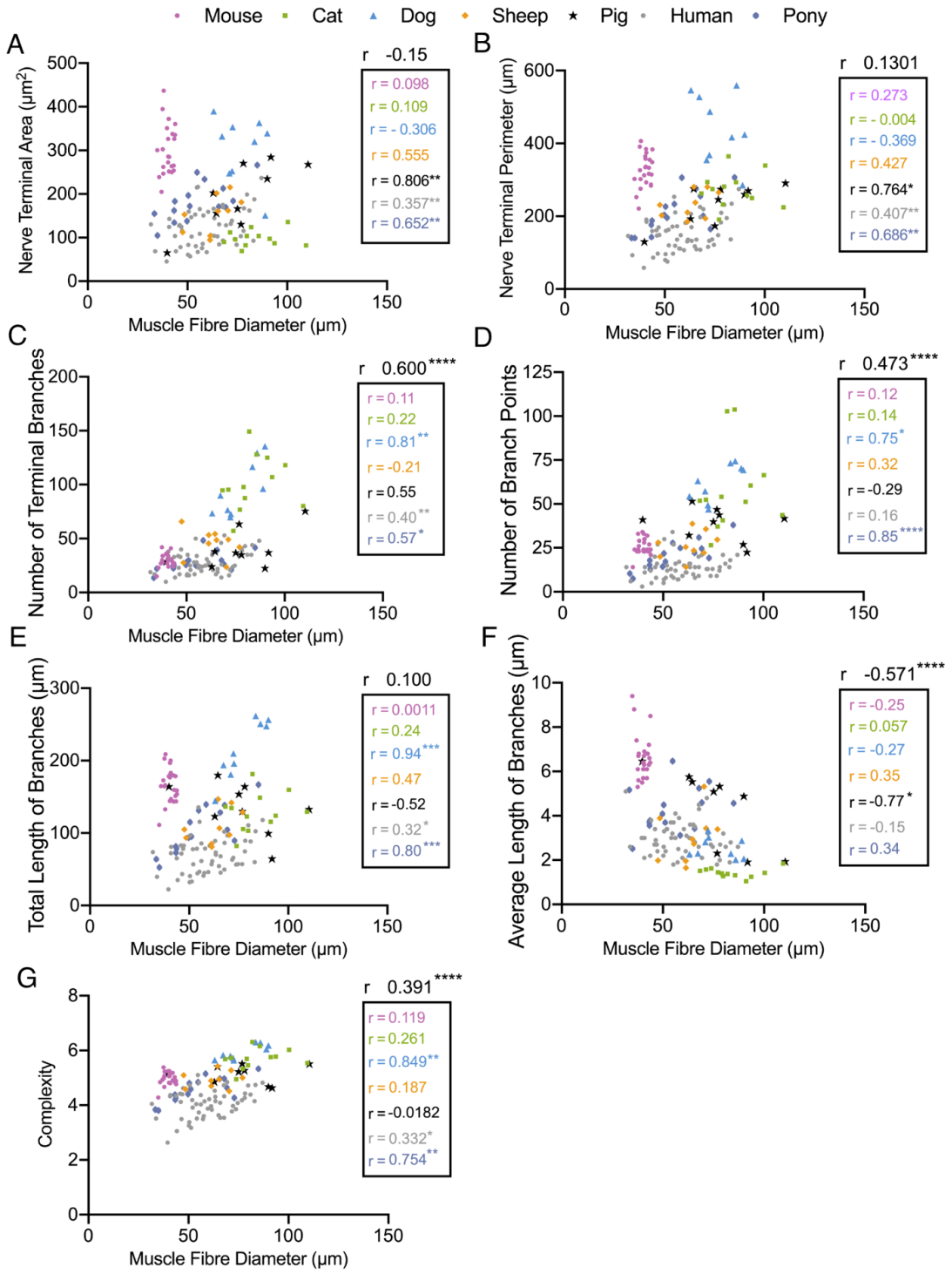

Figure 8-3: Correlation of pre-synaptic NMJ variables with muscle fibre diameter

(A–E) core variables, **(F–G)** derived pre-synaptic variables. Overall, the pony and human show the most correlation of pre-synaptic variables with muscle fibre diameter. Branching related variables have strong global correlation with muscle fibre diameter across all seven species. Each dot represents the average of one

muscle for the respective variable and muscle fibre diameter (n), within analysed species. (Mouse: N = 3 animals, n = 24 muscles; cat: N = 3, n = 12; dog: N = 3, n = 9; sheep: N= 3, n = 9; pig: N = 3, n = 9; human: N = 21, n = 72; pony: N = 5, n = 15) Mouse and human data from Jones et al., 2017.

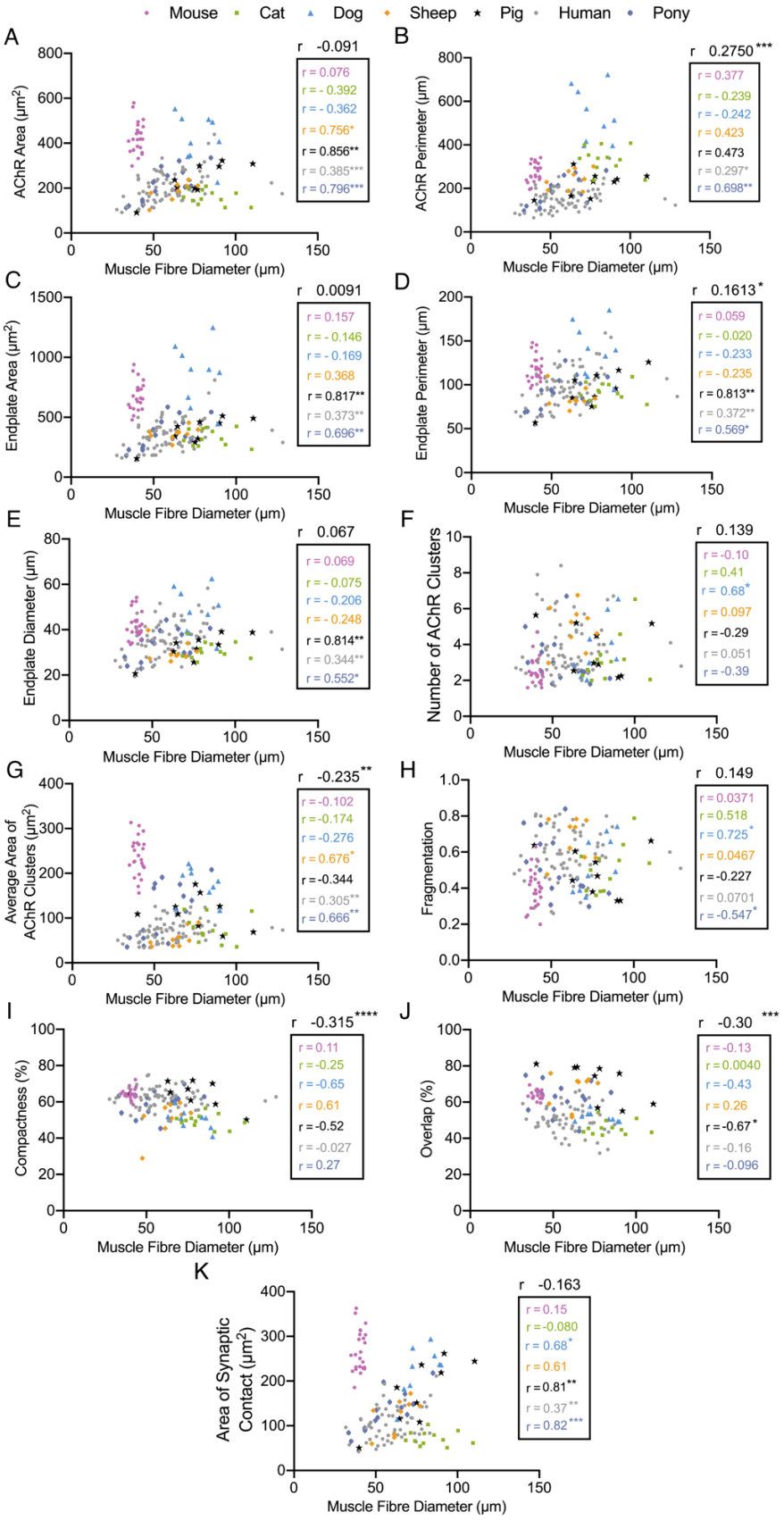

Figure 8-4: Correlation of post-synaptic NMJ variables with muscle fibre diameter

(A–F) core variables, (G–K) derived post-synaptic variables. Overall, the pony, human and pig show the most correlation of post-synaptic variables with muscle fibre diameter. Size related variables have strong within species correlation with muscle fibre diameter across these three species. Globally (across all seven species), only AChR perimeter, compactness and overlap have a *** or more significant linear relationship. Each dot represents the average of one muscle for the respective variable and muscle fibre diameter, within analysed species. (Mouse: N = 3 animals, n = 24 muscles; cat: N = 3, n = 12; dog: N = 3, n = 9; sheep: N= 3, n = 9; pig: N = 3, n = 9; human: N = 21, n = 72; pony: N = 5, n = 15) Mouse and human data from Jones et al., 2017.

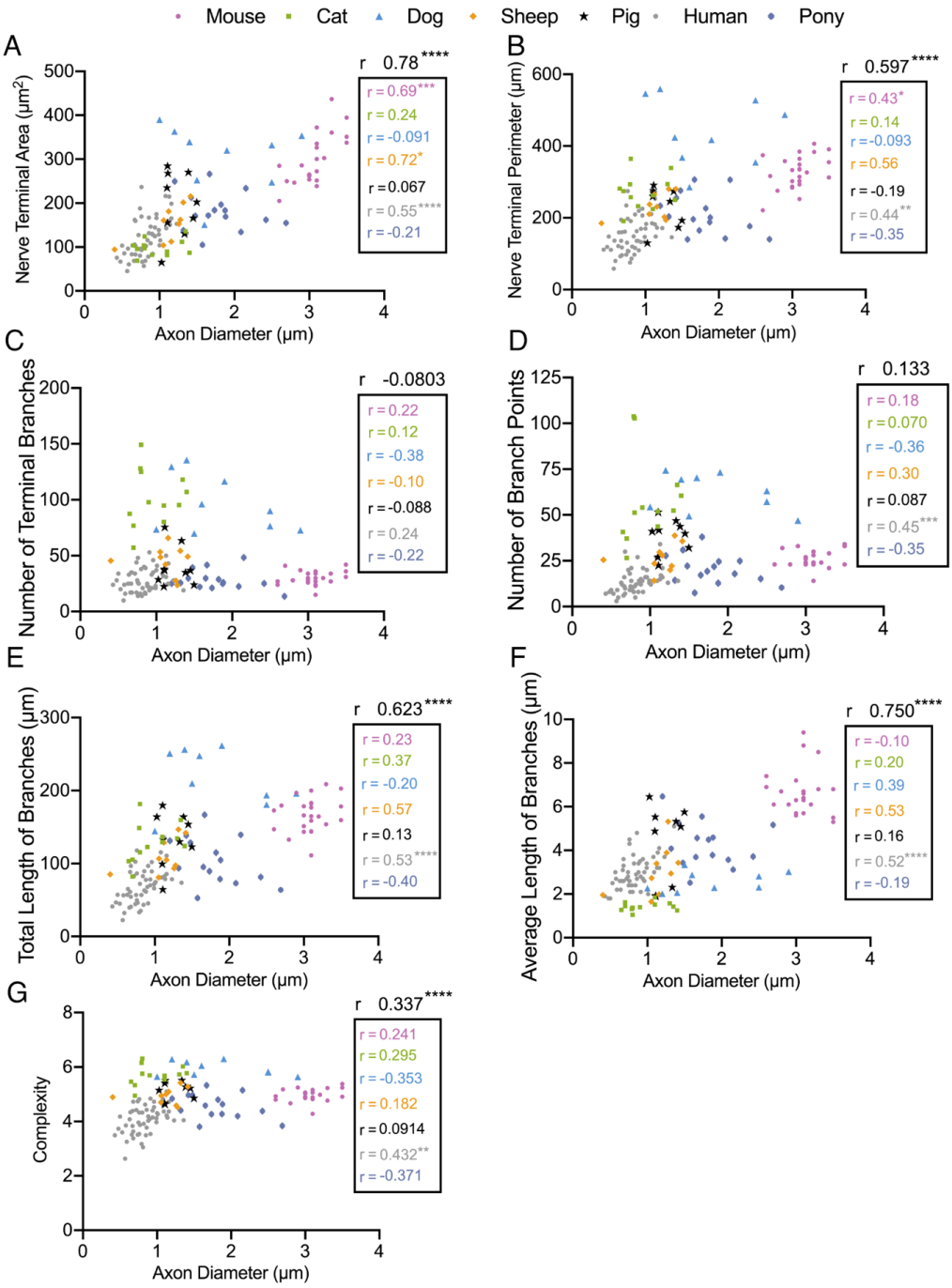

Figure 8-5: Correlation of pre-synaptic NMJ variables with axon diameter

(A–E) core variables, (F–G) derived pre-synaptic variables. Overall, human shows the most correlation of pre-synaptic variables with axon diameter. Branching associated core variables correlate less with axon diameter as in Figure 3 with muscle fibre diameter. Instead, size associated NMJ variables correlate strongly with axon diameter (A–B). Additionally, (E–F) indicate a relationship between the increase in pre-synaptic nerve terminal with increase in axon diameter (A) as average and total branch

lengths increase with axon diameter. Each dot represents the average of one muscle for the respective variable and axon diameter, within analysed species. (Mouse: N = 3 animals, n = 24 muscles; cat: N = 3, n = 12; dog: N = 3, n = 9; sheep: N= 3, n = 9; pig: N = 3, n = 9; human: N = 21, n = 72; pony: N = 5, n = 15) Mouse and human data from Jones et al., 2017.

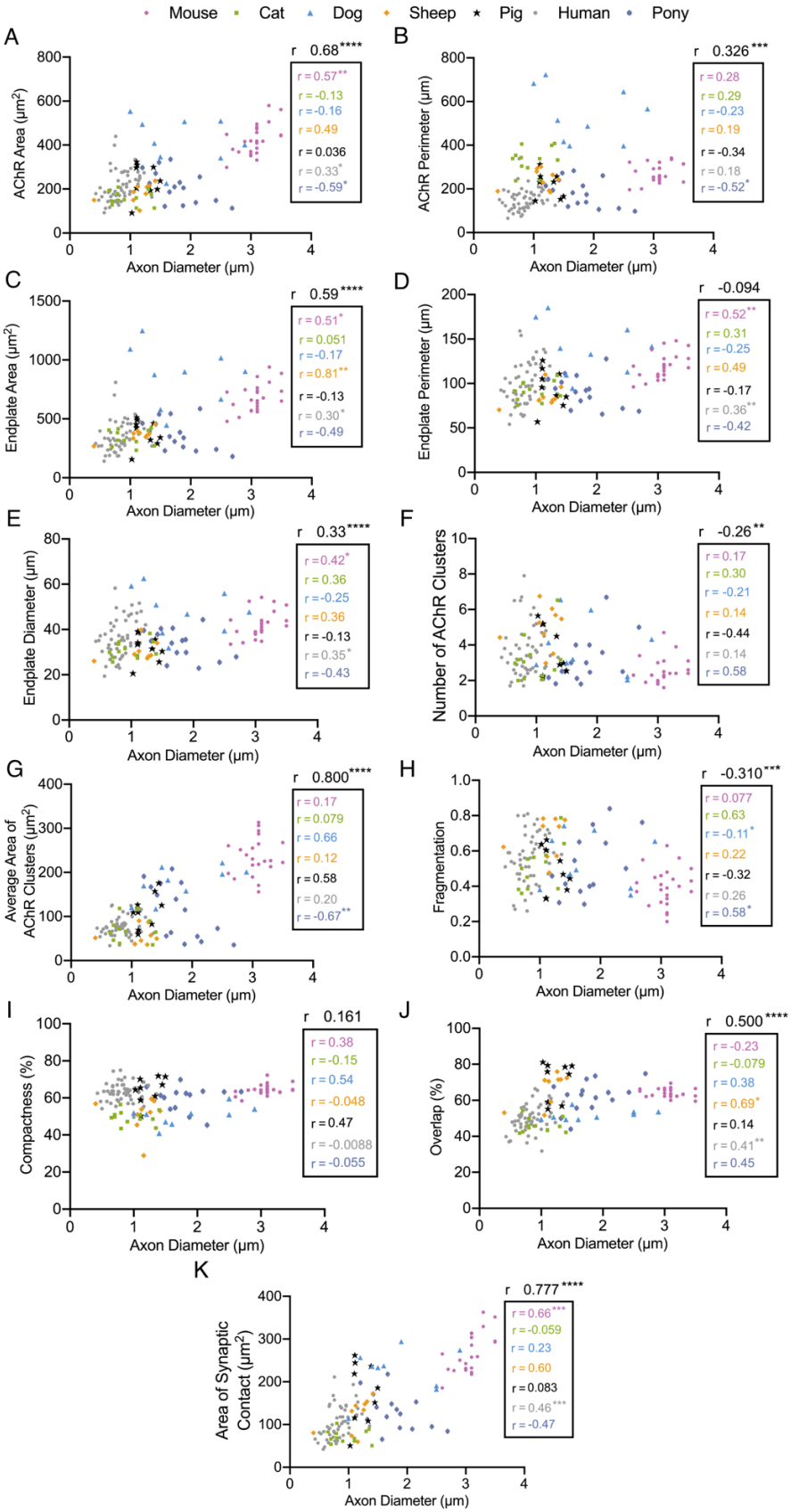

Figure 8-6: Correlation of post-synaptic NMJ variables with axon diameter

(A–F) core variables, (G–K) derived post-synaptic variables. Overall, the huma, mouse and pony show the most correlation of post-synaptic variables with axon diameter. Global correlation with axon diameter is stronger than within species correlation. Globally (across all seven species), endplate perimeter and compactness show no significant linear relationship. However, only NMJ area associated variables: AChR area, endplate area, average area of AChR clusters and area of synaptic contact depict a positive correlation with increasing axon diameter. Each dot represents the average of one muscle for the respective variable and axon diameter, within analysed species. (Mouse: N = 3 animals, n = 24 muscles; cat: N = 3, n = 12; dog: N = 3, n = 9; sheep: N= 3, n = 9; pig: N = 3, n = 9; human: N = 21, n = 72; pony: N = 5, n = 15) Mouse and human data from Jones et al., 2017.